Final Report
NASA Grant NAG 1-1613

"Shape Optimization by Bayesian-Validated Computer-Simulation Surrogates"

Principal Investigator:
Professor Anthony T. Patera
Department of Mechanical Engineering
Massachusetts Institute of Technology

December 30, 1997

SUMMARY OF WORK

The application of large-scale simulation to problems in shape optimization is very difficult for (at least) three reasons. First, the objectives can not always be stated *a priori*, and thus there is reluctance to expend resources. Second, simulations are still very expensive, at least for most complex physical problems, and thus optimization — which calls for repeated appeal to the forward problem — is often prohibitively costly. Third, many interesting problems in shape optimization also require variations in topology; the latter introduces singularities that frustrate many classical optimization procedures.

In this grant, we have proposed an approach to shape optimization that addresses, or at least mitigates, these difficulties. First, as regards how the problem is posed, we have applied concepts from multi-criterion optimization theory, in particular, Pareto theory. The Pareto formulation permits the designer to identify (monotonic) preferences in certain performance metrics (e.g., lift and drag), and then obtain a trade-off curve between these variables; all points on this trade-off curve are optimal in the sense that there is no design point at which both metrics can be improved (e.g., both lift increased and drag decreased). This trade-off curve can then be used to help the designer identify the right balance between different preferences, and determine the optimal operating point once these preferences are established.

Pareto optimization has been used only rarely (if ever) for complex problems in fluid dynamics because the determination of the trade-off curve constitutes a difficult min-max problem that requires many appeals to the (expensive) simulation. Our approach to alleviating this computational bottleneck is to replace the simulation with a simulation surrogate. In particular, we first construct a model, or surrogate, of the input-output behavior of the simulation — based on some small set of input-output pairs — and then use this surrogate, not the original simulation, in the resulting (Pareto) optimization. The surrogate, unlike the original simulation, is very inexpensive to evaluate, and thus extensive optimization can be performed; of course, the surrogate may also be significantly less accurate than the originating simulation.

To address the accuracy question, we have developed an extensive statistical validation procedure and associated theory for understanding how well a surrogate is performing, and whether any particular surrogate-predicted result can be trusted. The latter is, in fact, facilitated by the Pareto framework, since the region of input space of interest is narrowed to the pre-image of the trade-off curve. In particular, if the number of performance metrics of interest (e.g., lift, drag) is small, the Pareto pre-image will typically be a low-dimensional manifold, even if there are many design variables (inputs).

Finally, in order to treat the topology issue, we have implemented a level-set geometry description within the surrogate context. In this approach, shapes are described as level sets of parametrized functions such that (discontinuous) changes in geometry can be described by continuous changes in parameters which, in turn, correspond to continuous changes in the performance metrics. The latter thus permits the use of gradient information, critical to any efficient search algorithm.

The ingredients described above have been demonstrated in the simulation-based optimization of a compact (laminar-flow) heat exchanger. The performance metrics in the Pareto analysis are the pumping power and heat removal; the simulation is a full unsteady Navier-Stokes calculation, on the basis of which a simple (radial-basis function) surrogate input-output model is constructed; level sets are used to describe the geometry of the eddy promoters through which the flow is excited and the thermal-hydraulic performance improved.

The results of this study indicate that our approach can prove quite effective in practice, permitting us to address problems not amenable to other techniques. However simple ("connect-the-dot") surrogate methods are fundamentally limited to rather low-dimensional inputs spaces; although the Pareto approach permits us to validate a surrogate over a low-dimensional manifold, we must first construct the surrogate over the entire input space. As is well-known, approximation in many dimensions is plagued by the "curse of dimensionality" — there are simply too few points in each coordinate to represent the function unless a prohibitively expensive (exponential) number of input-output pairs is used.

One promising approach to improving the dimensionality scaling of surrogates is to exploit state-space based models — models that contain not only simple input-output information, but also information originating in the underlying mathematical system that describes the phenomenon. In a follow-on grant we will be studying this possibility, using for our "surrogate" a low-dimensional numerical approximation, and for our validation procedure a new form of *a posteriori* error estimation theory. The latter also replaces the statistical results of our earlier work with purely deterministic bounds (albeit at some loss in generality).

A detailed description of the results of the current grant are included in Appendix A in the form of a recently completed Ph.D. thesis by John Otto.

PUBLICATIONS

1. M.E. Kambourides, S. Yesilyurt, and A.T. Patera, *Nonparametric-validated computer-simulated surrogates: A Pareto formulation*. International Journal of Numerical Methods in Engineering, to appear.
2. J.C. Otto, D. Landman, and A.T. Patera, *A surrogate approach to the experimental optimization of multielement airfoils*. Technical Report, AIAA Paper 96-4138CP, 1996.
3. J.C. Otto, M. Paraschivoiu, S. Yesilyurt, and A.T. Patera. *Bayesian-validated computer-simulation surrogates for optimization and design*. In N.M. Alexandrov and M.Y. Hussaini, eds., Multidisciplinary Design Optimization: State of the Art, pp. 368-392, 1995.
4. J.C. Otto, M. Paraschivoiu, S. Yesilyurt, and A.T. Patera, *Computer-simulation surrogates for optimization: Application to trapezoidal ducts and axisymmetric bodies*. Technical Report, Proceedings of the Forum on CFD for Design and Optimization, ASME International Mechanical Engineering Conference and Exposition, 1995.
5. J.C. Otto, M. Paraschivoiu, S. Yesilyurt, and A.T. Patera. *Bayesian-validated computer-simulation surrogates for optimization and design: Error estimates and applications*. IMACS Journal of Mathematics and Computers in Simulation, to appear.
6. S. Yesilyurt, C. Ghaddar, M. Cruz, and A.T. Patera, *Bayesian-validated surrogates for noisy computer simulations; application to random media*. SIAM Journal of Scientific Computing, **17** (1996), pp. 973-992.
7. S. Yesilyurt and A.T. Patera, *Surrogates for numerical simulation; optimization of eddy-promoter heat exchangers*. Comp. Methods Appl. Mech. Engr., **121** (1995), pp. 231-257.
8. M. Paraschivoiu and A.T. Patera, *A hierarchical duality approach to bounds for the outputs of partial differential equations*, Comp. Meth. Appl. Mech. Engrg., to appear.
9. M. Paraschivoiu, J. Peraire, and A.T. Patera, A posteriori *finite element bounds for linear-functional outputs of elliptic partial differential equations*, Comp. Meth. Appl. Mech. Engrg., **150** (1997), pp. 289-312.
10. M. Paraschivoiu, J. Peraire, Y. Maday, and A.T. Patera, *Fast bounds for outputs of partial differential equations*, in J.A. Burns, E.M. Cliff, and B. Grossman, eds., Proceedings AFOSR Workshop on Optimal Design and Control, Washington, D.C., to appear.
11. J. Peraire and A.T. Patera, *Bounds for linear-functional outputs of coercive partial differential equations: local indicators and adaptive refinement*, in P. Ladeveze and J.T. Oden, eds., Proceedings of the Workshop on New Advances in Adaptive Computational Methods in Mechanics, Cachan, France, Elsevier, 1997.

APPENDIX A

A Nonparametric–Validated Surrogate Approach to Shape Optimization Using a Level–Set Based Geometry Description

by

John C. Otto

B.S., Aeronautical and Astronautical Engineering, University of Illinois (1990)
M.S., Fluid Mechanics and Thermal Sciences, George Washington University(1993)

Submitted to the Department of Aeronautics and Astronautics
in partial fulfillment of the requirements for the degree of

Doctor of Philosophy

at the

MASSACHUSETTS INSTITUTE OF TECHNOLOGY

November 1997

Author .....
Department of Aeronautics and Astronautics
November 25, 1997

Certified by .....
Anthony T. Patera
Professor of Mechanical Engineering
Thesis Supervisor

Certified by .....
Mark Drela
Associate Professor of Aeronautics and Astronautics

Certified by .....
James D. Paduano
Assistant Professor of Aeronautics and Astronautics

Accepted by .....
Jaime Peraire
Chairman, Departmental Committee on Graduate Students

A Nonparametric–Validated Surrogate Approach to Shape Optimization Using a Level–Set Based Geometry Description

by

John C. Otto

Submitted to the Department of Aeronautics and Astronautics
on November 25, 1997, in partial fulfillment of the
requirements for the degree of
Doctor of Philosophy

Abstract

A nonparametric–validated, surrogate approach to optimization has been applied to the computational optimization of eddy–promoter heat exchangers and to the experimental optimization of a multielement airfoil. In addition to the baseline surrogate framework, a surrogate–Pareto framework has been applied to the two–criteria, eddy–promoter design problem. The Pareto analysis improves the predictability of the surrogate results, preserves generality, and provides a means to rapidly determine design trade–offs. Significant contributions have been made in the geometric description used for the eddy–promoter inclusions as well as to the surrogate framework itself.

A level–set based, geometric description has been developed to define the shape of the eddy–promoter inclusions. The level–set technique allows for topology changes (from single–body, eddy–promoter configurations to two–body configurations) without requiring any additional logic. The continuity of the output responses for input variations that cross the boundary between topologies has been demonstrated. Input–output continuity is required for the straightforward application of surrogate techniques in which simplified, interpolative models are fitted through a construction set of data.

The surrogate framework developed previously has been extended in a number of ways. First, the formulation for a general, two–output, two–performance metric problem is presented. Surrogates are constructed and validated for the outputs. The performance metrics can be functions of both outputs, as well as explicitly of the inputs, and serve to characterize the design preferences. By segregating the outputs and the performance metrics, an additional level of flexibility is provided to the designer. The validated outputs can be used in future design studies and the error estimates provided by the output validation step still apply, and require no additional appeals to the expensive analysis. Second, a candidate–based *a posteriori* error analysis capability has been developed which provides probabilistic error estimates on the true performance for a design randomly selected near the surrogate–predicted optimal design.

Thesis Supervisor: Anthony T. Patera
Title: Professor of Mechanical Engineering

Acknowledgments

Foremost, I would like to acknowledge the immeasurable guidance, help, and encouragement provided by Professor Anthony T. Patera. Beyond anyone else, he made this work not only possible, but immensely enjoyable, and for that I am extremely grateful.

I also thank those in my research group, none of whom were ever too busy for a discussion or to offer assistance, especially Dr. Serhat Yeşilyurt, Dr. Marius Paraschivoiu, Dr. Chahid Ghaddar, Nicolas Hadjiconstantinou, Miltos Kambourides, Dr. Mariano E. Gurfinkel, Matteo Pedercini, and Jeremy Teichman. I would also like to thank everyone else in the Fluid Mechanics Laboratory who helped to make the lab such an outstanding place to work. Because of them, I was always able to look forward to coming in to work.

I thank Professor Drew Landman at Old Dominion University for providing the experimental data used in Chapter 6 and for many helpful discussions.

I am very grateful for the opportunities afforded me during my time at NASA Langley Research Center. Many people at LaRC had an enormous influence on me and I benefited from discussions with all of them. I would especially like to thank Dr. Ajay Kumar for giving me the chance to begin down this path, Dr. Thomas A. Zang, Dr. Natalia Alexandrov, Dr. R. Michael Lewis at ICASE, and Dr. Virginia Torczon at the College of William and Mary.

Finally, I would like to thank my wife Karen, who has never failed to support me throughout this work, and has done so despite being under the identical pressures of pursuing her own doctorate. Countless times she has had to carry the load for two. Her unlimited love and encouragement kept me going and I will forever be grateful that we have a lifetime together.

This work was supported by NASA Grant NAG 1-1613, AFSOR Grant F49620-97-0052, and the NASA Graduate Training Program.

Contents

List of Figures

List of Tables

Chapter 1

Introduction

1.1 Motivation

The unprecedented advances in both computational and simulation capabilities have spurred a shift in focus from the development, improvement, and application of single-analysis techniques, to the incorporation of high-fidelity simulations into formal design optimization frameworks. Although formal optimization techniques have been widely used in structural design [34, 75], they have only recently been used regularly in fluids applications. Computational fluid dynamics simulations are typically very CPU-intensive, and when directly inserted into optimization routines as a function-call, the evolution of the design to a local optimal will advance extremely slowly. The lack of interactivity that characterizes such an approaches may be acceptable in the very late stages of the design, but is unacceptable in the early stages of design in which widely varying configurations are often examined and trade studies are typically conducted.

Preliminary design is, intrinsically, an interactive process. It requires that a large number of assessments be made rapidly as design parameters are changed and updated. Furthermore, as more is learned about the design in terms of its performance and reaction to changes in input quantities, goals are likely to evolve and change as well. Methods in which each design cycle requires hours, or even days, are clearly not useful during the evolutionary stages of preliminary design in which flexibility and interactivity are most valuable.

An approach that has been widely pursued in an attempt to shift as much information as possible from the late stages of the design process, where radical changes are much too costly to be practical, to the early stages, where many design scenarios and configurations are considered, is through analysis–approximation schemes. Fundamental to such approaches is the notion that the extremely high simulation cost can be front-loaded, and precisely budgeted to the construction of simulation *surrogates*: inexpensive input-output functions that duplicate the responses of the high-fidelity simulation. The simulation surrogates can then be coupled with the formal optimization techniques, the result of which is a

(potentially) highly-accurate, interactive design framework.

The primary drawback to surrogate-based optimization approaches is the uncertainty that is introduced, both in terms of how the performance predicted by the high-fidelity simulation differs from that of the surrogate near particular designs, *predictability*, and also as to how a surrogate-predicted optimal design point compares to the simulation-based optimal design point, *optimality* [7]. Beyond post-evaluation of surrogate-predicted design points with the simulation, both predictability and optimality are often times ignored in surrogate-based optimization methods reported elsewhere. The validation and error analysis steps of the nonparametric-validated surrogate framework described, and applied, in Chapters 4—5 seeks to address these issues.

A second issue in design optimization is how to best parameterize the surfaces of the object to be optimized. A great deal of effort has focused on shape parameterizations. In the work presented here, the underlying desire to examine shape-families that include multiple topologies (single and two-body configurations), and to treat the entire family in a unified approach, has greatly restricted the types of methods that are appropriate. The problem central to this thesis is of an eddy-promoter heat exchanger. The desire to extend the design problems beyond the single cylinder designs examined in previous work [41, 77, 79], and the potential beneficial interaction that may result from two-body configurations, has motivated the requirement that the shape-family encompass multiple topologies.

1.2 Design Optimization

Formal design optimization procedures have received increased attention in the fluid dynamics community recently. Both the increased computer capabilities and the improvements in computational fluid dynamics codes in terms of robustness and capabilities have contributed to the gradual shift to formalized design optimization. In general, the optimization approaches that have been pursued can be broken into two broad categories: *on-line*, direct insertion approaches in which the CFD simulation serves as a function call inside of the optimization routine, and *off-line*, surrogate approaches in which the CFD simulation is used to construct simplified input-output models that are then used in the formal optimization routines. Each approach has associated advantages and drawbacks that make the choice between which is *best* problem dependent.

The primary advantage to on-line optimization strategies is that they can handle problems with a large number of input (design) variables very efficiently. Optimization methods are typically gradient based, and restricted to local searches, which reduces the effective dimension of the problem to that of the low-dimensional manifold traversed during the optimization process. Issues as to whether a local or global optimal point is achieved at the end of the process remain, but at the least, the local searches can be accomplished with

a moderate number of appeals to the analysis even for problems with very large (in terms of independent inputs) problems. An additional advantage, in the context of the comparison between on-line and off-line strategies, is that upon completion of the on-line design optimization, a true optimal point is obtained.

The biggest drawback to on-line optimization approaches is the inordinate amount of CPU time that they usually require. The underlying analysis codes are often very expensive, requiring on the order of hours of CPU time for a single analysis case. Not only is the computational time inordinately large, it is very difficult to know *a priori* how many simulation evaluations will be required by the optimizer, making accurate resource budgeting impossible. Scenarios in which computational resources are exhausted before a meaningful design is obtained can be easily envisioned. Furthermore, as more is learned about the design during its evolution, goals and specifications often need to be modified as well. Changes in design parameters require an entirely new set of simulation analyses to perform the requisite design optimization update. The large computational cost of the on-line techniques greatly reduces the flexibility of the design process and makes interactivity out of the question. Secondarily, integration of the analysis code with the optimization routine can be difficult, especially for multidisciplinary optimization applications, irregularities in the analysis response can cause convergence problems, and finally, the incorporation of data from outside sources is difficult.

Off-line, surrogate optimization approaches offer a number of advantages that directly address the disadvantages of on-line optimization. First, by design, the input-output surrogates are trivial to evaluate, ensuring that the optimization process can be completed in a reasonable amount of time and global optimal points can be obtained. The computational burden is placed on the construction of the input-output surrogates which occurs prior to any optimization. Because surrogate construction is performed off-line, and because the cost of a single analysis can be accurately estimated, available resources can be precisely budgeted. Design goals can be changed, and new optimal points obtained, throughout the process, and interactivity is preserved. Integration is greatly simplified as all information is contained in a simplified input-output function, smoothness can be enforced on the surrogates, and data from outside sources is readily incorporated into the surrogate construction process.

As already stated, the primary drawback to approximate optimization strategies is a consequence of the surrogate-for-simulation error. The construction of surrogates in high dimension input spaces is difficult, and as will be shown in Chapter 4, design predictability deteriorates rapidly with increased input dimension. The validation and *a posteriori* error analysis stages of the surrogate framework seek to address the errors that are incurred when optimizing with respect to a simplified model as opposed to the high-fidelity analysis.

1.2.1 Approximate Optimization Techniques

Approximate optimization techniques have been pursued in wide range of optimization contexts [3]. Central to the notion of approximate optimization is that a (typically) expensive analysis represents the truth. Direct insertion of the analysis code into the optimization routine is prohibited by the high cost associated with each appeal to the analysis and a simplified model (a surrogate) is typically used in place of the analysis. The only requirement is that the surrogate approximate the relevant input–output relationships of the analysis. An obvious approach is to sample the analysis at a set of input points, obtain the corresponding outputs, and form a response surface [10]. The response surface serves as a simulation surrogate in the optimization [21, 67]. The surrogates can also be lower fidelity, less expensive simulations. Variable–complexity, response surface strategies [32] incorporate a hierarchy of approximations into the optimization process.

The distinction that is made between the high–fidelity analysis and the simplified approximation can be made more general. For example, an experiment may serve as the truth and a simplified input–output model would be the surrogate. An application of this type has been examined in Chapter 6 and is also reported in [54].

1.2.2 Nonparametric–Validated Surrogate–Based Optimization

The key feature that is lacking in many approximate optimization strategies is a rigorous, well–integrated means for error estimation. Post evaluation of the surrogate–predicted designs is widely used and provides the requisite information to determine how a design actually performs. However, many times even a single simulation evaluation will destroy the interactivity of the design process. In situations in which several designs are selected, the cost of appealing to the analysis for each design become prohibitive. Also, in many situations the analysis may not be readily available during the design phase (certainly the case for the experimental optimization problem in Chapter 6). Finally, while post evaluation does inform the designer as to how the selected point performs, it provides no guidance as to what should be done if design goals are not met and does not give any information as to how nearby points perform. Post evaluation does not address how surrogate–predicted optimal designs relate to true optimal designs.

The nonparametric–validated surrogate framework seeks to address the surrogate–for–simulation error. The baseline framework [77, 79] can be broken into three steps: (1) Off–line surrogate construction and validation. (2) Surrogate–based design optimization. (3) *A posteriori* error analysis. The framework can accept and assess any combination of surrogate and truth simulation (or experiment), and is valid regardless of the approximation quality of the surrogate. The results are rigorous, based only on verifiable assumptions, and require no additional parameters which typically must be estimated. Additionally, the error

estimates apply to the *specific* design (or region near the design) and precisely quantify the response. By contrast, root-mean-square errors used in the context of response surfaces [10] provide an assessment of the overall surrogate approximation accuracy but can not be easily applied to analysis of surrogate-predicted optimal designs.

he baseline surrogate framework was first developed by [77, 79] for non-noisy simulations. It has been extended to the analysis of simulations with noisy outputs [78, 77] in which the output error is symmetric and unbounded. The original, baseline framework has been extended to a more general, scaled-error formulation for multiple outputs [57] and more sophisticated elemental, sequential, and adaptive techniques have been developed as well [55, 56]. Finally, surrogate methods have been coupled with Pareto analysis for problems with multiple, competing performance goals [36, 37].

The surrogate methods have been applied to a wide range of problems. The eddy-promoter heat exchanger that is examined in Chapters 2—5 has also served as an illustrative problem in [36, 77, 79]. The baseline surrogate framework has been used to optimize the profile of axisymmetric bodies of revolution in Stokes flow [55, 56, 57]. The noisy output formulation has been applied to conduction in random media [78, 77] and the elemental and sequential/adaptive techniques have been applied to the conduction problem of a composite [55] and design of trapezoidal ducts [56].

In this thesis, the baseline surrogate framework with error scaling given in [57] is first applied to the eddy-promoter heat exchanger design problem that is characterized by two performance metrics. The performance metrics are functions of outputs from the simulation as well as explicitly of one of the design inputs. The surrogate framework has been extended to assess a general two output, two performance metric problem in which the simulation outputs are validated. By validating the outputs instead of the performance metrics, an additional level of flexibility is afforded the designer in that the validated output can be used in later design studies with modified performance metrics. A distinction is made between the inputs which are modeled to construct the output surrogates, and those for which the performance metric response is known analytically. By separating the design inputs in this way, the greatest advantage can be taken of what is known analytically. The surrogate theory has also been extended to assess the error on a design point randomly drawn near the surrogate predicted optimal design. The original surrogate framework made an assessment of the surrogate error incurred for regions of points near the surrogate-predicted optimal point.

Second, because the eddy-promoter problem is characterized by two, competing performance metrics, and because the output surrogates and hence the performance metrics are very inexpensive to evaluate, a Pareto formulation of the problem is pursued. An extremely valuable synergy between the Pareto analysis and the surrogate methods has been identified [36] in previous work. In high input dimensions, the predictability results of the surrogate

framework become very poor. To alleviate the loss in predictability, a Pareto analysis is pursued which reduces the effective dimension of the problem from the number of inputs to one less than the number of performance metrics. For the two performance metrics eddy–promoter problem, the Pareto analysis reduces the optimization problem to that of a single parameter and sacrifices very little generality in the process. A fine–grained Pareto analysis of the eddy–promoter problem using the simulation is totally out of the question and a surrogate strategy is necessary to make the problem tractable.

Finally, in Chapter 6, the baseline surrogate framework is applied to the experimental optimization of the three–element airfoil. The experiment is assumed to be deterministic, and the non–noisy formulation is used.

1.3 Shape Optimization

The eddy–promoter, heat exchanger that serves as the central example for the majority of this thesis falls into the wide class of shape optimization problems [63, 65]. Shape optimization problems are present in most engineering disciplines. The general structural design problem of determining the optimal truss is one such problem. For the truss problem, the thickness, length, positions, and possibly the existence of the various components must be determined and serve as inputs. Numerous shape problems can be found in the field aerodynamics. The optimization of a wing (both planform and the cross–sectional airfoil shape) to achieve desired lift, drag, and stall characteristics is frequently considered and of critical importance for aircraft design. The design of a wind–tunnel nozzle contour to achieve a prescribed flow profile in the test section is another example of shape optimization.

1.3.1 Topology

An important consideration in some shape optimization problems is that of topology. In truss problems [6], not only do elements need to be sized in terms of thicknesses and lengths, but connectivities and existence must also be considered. This extends truss optimization from simply that of sizing to include topology of the truss components as well. Several approaches to topology optimization have been demonstrated on structural optimization problems. The first approach is the ground structure method in which a given set of connections is allowed between a fixed set of nodes, and the problem is posed as a continuous optimization problem in which sizes can go to zero. Zero sized truss components imply no connection between the two nodes [4]. This approach is restrictive in that the connectivity (or the family of allowable connectivities) is assumed at the outset.

The second approach to topology optimization, homogenization methods [4, 5, 16, 72], seeks to treat the problem in a more unified, pseudo–continuous sense. In a homogenization formulation, the distribution of a material property (e.g. modulus or density) serves as the

design variable, and the design is optimized for a given objective. Regions of the structure in which the value of the material property falls below a given cutoff are assumed to be voids in the structure. Because an underlying mesh is required, the resulting truss must often times "cleaned up" to smooth boundaries. The post-optimization smoothing that is required calls into question the actual optimality of the resulting structure.

A third strategy used to find the optimal topology of a structure, zero-one methods [1, 29], discretizes the solution domain into a a mesh of points and each point is systematically turned "on" and "off" until an optimum is achieved. The problem is thus reduced to the combinatorial optimization problem of finding the best set of material points that satisfy the constraints and minimizes the objective.

While such treatments of topology optimization have been effective in many instances for solid mechanics applications, they are not directly applicable to fluid problems and are still more unsuitable for surrogate-optimization approaches. Topology is an important consideration, however, for some classes of fluid problems and should therefore not be neglected. The particular application explored in this thesis, the eddy-promoter heat exchanger, is one example of a problem that can benefit greatly from a unified treatment of multiple topologies. In particular, situations in which two bodies may favorably interact, and which may be more efficient than single body configurations, can be easily envisioned.

None of the strategies pursued for the structural topology optimization are directly relevant or applicable to the eddy-promoter problem. Homogenization techniques do not have an analogous extension to fluid problems that is physically reasonable. The discrete zero-one methods could be applied but suffer from several drawbacks. First, for the very expensive analysis that is used for the eddy-promoter problem, the combinatorial optimization problem would be prohibitively expensive. A sufficiently refined discretization of the solution domain would make the problem still more intractable. Second, the zero-one techniques are not at all applicable to the surrogate techniques (e.g. a smooth input-output function can not be fit through a 20×20 mesh of discrete zero-one inputs) that are required to make the problem computationally possible. Third, and finally, the resulting optimal shapes are non-smooth and are likely not optimal in the sense of viscous dissipation. Post-processing of the optimal shapes to smooth the surfaces could be used, but relationship between the smoothed bodies and the true optimizers is unknown. The incompatibilities between the structural topology methods described above and the eddy-promoter design problem have motivated the development of a level-set based geometry description.

1.3.2 Level Set Geometry Description

The approach that has been developed to describe the geometry sacrifices the generality of the homogenization and zero-one techniques, but is more relevant to the eddy-promoter class of fluid problems. It is a level-set based technique and has several advantages. First,

it provides an unified (albeit restricted) approach to topology optimization in that no additional logic is needed to distinguish between single or multiple body configurations. Second, it is directly applicable to surrogate approaches as it is efficient in terms of the number of inputs that are required and, most importantly, the input–output function is continuous across a topology change. Third, the family of shapes that are described by the level–set method are a superset of the cylindrical family studied elsewhere [40, 77, 79] making the results directly relevant to previous studies. Finally, it can be extended to more complex geometries and topologies in a rational way. The geometry is defined using superposition principles and a core, generating function. By systematically adding core functions to the overall shape function, richer families of bodies can be defined, and a wider class of topologies can be considered. For the problem examined here, two distinct topologies are considered: single–body and two–body configurations.

Level–set methods have been used previously to describe the domain in shape optimization problems [12, 80]. More recently, level–set methods have been widely applied to problems that involve propagating surfaces or interfaces [53]. This includes problems such as flame propagation and material boundary evolution. Level set methods have also been applied to character recognition (the determination of true character boundaries) [52] and image enhancement in the presence of noise. One of the principle strengths of level–set methods is their ability to handle difficult geometries including sharp corners, cusps, and topological changes [13]. The specific method used to describe the geometries is given in Section 2.5.

1.4 Overview of the Thesis

In the first chapter of this thesis, the eddy–promoter problem is described. The configurations, governing equations, shapes descriptions and summary of the fundamental design inputs, outputs, and performance metrics are included. In the second chapter, the numerical solution techniques used to solve the governing equations are detailed. The baseline surrogate framework is applied to the eddy–promoter problem in the third chapter and the Pareto surrogate approach is applied to the eddy–promoter problem in the fourth chapter. At the end of the fourth chapter, key features of the baseline and Pareto approaches are compared and contrasted. In the fourth chapter, the baseline surrogate approach is applied to the experimental optimization of a three element airfoil. Finally, some concluding remarks are given in the final chapter followed by appendices that contain surrogate proofs, details of the numerical implementation, and the surrogate input–output functions.

Chapter 2

Eddy–Promoter Heat Exchanger

A natural byproduct of almost all mechanical processes is unwanted heat. The amount of work in the field of heat transfer problems in general has reached such a critical mass that reviews of heat transfer reviews are available [19]. Additionally, heat exchangers are present in almost all mechanical systems and have received a great deal of attention as well [25, 76]. The requirement that the heat be efficiently dissipated to preserve mechanical integrity without incurring undue performance penalties has helped to support a very active field of research focused on heat transfer enhancement.

One approach to the removal of heat from a surface is through a laminar flow heat exchanger. In such an exchanger, heat is transfered from a generation source into a fluid medium and carried downstream. A number of ways exist to enhance the heat transfer away from the wall of the channel and into the fluid medium. These include active mechanisms such as oscillatory pumping of the fluid or passive enhancement in which wall contouring or flow obstacles are introduced into the fluid channel to increase mixing. For all of the methods, the intent is to increase the convective heat transfer by increasing the mass transport away from the wall.

The heat exchanger geometry introduced in this chapter, and used as an example in Chapters 4 and 5, uses a passive enhancement strategy in which flow obstacles are introduced to lower the critical Reynolds number. The exchanger, as defined here, could be a subsystem in a much larger industrial heat exchanger device or could be a very close approximation to a design that might be used in a space-limited application such as the cooling of electronic devices. The enhancement geometries studied here take as a departure point work performed earlier in which cylindrical inclusions (eddy-promoters) were studied [41]. The cylindrical eddy-promoters greatly reduce the Reynolds number at which flow instabilities develop. The onset of instabilities have been observed at Reynolds numbers as low as 125 when the eddy-promoters are present [40]. The presence of the eddy-promoter inclusions greatly increases the temperature convection in the channel and therefore, improves the heat transfer. The family of eddy-promoter geometries studied here include cylindrical

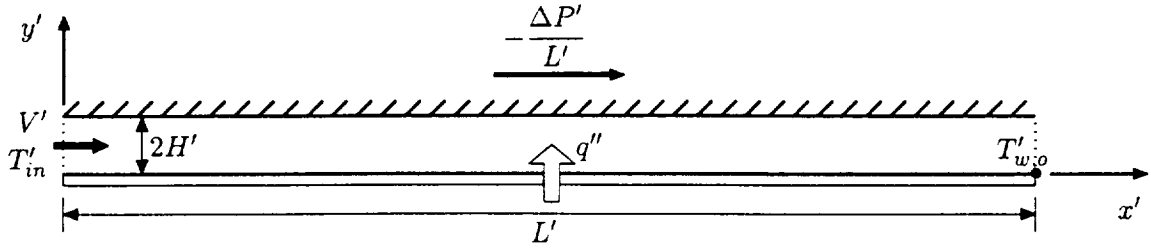

Figure 2-1: General geometry for the heat-exchanger configuration.

inclusions, oblong inclusions at various orientations, and two body configurations. A unified geometry description has been developed to describe the full family of geometries that preserves continuity in the input-output functions. The geometry description is based on level-set methods and is described in Section 2.5.

In this Chapter, the general configuration and design goals for the eddy-promoter heat exchanger problem are presented. A description of the heat exchanger configuration and the simplifications made for later computations are presented first. Second, the governing equations and the scalings that are made to reduce the problem to nondimensional form are described. Third, the engineering goals for the problem are discussed and the nondimensional formulation for the design problem are given. Fourth, the Pareto formulation is presented followed by the level-set based geometry description. Finally, the reduced formulation for the eddy-promoter design problem is presented in terms of the design inputs, design spaces, outputs, and performance metrics.

2.1 Physical Problem

The general configuration of the heat exchanger is given in Figure 2-1. The flow is from left to right and is driven by an applied pressure gradient $-\frac{\Delta P'}{L'}$. The channel length is L' and the channel half height is H'. The temperature of the fluid at the inflow is T'_{in}, the wall temperature at the outlet is $T'_{w,o}$, and the channel average velocity V' is

$$V' = \frac{1}{2H'} \int_0^{2H'} u' dy', \tag{2.1}$$

where u' is the x'-component of the vector velocity $\mathbf{u}' = (u', v')$. There is is a uniform heat flux q'' through the lower wall and the upper wall is assumed to be insulated. The objective is to transfer as much heat as possible through the lower wall, into the fluid stream, and out of the heat exchanger channel.

A number of methods exist to effect better transfer of heat into the fluid medium. These include unsteady pumping, grooved walls, and the inclusion of periodically-spaced, cylin-

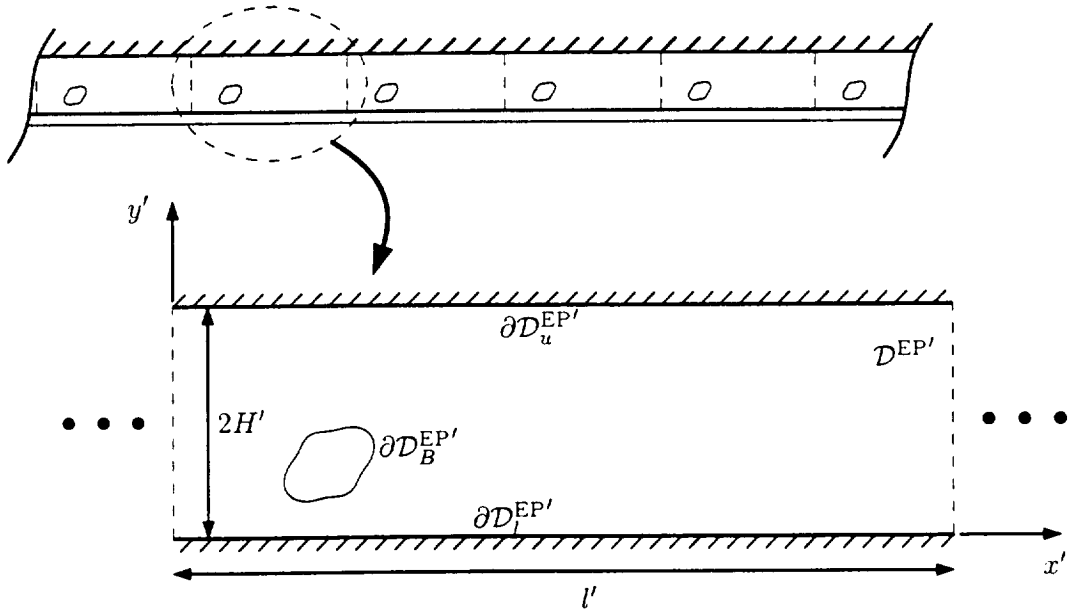

Figure 2-2: General geometry eddy-promoter, heat-exchanger configuration (top) showing one periodicity cell (bottom).

drical obstructions referred to as eddy-promoters. In this work, the focus will be exclusively on the eddy-promoter configurations, a segment of which is shown at the top of Figure 2-2. The periodicity spacing (the length between inclusions) for the eddy-promoters is l'. The primary effect that the eddy-promoters have on the flow is to trip instabilities at greatly reduced Reynolds numbers than observed for plane channel flows. Two-dimensional, linear instabilities are observed in channel flows at Reynolds numbers based on the channel half height H' of approximately 5500 [17, 60]. For properly placed and sized cylindrical eddy-promoters, the onset of two-dimensional flow instabilities have been observed numerically and experimentally at Reynolds numbers as low as 125 [40, 41]. The unsteady flow increases the convective transfer of heat away from the wall and increases the efficiency of the exchanger.

As already stated, the heat transfer can be increased by the inclusion of obstacles in the flow to induce instabilities at lower Reynolds numbers. While the periodically spaced flow obstacles do increase the heat transfer, the increase comes at the cost of a higher pressure drop and greater viscous dissipation. The result of the higher pressure drop is that a more powerful fluid pump must be employed, increasing the cost and complexity of the exchanger. Additionally, excessive viscous dissipation, pressure forces, and shear stresses produce larger structural loads that must be balanced by stronger materials to avoid fatigue failures.

The effectiveness of the exchanger can be quantified by two characteristics: how much heat it can transfer away from the hot wall and how much effort is required to accomplish the

transfer. The two quantities that characterize the exchanger are, in most instances, at odds with each other. Clearly, the heat exchanger design is an example of a thermal–hydraulic trade–off problem. In words, the goal of the heat–exchanger problem is to maximize the heat transfered into the fluid medium and carried downstream while holding the required pumping power as low as possible. These competing goals form the trade–off problem.

2.2 Governing Equations

The total exchanger length L' is assumed to be such that the flow is fully developed in x'. Additionally, the flow is assumed to be independent of the spanwise coordinate and is modeled as a two–dimensional problem.. Furthermore, for a periodicity spacing, l', between eddy–promoter inclusions that is also sufficiently long, the fluid solution will be also be l'–periodic. With these two assumptions, the full exchanger length can be modeled with a single periodicity cell that enforces periodic boundary conditions at each end.

The flow solution for the full channel shown in Figure 2-2 is modeled by a single periodicity cell as depicted in the lower half of Figure 2-2. The fluid flow solution is governed by the incompressible Navier–Stokes equations and it is assumed that all fluid properties are held constant and are independent of the fluid temperature. The equations governing the fluid flow, in dimensional form are

$$\rho\frac{\partial \mathbf{u}'}{\partial t'} + \rho\mathbf{u}'\cdot\nabla'\mathbf{u}' - \mu\nabla'^2\mathbf{u}' + \nabla'\pi' = 0, \tag{2.2}$$

$$\nabla'\cdot\mathbf{u}' = 0, \tag{2.3}$$

where ρ is the fluid density, μ is the fluid viscosity, and π' is the pressure. No–slip boundary conditions are enforced on the velocity along solid walls

$$\mathbf{u}' = 0 \text{ on } \partial\mathcal{D}_l^{\mathrm{EP}'},\ \partial\mathcal{D}_u^{\mathrm{EP}'},\ \partial\mathcal{D}_B^{\mathrm{EP}'}, \tag{2.4}$$

and left–right periodicity is enforced on the flow velocity and derivatives

$$\mathbf{u}'(x'=0,y',t') = \mathbf{u}'(x'=l',y',t'), \tag{2.5}$$

$$\mathbf{u}'_{x'}(x'=0,y',t') = \mathbf{u}'_{x'}(x'=l',y',t'), \tag{2.6}$$

$$\mathbf{u}'_{y'}(x'=0,y',t') = \mathbf{u}'_{y'}(x'=l',y',t'). \tag{2.7}$$

The pressure $\pi'(\mathbf{x}',t')$ has the form

$$\pi'(\mathbf{x}',t') = p'(\mathbf{x}',t') - \frac{\Delta P'}{L}x', \tag{2.8}$$

where $\mathbf{x}' = (x', y')$ is the vector of coordinate directions in two-dimensions and $-\frac{\Delta P'}{L}$ is the pressure gradient that drives the flow. The periodic part of the pressure, $p'(\mathbf{x}', t')$, satisfies

$$p'(x' = 0, y', t') = p(x' = l, y', t'). \tag{2.9}$$

The temperature is governed by the scalar, convection-diffusion equation

$$\frac{\partial T'}{\partial t'} + \nabla' \cdot (\mathbf{u}' T') = \alpha \nabla'^2 T', \tag{2.10}$$

where T' is the full temperature solution and $\alpha = \frac{\kappa}{\rho c_p}$ is the thermal diffusivity. For this equation to hold, it is assumed that the thermal conductivity, κ, is independent of the temperature, that diffusion can be neglected, and that there is no internal heat generation. The boundary conditions for the temperature are the prescribed uniform heat flux through the lower wall

$$\kappa \nabla' T' \cdot \hat{\mathbf{n}} = q'' \text{ on } \partial \mathcal{D}_l^{\mathrm{EP}'}, \tag{2.11}$$

and zero heat flux (insulating surfaces) through the eddy-promoter body surface and the upper wall

$$\kappa \nabla' T' \cdot \hat{\mathbf{n}} = 0 \text{ on } \partial \mathcal{D}_B^{\mathrm{EP}'}, \ \partial \mathcal{D}_u^{\mathrm{EP}'}. \tag{2.12}$$

The heat flux q'' is assumed positive for heat transfer into the domain and $\hat{\mathbf{n}}$ is the unit outward normal.

The full temperature, T', is decomposed into two components

$$T'(\mathbf{x}', t') = \theta'(\mathbf{x}', t') + \gamma' x'. \tag{2.13}$$

The linear part of Equation 2.13 is the most general form for which there is a unique solution such that $\theta'(\mathbf{x}', t')$ satisfies periodicity [30]

$$\theta'(x' = 0, y', t') = \theta'(x' = l, y', t'). \tag{2.14}$$

The derivation of the coefficient γ' is given below.

The governing equation for θ' is obtained by substituting Equation 2.13 into the temperature equation 2.10

$$\frac{\partial \theta'}{\partial t'} + \nabla' \cdot (\mathbf{u}' \theta') = \alpha \nabla'^2 \theta' - \gamma' \mathbf{u}' \hat{\mathbf{e}}_1, \tag{2.15}$$

where $\hat{\mathbf{e}}_1 = (1, 0)$ is the unit vector in the x-direction. The boundary conditions on θ' are obtained similarly and are

$$\kappa \nabla' \theta' \cdot \hat{\mathbf{n}} = q'' \text{ on } \partial \mathcal{D}_l^{\mathrm{EP}'}, \tag{2.16}$$

$$\kappa \nabla' \theta' \cdot \hat{\mathbf{n}} = -\kappa \gamma' \hat{n}_1 \text{ on } \partial \mathcal{D}_B^{\mathrm{EP}'}, \ \partial \mathcal{D}_u^{\mathrm{EP}'}, \tag{2.17}$$

where $\hat{n}_1$ is the component of the unit outward normal vector, $\hat{\mathbf{n}} = (\hat{n}_1, \hat{n}_2)$, in the x'-direction.

Because solution domain $\mathcal{D}^{\mathrm{EP}'}$ is a single periodicity cell of the full heat exchanger shown at the top of Figure 2-2, the coefficient γ' in Equation 2.13 must be set such that heat does not build up in the channel, on average, over time scales of the order of period of the steady-periodic state. To determine the constant coefficient γ', the temperature Equation 2.10 is integrated over the solution domain $\mathcal{D}^{\mathrm{EP}'}$

$$\frac{\partial}{\partial t'} \int_{\mathcal{D}^{\mathrm{EP}'}} \theta' \, d\mathbf{x}' = - \int_{\mathcal{D}^{\mathrm{EP}'}} \nabla' \cdot [\mathbf{u}'(\theta' + \gamma' x)] \, d\mathbf{x}' + \int_{\mathcal{D}^{\mathrm{EP}'}} \alpha \nabla'^2 \theta' \, d\mathbf{x}'. \tag{2.18}$$

The first integral on the right hand side of Equation 2.18 is expanded, and Green's theorem is applied to obtain

$$\frac{\partial}{\partial t'} \int_{\mathcal{D}^{\mathrm{EP}'}} \theta' \, d\mathbf{x}' = - \int_{\partial \mathcal{D}^{\mathrm{EP}'}} \mathbf{u}' \theta' \cdot \hat{\mathbf{n}} \, dl' - \gamma' \int_{\mathcal{D}^{\mathrm{EP}'}} u' \, d\mathbf{x}' - \int_{\partial \mathcal{D}^{\mathrm{EP}'}} \alpha \nabla' \theta' \cdot \hat{\mathbf{n}} \, d\mathbf{x}'. \tag{2.19}$$

The requirement that T' be bounded as $t \to \infty$ is equivalent to enforcing that the left hand side of Equation 2.19 be zero when averaged over a length of time on the order of the solution period. The first term on the right hand side of Equation 2.19 goes to zero by the velocity boundary condition given in Equation 2.4 and the second term on the right hand side can be rewritten in terms of the flow rate

$$Q'(t) = \frac{1}{l'} \int_{\mathcal{D}^{\mathrm{EP}'}} u' \, d\mathbf{x}'. \tag{2.20}$$

For the problem examined here, the flow rate is fixed and $Q'(t) = Q'$. The expression for γ' is obtained by requiring that the remaining terms satisfy Equation 2.19 which can be rewritten as

$$\gamma' l' Q' = \alpha \int_{\partial \mathcal{D}^{\mathrm{EP}'}} \nabla' \theta' \cdot \hat{\mathbf{n}} \, dl'. \tag{2.21}$$

The boundary condition contributions from the body and upper wall in Equation 2.17 are substituted into the right hand side of Equation 2.21. The contribution from the body is zero because of integration around the closed contour $\partial \mathcal{D}_B^{\mathrm{EP}}$ and the contribution along the upper wall is zero because $\hat{n}_1|_{\partial \mathcal{D}_u^{\mathrm{EP}}} = 0$. The boundary condition contribution from the lower wall in Equation 2.16 is substituted into Equation 2.21 to obtain

$$\gamma' l' Q' = \alpha \int_{\partial \mathcal{D}_l^{\mathrm{EP}'}} \frac{q''}{\kappa} \, dl, \tag{2.22}$$

which is solved for γ' to get

$$\gamma' = \frac{\alpha q'}{2 \kappa H' V'}, \tag{2.23}$$

where the relation $Q' = H'V'$ has been substituted, and $q' = l'q''$ is the integrated heat flux

into the domain $\mathcal{D}^{\mathrm{EP}}$ through the lower wall $\partial\mathcal{D}_l^{\mathrm{EP}}$.

To this point, all quantities and equations have been given in dimensional form. To nondimensionalize the governing equations, and to simplify and generalize the solution process, the following scales are used. All lengths are scaled by the dimensional channel half-height H' resulting in a nondimensional channel height of $H = 2$. The velocities are scaled by $\frac{3}{2}V'$ which has been selected so that the nondimensional centerline velocity for plane Poiseuille flow is unity. The dimensional time is scaled by the ratio of the length scale to the velocity scale $\frac{2H'}{3V'}$ and the temperature is scaled by $\frac{q''H'}{\kappa}$. The scales are summarized below.

Velocity scale:	$\frac{3}{2}V'$
Length scale:	H'
Time scale:	$\frac{2H'}{3V'}$
Temperature scale:	$\frac{q''H'}{\kappa}$

The relative periodicity length l' and the full channel length L' are scaled by H' and resulting nondimensional lengths are

$$l = \frac{l'}{H'}, \qquad L = \frac{L'}{H'}, \tag{2.24}$$

respectively.

The scalings listed above are applied to the governing equations 2.2. 2.3. 2.15 and to the associated boundary conditions 2.4—2.7, 2.14. 2.16. and 2.17. The resulting equations are simplified to obtain the full set of nondimensional governing equations and boundary conditions. The velocity and pressure are governed by the incompressible. Navier-Stokes and continuity equations

$$\frac{\partial \mathbf{u}}{\partial t} + \mathbf{u}\cdot\nabla\mathbf{u} - \frac{1}{Re}\nabla^2\mathbf{u} + \nabla p = \mathbf{f}(t), \tag{2.25}$$

$$\nabla\cdot\mathbf{u} = 0, \tag{2.26}$$

with boundary conditions

$$\mathbf{u} = 0 \text{ on } \partial\mathcal{D}_l^{\mathrm{EP}},\ \partial\mathcal{D}_u^{\mathrm{EP}},\ \partial\mathcal{D}_B^{\mathrm{EP}}, \tag{2.27}$$

$$\mathbf{u}(x = 0, y, t) = \mathbf{u}(x = l, y, t). \tag{2.28}$$

$$\mathbf{u}_x(x = 0, y, t) = \mathbf{u}_x(x = l, y, t). \tag{2.29}$$

$$\mathbf{u}_y(x = 0, y, t) = \mathbf{u}_y(x = l, y, t). \tag{2.30}$$

The governing equation for the temperature reduces to

$$\frac{\partial\theta}{\partial t} + \mathbf{u}\cdot(\nabla\theta) = \frac{1}{RePr}\nabla^2\theta - \gamma u_1, \tag{2.31}$$

with boundary conditions

$$\nabla\theta \cdot \hat{\mathbf{n}} = 1 - \gamma\hat{n}_1 \text{ on } \partial\mathcal{D}_l^{\text{EP}}, \tag{2.32}$$

$$\nabla\theta \cdot \hat{\mathbf{n}} = -\gamma\hat{n}_1 \text{ on } \partial\mathcal{D}_B^{\text{EP}}, \ \partial\mathcal{D}_u^{\text{EP}}, \tag{2.33}$$

$$\theta(x = 0, y, t) = \theta(x = l, y, t). \tag{2.34}$$

$$\theta_x(x = 0, y, t) = \theta_x(x = l, y, t). \tag{2.35}$$

$$\theta_y(x = 0, y, t) = \theta_y(x = l, y, t). \tag{2.36}$$

The Reynolds and Prantl numbers are

$$Re = \frac{3V'H'}{2\nu}, \qquad Pr = \frac{\nu}{\alpha}, \tag{2.37}$$

and the Prantl number is held fixed at unity, $Pr = 1$, for all cases presented here. The nondimensional velocity, pressure, and temperature are

$$\mathbf{u} = \frac{2\mathbf{u}'}{3V'}, \qquad p = \frac{p'}{\rho\left(\frac{3}{2}V'\right)^2}, \qquad \text{and} \qquad \theta = \frac{\theta'}{\frac{q''H}{\kappa}}, \tag{2.38}$$

respectively and the nondimensional coefficient, γ, becomes

$$\gamma = \frac{3}{4RePr}. \tag{2.39}$$

The dimensional pressure π' has been expanded according to Equation 2.8. This yields a time–dependent forcing term on the right hand side of the x–component of Equation 2.25

$$f(t) = \frac{\frac{\Delta P'}{L}}{\rho\left(\frac{3}{2}V'\right)^2}, \tag{2.40}$$

where the full vector forcing term in Equation 2.25 is $\mathbf{f}(t) = (f(t), 0)$. The forcing term is the nondimensional pressure drop required to drive the flow at the prescribed Reynolds number. To be consistent with the velocity scaling $\frac{3}{2}V'$, the nondimensional, time dependent, forcing term $f(t)$ is set such that nondimensional flowrate given by

$$Q = \int_0^2 u(x, y, t)\, dy, \tag{2.41}$$

is a constant $Q = \frac{4}{3}$. The numerical implementation that has been used to to achieve the prescribed flow rate is detailed in Section 3.2.1.

2.3 Engineering Goals

The eddy-promoter heat exchanger design problem can be classified as a multicriteria design problem. The two criteria that characterize the design goals are the pumping power required to maintain the prescribed flowrate and the temperature rise along the lower wall. The two design criteria for this problem result in a classic trade-off problem in that design improvements, reduced pumping power and lower temperature rise, are competing goals and in many instances run counter to each other [66]. From the designer's point of view, it is best to postpone how to precisely balance and prioritize the two criterion until as late in the design process as possible. This will increase the flexibility and allow the designer to learn as much as possible before making decisions.

To accomplish the design goals, a number of independent variables can be adjusted. The independent variables are referred to as design (or input) variables. Of the full set of design variables, a subset consists of the vector of parameters $\mathbf{Z}'_{EP}$ that specify the geometric configuration of the eddy-promoter inclusions shown shaded in the lower part of Figure 2-2. The vector $\mathbf{Z}'_{EP}$ includes the parameters that describe the profile of the body surface as well as its placement in the channel. Additional design variables are the height of the channel configuration H', and the average fluid velocity V' defined in Equation 2.1. The total channel length L' is fixed as it is assumed to be set based on the specific application. The relative spacing between each eddy-promoter, l', can also serve as a design input but, for the remainder of the work presented here, it is also assumed fixed and is set such that $l = \frac{l'}{H'} = 6.666$. The value $l = 6.666$ matches that used in previous studies and has been shown to be a valid length for the existence of l-periodic solutions [40]. The fluid properties ρ, ν, κ, and α are all assumed fixed. The full, dimensional design input vector is

$$\mathbf{Z}' = (\mathbf{Z}'_{EP}, V', H'). \tag{2.42}$$

As stated in the first paragraph of this section, the two criteria that characterize the design are the dimensional pumping power required to achieve a prescribed average flow velocity V' and the temperature rise along the lower wall. The pumping power is given as

$$\mathcal{F}'_P(\mathbf{Z}') = \Delta P' V' H', \tag{2.43}$$

and is dependent on the input design vector $\mathbf{Z}$. The temperature rise is broken into two components and is

$$\delta T' = T'_{w,o} - T'_{m,i} \tag{2.44}$$

where $T'_{w,o}$ is the temperature at the outlet of the heat exchanger, and $T'_{m,i} = T'_m(x = 0)$ is the mixed mean temperature at the inlet of the exchanger. The mixed mean temperature

is defined as

$$T'_m(x) = \frac{1}{2H'V'} \int_0^{2H'} < u'(\mathbf{x},t)T'(\mathbf{x},t) > dy. \tag{2.45}$$

The brackets $< \cdot >$ in Equation 2.45 indicate a temporal average over a sufficiently long period of time to obtain the mean of the time-varying, steady-periodic solutions.

To nondimensionalize the problem, it is important to scale the optimization objectives by quantities that do not change as the design changes. This requirement simplifies the solution process but it also restricts the possible nondimensionalizations. The independent variables are scaled as well. The channel half-height H' is scaled by the total channel length L', which is fixed. For convenience, the inverse of the scaled channel half-height

$$\eta_L = \frac{L'}{H'}, \tag{2.46}$$

serves as the design variable. The eddy-promoter configuration variables are scaled relative to the channel half-height

$$\mathbf{Z}_{EP} = \frac{\mathbf{Z}'_{EP}}{H'}. \tag{2.47}$$

The average velocity V' is scaled by $\frac{2\nu}{3H'}$ which gives the Reynolds number, $Re = \frac{3V'H'}{2\nu}$, as a design variable. The full set of nondimensional design variables is then given as

$$\mathbf{p}_{full} = (\mathbf{Z}_{EP}, Re, \eta_L). \tag{2.48}$$

To scale the temperature objective, the temperature rise $\delta T'$ is first expanded as

$$\delta T' = \frac{q''L'}{\rho c_p V'H'} + \overline{\Delta T}' \tag{2.49}$$

where $\overline{\Delta T}' = < \overline{T'_m(x) - T'_w(x)} >$ and the over-bar indicates a spatial average in the x-direction over the length of the spacing between eddy-promoters, l'. The first term on the right hand side of Equation 2.49 corresponds to the mixed mean temperature rise along the exchanger length due to the uniform heat flux q'' and the second term is the heat that has been transfered into the fluid medium. Scaling the temperature rise by $\frac{q''L'}{\kappa}$ gives the desired result for the objective

$$\Theta(\mathbf{Z}_{EP}, Re, L) = \frac{\delta T'}{\frac{q''L'}{\kappa}} = \frac{1}{RePr} + \frac{1}{\eta_L Nu(\mathbf{Z}_{EP}, Re)} \tag{2.50}$$

where the Nusselt number is given by

$$Nu(\mathbf{Z}_{EP}, Re) = \frac{1}{< \overline{T_m(x) - T_w(x)} >} = \frac{1}{\overline{\overline{\Delta T}}} \tag{2.51}$$

and is the inverse of the nondimensional, temporally- and spatially-averaged difference

between the mixed-mean and wall temperatures.

The pumping power, $\mathcal{F}'_P(\mathbf{Z}')$, is scaled by $\frac{\rho\nu^3}{L'^2}$. The nondimensional pumping power is

$$\Psi(\mathbf{Z}_{EP}, Re, \eta_L) = \frac{\Delta P' V' H' L'^2}{\rho\nu^3}. \tag{2.52}$$

Introducing the nondimensional friction factor

$$\psi_0(\mathbf{Z}_{EP}, Re) = \frac{\frac{\Delta P'}{L'}}{\rho\left(\frac{3}{2}V'\right)^2}, \tag{2.53}$$

and substituting the expression into Equation 2.52 gives

$$\Psi(\mathbf{Z}_{EP}, Re, \eta_L) = \psi_0(\mathbf{Z}_{EP}, Re)\eta_L^3 Re^3. \tag{2.54}$$

where the nondimensional friction factor in Equation 2.53 is identically equal to the temporally averaged, pressure forcing term on the right hand side of Equation 2.25. The pressure forcing term is given in Equation 2.40 and the output form is

$$\psi_0(\mathbf{Z}_{EP}, Re) =< f(t; \mathbf{Z}_{EP}, Re) > . \tag{2.55}$$

To this point, no preference as to how to treat the two design criteria, $\Theta(\mathbf{Z}_{EP}, Re, \eta_L)$ and $\Psi(\mathbf{Z}_{EP}, Re, \eta_L)$, has been stated. The precise application and engineering constraints (e.g. available pumps, limits on temperature rise, etc.) would need to be known to determine the best formulation for the design problem. As an example, if the maximum temperature rise along the lower wall of the exchanger must be limited (say due to operating temperature limits on electrical components), the problem could be formulated as a constrained optimization problem

$$\min_{\{\mathbf{Z}_{EP}, Re, \eta_L\}} \Psi(\mathbf{Z}_{EP}, Re, \eta_L) \tag{2.56}$$

subject to

$$\Theta(\mathbf{Z}_{EP}, Re, \eta_L) \leq \overline{\theta}, \tag{2.57}$$

where $\overline{\theta}$ is the upper-bound constraint on the temperature performance criterion. Conversely, the problem could be formulated based on the maximum pumping power that can be supplied by the fluid pump. In that case, the two performance metrics in Equations 2.56 and 2.57 would be reversed and the upper-bound constraint in Equation 2.57 would be set based on the particular fluid pump. Ideally, it is best to put off such decisions until as late in the design process as possible to preserve generality. The design strategy that is used for the eddy-promoter problem combines the formulation presented in Section 2.4 and the

surrogate techniques presented in Chapters 4 and 5. The result is an extremely flexible design environment that addresses both constrained optimization problems mentioned above as well as a wide class of more general formulations.

Regardless of the problem formulation that is ultimately selected, upon solution of the nondimensional optimization problem, the physical heat exchanger quantities must be extracted from the nondimensional results. The steps are as follows: 1) Given the dimensional length of the heat-exchanger channel L', H' is determined from the optimization solution for η_L. 2) With H' known, the dimensional geometric configuration parameters $\mathbf{Z}'_{EP}$ can be obtained. 3) The Reynolds number implies (for fixed fluid quantities) the optimal V' given H'.

2.4 Optimization Problem – Pareto Formulation

The notion of Pareto-Optimality (PO) has its origins in the field of economics. The analysis was originally targeted towards the equilibrium conditions in an economy in which gains made by one consumer would be at the expense of at least one other consumer. The equilibrium point was first referred to by Edgeworth in 1881 [20] and the concept was refined and expanded by Pareto [59]. The application of Pareto analysis to engineering problems has only occurred recently, however.

There are several advantages to pursuing a Pareto analysis of multicriteria optimization problems when feasible. First, it can be shown that a wide class of multicriteria optimization formulations have a solution that is also PO. This is important in that by pursuing a Pareto analysis, one loses very little generality. The second advantage to a Pareto approach lies in the engineering relevance of the results. For a two-criteria optimization problem, the resulting family of PO solutions map to a curve in the two-dimensional criterion-space that provides a designer with the capability to rapidly assess trade-offs and to determine the impact of changing design goals interactively. Third, PO analysis has a beneficial impact on the practicality of the error estimates provided by the surrogate framework. This is a direct result of the reduction in effective dimension that is realized by the Pareto analysis. The result is that for a problem with a high input dimension (M), the dimension over which the surrogates are validated is reduced to one less than the number of performance metrics that characterize the design preferences, $(K-1)$. The input dimension reduction significantly improves the predictability and is discussed in Chapter 4.

In this section, the general formulation for the Pareto-optimization problem is presented first. Second, several classes of multiobjective problems that have solutions that are also Pareto-optimal are presented and discussed. Third, the methods used to determine the full set of Pareto-optimal solutions are described. Fourth, and finally, the generalization of the Pareto formulation to an arbitrary number of objectives is briefly presented.

2.4.1 Pareto-Optimal Solutions

Central to the Pareto analysis of a problem is the notion that the designer can articulate monotonic preferences on each performance metric. For all of the discussion of this section, it will be assumed that there are two ($K = 2$) performance metrics for which lower values correspond to better designs. Given a vector of design variables $\mathbf{p} \in \Omega$ and the design (or input) space $\Omega \subset \mathbb{R}^M$, the two performance metrics are $\Phi_1(\mathbf{p}) = \Phi_1(\phi_1(\mathbf{p}), \phi_2(\mathbf{p}), \mathbf{p}) : \Omega \rightarrow \mathbb{R}$ and $\Phi_2(\mathbf{p}) = \Phi_1(\phi_1(\mathbf{p}), \phi_2(\mathbf{p}), \mathbf{p}) : \Omega \rightarrow \mathbb{R}$. It is arbitrarily assumed that the performance metrics are functions of the two outputs, $\phi_1(\mathbf{p}) : \Omega \rightarrow \mathbb{R}$ and $\phi_2(\mathbf{p}) : \Omega \rightarrow \mathbb{R}$, as well as explicit functions of the input variables $\mathbf{p}$.

To define the Pareto-optimal sets, the notion of an achievable set

$$\mathcal{A} = \{s \in \mathbb{R}^2 \mid \exists\, \mathbf{p} \in \Omega \text{ s.t. } \Phi_1(\phi_1(\mathbf{p}), \phi_2(\mathbf{p}), \mathbf{p}) \leq s_1, \Phi_2(\phi_1(\mathbf{p}), \phi_2(\mathbf{p}), \mathbf{p}) \leq s_2\}, \quad (2.58)$$

is first introduced. The achievable set $\mathcal{A}$ is the the set of all possible output pairs $\mathbf{s} = (s_1, s_2)$ for which there is an input point $\mathbf{p} \in \Omega$ that has correspondingly better performance metric values. With the achievable set defined as above, the set of Pareto-optimal designs is then the set of designs for which the performance metric values lie on the non-horizontal, non-vertical boundary of $\mathcal{A}$ not at infinity. This boundary, denoted $\partial\mathcal{A}$, is depicted on the left in Figure 2-3 as the solid line and is termed the Pareto-optimal output manifold. The PO output manifold is also sometimes referred to as the efficient frontier [71] or the trade-off curve [66]. The inverse map of the PO output manifold back to the input space is determined from the performance metrics

$$\mathcal{L}^{\mathcal{A}} = \{\mathbf{p} \in \Omega \mid \exists\, \mathbf{s} \in \partial\mathcal{A} \text{ s.t. } \Phi_1(\phi_1(\mathbf{p}), \phi_2(\mathbf{p}), \mathbf{p}) = s_1, \Phi_2(\phi_1(\mathbf{p}), \phi_2(\mathbf{p}), \mathbf{p}) = s_2\}. \quad (2.59)$$

and $\mathcal{L}^{\mathcal{A}} \subset \Omega$ is denoted the PO input manifold. The PO input manifold $\mathcal{L}^{\mathcal{A}}$ is shown as solid lines on the right side of Figure 2-3 and the outline of the design space Ω is shown as a dashed line. Figure 2-3 depicts $\partial\mathcal{A}$ and $\mathcal{L}^{\mathcal{A}}$ as very well behaved, $(K-1)$-dimensional manifolds. There is no justification for such behavior in general, especially as regards $\mathcal{L}^{\mathcal{A}}$, but for relatively smooth, well defined performance metrics it is reasonable to expect some regularity.

The design optimization interest is in the designs described by input points, $\mathbf{p}^*$, that lie on $\mathcal{L}^{\mathcal{A}}$, $\mathbf{p}^* \in \mathcal{L}^{\mathcal{A}}$. These design points can rightfully be called the "best" or most efficient designs based on the performance metrics. This is illustrated by considering the input point $\mathbf{p}'$ with the corresponding output pair $(\Phi_1(\mathbf{p}'), \Phi_2(\mathbf{p}')) \notin \partial\mathcal{A}$. For such a point, there always exists a point $\mathbf{p}^* \in \mathcal{L}^{\mathcal{A}}$ that has output pair $(\Phi_1(\mathbf{p}^*), \Phi_2(\mathbf{p}^*)) \in \partial\mathcal{A}$ and that satisfies either

$$\Phi_1(\mathbf{p}^*) \leq \Phi_1(\mathbf{p}') \text{ and } \Phi_2(\mathbf{p}^*) < \Phi_2(\mathbf{p}'), \quad (2.60)$$

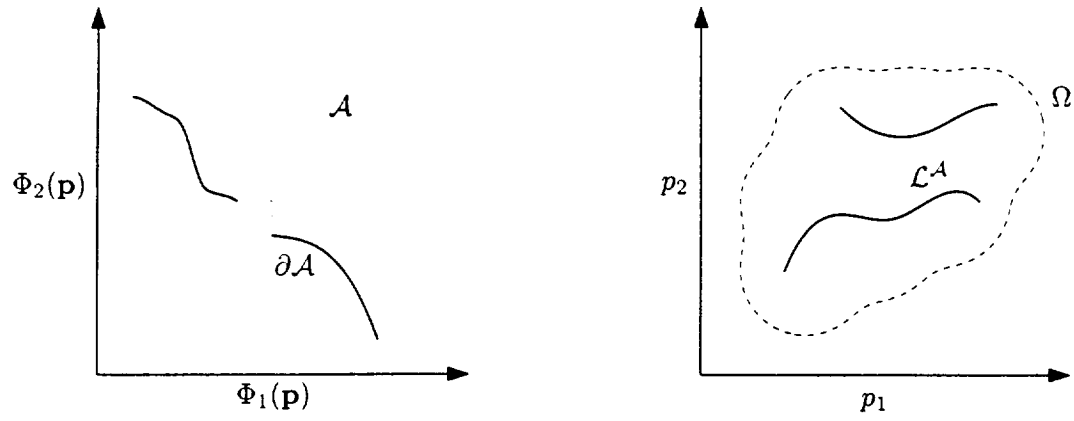

Figure 2-3: A schematic the Pareto-optimal output (left) and input (right) manifolds.

or

$$\Phi_1(\mathbf{p}^*) < \Phi_1(\mathbf{p}') \text{ and } \Phi_2(\mathbf{p}^*) \leq \Phi_2(\mathbf{p}'). \tag{2.61}$$

In words, Equations 2.60 and 2.61 indicate that for a point $\mathbf{p}'$ that is not PO, there will always exist a point $\mathbf{p}^*$ that performs at least as well in terms of the first performance metric $\Phi_1(\mathbf{p}')$ and improves upon second performance metric $\Phi_2(\mathbf{p}')$ or (conversely) that performs at least as well as $\Phi_2(\mathbf{p}')$ but improves upon $\Phi_1(\mathbf{p}')$.

Finally, it is noted that the entire boundary of $\mathcal{A}$ does not correspond to PO designs. From the discussion of the previous paragraph, it is obvious that designs that correspond to horizontal or vertical segments of the boundary are not PO. The reason for this is that for such designs, there will always be another design input point that improves on one of the performance metrics without increasing the other. For all of the discussions of $\partial\mathcal{A}$, and the corresponding $\mathcal{L}^{\mathcal{A}}$, it is assumed that all points that are not PO have been eliminated. This has been suggested on the left side of Figure 2-3 by denoting $\partial\mathcal{A}$ as the solid line only.

2.4.2 Relationship to Other Multi–Objective Problems

The advantage of pursuing a Pareto analysis is that it is, in fact, a generalization of many multi–objective problems in that solutions to the given multi–objective optimization problem, $\mathbf{p}^*_{MO}$, are Pareto optimal: $\mathbf{p}^*_{MO} \in \mathcal{L}^{\mathcal{A}}$. For example, the single performance metric minimization problems,

$$\mathbf{p}_1^* = \arg\min_{\mathbf{p}\in\Omega} \Phi_1(\mathbf{p}), \tag{2.62}$$

and

$$\mathbf{p}_2^* = \arg\min_{\mathbf{p}\in\Omega} \Phi_2(\mathbf{p}), \tag{2.63}$$

both have solutions that lie on $\mathcal{L}^{\mathcal{A}}$, $\mathbf{p}_1^* \in \mathcal{L}^{\mathcal{A}}$ and $\mathbf{p}_2^* \in \mathcal{L}^{\mathcal{A}}$. In fact, the performance metric pairs that correspond to $\mathbf{p}_1^*$ and $\mathbf{p}_2^*$ lie at the extreme ends of $\mathcal{A}$.

As a second example, if the objective is the weighted sum of the performance metrics, $\varphi(\mathbf{p}) = a_1\Phi_1(\mathbf{p}) + a_2\Phi_2(\mathbf{p})$, then

$$\mathbf{p}^* = \arg\min_{\mathbf{p}\in\Omega} \varphi(\mathbf{p}) \tag{2.64}$$

is PO as well and can be found on the PO input manifold $\mathcal{L}^{\mathcal{A}}$, $\mathbf{p}^* \in \mathcal{L}^{\mathcal{A}}$.

In general, for any non-decreasing functions $\varphi(\Phi_1(\mathbf{p}), \Phi_2(\mathbf{p}), \mathbf{p})$ and $b(\Phi_1(\mathbf{p}), \Phi_2(\mathbf{p}), \mathbf{p})$ that are not explicitly functions of the input vector $\mathbf{p}$, a solution to

$$\mathbf{p}^* = \arg\min_{\mathbf{p}\in\Omega} \varphi_1(\Phi_1(\mathbf{p}), \Phi_2(\mathbf{p}), \mathbf{p}) \tag{2.65}$$

subject to

$$b(\Phi_1(\mathbf{p}), \Phi_2(\mathbf{p}), \mathbf{p}) \leq 0 \tag{2.66}$$

will lie on the PO input surface $\mathcal{L}^{\mathcal{A}}$. This generality in the PO solutions allows the designer to eliminate uninteresting designs but ensures that sufficient flexibility remains to change the design goals as the design itself evolves. This flexibility is extremely important because many times, precise goals can not be defined at the outset of the design process.

2.4.3 Determination of $\partial\mathcal{A}$ and $\mathcal{L}^{\mathcal{A}}$

To find $\mathcal{L}^{\mathcal{A}}$, the multicriteria problem is reduced to a series of scalar problems parameterized by $w \in \mathcal{W} = [0, 1]$. A min—max formulation for the scalar sub-optimization problems is used as it is guarantees that non-convex portions of $\mathcal{L}^{\mathcal{A}}$ are obtained [22, 14].

Given the scalarization parameter $w \in \mathcal{W}$, the scalar problem

$$\xi(w) = \arg\min_{\mathbf{p}\in\Omega} \max(w\Phi_1(\mathbf{p}), (1-w)\Phi_2(\mathbf{p})), \quad w \in \mathcal{W}, \tag{2.67}$$

is solved for a sufficiently refined $\mathcal{W}$. The curve $\xi(\mathcal{W})$ (with segments corresponding horizontal and vertical segments of the boundary of $\mathcal{A}$ removed) is the PO input surface $\mathcal{L}^{\mathcal{A}}$. The corresponding PO output manifold is obtained from $\xi(\mathcal{W})$ and the performance metrics, given by

$$\partial\mathcal{A} = (\Phi_1(\xi(\mathcal{W})), \Phi_2(\xi(\mathcal{W}))). \tag{2.68}$$

It is immediately obvious that it can be an extremely time consuming and difficult process to find $\xi(\mathcal{W})$ to an adequately fine resolution for even moderately complex (expensive) performance metrics, $\Phi_1(\mathbf{p})$ and $\Phi_2(\mathbf{p})$. Each solution to 2.67 is itself an optimization problem. The prohibitive cost of obtaining $\xi(\mathcal{W})$ is the primary reason why Pareto analysis is not typically pursued for complex engineering problems.

Note that in this discussion, it is assumed that the $\xi(\mathcal{W})$ obtained from the scalarization process (2.67) has been "cleaned up" to remove duplicate points and horizontal and vertical segments of the boundary of $\mathcal{A}$ that, by definition, are not PO.

2.4.4 Generalization to Arbitrary Output Dimension

The notion of Pareto-Optimal solutions can be extended to an arbitrary number of performance metrics $\Phi_1(\mathbf{p}), \ldots, \Phi_K(\mathbf{p})$. For the K performance metrics (for all of which it is assumed that lower is better) the PO output manifold is the $(K-1)$-dimensional manifold that represents the boundary of the achievable set $\mathcal{A}_K$ not at infinity. Here $\mathcal{A}_K$ is

$$\mathcal{A}_K = \{\mathbf{s} \in I\!R^K \mid \exists\, \mathbf{p} \in \Omega \text{ s.t. } \Phi_1(\phi_1(\mathbf{p}), \phi_2(\mathbf{p}), \mathbf{p}) \leq s_1, \ldots, \Phi_K(\phi_1(\mathbf{p}), \phi_2(\mathbf{p}), \mathbf{p}) \leq s_K\}. \tag{2.69}$$

In three dimensions, this can be visualized as the surface of the three-dimensional achievable set volume in the first quadrant that is "nearest" the origin.

In higher dimensions, the surfaces can not be easily visualized but can be described with the min-max scalarization process similar to 2.67 [35]. Given the $K-1$ scalarization parameters $\mathbf{w} = (w_1, \ldots, w_{K-1}) \in \mathcal{W}_{K-1}$, where

$$\mathcal{W}_{K-1} = \left\{ \mathbf{v} \in I\!R^{K-1} \mid 0 \leq v_i \leq 1, \sum_{i=1}^{K-1} v_i \leq 1 \right\}, \tag{2.70}$$

the PO input manifold can be found by solving

$$\xi(\mathbf{w}) = \arg\min_{\mathbf{p}\in\Omega} \max \left(w_1\Phi_1(\mathbf{p}), \ldots, w_{K-1}\Phi_{K-1}(\mathbf{p}), \left(1 - \sum_{i=1}^{K-1} w_i\right) \Phi_K(\mathbf{p}) \right), \quad \mathbf{w} \in \mathcal{W}_{K-1}, \tag{2.71}$$

where the scalarization vector space is $\mathcal{W}_{K-1} \subset [0,1]^{K-1}$. As before, the PO output manifold is given by

$$\partial\mathcal{A}_K = (\Phi_1(\xi(\mathcal{W}_{K-1})), \Phi_2(\xi(\mathcal{W}_{K-1}))), \tag{2.72}$$

and finite-sized portions of $\partial\mathcal{A}_K$ for which at least one of the performance metrics is constant have been assumed removed.

In practice, assuming very inexpensive performance metric functions, it may be possible to obtain and manage the data required to visualize and sample a three criteria ($K = 3$) Pareto analysis. As noted above, for a three criteria optimization problem, the PO output manifold is a surface of a three-dimensional volume (the achievable set) and the PO input manifold can be visualized versus the two scalarization parameters as surfaces. With a sufficient amount of data, boundaries between disconnected subsets of $\mathcal{L}^{\mathcal{A}}$ can be accurately determined. For problems in which $K > 3$, the PO manifolds become very difficult to visualize (volumetric manifolds in four-space for $K = 4$) and dimensionalization issues make

it computationally difficult to precisely determine the boundaries between disconnected subsets of $\mathcal{L}^{\mathcal{A}}$. With these considerations in mind, it can be concluded that the Pareto analysis is best suited for $K = 2$ problems and, possibly, could be useful for $K = 3$ problems. Fortunately, a large number of problems of interest can be meaningfully expressed as two-criteria optimization problems.

2.5 Eddy–Promoter Shape Description

The effectiveness of cylindrical eddy-promoters as heat transfer enhancement devices has been studied extensively [40, 77, 79]. For the eddy-promoter optimization problem studied here, the intent is to expand upon the the cylindrical family of designs that have been studied previously. It is important that the definition of the design space include cylindrical geometries so that improvements to optimal cylindrical configurations can be identified. Another desire is for the design space to include topologically changing geometries: specifically it should include single bodies as well as two-body configurations.

The motivation behind examining two-body configurations is the possibility that the two bodies could favorably interact to improve the heat transfer beyond what is possible with a single body. The multiple-topology design space presents a particular challenge in that the definition of the shape parameterization must be consistent and continuous with respect to the outputs so that surrogates can be constructed.

In this work, a shape parameterization has been developed that describes a family of geometries that is a superset of the cylindrical family studied previously. The shape parameterization presented encompasses a richer set of single-body geometries than simply circular cylinders, and includes two-body geometries as well. To accomplish this, a level-set based shape description has been developed.

2.5.1 Level Set Methods – Shape Generation Example

To describe the geometry of the eddy promoters, $\mathbf{Z}_{EP}$, a level-set [80, 64] based approach has been developed. Level-set methods have been applied to problems that involve propagating surfaces or interfaces [53]. This includes problems such as flame propagation and material boundary evolution. Level set methods have also been applied to character recognition (the determination of true character boundaries) and image enhancement in the presence of noise. One of the principle strengths of level-set methods is their ability to handle difficult geometries including sharp corners, cusps, and topological changes [13].

In the general level-set based shape generation case, a domain of possible shape geometries $\Omega^{\mathcal{B}} \subset I\!R^d$ in which the entire family of shape boundaries will lie is introduced where d (= 2 or 3) is the dimension of the shapes to be generated. For the generation of two-dimensional geometries ($d = 2$), a generating function $\mathcal{G}(\mathbf{x}, \omega) : \Omega^{\mathcal{B}} \rightarrow I\!R$ parameterized by

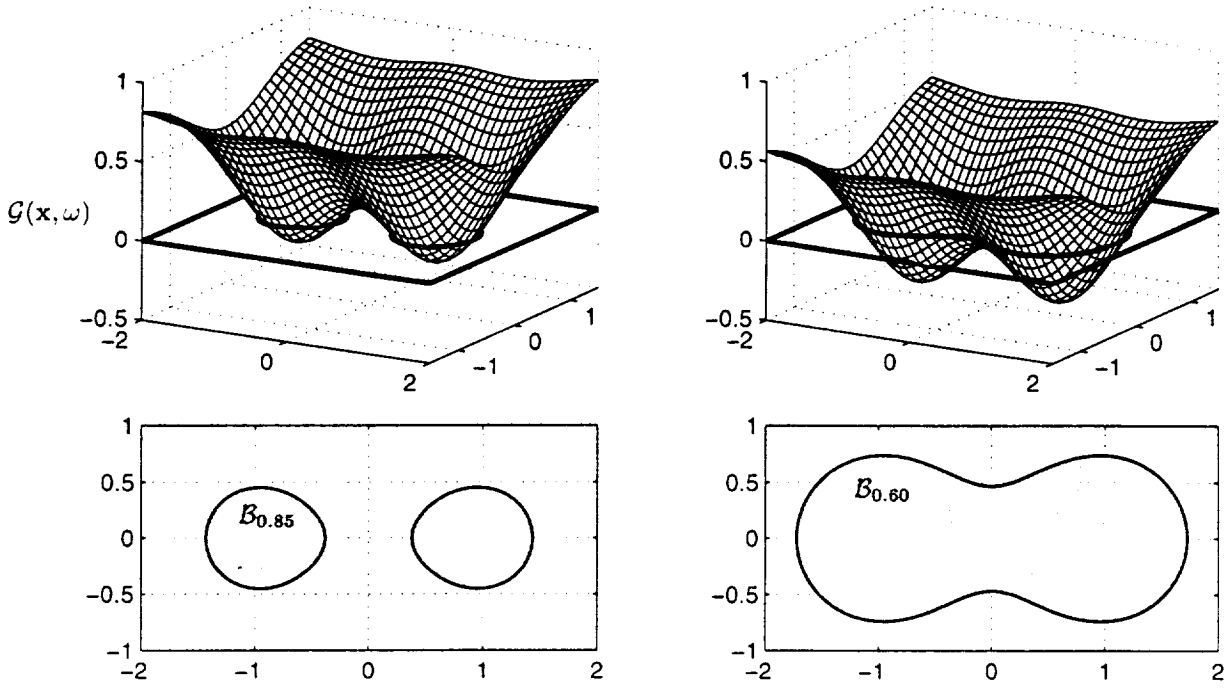

Figure 2-4: Mesh plots of the level-set generating function $\mathcal{G}(x,y;\omega)$ for $\omega = 0.85$ (left) and $\omega = 0.60$ (right). The resulting, closed shape geometries are shown shaded below each generating function.

the vector $\omega = (\omega_1, \ldots, \omega_{N^\omega}) \in A$ is selected where the Cartesian coordinate directions are $\mathbf{x} = (x, y)$, the shape generation domain is $\Omega^{\mathcal{B}} \subset I\!R^2$, and the input parameter domain is $A \subset I\!R^{N^\omega}$. The boundary of the shape geometry, $\mathcal{B}_\omega$, is defined by the level-set

$$\mathcal{B}_\omega = \{\mathbf{x} \in \Omega^{\mathcal{B}} \mid \mathcal{G}(\mathbf{x};\omega) \leq 0\}, \tag{2.73}$$

and is parameterized by the vector ω. In words, the body $\mathcal{B}_\omega$ consists of all points in the $\mathbf{x}$-plane for which the level-set generating function $\mathcal{G}(\mathbf{x};\omega)$ is less than zero. For a properly chosen generating function, this set is closed over the range of $\omega \in A$ although it can be disconnected.

To illustrate the level-set shape description described above, the sample generating function

$$\mathcal{G}(\mathbf{x};\boldsymbol{\omega}) = \omega_1 - \mathrm{e}^{-[(x-1)^2+y^2]} - \mathrm{e}^{-[(x+1)^2+y^2]}, \tag{2.74}$$

defined over the shape domain $\Omega^{\mathcal{B}} = [-2.0, 2.0] \times [-1.0, 1.0]$, and parameterized by the single variable $\omega = \omega_1$ is selected. The parameter ω_1 serves to select particular geometries from the family defined by Equation 2.74 for the full parameter range $\omega \in A = [0.5, 1.0]$. Mesh plots of the generating function and shaded, two-dimensional plots of the resulting

shape geometries are given in Figure 2-4. The single shape parameter is set to $\omega_1 = 0.85$ for the body on the left in Figure 2-4 and $\omega_1 = 0.60$ for the body on the right. For even this very simple case, the connectivity of the resulting geometry $\mathcal{B}_\omega$ can change discontinuously for a continuously changing shape parameter ω. This is a critical result for the ultimate application of surrogate–based shape optimization explored later.

The very simple level-set shape generation procedure described above can be easily extended by introducing a more general generating function. One approach is to treat the general form of the exponential function on which Equation 2.74 is based

$$\mathcal{G}_i(\mathbf{x};\omega) = \beta_i e^{-[(x-x_{c_i})^2+(y-y_{c_i})^2]}, \tag{2.75}$$

as the core for a more complex level-set function that is results from the application of superposition techniques. The level-set functions formed in this manner describe more general shapes. Each base exponential function has an associated center (x_{ci}, y_{ci}) and strength β_i. For N^e exponential functions, this yields a generating function of the form

$$\mathcal{G}(\mathbf{x};\omega) = \beta_0 - \sum_{i=1}^{N^e} \mathcal{G}_i(\mathbf{x};\omega) = \beta_0 - \sum_{i=1}^{N^e} \beta_i e^{-[(x-x_{c_i})^2+(y-y_{c_i})^2]} \tag{2.76}$$

where the vector of shape parameters is $\omega = \{(\beta_i, x_{cj}, y_{cj}) \mid i = 0, \ldots, N^e, j = 1, \ldots, N^e\}$. With the additional exponential functions and the greater flexibility afforded by the shape parameters, a much richer family of geometries can be defined.

The level-set function in Equation 2.76 was explored for the eddy-promoter problem. It produces smooth bodies that can change topologies (from a single body to more than one) and also satisfies the preference that the description procedure include cylinders. The family of geometries that it produces, however, does not include more elongated, oval shaped bodies without increasing the number of exponential functions beyond what is feasible for accurate surrogate construction. For this reason, a different shape generation function, described in the next section, has been developed.

2.5.2 Ideal Flow — Doublet Description

Although not explicitly stated as such, level-set ideas have been used extensively in classical aerodynamic analyses [2]. The underlying assumption in these approaches is that the true flow solution over a body can be approximated by an ideal flow solution over the body [38] with an appropriate circulation superimposed to satisfy flow tangency at sharp trailing edges. The body surface in ideal flow analyses is a streamline of the ideal flow solution and general geometries can be analyzed by enforcing flow tangency on the body surface at discrete points[42].

Ideal fluid solutions can be expressed by a fluid potential function ϕ_I or stream function

ψ_I, both of which satisfy Laplace's equation

$$\nabla^2 \phi_I = 0, \qquad \nabla^2 \psi_I = 0. \tag{2.77}$$

The fluid velocities $\mathbf{u} = (u, v)$ are given by

$$u = \frac{\partial \phi_I}{\partial x} = \frac{\partial \psi_I}{\partial y}, \tag{2.78}$$

$$v = \frac{\partial \phi_I}{\partial y} = -\frac{\partial \psi_I}{\partial x}. \tag{2.79}$$

The velocity solution $\mathbf{u}$ is for an incompressible, irrotational, inviscid fluid flow. Because of linearity, the superposition of flow solutions for which the velocities are given by 2.78 and 2.79, and that that satisfy 2.77, will also satisfy the ideal flow governing equation. This superposition property is used to generate solutions over general body geometries.

The ideal flow solution for the flow over a cylinder is described by the superposition of a uniform flow and a doublet. A uniform flow $u(x, y) = U_\infty$ is described by the stream function

$$\psi_I^{\text{uniform}} = U_\infty y. \tag{2.80}$$

A doublet is obtained by placing an equal strength source–sink pair a finite distance apart on the x–axis and taking the limit as the distance between the source–sink pair goes to zero. The stream function for a doublet of strength λ and center (x_c, y_c) is

$$\psi_I^{\text{doublet}} = -\frac{\lambda(y - y_c)}{(x - x_c)^2 + (y - y_c)^2}. \tag{2.81}$$

The stream function solution for the flow over a cylinder centered at the origin is obtained from the superposition of 2.80 and 2.81 for $(x_c, y_c) = (0, 0)$,

$$\psi_I^{\text{cylinder}} = \psi_I^{\text{uniform}} + \psi_I^{\text{doublet}} = U_\infty y - \frac{\lambda y}{x^2 + y^2}. \tag{2.82}$$

The cylinder surface is defined by the $\psi_I^{\text{cylinder}} = 0$ streamline (excluding the portions of the streamline on the x–axis) and the cylinder has radius $R_{\text{cylinder}} = \sqrt{\lambda / U_\infty}$. The relevance of this shape description to the original cylindrical eddy-promoter optimization problem studied previously [40, 77, 79] is readily apparent. By fixing the value of U_∞, the doublet strength λ then serves the sizing input analogous to d, the diameter of the cylinder. The position input, a, (measured from the lower wall of the channel) is the same as before giving the two-dimensional input vector $\mathbf{Z}_{EP}^{\text{cylinder}} = (\lambda, a)$.

The superposition idea described above can be further extended with the incorporation of a second doublet. The additional doublet allows for changes of topology (connectivity)

similar to the example level-set shape generation procedure described in 2.5.1 and the results of which are plotted in Figure 2-4. To accomplish this, one doublet of strength λ_1 is positioned at the origin and a second doublet of strength λ_2 is positioned at $(r_d, 0)$. The uniform flow velocity is set to unity, $U_\infty = 1$. The stream function for this configuration is then

$$\psi_I = y - \frac{\lambda_1 y}{x^2 + y^2} - \frac{\lambda_2 y}{(x - r_d)^2 + y^2}, \tag{2.83}$$

and the geometry is given by the $\psi_I = 0$ streamline with the segments on the x-axis removed. The parameters $(r_d, \lambda_1, \lambda_2)$ determine the specific geometry that is selected. If the vector of inputs $(r_d, \lambda_1, \lambda_2) \in \Omega^{DD}$ is assumed to range over the input space $\Omega^{DD} \subset I\!R^3$, then the connectivity of the resulting geometry (one or two distinct bodies) will depend on the values of $(r_d, \lambda_1, \lambda_2)$ and distinct regions of Ω^{DD} can be identified that correspond to single-body geometries, Ω_1^{DD}, or to two-body geometries, Ω_2^{DD}, and $\Omega^{DD} = \Omega_1^{DD} \cup \Omega_2^{DD}$.

The original intent of defining a family of bodies that is a superset of the cylindrical configuration is satisfied for $r_d = 0$. When $r_d = 0$, a cylinder of diameter $d = \sqrt{\lambda_1 + \lambda_2}$ is obtained. The two-doublet generating function in Equation 2.83 is the form used for the eddy-promoter shape description described in the next section.

2.5.3 Eddy-Promoter Geometry Generation Procedure

The full set of geometry inputs for the two-doublet shape description are shown in Figure 2-5. These include the strengths of the two doublets, λ_1 and λ_2, the position of the second doublet center relative to the first, (x_d, y_d), and the position of the pair in the channel measured from the lower wall, Y. The distance between the two doublets in Equation 2.83 is $r_d = \sqrt{x_d^2 + y_d^2}$. The procedure implemented to obtain the geometrically meaningful set of inputs $\mathbf{Z}_{EP} = (x_d, y_d, Y, \lambda_1, \lambda_2)$ from the normalized, eddy-promoter, geometric design vector $\mathbf{p}_Z = (p_{Z_1}, \ldots, p_{Z_5}) \in \Omega_Z = [0, 1]^5$ is described below.

The generation procedure defines the geometric design space Ω_Z in terms of a set of geometrically meaningful limits put on the resulting eddy-promoter configurations. Because of the difficulty of solving problems on highly stretched finite element meshes, the eddy-promoter bodies are never allowed within t_0 of the upper or lower wall. The range of the of geometric input x_d is set such that $x_{\min} \leq x_d \leq x_{\max}$ and a limit is set on the total doublet strength $\lambda_T = \lambda_1 + \lambda_2$ of $\lambda_{\min} \leq \lambda_T \leq \lambda_{\max}$. Upper and lower limits are also set on the strengths of each individual doublet $\lambda_{1\min} \leq \lambda_1 \leq \lambda_{1\min}$ and $\lambda_{2\min} \leq \lambda_2 \leq \lambda_{2\min}$. The generation procedure that satisfies the geometric requirements listed above consists of the following 7 steps:

1. The value of x_d is set based on the normalized input p_{Z_1}; $x_d = x_{\min} + p_{Z_1}(x_{\max} - x_{\min})$.

2. The total doublet strength is set based on the normalized input p_{Z_5}: $\lambda_T = \lambda_{\min} +$

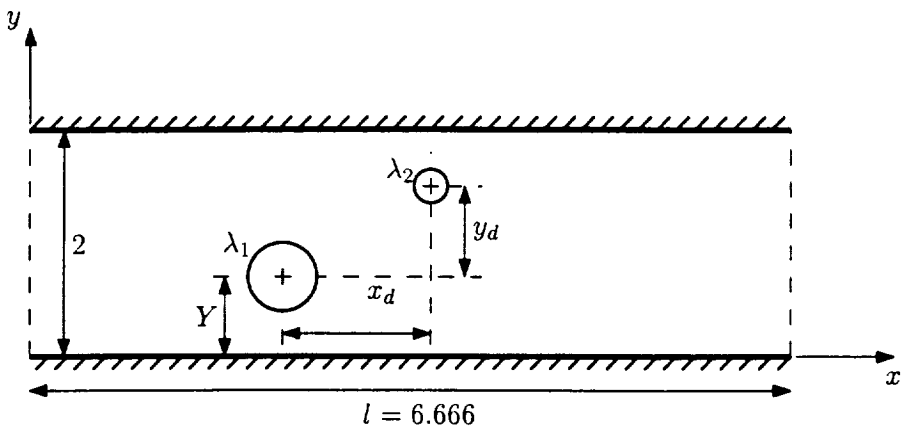

Figure 2-5: General geometry for the two-body eddy-promoter configuration.

$p_{Z_5}(\lambda_{\max} - \lambda_{\min})$

3. The total doublet strength distribution parameter, α, is set such that $\alpha_{\min} \leq \alpha \leq \alpha_{\max}$. The limits are dependent on the total strength and are $\alpha_{\min} = \frac{\lambda_{\min}}{2\lambda_T}$ and $\alpha_{\max} = 1 - \alpha_{\min}$. The distribution is set according to p_{Z_3}: $\alpha = \alpha_{\min} + p_{Z_3}(\alpha_{\max} - \alpha_{\min})$.

4. The strength of each doublet is set based on α and λ_T; $\lambda_1 = \alpha\lambda_T$ and $\lambda_2 = (1-\alpha)\lambda_T$.

5. Set the value y_d for the y-position of generator two relative to generator one based on p_{Z_2}: $y_d = y_{\min} + p_{Z_2}(y_{\max} - y_{\min})$. The limits on y_d are dependent on the values of λ_1, λ_2, and t_0 and are $y_{\min} = -2(1-t_0) + \sqrt{\lambda_1} + \sqrt{\lambda_2}$ and $y_{\max} = 2(1-t_0) - \sqrt{\lambda_1} - \sqrt{\lambda_2}$.

6. Generate the bodies based on the input values (x_d, y_d), λ_1, and λ_2 and find the minimum and maximum extent of the configuration in the y-direction. This requires placing a doublet of strength λ_1 at the origin, a second doublet of strength λ_2 at $(0, r_d)$, finding the body surface, and rotating the configuration by δ. The maximum and minimum vertical extent of the eddy-promoter configuration, $y^{\mathcal{B}}_{\min}$ and $y^{\mathcal{B}}_{\max}$, are used to set the final limits on Y.

7. Set Y according to p_{Z_4}; $Y = Y_{\min} + p_{Z_4}(Y_{\max} + Y_{\min})$. The limits on Y are functions of $y^{\mathcal{B}}_{\min}$, $y^{\mathcal{B}}_{\max}$, and t_0 and are $Y_{\min} = t_0 - y^{\mathcal{B}}_{\min}$ and $Y_{\max} = (2.0 - t_0) - y^{\mathcal{B}}_{\max}$.

This somewhat involved set of steps must be performed to generate the bodies because simply positioning one doublet at $(0,0)$ and a second at (x_d, y_d) will not produce a closed contour (or two closed contours) unless $y_d = 0$. This requires the superposition of two doublets on the same axis and then the rotation to define the bodies in the channel. It is important to note that for the cases in which two distinct bodies are described, the resulting bodies are not circular cylinders. However, in the limit as the distance between the doublet

centers approach infinity, the bodies approach circular cylinders of radius $R_1 = \sqrt{\lambda_1}$ and $R_2 = \sqrt{\lambda_2}$.

Matlab [47] has served extensively for the shape generation. The steps described above have been coded into a Matlab routine that takes as input a sequence of normalized inputs $\mathbf{p}_Z$, and writes as output a file that contains the surface node coordinates for each input, design point $\mathbf{p}_Z$. The node coordinate file is read by the mesh generator to build the finite element solution mesh.

As already mentioned, the primary benefit to defining the shapes in this manner is that it allows for topology changes relative to smoothly changing input parameters. This capability permits optimization over a wider range of configurations without having to resort to discrete optimization procedures. The most important characteristic of geometrically describing a shape space with more than one distinct topology in a level-set based approach such as this is that the input-output relationship can be expected to be continuous (and possibly smooth). This property is demonstrated empirically in Section 2.5.4.

The level-set method described above can be extended through the incorporation of additional doublets to allow the definition of more geometrically rich body profiles. Approaches such as this are very common in ideal flow analysis of airfoils. Finally, through the careful selection of generating functions that consistently define bodies for arbitrary (x_i, y_i), the method could be extended to still more complex topologies.

The above described steps generate a set of shapes that obey the geometric constraints. It also ensures that that the entire normalized input space Ω_Z corresponds to feasible designs. In the next section, an example that illustrates the topology change is given. The example shows the smooth transition from one to two distinct eddy-promoter bodies, and gives empirical evidence that the input-output functions are continuous across a topology change.

2.5.4 Input–Output Response Example

To demonstrate, at least empirically, that the relationship between the normalized geometric inputs, $\mathbf{p}_Z$, and the outputs is continuous across a topology change, the finite element simulation described in Chapter 3 has been used to approximate two of the outputs. Only one of the normalized inputs, p_{Z_1}, of the full normalized input vector $\mathbf{p}_Z$ has been has been varied. The first component of the normalized geometric input vector corresponds to the physical coordinate x_d shown in Figure 2-5. The bounds on x_d have been set to $x_{\min} = 0.00$ and $x_{\max} = 0.75$ and $p_{Z_1} \in [0, 1]$. A total of 21 geometries have been generated with the values of p_{Z_1} clustered near the value at which the topology change occurs. The remaining, normalized geometric inputs have been fixed such that $\mathbf{p}_Z = (p_{Z_1}, 0.60, 0.50, 0.50, 0.50)$. The lower and upper limits of the geometric quantities that correspond to fixed normalized inputs are $\lambda_{\min} = 0.109$, $\lambda_{\max} = 0.109$, $\alpha_{\min} = 0.85$, and $\alpha_{\max} = 0.85$. With the above information,

the geometry generation procedure described in Section 2.5.3 has been used to compute the surface coordinates for each input $\mathbf{p}_Z$. Representative eddy–promoter configurations produced by this set of inputs are plotted in the top half of Figure 2-6.

For the computational case examined here, the Reynolds number has been set to $Re = 250$. The two outputs of interest are obtained from the finite element simulation and are

$$\theta_0^{FE} = \theta_0^{FE}(\mathbf{p}_Z) = \frac{1}{Nu(\mathbf{Z}_{EP}(\mathbf{p}_Z), Re = 250)}, \tag{2.84}$$

$$\psi_0^{FE} = \psi_0^{FE}(\mathbf{p}_Z) =< f(t; \mathbf{Z}_{EP}(\mathbf{p}_Z), Re = 250) > \tag{2.85}$$

where Nu is the Nusselt number given in Equation 2.51, and $f(t; \mathbf{Z}_{EP}, Re = 250)$ is the time-dependent forcing term in Equation 2.25 required to achieve the prescribed flow rate. The results of the computational study are given in Figure 2-6. Selected eddy–promoter geometries from the sample set are plotted in the upper half of the figure. The output responses versus geometric input value x_d are plotted in the lower half of the figure. The normalized input p_{Z_1} is a simple linear scaling of x_d; therefore, the output response plots versus p_{Z_1} would tell the identical story to those in Figure 2-6. In the output response plots, the dashed line indicates the approximate value of x_d for which the topology change occurs. Single–body configurations have x_d values to the left of the dashed line and two–body configurations lie on the right. The results plotted in Figure 2-6 support the assertion that the input–output relationship remains continuous across topology changes. In fact, the first derivative appears to be continuous as well, further supporting (empirically) that the geometric description used for the eddy–promoter problem is well suited for the surrogate–based optimization techniques applied in Chapters 4 and 5.

2.6 Reduced Problem for the Eddy–Promoter Example

In this section, the particular set of inputs used for the eddy–promoter example problem and the corresponding design space are described. Second, the outputs of interest and the inputs of which they are functions are restated. Finally, the performance metrics that characterize the design preferences for the eddy–promoter design problem are presented.

2.6.1 Inputs and Input Domain

The full set of physical inputs are the variables that specify the specific geometry of the eddy–promoter inclusions $\mathbf{Z}_{EP} = (x_d, y_d, Y, \lambda_1, \lambda_2)$ as well as the nondimensional, inverse channel height η_L. For the eddy–promoter problem examined in the Chapters 4 and 5, a reduced set of inputs is used. The generator strengths, λ_1 and λ_2, are fixed and the remainder of the geometric variables, x_d, y_d, and Y serve as inputs. This gives a reduced

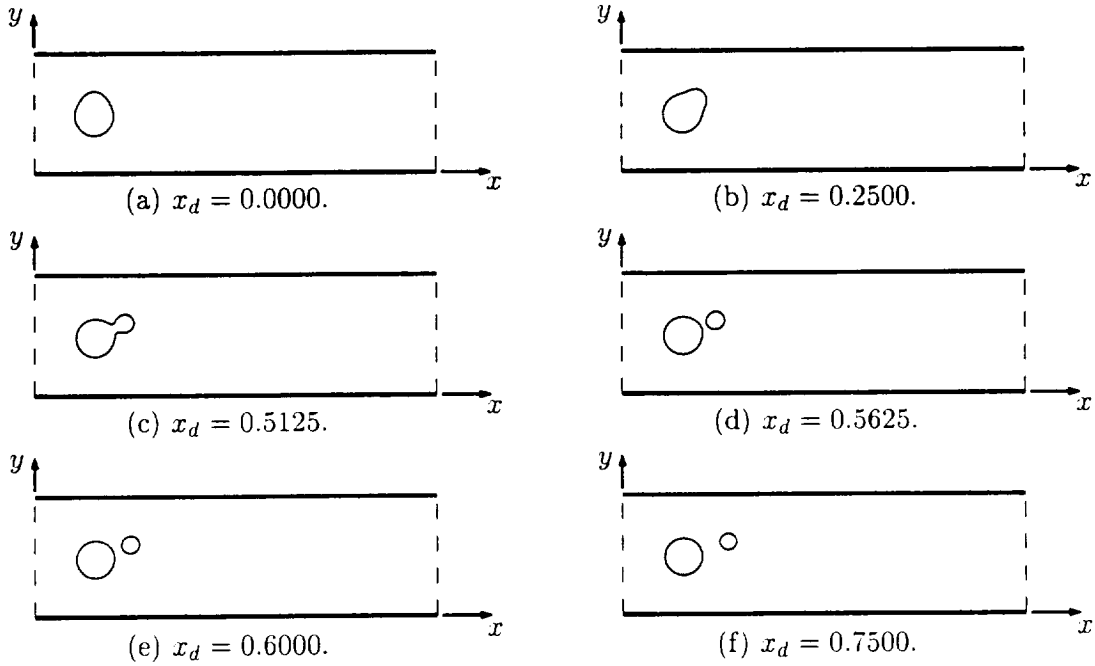

(a) $x_d = 0.0000$. (b) $x_d = 0.2500$.

(c) $x_d = 0.5125$. (d) $x_d = 0.5625$.

(e) $x_d = 0.6000$. (f) $x_d = 0.7500$.

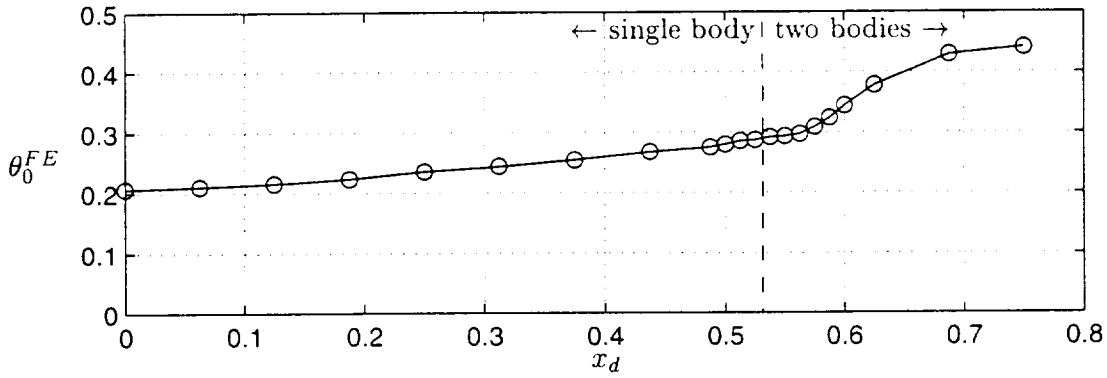

(g) Temperature response θ_0^{FE} versus x_d.

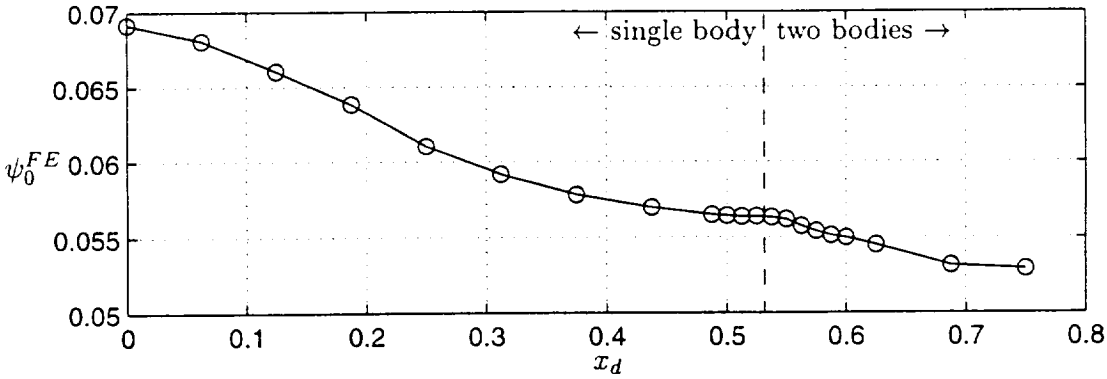

(h) Pressure forcing response ψ_0^{FE} versus x_d.

Figure 2-6: Input-output response results for a topology change. Selected eddy-promoter configurations are given in (a)—(f) and the output responses are plotted in (g) and (h) versus the geometric input x_d.

set for the normalized input vector

$$\mathbf{p} = (p_1, \ldots, p_4) \in \Omega = [0,1]^4 \tag{2.86}$$

which has $M = 4$ inputs and is a member of the normalized design space Ω. The fixed generator strengths are $\lambda_1 = 0.0871$, and $\lambda_2 = 0.1065$. The relationships between the normalized inputs $\mathbf{p}$ and the geometric quantities (x_d, y_d, Y, η_L) are

$$x_d = x_{\min} + p_1(x_{\max} - x_{\min}), \tag{2.87}$$

$$y_d = y_{\min} + p_2(y_{\max} - y_{\min}), \tag{2.88}$$

$$Y = Y_{\min} + p_3(Y_{\max} - Y_{\min}), \tag{2.89}$$

$$\eta_L = \eta_{L\min} + p_4(\eta_{L\max} - \eta_{L\min}), \tag{2.90}$$

where $x_{\min} = 0.0$, $x_{\max} = 3.5$, $y_{\min}$, $y_{\max}$, $Y_{\min}$, and $Y_{\max}$ are each determined based on $t_0 = 0.15$ and the generation steps described in Section 2.5.3, $\eta_{L\min} = 13.332$, and $\eta_{L\max} = 106.656$. The limits on the inverse channel height correspond to a range, for the full heat exchanger, from 4 periodicity lengths, l, through 32 periodicity lengths. The periodicity length is held fixed at $l = 6.666$.

For convenience in the latter sections of the thesis, it will be necessary to make a distinction between the inputs for which the performance metric response must be modeled, either by the finite element simulation or by surrogates, and the inputs for which the performance metric response is known analytically. The vector of modeled inputs $\mathbf{p}_m \in \Omega_m = [0,1]^3$ consists of the first three components given in Equation 2.86

$$\mathbf{p}_m = (p_1, p_2, p_3), \tag{2.91}$$

where the relationships in Equations 2.87—2.89 and the steps described in Section 2.5.3 are applied to relate the normalized inputs to the geometric quantities. The analytic input $\mathbf{p}_a \in \Omega_a = [0,1]$ corresponds to the inverse channel height

$$\mathbf{p}_a = (p_4). \tag{2.92}$$

where p_4 is the identical input to that given in Equation 2.86 and which can be related to η_L through Equation 2.90.

The design domain is likewise decomposed into modeled, $\Omega_m = [0,1]^{M_m}$, and analytic, $\Omega_a = [0,1]^{M_a}$, subspaces of Ω where the number of modeled inputs is $M_m = 3$ and the number of analytic inputs is $M_a = 1$. The full design domain is the tensor product given

by

$$\Omega = \Omega_m \times \Omega_a, \tag{2.93}$$

and the full design vector is

$$\mathbf{p} = (\mathbf{p}_m, \mathbf{p}_a) \in \Omega. \tag{2.94}$$

2.6.2 Outputs

The two-body, eddy-promoter problem has two outputs of interest. The outputs are each functions of the modeled design inputs, $\mathbf{p}_m$. The first output is the time-average of the nondimensional pressure gradient given in Equation 2.40 and expressed as

$$\psi_0(\mathbf{p}_m) = < \mathcal{F}(\mathbf{p}_m, t) > = < f(t) > \tag{2.95}$$

where as before, $< \cdot >$ refers to a time-average over a sufficiently long time.

The second output is the inverse Nusselt

$$\theta_0(\mathbf{p}_m) = \overline{\Delta T}(\mathbf{p}_m) = \frac{1}{Nu(\mathbf{p}_m)} \tag{2.96}$$

and is defined in Equation (2.51).

2.6.3 Performance Metrics

The performance metrics have been described in detail in Section 2.3 and will only be restated here. The metrics have been selected to characterize the design preference for the full eddy-promoter heat exchanger, a segment of which is shown at the top in Figure 2-2. The engineering goals of the design problem are to transfer as much heat as possible into the channel and to do so with as little pressure drop as necessary.

The performance metrics are functions of the modeled inputs $\mathbf{p}_m$ through the output functions $\psi_0(\mathbf{p}_m)$ and $\theta_0(\mathbf{p}_m)$ and, although not the case for this problem, could be explicit functions of the modeled inputs as well. The performance metrics are functions of the analytic inputs $\mathbf{p}_a$ explicitly. In fact, the analytic relationship between the performance metrics and $\mathbf{p}_a$ is known.

The first performance metric is the nondimensional pumping power

$$\Psi(\mathbf{p}) = \Psi(\phi_0(\mathbf{p}_m), \mathbf{p}) = \log_{10}\left[\psi_0(\mathbf{p}_m) Re^3 \eta_L^3\right] \tag{2.97}$$

which is a function of the output $\phi_0(\mathbf{p}_m)$ and of the analytic input $\mathbf{p}_a$ through the nondimensional, inverse channel length η_L. The response of $\Psi(\mathbf{p})$ to the input $\mathbf{p}_a$ is known analytically through the normalization relationship in Equation 2.90.

The second performance metric is the nondimensional wall temperature difference

$$\Theta(\mathbf{p}) = \Theta(\theta_0(\mathbf{p}_m), \mathbf{p}) = \log_{10}\left[\frac{1}{RePr} + \theta_0(\mathbf{p}_m)\frac{1}{\eta_L}\right] \tag{2.98}$$

which, similarly to $\Psi(\mathbf{p})$, is a function of the output $\theta_0(\mathbf{p}_m)$ and of the analytic input $\mathbf{p}_a$ through the nondimensional, inverse channel length η_L. The response of $\Theta(\mathbf{p})$ to $\mathbf{p}_a$ is also known analytically through Equation 2.90.

Chapter 3

Numerical Approach

In this section, the numerical approach used to solve the governing equations 2.25, 2.26, 2.31 is described. A second-order accurate in time, semi-implicit, split time advancement scheme has been used [23]. The spatial discretization uses a Galerkin finite element approach with triangular elements. Second order, isoparametric elements are used to approximate the velocity and temperature solutions and first order, linear elements are used to approximate the pressure. A variable time-stepping scheme has been employed to allow the time-step size to vary as the solution is advanced so that the Courant condition is satisfied.

In the following sections, the details of the numerical approach are presented. First, the spatial discretization is described including the elemental matrix treatment, the strategy used to form the convection operators *on-the-fly*, and the required quadrature accuracy to ensure that heat does not build up. Second, the second-order accurate, temporal discretization is presented, the method used to achieve the prescribed, constant flowrate is given, and the iterative and direct solvers used to invert the matrices are described. Finally, a sample of the code performance for a representative problem and for the various solver options is presented.

3.1 Finite-Element, Spatial Discretization

For symbolic expediency, in this section the velocity vector components will be expressed indicially, $\mathbf{u} = (u_1, u_2)$. This runs counter to the (u, v) form used in the remainder of this thesis but greatly simplifies the presentation of the numerical implementation. The variational weak form of the governing equations 2.25, 2.26, 2.31 over the solution domain Ω for the solution variables $\mathbf{u}(\mathbf{x}, t) \in [H^1_{\#0}(\Omega)]^2$, $p(\mathbf{x}, t) \in L^2_{\#0}(\Omega)$, and $\theta(\mathbf{x}, t) \in H^1_{\#}(\Omega)$ is

$$(v_i, \frac{\partial u_i}{\partial t}) + (v_i, \mathbf{u} \cdot \nabla u_i) + \frac{1}{Re}(\nabla v_i, \nabla u_i) - (\nabla v_i, p) = (v_i, f_i), \quad i = 1, 2,$$
$$\forall \mathbf{v} \in [H^1_{\#0}(\Omega)]^2. \quad (3.1)$$

$$(\nabla \cdot \mathbf{u}, q) = 0, \quad \forall q \in L^2_{\#0}(\Omega), \tag{3.2}$$

and

$$(w, \theta_t) + (w, \mathbf{u} \cdot (\nabla\theta)) + \frac{1}{RePr}(\nabla w, \nabla\theta) = -\gamma(w, \mathbf{u} \cdot \hat{\mathbf{e}}_1) + \frac{1}{RePr}\ell_{\partial\Omega_l}(w), \quad \forall w \in H^1_{\#0}(\Omega), \tag{3.3}$$

where

$$\ell_{\partial\Omega_l}(w) = \int_{\partial\Omega_l} w\, dl, \tag{3.4}$$

Ω_l is the lower wall of the computational domain, $L^2_{\#0}(\Omega)$ is the set of all x_1–periodic functions that are square integrable, and $H^1_{\#0}(\Omega)$ is the set of all x_1–periodic functions that are square integrable and have first derivatives that are also square integrable. The product (a, b) is defined as

$$(a, b) = \int_\Omega a\, b\, d\mathbf{x}. \tag{3.5}$$

A finite element, spatial discretization of the governing equations is pursued. A $\mathbb{P}_2$–$\mathbb{P}_1$ (Taylor–Hood [70]) elemental basis is selected. With this choice, the velocity and temperature solutions are represented by second order triangular element and the pressure is treated with linear triangular elements. The reason for choosing the Taylor–Hood elements is that it is known to satisfy the inf-sup condition [33] for the existence of a unique solution and can be conveniently implemented. The second order node points consist of the vertices of each element as well as the midpoints along each element side and the linear "pressure" mesh is simply a subset of the second order mesh consisting of only the node points at the vertex of each element.

The full solution domain Ω is subdivided into $\mathcal{N}^{el}$ triangular elements such that

$$\Omega = \bigcup_{k_e=1}^{\mathcal{N}^{el}} \Omega^{k_e}, \tag{3.6}$$

and Ω^{k_e} is the triangular element with index k_e. The discrete solution to the governing equations 3.1–3.3 can then be expressed as: Find $\mathbf{u}^h(\mathbf{x}, t) \in [V_h]^2$, $p^h(\mathbf{x}, t) \in P_h$, and $\theta^h(\mathbf{x}, t) \in V_h$ where the following are satisfied

$$(v_i, \frac{\partial u_i^h}{\partial t}) + (v_i, \mathbf{u}^h \cdot \nabla u_i^h) + \frac{1}{Re}(\nabla v_i, \nabla u_i^h) - (\nabla v_i, p_h) = (v_i, f_i^h), \quad i = 1, 2, \quad \forall \mathbf{v} \in [V_h]^2, \tag{3.7}$$

$$(\nabla \cdot \mathbf{u}^h, q) = 0, \quad \forall q \in P_h, \tag{3.8}$$

$$(w, \theta_t^h) + (w, \mathbf{u}^h \cdot (\nabla\theta^h)) + \frac{1}{RePr}(\nabla w, \nabla\theta^h) = -\gamma(w, \mathbf{u}^h \cdot \hat{\mathbf{e}}_1) + \frac{1}{RePr}\int_{\partial\Omega_l} w\, dS, \quad \forall w \in V_h. \tag{3.9}$$

The superscript 'h' refers to the discrete solution and the discrete subspaces are defined as

$$P_h = \{v|_{\Omega^{k_e}} \in I\!P_1(\Omega^{k_e})\} \cap C^2_{\#0}(\Omega), \tag{3.10}$$

$$V_h = \{v|_{\Omega^{k_e}} \in I\!P_2(\Omega^{k_e})\} \cap H^1_{\#0}(\Omega), \tag{3.11}$$

where $C^2_{\#0}(\Omega)$ is the space of all x_1-periodic functions that are continuous and have zero average.

A Galerkin finite element approach, in which the solution and test function bases are identical, is pursued. A global basis for the velocity and temperature is introduced

$$\phi_i(\mathbf{x}_j) = \delta_{ij}, \quad 1 \le i,j \le \mathcal{N}^v, \qquad V_h = \text{span}\{\phi_i,\ i = 1,\ldots,\mathcal{N}^v\}, \tag{3.12}$$

where $\mathcal{N}^v$ is the number of global second order nodes and $\mathbf{x}_j$ is the global coordinate of node j. The basis is used to express a general function v over the full solution domain Ω as

$$v^h(\mathbf{x}) = \sum_{n=1}^{\mathcal{N}^v} v_n \phi_n(\mathbf{x}) \tag{3.13}$$

where $v_i = v(\mathbf{x}_i)$. Similarly, a second basis for the pressure is introduced

$$\psi_i(\mathbf{x}_j) = \delta_{ij}, \quad 1 \le i,j \le \mathcal{N}^p, \qquad P_h = \text{span}\{\psi_i,\ i = 1,\ldots,\mathcal{N}^p\}, \tag{3.14}$$

where $\mathcal{N}^p$ is the number of global pressure nodes. The basis is used to express the general function q, discretely over Ω as

$$q^h(\mathbf{x}) = \sum_{n=1}^{\mathcal{N}^p} q_n \psi_n(\mathbf{x}) \tag{3.15}$$

and, as before, $q_i = q(\mathbf{x}_i)$.

To proceed with the discretization, the solution variables and the test functions are expanded with the appropriate basis function defined above. The expanded forms

$$\begin{aligned}
\mathbf{u}^h &= \sum_{n=1}^{\mathcal{N}^v} \mathbf{u}_n \phi_n(\mathbf{x}), & \mathbf{v} &= \sum_{n=1}^{\mathcal{N}^v} \mathbf{v}_n \phi_n(\mathbf{x}), \\
p^h &= \sum_{n=1}^{\mathcal{N}^p} p_n \psi_n(\mathbf{x}), & q &= \sum_{n=1}^{\mathcal{N}^p} q_n \psi_n(\mathbf{x}), \\
\theta^h &= \sum_{n=1}^{\mathcal{N}^v} \theta_n \phi_n(\mathbf{x}), & w &= \sum_{n=1}^{\mathcal{N}^v} w_n \phi_n(\mathbf{x}).
\end{aligned} \tag{3.16}$$

are substituted into Equations 3.7–3.9. The resulting spatially-discrete, governing equations

are obtained

$$\mathbf{B}\frac{\partial u_i}{\partial t} + \mathbf{C}(\mathbf{u})u_i + \frac{1}{Re}\mathbf{A}u_i - \mathbf{D}_i^T p = \mathbf{B}f_i, \quad i = 1, 2, \tag{3.17}$$

$$\mathbf{D}_i u_i = 0, \tag{3.18}$$

$$\mathbf{B}\theta_t + \mathbf{C}(\mathbf{u})\theta + \frac{1}{RePr}\mathbf{A}\theta = -\gamma\mathbf{B}(\mathbf{u}\cdot\hat{\mathbf{e}}_1), \tag{3.19}$$

where, for convenience, the superscript 'h' has been dropped. The finite element matrices are

$$\mathbf{B}_{ij} = \int_\Omega \phi_i\phi_j \, d\mathbf{x} \tag{3.20}$$

$$\mathbf{A}_{ij} = \int_\Omega \nabla\phi_i \cdot \nabla\phi_j \, d\mathbf{x} \tag{3.21}$$

$$\mathbf{D}_{1ij} = \int_\Omega \phi_{i,1}\psi_j \, d\mathbf{x}, \quad \mathbf{D}_{2ij} = \int_\Omega \phi_{i,2}\psi_j \, d\mathbf{x} \tag{3.22}$$

$$\mathbf{C}_{ij}(\mathbf{u}) = \int_\Omega \mathbf{u}\nabla\phi_i\phi_j \, d\mathbf{x} \tag{3.23}$$

The finite elemental matrices given in Equations 3.20—3.23 are evaluated elementally, and a direct stiffness summation procedure is used to apply the corresponding global matrix operators when needed.

3.1.1 Elemental Matrices – $\mathbb{P}_2$ Isoparametric Formulation

At the elemental level, each element is transformed from the Cartesian coordinate system to an elemental coordinate system through a a transformation. For subparametric elements, an affine transformation is used. For such a transformation, the elemental coordinates $\boldsymbol{\xi} = (\xi_1, \xi_2, \xi_3)$ take the form

$$\begin{aligned} \xi_1 &= a_1 + b_1 x + c_1 y, \\ \xi_2 &= a_2 + b_2 x + c_2 y, \\ \xi_3 &= a_3 + b_3 x + c_3 y, \end{aligned} \tag{3.24}$$

where the coefficients are given by

$$\begin{aligned} a_1 &= \frac{(x_2y_3 - x_3y_2)}{2A}, \quad b_1 = \frac{(y_2 - y_3)}{2A}, \quad c_1 = \frac{(x_3 - x_2)}{2A}, \\ a_2 &= \frac{(x_3y_1 - x_1y_3)}{2A}, \quad b_2 = \frac{(y_3 - y_1)}{2A}, \quad c_2 = \frac{(x_1 - x_3)}{2A}, \\ a_3 &= \frac{(x_1y_2 - x_2y_1)}{2A}, \quad b_3 = \frac{(y_1 - y_2)}{2A}, \quad c_3 = \frac{(x_2 - x_1)}{2A}, \end{aligned} \tag{3.25}$$

and A is the area of the element. Note that only two of the affine coordinates are independent (as expected for $\mathbb{R}^2$) and the the relationship that $\xi_1 + \xi_2 + \xi_3 = 1$ holds. If subparametric

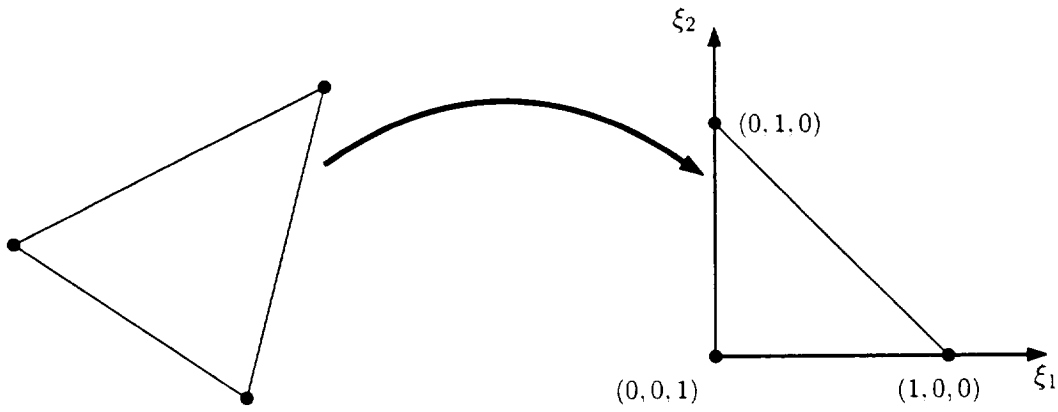

Figure 3-1: Affine mapping from the $\mathbf{x}$-plane to barycentric coordinates $\boldsymbol{\xi} = (\xi_1, \xi_2, \xi_3)$.

elements are used, the expressions in Equations 3.24 and 3.25 allow the elemental matrices to be evaluated analytically. Because isoparametric elements have been used in this work, the elemental matrices can not be evaluated analytically and the relationship in Equations 3.24 and 3.25 can not be applied. Instead Gaussian quadrature must be used to evaluate the elemental matrices' integrals.

Over element k_e, a function can be expressed in terms of the elemental, linear basis functions as

$$q^{k_e}(\boldsymbol{\xi}) = \sum_{i=1}^{3} q_i^{k_e} \widehat{h}_i(\boldsymbol{\xi}), \tag{3.26}$$

where the linear basis functions are

$$\widehat{h}_1(\boldsymbol{\xi}) = \xi_1, \qquad \widehat{h}_2(\boldsymbol{\xi}) = \xi_2, \qquad \widehat{h}_3(\boldsymbol{\xi}) = \xi_3, \tag{3.27}$$

and $q_i^{k_e}$ is the function value at node i of the element k_e. Similarly, a function can be expressed in terms of the elemental, second order basis functions as

$$v^{k_e}(\boldsymbol{\xi}) = \sum_{i=1}^{6} v_i^{k_e} h_i(\boldsymbol{\xi}), \tag{3.28}$$

where the second order basis functions are

$$\begin{aligned} h_1(\boldsymbol{\xi}) &= \xi_1(2\xi_1 - 1), & h_4(\boldsymbol{\xi}) &= 4\xi_1\xi_2, \\ h_2(\boldsymbol{\xi}) &= \xi_2(2\xi_2 - 1), & h_5(\boldsymbol{\xi}) &= 4\xi_2\xi_3, \\ h_3(\boldsymbol{\xi}) &= \xi_3(2\xi_3 - 1), & h_6(\boldsymbol{\xi}) &= 4\xi_3\xi_1. \end{aligned} \tag{3.29}$$

The derivatives of the basis functions with respect to the barycentric coordinates, $\boldsymbol{\xi}$, are

obtained from the expressions in Equation 3.29, and the relationship that $\xi_3 = 1 - \xi_1 + \xi_2$ and are

$$\begin{aligned}
\frac{\partial h_1(\boldsymbol{\xi})}{\partial \xi_1} &= 4\xi_1 - 1, & \frac{\partial h_1(\boldsymbol{\xi})}{\partial \xi_2} &= 0, \\
\frac{\partial h_2(\boldsymbol{\xi})}{\partial \xi_1} &= 4\xi_2 - 1, & \frac{\partial h_2(\boldsymbol{\xi})}{\partial \xi_2} &= 0, \\
\frac{\partial h_3(\boldsymbol{\xi})}{\partial \xi_1} &= 4(\xi_1 + \xi_2) - 3, & \frac{\partial h_3(\boldsymbol{\xi})}{\partial \xi_2} &= 4(\xi_1 + \xi_2) - 3, \\
\frac{\partial h_4(\boldsymbol{\xi})}{\partial \xi_1} &= 4\xi_2, & \frac{\partial h_4(\boldsymbol{\xi})}{\partial \xi_2} &= 4\xi_1, \\
\frac{\partial h_5(\boldsymbol{\xi})}{\partial \xi_1} &= -4\xi_2, & \frac{\partial h_5(\boldsymbol{\xi})}{\partial \xi_2} &= 4(1 - \xi_1 - 2\xi_2), \\
\frac{\partial h_6(\boldsymbol{\xi})}{\partial \xi_1} &= 4(1 - 2\xi_1 - \xi_2), & \frac{\partial h_6(\boldsymbol{\xi})}{\partial \xi_2} &= -4\xi_1.
\end{aligned} \tag{3.30}$$

A direct stiffness summation procedure is used to form the matrices given in Equations 3.20–3.23 based on elemental components. This is accomplished by using the local basis functions given in Equations 3.27 and 3.29 and transforming the integrals to $\boldsymbol{\xi}$-space. For example, the elemental contribution for stiffness matrix is

$$\mathbf{A}_{ij}^{k_\epsilon} = \int_{\Omega^{k_\epsilon}} J(\boldsymbol{\xi}) \left(\frac{\partial h_i(\boldsymbol{\xi})}{\partial x} \frac{\partial h_j(\boldsymbol{\xi})}{\partial x} + \frac{\partial h_i(\boldsymbol{\xi})}{\partial y} \frac{\partial h_j(\boldsymbol{\xi})}{\partial y} \right) d\boldsymbol{\xi}, \tag{3.31}$$

where the Jacobian $J(\boldsymbol{\xi})$ is given as

$$J(\boldsymbol{\xi}) = \frac{\partial x}{\partial \xi_1} \frac{\partial y}{\partial \xi_2} - \frac{\partial x}{\partial \xi_2} \frac{\partial y}{\partial \xi_1} \tag{3.32}$$

and is a function of the coordinate $\boldsymbol{\xi}$ because of the isoparametric implementation. The (x, y)–coordinates are expanded in terms of the basis functions in Equation 3.29 as

$$x(\boldsymbol{\xi}) = \sum_{i=1}^{6} x_i h_i(\boldsymbol{\xi}), \quad y(\boldsymbol{\xi}) = \sum_{i=1}^{6} y_i h_i(\boldsymbol{\xi}). \tag{3.33}$$

Plugging the coordinate expressions into Equation 3.32 gives

$$J(\boldsymbol{\xi}) = \left(\sum_{i=1}^{6} x_i \frac{\partial h_i(\boldsymbol{\xi})}{\partial \xi_1} \right) \left(\sum_{i=1}^{6} y_i \frac{\partial h_i(\boldsymbol{\xi})}{\partial \xi_2} \right) - \left(\sum_{i=1}^{6} x_i \frac{\partial h_i(\boldsymbol{\xi})}{\partial \xi_2} \right) \left(\sum_{i=1}^{6} y_i \frac{\partial h_i(\boldsymbol{\xi})}{\partial \xi_1} \right) \tag{3.34}$$

which is now expressed entirely in terms of the $\boldsymbol{\xi}$ coordinates.

The derivatives within the parentheses in 3.31 (of the elemental basis functions with

respect to x and y) are expanded as

$$\frac{\partial h_i(\boldsymbol{\xi})}{\partial x} = \frac{\partial h_i(\boldsymbol{\xi})}{\partial \xi_1}\frac{\partial \xi_1}{\partial x} + \frac{\partial h_i(\boldsymbol{\xi})}{\partial \xi_2}\frac{\partial \xi_2}{\partial x}, \tag{3.35}$$

$$\frac{\partial h_i(\boldsymbol{\xi})}{\partial y} = \frac{\partial h_i(\boldsymbol{\xi})}{\partial \xi_1}\frac{\partial \xi_1}{\partial y} + \frac{\partial h_i(\boldsymbol{\xi})}{\partial \xi_2}\frac{\partial \xi_2}{\partial y}. \tag{3.36}$$

To obtain derivatives of the elemental coordinates with respect to the Cartesian coordinates, the relationships

$$dx = x_{\xi_1} d\xi_1 + x_{\xi_2} d\xi_2, \tag{3.37}$$

$$dy = y_{\xi_1} d\xi_1 + y_{\xi_2} d\xi_2, \tag{3.38}$$

are solved for the differentials $d\xi_1$ and $d\xi_2$. This gives the expressions

$$d\xi_1 = \frac{y_{\xi_2} dx - x_{\xi_2} dy}{x_{\xi_1} y_{\xi_2} - x_{\xi_2} y_{\xi_1}}, \tag{3.39}$$

$$d\xi_2 = \frac{x_{\xi_1} dx - y_{\xi_1} dy}{x_{\xi_1} y_{\xi_2} - x_{\xi_2} y_{\xi_1}}, \tag{3.40}$$

from which the desired results are easily obtained. Recognizing that the denominators in Equations 3.39 and 3.40 are the Jacobian (3.34), the expressions for the derivatives of the elemental coordinates with respect to the Cartesian coordinates are

$$\begin{aligned} \frac{\partial \xi_1}{\partial x} &= \frac{y_{\xi_2}}{J(\boldsymbol{\xi})}, & \frac{\partial \xi_1}{\partial y} &= -\frac{x_{\xi_2}}{J(\boldsymbol{\xi})}, \\ \frac{\partial \xi_2}{\partial x} &= -\frac{y_{\xi_1}}{J(\boldsymbol{\xi})}, & \frac{\partial \xi_2}{\partial y} &= \frac{x_{\xi_1}}{J(\boldsymbol{\xi})}. \end{aligned} \tag{3.41}$$

Again, the derivatives of the Cartesian coordinates with respect to the elemental coordinates can be obtained, as they were for the Jacobian in Equation 3.34, by using the expressions in Equation 3.33.

An expression for the stiffness matrix that is entirely in terms of the elemental coordinates, $\boldsymbol{\xi}$, can be obtained by first substituting Equation 3.41 into Equations 3.35 and 3.36 to obtain

$$\frac{\partial h_i(\boldsymbol{\xi})}{\partial x} = \frac{1}{J(\boldsymbol{\xi})}\left(\frac{\partial h_i(\boldsymbol{\xi})}{\partial \xi_1}\frac{\partial y}{\partial \xi_2} - \frac{\partial h_i(\boldsymbol{\xi})}{\partial \xi_2}\frac{\partial y}{\partial \xi_1}\right), \tag{3.42}$$

$$\frac{\partial h_i(\boldsymbol{\xi})}{\partial y} = \frac{1}{J(\boldsymbol{\xi})}\left(\frac{\partial h_i(\boldsymbol{\xi})}{\partial \xi_2}\frac{\partial x}{\partial \xi_1} - \frac{\partial h_i(\boldsymbol{\xi})}{\partial \xi_1}\frac{\partial x}{\partial \xi_2}\right). \tag{3.43}$$

Finally, substituting Equations 3.42 and 3.43 into Equation 3.31 gives an expression for the stiffness matrix that is a function of $\boldsymbol{\xi}$ only

$$\mathbf{A}_{ij}^{k_e}(\boldsymbol{\xi}) = \int_{\Omega^{k_e}} \frac{1}{J(\boldsymbol{\xi})}\left[\left(\frac{\partial h_i(\boldsymbol{\xi})}{\partial \xi_1}\frac{\partial y}{\partial \xi_2} - \frac{\partial h_i(\boldsymbol{\xi})}{\partial \xi_2}\frac{\partial y}{\partial \xi_1}\right)\left(\frac{\partial h_j(\boldsymbol{\xi})}{\partial \xi_1}\frac{\partial y}{\partial \xi_2} - \frac{\partial h_j(\boldsymbol{\xi})}{\partial \xi_2}\frac{\partial y}{\partial \xi_1}\right) +$$

$$\left(\frac{\partial h_i(\boldsymbol{\xi})}{\partial \xi_2}\frac{\partial x}{\partial \xi_1} - \frac{\partial h_i(\boldsymbol{\xi})}{\partial \xi_1}\frac{\partial x}{\partial \xi_2}\right)\left(\frac{\partial h_j(\boldsymbol{\xi})}{\partial \xi_2}\frac{\partial x}{\partial \xi_1} - \frac{\partial h_j(\boldsymbol{\xi})}{\partial \xi_1}\frac{\partial x}{\partial \xi_2}\right)\Big] d\boldsymbol{\xi}, \quad (3.44)$$

where the Jacobian, $J(\boldsymbol{\xi})$, is given in Equation 3.34.

The remainder of the elemental matrices are obtained by following the same procedure as was used for the stiffness matrix. The resulting expression for the mass matrix is

$$\mathbf{B}_{ij}^{k_e}(\boldsymbol{\xi}) = \int_{\Omega^{k_e}} J(\boldsymbol{\xi}) h_i(\boldsymbol{\xi}) h_i(\boldsymbol{\xi})\, d\boldsymbol{\xi}. \quad (3.45)$$

The gradient matrix in Equation 3.22 is split into two components; the first for the derivative in the x-direction and the second for the derivative in the y-direction. The resulting two matrices are

$$\mathbf{D}_{1}{}_{ij}^{k_e}(\boldsymbol{\xi}) = \int_{\Omega^{k_e}} \left(\frac{\partial h_i(\boldsymbol{\xi})}{\partial \xi_1}\frac{\partial y}{\partial \xi_2} - \frac{\partial h_i(\boldsymbol{\xi})}{\partial \xi_2}\frac{\partial y}{\partial \xi_1}\right) \widehat{h}_j(\boldsymbol{\xi})\, d\boldsymbol{\xi}, \quad (3.46)$$

$$\mathbf{D}_{2}{}_{ij}^{k_e}(\boldsymbol{\xi}) = \int_{\Omega^{k_e}} \left(\frac{\partial h_k(\boldsymbol{\xi})}{\partial \xi_2}\frac{\partial x}{\partial \xi_1} - \frac{\partial h_k(\boldsymbol{\xi})}{\partial \xi_1}\frac{\partial x}{\partial \xi_2}\right) \widehat{h}_j(\boldsymbol{\xi})\, d\boldsymbol{\xi}, \quad (3.47)$$

and it is interesting to note that the Jacobians completely cancel in the above expressions.

The elemental component of the full convection operator in Equation 3.23 is broken into its directional components. The velocity vector that is embedded in the integral is expanded with the local basis functions similarly to Equation 3.33. The expansion allows the velocity values at the nodes to be taken out of the integral. The elemental convection operator is

$$\mathbf{C}_{ij}^{k_e}(\mathbf{u}^{k_e}) = \sum_{i=1}^{6} (u_1)_i^{k_e}\, \mathbf{C}_{1}{}_{ijk}^{k_e} + \sum_{i=1}^{6} (u_2)_i^{k_e}\, \mathbf{C}_{2}{}_{ijk}^{k_e}, \quad (3.48)$$

where the convection operators take the form

$$\mathbf{C}_{1}{}_{ijk}^{k_e}(\boldsymbol{\xi}) = \int_{\Omega^{k_e}} h_i(\boldsymbol{\xi}) h_j(\boldsymbol{\xi}) \left(\frac{\partial h_k(\boldsymbol{\xi})}{\partial \xi_1}\frac{\partial y}{\partial \xi_2} - \frac{\partial h_k(\boldsymbol{\xi})}{\partial \xi_2}\frac{\partial y}{\partial \xi_1}\right) d\boldsymbol{\xi}, \quad (3.49)$$

$$\mathbf{C}_{2}{}_{ijk}^{k_e}(\boldsymbol{\xi}) = \int_{\Omega^{k_e}} h_i(\boldsymbol{\xi}) h_j(\boldsymbol{\xi}) \left(\frac{\partial h_k(\boldsymbol{\xi})}{\partial \xi_2}\frac{\partial x}{\partial \xi_1} - \frac{\partial h_k(\boldsymbol{\xi})}{\partial \xi_1}\frac{\partial x}{\partial \xi_2}\right) d\boldsymbol{\xi}. \quad (3.50)$$

For subparametric elements in which the second order nodes are at the midpoints of the vertices, the elemental matrices in Equations 3.44-3.50 can be evaluated analytically. However, subparametric elements introduce 'skin' [69] errors along curved boundaries. To reduce the skin errors, isoparametric elements are used along the curved boundaries. With the isoparametric elements, it is not possible to compute the integrals of the elemental matrices analytically, and Gaussian quadrature is used instead. Using Gaussian quadrature, the integral of a function $g(\boldsymbol{\xi}) : \Omega^{k_e} \rightarrow \mathbb{R}$ is approximated as

$$\int_{\Omega^{k_e}} g(\boldsymbol{\xi}) d\boldsymbol{\xi} \approx \text{area}^{k_e} \sum_{i=1}^{\mathcal{N}^q} \varpi_i g(\boldsymbol{\xi}_i), \quad (3.51)$$

where area^{k_e} is the area of element k_e. The weight at point i is ϖ_i and the position to evaluate the integrand is quadrature point $\boldsymbol{\xi}_i$. When used for the matrix evaluations, the area of the elements in ξ-coordinates is always area$^{k_e} = 1/2$. A 5^{th}-order Gaussian quadrature scheme in which $\mathcal{N}^q = 7$ has been used for all of the simulations. The weights, ϖ_i, and quadrature points, $\boldsymbol{\xi}_i$, are given in Appendix C.1.

3.1.2 Convection Operator Treatment

The elemental stiffness, mass, and gradient matrices in Equations 3.44–3.47 are computed for each element $k_e = 1, \ldots, \mathcal{N}^{el}$ and stored in three-dimensional arrays during the initialization phase of each run of the Navier-Stokes code. Neglecting symmetries, the storage required for each of the stiffness matrix, mass matrix, and the two gradient matrices combined, is $6 \times 6 \times \mathcal{N}^{el}$, which is not unreasonable from a memory standpoint. However, each convection operator requires $6 \times 6 \times 6 \times \mathcal{N}^{el}$ for storage which has a dominant impact on the code memory requirement. While this issue is only moderately significant for the two-dimensional solver, it dominates the storage for three-dimensional problems and severely limits the size of problemsthat can be solved.

Fortunately, the application of the convection operator can be evaluated for each time-step as needed (on-the-fly) at the expense of only a moderate increase in computational effort. This completely eliminates the overwhelming storage penalty. To demonstrate the scheme used, the convection operator term in the u-momentum equation is used as an example. The velocity vector in two-dimensions is $\mathbf{u} = (u_1, u_2)$. The variational weak form for this term is

$$\begin{aligned}
(w, \mathbf{u} \cdot \nabla u_1) &= \int_{\widehat{\Omega}^{k_e}} w\mathbf{u} \cdot \nabla u_1 \, d\mathbf{x} \\
&= \int_{\Omega^{k_e}} J(\boldsymbol{\xi}) w\mathbf{u} \cdot \nabla u_1 \, d\boldsymbol{\xi} \\
&= \int_{\Omega^{k_e}} J(\boldsymbol{\xi}) w \left(u_1 \frac{\partial u_1}{\partial x} + u_2 \frac{\partial u_1}{\partial y} \right) d\boldsymbol{\xi} \\
&= \int_{\Omega^{k_e}} J(\boldsymbol{\xi}) w u_1 \frac{\partial u_1}{\partial x} \, d\boldsymbol{\xi} + \int_{\Omega^{k_e}} J(\boldsymbol{\xi}) w u_2 \frac{\partial u_1}{\partial y} \, d\boldsymbol{\xi}
\end{aligned} \tag{3.52}$$

where w is the test function. The test function and the velocities are expanded in terms of the elemental basis functions

$$w^{k_e}(\boldsymbol{\xi}) = \sum_{i=1}^{6} w_i^{k_e} h_i(\boldsymbol{\xi}), \quad u_1^{k_e}(\boldsymbol{\xi}) = \sum_{i=1}^{6} (u_1)_i^{k_e} h_i(\boldsymbol{\xi}), \quad u_2^{k_e}(\boldsymbol{\xi}) = \sum_{i=1}^{6} (u_2)_i^{k_e} h_i(\boldsymbol{\xi}), \tag{3.53}$$

where $w_i^{k_e}$, $(u_1)_i^{k_e}$, and $(u_2)_i^{k_e}$ are the values of the test function and the velocities at node i of element k_e.

If only the first term on the last line of Equation 3.52 is considered first, the expansions

in Equation 3.53 and the result given in Equation 3.49 can be used to obtain

$$\int_{\Omega^{k_e}} J(\boldsymbol{\xi}) w u_1 \frac{\partial u_1}{\partial x}\, d\boldsymbol{\xi} = \sum_{i=1}^{6}\sum_{j=1}^{6}\sum_{k=1}^{6} w_i^{k_e} (u_1)_j^{k_e} (u_1)_k^{k_e} \mathbf{C}_{1_{ijk}}^{k_e}(\boldsymbol{\xi}). \tag{3.54}$$

Similarly, using the same expansions and the convection operator in Equation 3.50, the last term on the last line of Equation 3.52 can be written as

$$\int_{\Omega^{k_e}} J(\boldsymbol{\xi}) w u_2 \frac{\partial u_1}{\partial y}\, d\boldsymbol{\xi} = \sum_{i=1}^{6}\sum_{j=1}^{6}\sum_{k=1}^{6} w_i^{k_e} (u_2)_j^{k_e} (u_1)_k^{k_e} \mathbf{C}_{2_{ijk}}^{k_e}(\boldsymbol{\xi}). \tag{3.55}$$

Recognizing the the convection operators in Equations 3.49 and 3.50 are of the form

$$\mathbf{C}_{1_{ijk}}^{k_e}(\boldsymbol{\xi}) = \int_{\widehat{\Omega}^{k_e}} G_{ijk}^{C_1}(\boldsymbol{\xi})\, d\boldsymbol{\xi}, \qquad \mathbf{C}_{2_{ijk}}^{k_e}(\boldsymbol{\xi}) = \int_{\widehat{\Omega}^{k_e}} G_{ijk}^{C_2}(\boldsymbol{\xi})\, d\boldsymbol{\xi}, \tag{3.56}$$

where

$$G_{ijk}^{C_1}(\boldsymbol{\xi}) = h_i(\boldsymbol{\xi}) h_j(\boldsymbol{\xi}) \left(\frac{\partial h_k(\boldsymbol{\xi})}{\partial \xi_1}\frac{\partial y}{\partial \xi_2} - \frac{\partial h_k(\boldsymbol{\xi})}{\partial \xi_2}\frac{\partial y}{\partial \xi_1} \right), \tag{3.57}$$

$$G_{ijk}^{C_2}(\boldsymbol{\xi}) = h_i(\boldsymbol{\xi}) h_j(\boldsymbol{\xi}) \left(\frac{\partial h_k(\boldsymbol{\xi})}{\partial \xi_2}\frac{\partial x}{\partial \xi_1} - \frac{\partial h_k(\boldsymbol{\xi})}{\partial \xi_1}\frac{\partial x}{\partial \xi_2} \right), \tag{3.58}$$

and evaluating the integrals by Gaussian quadrature as in Equation 3.51 gives the following expressions

$$\int_{\Omega^{k_e}} J(\boldsymbol{\xi}) w u_1 \frac{\partial u_1}{\partial x}\, d\boldsymbol{\xi} \approx \frac{1}{2}\sum_{l=1}^{\mathcal{N}^q}\sum_{i=1}^{6}\sum_{j=1}^{6}\sum_{k=1}^{6} \varpi_l w_i^{k_e} (u_1)_j^{k_e} (u_1)_k^{k_e} G_{ijk}^{C_1}(\boldsymbol{\xi}_l), \tag{3.59}$$

$$\int_{\Omega^{k_e}} J(\boldsymbol{\xi}) w u_2 \frac{\partial u_1}{\partial y}\, d\boldsymbol{\xi} \approx \frac{1}{2}\sum_{l=1}^{\mathcal{N}^q}\sum_{i=1}^{6}\sum_{j=1}^{6}\sum_{k=1}^{6} \varpi_l w_i^{k_e} (u_1)_j^{k_e} (u_2)_k^{k_e} G_{ijk}^{C_2}(\boldsymbol{\xi}_l). \tag{3.60}$$

where $\boldsymbol{\xi}_l$ is the coordinate of quadrature point l.

The summations over i in Equations 3.59 and 3.60 are dropped because the solution will be for *any* test function $w_i^{k_e} \in V_h$. The expressions for the convection operators could be implemented in a code with nested summations exactly as suggested by Equations 3.59 and 3.60, but this would be extremely inefficient. Instead, by expanding the expressions for $G_{ijk}^{C_1}(\boldsymbol{\xi}_l)$ and $G_{ijk}^{C_2}(\boldsymbol{\xi}_l)$, the terms in Equations 3.59 and 3.60 precomputed and stored inside of the direct stiffness summation procedure. This greatly reduces the number of operations from a brute-force implementation.

First, for Equation 3.59, the regrouping takes the form

$$\frac{1}{2}\sum_{l=1}^{\mathcal{N}^q}\sum_{j=1}^{6}\sum_{k=1}^{6} \varpi_l (u_1)_j^{k_e} (u_1)_k^{k_e} G_{ijk}^{C_1}(\boldsymbol{\xi}_l) =$$

$$\frac{1}{2}\sum_{l=1}^{\mathcal{N}^q}\varpi_l\left[h_i(\boldsymbol{\xi}_l)\left(\sum_{j=1}^{6}(u_1)_j^{k_e}h_j(\boldsymbol{\xi}_l)\right)\left(\sum_{j=1}^{6}(u_1)_j^{k_e}\left(\frac{\partial h_j(\boldsymbol{\xi}_l)}{\partial\xi_1}\frac{\partial y}{\partial\xi_2}-\frac{\partial h_j(\boldsymbol{\xi}_l)}{\partial\xi_2}\frac{\partial y}{\partial\xi_1}\right)\right)\right]. \quad (3.61)$$

Similarly, the regrouped form for Equation 3.60 is

$$\frac{1}{2}\sum_{l=1}^{\mathcal{N}^q}\sum_{j=1}^{6}\sum_{k=1}^{6}\varpi_l(u_1)_j^{k_e}(u_2)_k^{k_e}G_{ijk}^{C_2}(\boldsymbol{\xi}_l) =$$
$$\frac{1}{2}\sum_{l=1}^{\mathcal{N}^q}\varpi_l\left[h_i(\boldsymbol{\xi}_l)\left(\sum_{j=1}^{6}(u_1)_j^{k_e}h_j(\boldsymbol{\xi}_l)\right)\left(\sum_{j=1}^{6}(u_2)_j^{k_e}\left(\frac{\partial h_j(\boldsymbol{\xi}_l)}{\partial\xi_2}\frac{\partial x}{\partial\xi_1}-\frac{\partial h_j(\boldsymbol{\xi}_l)}{\partial\xi_1}\frac{\partial x}{\partial\xi_2}\right)\right)\right]. \quad (3.62)$$

At this point, all that remains is to clean up the terms in Equations 3.61 and 3.62. The j- and k-summation terms in Equations 3.61 and 3.62 can be precomputed at each quadrature point and stored. The terms are

$$I^C(\underline{u}_1^{k_e},\boldsymbol{\xi}_l)=\sum_{j=1}^{6}(u_1)_j^{k_e}h_j(\boldsymbol{\xi}_l), \quad (3.63)$$

$$I^C(\underline{u}_2^{k_e},\boldsymbol{\xi}_l)=\sum_{j=1}^{6}(u_2)_j^{k_e}h_j(\boldsymbol{\xi}_l). \quad (3.64)$$

$$I_x^C(\underline{u}_1^{k_e},\boldsymbol{\xi}_l)=\sum_{j=1}^{6}(u_1)_j^{k_e}\left(\frac{\partial h_j(\boldsymbol{\xi}_l)}{\partial\xi_1}\frac{\partial y}{\partial\xi_2}-\frac{\partial h_j(\boldsymbol{\xi}_l)}{\partial\xi_2}\frac{\partial y}{\partial\xi_1}\right). \quad (3.65)$$

$$I_y^C(\underline{u}_2^{k_e},\boldsymbol{\xi}_l)=\sum_{j=1}^{6}(u_2)_j^{k_e}\left(\frac{\partial h_j(\boldsymbol{\xi}_l)}{\partial\xi_2}\frac{\partial x}{\partial\xi_1}-\frac{\partial h_j(\boldsymbol{\xi}_l)}{\partial\xi_1}\frac{\partial x}{\partial\xi_2}\right). \quad (3.66)$$

where $\underline{u}_1^{k_e}=((u_1)_1^{k_e},\ldots,(u_1)_6^{k_e})$ and $\underline{u}_2^{k_e}=((u_2)_1^{k_e}\ldots,(u_2)_6^{k_e})$ are vectors of the velocity components at each node of element k_e. A vector $\mathcal{N}^q$ long is required to store each of the terms in Equations 3.63-3.66. Additionally, the values of the basis functions and the derivatives of the basis functions can be precomputed at each quadrature point, further reducing the operations needed during the time advancement. The only elementally-dependent quantities that are needed for the above calculations are for $\underline{u}_1^{k_e}$, $\underline{u}_2^{k_e}$, and the derivatives of x and y with respect to the elemental coordinates. The derivatives are computed as they are for the expression in Equation 3.34.

Finally, inside of the loop over the elements of the direct stiffness summation procedure, the terms $I^C(\underline{u}^{k_e},\boldsymbol{\xi}_l)$, $I^C(\underline{v}^{k_e},\boldsymbol{\xi}_l)$, $I_x^C(\underline{u}^{k_e},\boldsymbol{\xi}_l)$, $I_x^C(\underline{v}^{k_e},\boldsymbol{\xi}_l)$, $I_y^C(\underline{u}^{k_e},\boldsymbol{\xi}_l)$, and $I_y^C(\underline{v}^{k_e},\boldsymbol{\xi}_l)$ are computed and stored in $\mathcal{N}^q$-length vectors. For the elemental computations, the terms $I^C(\underline{u}^{k_e},\boldsymbol{\xi}_l)$ and $I^C(\underline{v}^{k_e},\boldsymbol{\xi}_l)$ each require $2\times6\times\mathcal{N}^q$ operations and the terms $I_x^C(\underline{u}^{k_e},\boldsymbol{\xi}_l)$, $I_x^C(\underline{v}^{k_e},\boldsymbol{\xi}_l)$, $I_y^C(\underline{u}^{k_e},\boldsymbol{\xi}_l)$, and $I_y^C(\underline{v}^{k_e},\boldsymbol{\xi}_l)$ each require $5\times6\times\mathcal{N}^q$ operations. The derivatives of the spatial coordinates with respect to the ξ-coordinates in Equations 3.65 and 3.66 require $8\times6\times\mathcal{N}^q$ operations. The effect of the convection operator is added to the the

right hand side of the discrete equations with a direct stiffness summation procedure. The elemental contributions to the right hand sides of the x- and y-momentum equations are

$$RHS_{1_i}^{k_e} = \frac{1}{2}\sum_{l=1}^{\mathcal{N}^q} \varpi_l h_i(\boldsymbol{\xi}_l)\left[I^C(\underline{u}_1^{k_e},\boldsymbol{\xi}_l)I_x^C(\underline{u}_1^{k_e},\boldsymbol{\xi}_l) + I^C(\underline{u}_2^{k_e},\boldsymbol{\xi}_l)I_y^C(\underline{u}_1^{k_e},\boldsymbol{\xi}_l)\right], \tag{3.67}$$

$$RHS_{2_i}^{k_e} = \frac{1}{2}\sum_{l=1}^{\mathcal{N}^q} \varpi_l h_i(\boldsymbol{\xi}_l)\left[I^C(\underline{u}_1^{k_e},\boldsymbol{\xi}_l)I_x^C(\underline{u}_2^{k_e},\boldsymbol{\xi}_l) + I^C(\underline{u}_2^{k_e},\boldsymbol{\xi}_l)I_y^C(\underline{u}_2^{k_e},\boldsymbol{\xi}_l)\right], \tag{3.68}$$

respectively.

The total operation count required to apply the stored convection operators to both momentum equations is $1512\times\mathcal{N}^{el}$. The total number of operations required to compute the right hand side contributions in Equations 3.67 and 3.68, and to apply them globally to both momentum equations using the direct stiffness summation procedure, is $2712\times\mathcal{N}^q\mathcal{N}^{el}$. For a 5^{th}-order quadrature scheme in which $\mathcal{N}^q = 7$, the on-the-fly evaluation requires roughly 13 times as many operations to apply convection contribution full-storage technique. However, the memory requirement is reduced from $2\times6^3\times\mathcal{N}^{el}$ for the full-storage technique to roughly $30\times\mathcal{N}^q$ for the on-the-fly evaluation, which is trivial compared to storage needed for the other elemental matrices.

3.1.3 Temperature Solution Periodicity

Care must be taken in the solution of the governing equation for the periodic part of the temperature given in Equation 2.31. For the continuous equation, it has been shown in Section 2.2 that the last term on the right hand side of Equation 2.31 will ensure that there will not be a build-up of heat over long periods of time. This is not guaranteed for the discrete case. If, however, a sufficiently accurate Gaussian quadrature scheme is used, it can be shown that the discrete equations will be exactly satisfied by the value of γ given in Equation 2.39.

For convenience, the weak form of the periodic temperature Equation 3.3 is repeated

$$(w,\theta_t) + (w,\mathbf{u}\cdot(\nabla\theta)) + \frac{1}{RePr}(\nabla w,\nabla\theta) = -\gamma(w,\mathbf{u}\cdot\hat{\mathbf{e}}_1) + \frac{1}{RePr}\ell_{\partial\Omega_l}(w). \tag{3.69}$$

A procedure similar to that used in Section 2.2 to find γ' is followed for the discrete equations to determine the required accuracy for the Gaussian quadrature rule so that for $\gamma = \frac{3}{4RePr}$, heat does build up over long time periods. Integrating the equation over the discrete solution domain Ω is equivalent to setting the test function $w = 1$.

First, the requirement that heat not build up over long time periods is equivalent to requiring that

$$< (w,\theta_t) >= \frac{1}{\tau}\int_t^{t+\tau} (w,\theta_t)\,dt = 0, \tag{3.70}$$

for $w = 1$, and τ on the the order of the period of the steady-periodic state. In the discrete case, the time-average in Equation 3.70 is equivalent to summing the 2^{nd}-order, implicit, backward difference stencil over a sufficient number of time-steps. Because the coefficients of the stencil given in Equation 3.83 sum to zero, inner terms of the summation cancel exactly, and Equation 3.70 is satisfied discretely when averaged over enough time-steps.

For the second term on the left hand side of 3.69 to be zero when $w = 1$, the quadrature rule must be sufficiently accurate so that the integral over each element for $w = 1$ is exactly evaluated. The test function w will be is included in the elemental integrals. At the end of the analysis, setting $w = 1$ will be equivalent to evaluating the integral over the element. The integral in terms of the elemental coordinates $\boldsymbol{\xi}$ is expressed as

$$\int_{\widehat{\Omega}^{k_e}} w\nabla\cdot(\mathbf{u}\theta)\,d\mathbf{x} = \int_{\Omega^{k_e}} wJ(\boldsymbol{\xi})\nabla\cdot(\mathbf{u}\theta)\,d\boldsymbol{\xi}. \tag{3.71}$$

The solution values and test function inside of the integral are expanded according to the elemental basis functions in Equation 3.28 to obtain

$$w(\boldsymbol{\xi}) = \sum_{i=1}^{6} w_i^{k_e} h_i(\boldsymbol{\xi}), \tag{3.72}$$

$$(\mathbf{u}\theta)(\boldsymbol{\xi}) = \sum_{i=1}^{6} (\mathbf{u}\theta)_i^{k_e} h_i(\boldsymbol{\xi}). \tag{3.73}$$

$$\frac{\partial(\mathbf{u}\theta)(\boldsymbol{\xi})}{\partial x} = \sum_{i=1}^{6}(\mathbf{u}\theta)_i^{k_e}\frac{\partial h_i(\boldsymbol{\xi})}{\partial x} = \sum_{i=1}^{6}(\mathbf{u}\theta)_i^{k_e}\frac{1}{J(\boldsymbol{\xi})}\left(\frac{\partial h_i(\boldsymbol{\xi})}{\partial\xi_1}\frac{\partial y}{\partial\xi_2} - \frac{\partial h_i(\boldsymbol{\xi})}{\partial\xi_2}\frac{\partial y}{\partial\xi_1}\right), \tag{3.74}$$

$$\frac{\partial(\mathbf{u}\theta)(\boldsymbol{\xi})}{\partial y} = \sum_{i=1}^{6}(\mathbf{u}\theta)_i^{k_e}\frac{\partial h_i(\boldsymbol{\xi})}{\partial y} = \sum_{i=1}^{6}(\mathbf{u}\theta)_i^{k_e}\frac{1}{J(\boldsymbol{\xi})}\left(\frac{\partial h_i(\boldsymbol{\xi})}{\partial\xi_2}\frac{\partial x}{\partial\xi_1} - \frac{\partial h_i(\boldsymbol{\xi})}{\partial\xi_1}\frac{\partial x}{\partial\xi_2}\right). \tag{3.75}$$

Note that a modified expansion has been used in which the velocity-temperature product is treated as one variable. This form has been implemented in the code and allows a lower quadrature rule be used than if the velocity and temperature were expanded separately. By substituting Equations 3.72—3.75 into Equation 3.71, the convection term of the temperature equation is written as

$$\begin{aligned}
\int_{\widehat{\Omega}^{k_e}} w\nabla\cdot(\mathbf{u}\theta)\,d\mathbf{x} &= \int_{\widehat{\Omega}^{k_e}} \sum_{j=1}^{6} w_j^{k_e} h_j(\boldsymbol{\xi})\left[\sum_{i=1}^{6}(\mathbf{u}\theta)_i^{k_e} D_{x_i}^{k_e}(\boldsymbol{\xi}) + \sum_{i=1}^{6}(\mathbf{v}\theta)_i^{k_e} D_{y_i}^{k_e}(\boldsymbol{\xi})\right] \\
&= \sum_{j=1}^{6} w_j^{k_e}\sum_{i=1}^{6}(\mathbf{u}\theta)_i^{k_e}\int_{\widehat{\Omega}^{k_e}} h_j(\boldsymbol{\xi}) D_{x_i}^{k_e}(\boldsymbol{\xi})\,d\boldsymbol{\xi} + \\
&\quad \sum_{j=1}^{6} w_j^{k_e}\sum_{i=1}^{6}(\mathbf{v}\theta)_i^{k_e}\int_{\widehat{\Omega}^{k_e}} h_j(\boldsymbol{\xi}) D_{x_i}^{k_e}(\boldsymbol{\xi})\,d\boldsymbol{\xi},
\end{aligned} \tag{3.76}$$

where the substitutions

$$D_{x_i}^{k_e}(\boldsymbol{\xi}) = \frac{\partial h_i(\boldsymbol{\xi})}{\partial \xi_1}\frac{\partial y}{\partial \xi_2} - \frac{\partial h_i(\boldsymbol{\xi})}{\partial \xi_2}\frac{\partial y}{\partial \xi_1}, \tag{3.77}$$

$$D_{y_i}^{k_e}(\boldsymbol{\xi}) = \frac{\partial h_i(\boldsymbol{\xi})}{\partial \xi_2}\frac{\partial x}{\partial \xi_1} - \frac{\partial h_i(\boldsymbol{\xi})}{\partial \xi_1}\frac{\partial x}{\partial \xi_2}, \tag{3.78}$$

have been made. For $w = 1$, the basis functions $h_j(\boldsymbol{\xi})$ in the integrals of Equation 3.76 can be neglected. The highest remaining power, in terms of the components of $\boldsymbol{\xi} = (\xi_1, \xi_2)$, in the integrals are of 2^{nd}-order. This implies that the integral will be evaluated exactly for each element, and subsequently for the summation over all elements of the domain, when a Gaussian quadrature scheme of at least order two is used. As stated in Appendix C.1, a 5^{th}-order quadrature scheme has been used that satisfies this requirement.

The third term on the left hand side of Equation 3.69 goes to zero for $w = 1$ from taking the gradient of the constant function, $\nabla w = 0$. All that remains is to show that the two terms on the right hand side exactly balance. The first term on the right hand side is integrated over the solution domain Ω by setting $w = 1$. Evaluating the discrete integral gives

$$-\gamma(w = 1, \mathbf{u} \cdot \hat{\mathbf{e}}_1) = -\gamma Q l. \tag{3.79}$$

where the result is dependent on the flowrate. The flowrate is prescribed $Q = \frac{4}{3}$ and is exactly enforced as described in Section 3.2.1.

The final term on the right hand side of 3.69 is evaluated for $w = 1$ to get

$$\frac{1}{RePr}\ell_{\partial\Omega_l}(w = 1) = \frac{l}{RePr}. \tag{3.80}$$

The sum of Equations 3.79 and 3.80 must be zero. Solving for γ gives the desired result

$$\gamma = \frac{3}{4RePr}. \tag{3.81}$$

The accuracy for the Gaussian quadrature rule necessary to evaluate the discrete integrals exactly, and to ensure that for γ given in Equation 3.81 that heat will not build up in the periodic domain is determined by the integrands in Equation 3.76. The quadrature rule must be such that a second order polynomial function is integrated exactly. A 5^{th}-order scheme has been used which meets (exceeds) this requirement.

3.2 Temporal Discretization — Split Time–Stepping

The spatially discrete, analytic in time, governing equations are given in Equations 3.17–3.19. The temporal discretization pursued is a semi–implicit, fractional time–stepping scheme [23, 28]. This approach reduces the time–advancement problem to a sequence of

smaller subproblems and allows the convection operator to be treated explicitly while the remainder (the Stokes subproblem) is advanced implicitly. In the scheme that has been used here, a 3^{rd}-order accurate, explicit Adams-Bashforth integration scheme is used to advance the nonlinear convection terms, and a 2^{nd}-order accurate, implicit backward difference scheme is applied to the Stokes subproblem.

A variable time-step formulation is used. The reason for this approach is that, due to the unsteady nature of the solutions, the stability criterion is likely to vary significantly as the solution is advanced. It is difficult to determine *a priori* a time-step that will be stable for the entire solution evolution, and it is inefficient (from a computational effort standpoint) to use the minimum step-size for the entire solution advancement even if it could be determined. The semi-implicit form for the velocity equations is

$$\mathbf{B}(\zeta_1\mathbf{u}_i^{n+1} + \zeta_2\mathbf{u}_i^{n} + \zeta_3\mathbf{u}_i^{n-1}) + \frac{1}{Re}\mathbf{A}\mathbf{u}_i^{n+1} - \mathbf{D}_i^T p^{n+1} = \sum_{q=0}^{2} \beta_q \mathbf{C}(\mathbf{u}^{n-q})\mathbf{u}_i^{n-q} + \mathbf{B}\mathbf{f}_i^{n+1}, \quad i = 1, 2, \tag{3.82}$$

where the 2^{nd}-order, backward Euler coefficients are

$$\zeta_1 = \frac{2\Delta t_n + \Delta t_{n-1}}{\Delta t_n(\Delta t_n + \Delta t_{n-1})}, \quad \zeta_2 = -\frac{\Delta t_n + \Delta t_{n-1}}{\Delta t_n \Delta t_{n-1}}, \quad \zeta_3 = \frac{\Delta t_n}{\Delta t_n(\Delta t_n + \Delta t_{n-1})}. \tag{3.83}$$

As expected, for the constant time-step case where $\Delta t_{n-1} = \Delta t_n = \Delta t$, the coefficients in Equation 3.83 reduce to give the well known finite-difference stencil for the first derivative

$$g'(t)|^{n+1} = \frac{3g^{n+1} - 4g^n + g^{n-1}}{2\Delta t} + O(\Delta t^2). \tag{3.84}$$

The coefficients β_q, $q = 0, 1, 2$, have been derived in Appendix C.2 and are

$$\beta_0 = \frac{\Delta t_n}{12}\left[\frac{12\Delta t_{n-1}(\Delta t_{n-1} + \Delta t_{n-2}) + 6\Delta t_n(2\Delta t_{n-1} + \Delta t_{n-2}) + 4\Delta t_n^2}{\Delta t_{n-1}(\Delta t_{n-1} + \Delta t_{n-2})}\right], \tag{3.85}$$

$$\beta_1 = \frac{\Delta t_n}{12}\left[\frac{6\Delta t_n(\Delta t_{n-1} + \Delta t_{n-2}) + 4\Delta t_n^2}{\Delta t_{n-1}\Delta t_{n-2}}\right], \tag{3.86}$$

$$\beta_2 = \frac{\Delta t_n}{12}\left[\frac{6\Delta t_n\Delta t_{n-1} + 4\Delta t_n^2}{\Delta t_{n-2}(\Delta t_{n-1} + \Delta t_{n-2})}\right]. \tag{3.87}$$

The terms in Equation 3.82 can be collected to obtain

$$\mathbf{H}\mathbf{u}_i^{n+1} - \mathbf{D}_i^T p^{n+1} = -\mathbf{B}(\zeta_2\mathbf{u}_i^{n} + \zeta_3\mathbf{u}_i^{n-1}) - \sum_{q=0}^{2} \beta_q \mathbf{C}(\mathbf{u}^{n-q})\mathbf{u}_i^{n-q} + \mathbf{B}\mathbf{f}^{n+1}, \quad i = 1, 2, \tag{3.88}$$

where $\mathbf{H}$ is the second-order, Helmholtz operator

$$\mathbf{H} = \frac{1}{Re}\mathbf{A} + \zeta_1 \mathbf{B}. \tag{3.89}$$

The fractional splitting scheme approximates semi-implicit form in Equation 3.82 with a sequence of smaller steps. The result is

$$\mathbf{H}\tilde{\mathbf{u}}^{n+1} = \mathbf{D}^T \tilde{p}^{n+1} - \mathbf{B}(\zeta_2 \mathbf{u}^n + \zeta_3 \mathbf{u}^{n-1}) - \sum_{q=0}^{2} \beta_q \mathbf{C}(\mathbf{u}^{n-q})\mathbf{u}^{n-q} + \mathbf{B}\mathbf{f}^{n+1}, \tag{3.90}$$

$$\mathbf{E}p_{\text{corr}} = -\zeta_1 \mathbf{D}\tilde{\mathbf{u}}^{n+1} \tag{3.91}$$

$$\mathbf{u}^{n+1} = \tilde{\mathbf{u}}^{n+1} - \frac{1}{\zeta_1}\mathbf{B}^{-1} p_{\text{corr}}, \tag{3.92}$$

$$p^{n+1} = \tilde{p}^{n-1} + p_{\text{corr}} \tag{3.93}$$

where $\tilde{\mathbf{u}}^{n+1}$ is an intermediate approximation to the velocity at step $n+1$. $\mathbf{E}$ is the consistent Poisson operator

$$\mathbf{E} = \mathbf{D}_1 \mathbf{B}^{-1} \mathbf{D}_1^T + \mathbf{D}_2 \mathbf{B}^{-1} \mathbf{D}_2^T. \tag{3.94}$$

$p_{\text{corr}} = p^{n+1} - \tilde{p}^{n+1}$ is the pressure correction term. and $\tilde{p}^{n+1}$ is an approximation to the pressure at time step $n+1$ and is simply a linear extrapolation from the previous two time steps

$$\tilde{p}^{n+1} = p^n + (p^n + p^{n-1})\frac{\Delta t_n}{\Delta t_{n-1}}. \tag{3.95}$$

The solution steps of Equations 3.90–3.93 are as follows; (3.90) approximate the pressure at $n+1$ and solve for an intermediate velocity $\tilde{\mathbf{u}}^{n+1}$, (3.91) solve for a pressure correction term p_{corr} by enforcing divergence-free flow. (3.92) use the pressure correction term to correct the velocity approximation, (3.93) use the pressure correction term to update the pressure.

The governing equation for the periodic part of the temperature, θ, is decoupled from the flow equations, and is updated after the flow solution is updated. An identical scheme is used to advance Equation 3.19 in time. The resulting, semi-implicit, fully discrete equation is

$$\mathbf{H}_\theta \theta^{n+1} = -\mathbf{B}(\zeta_2 \theta^n + \zeta_3 \theta^{n-1}) - \sum_{q=0}^{2} \beta_q \mathbf{C}(\mathbf{u}^{n-q})\theta^{n-q} - \gamma \mathbf{B}(\mathbf{u}^{n+1} \cdot \hat{\mathbf{e}}_1), \tag{3.96}$$

where $\mathbf{H}_\theta$ is the temperature Helmholtz matrix

$$\mathbf{H}_\theta = \frac{1}{RePr}\mathbf{A} + \zeta_1 \mathbf{B}. \tag{3.97}$$

The inversion of the Helmholtz operator $\mathbf{H}$ in Equation 3.90 and of $\mathbf{H}_\theta$ in Equation 3.96 are elliptic solves and can be accomplished with an iterative, conjugate gradient algorithm, or with a direct, sparse LU-factorization. Because $\mathbf{H}$ and $\mathbf{H}_\theta$ are well conditioned, Equa-

tions 3.90 and 3.96 can be solved very efficiently with a preconditioned conjugate gradient method. Inverting the $\mathbf{E}$ operator in Equation 3.90 is more difficult as the conditioning is very sensitive to the homogeneity of the finite element mesh. For solution schemes in which all inversions are iterative, it requires the bulk of the solution time. Because $\mathbf{E}$ is much smaller than the other matrices (its size is determined by $\mathcal{N}^p < \mathcal{N}^v$) and its inversion dominates the solution time, it is the best candidate for treatment with a direct solver. Details of both the iterative and direct solvers used in the code are given in Section 3.2.2.

In both 3.91 (inside of the Poission operator) and 3.92, the mass matrix $\mathbf{B}$ must be inverted. For a spectral element spatial discretization, this is a trivial matter as the elemental mass matrices are diagonal. However, the mass matrix for the $I\!P_2$, triangular elements is not diagonal, and therefore must be inverted with either an iterative solver or direct, sparse solver. To avoid the additional matrix inversions resulting from the use of the full mass matrix, the diagonally lumped mass matrix has been substituted. The elemental, diagonally lumped mass matrix $\tilde{\mathbf{B}}^{k_e}$ for element k_e is

$$\tilde{\mathbf{B}}^{k_e} = \frac{\mathbf{B}_{ii}^{k_e}}{\mathrm{Trace}(\mathbf{B}^{k_e})} |\widehat{\Omega}^{k_e}|, \quad i = 1, \ldots, 6, \tag{3.98}$$

where $|\widehat{\Omega}^{k_e}|$ is the area of element $\widehat{\Omega}^{k_e}$ computed from the full elemental mass matrix and is

$$|\widehat{\Omega}^{k_e}| = \sum_{i=1}^{6} \sum_{j=1}^{6} \mathbf{B}_{ij}^{k_e}. \tag{3.99}$$

3.2.1 Flow–Rate Specification — Green's Function

In this section, the method used to determine the time-dependent, pressure forcing term $\mathbf{f}^{n+1} = (f^{n+1}, 0)$ in Equation 3.90 is described. The value of the f^{n+1} must be set to achieve the desired average flow velocity $V = \frac{2}{3}$. This is accomplished by first solving in a preprocessing stage for a Green's function $\mathbf{u}^*$. The Green's function is obtained by solving the 'Stokes-like' part of the spatially discrete Equations 3.17 and 3.18 for a unit pressure forcing term. Then, the full set of governing equations are advanced in time, neglecting the pressure forcing in Equation 3.90, and, after each time step, superposition is used to achieve the correct flow rate and to determine the required value of f^{n+1}.

The preprocessing step (which only needs to be solved once) consists of solving the Stokes equation

$$\mathbf{H}\mathbf{u}_i^* = \mathbf{B}\underline{\mathbf{1}} + \mathbf{D}_i^T p^*, \quad i = 1, 2, \tag{3.100}$$

for the velocity $\mathbf{u}^* = (u_1^*, u_2^*)$ and the pressure p^*. The unit forcing $\underline{\mathbf{1}} = (\underline{1}, 0)$ is a vector of ones on the x-equation nodes only. The finite element matrices are identical to those in

Equation 3.90. The flowrate is computed

$$Q^* = \frac{1}{2l}\int_{\mathcal{D}^{\mathrm{EP}}} u^*\, d\mathbf{x}, \tag{3.101}$$

and is used to determine the pressure forcing term $f(t)$. The intermediate velocity $\mathbf{u}^*$ and pressure p^* solutions will be superimposed with the time–step solution to determine the correct Navier–Stokes solution.

The second, time–advancement phase of the solution proceeds exactly as outlined in Equations 3.90–3.93, but with the forcing term neglected. The modified, intermediate solution phase has the steps.

$$\mathbf{H}\widetilde{\mathbf{u}_I}^{n+1} = \mathbf{D}^T\widetilde{p_I}^{n+1} - \mathbf{B}(\zeta_2\mathbf{u}_I{}^n + \zeta_3\mathbf{u}_I{}^{n-1}) - \sum_{q=0}^{2}\beta_q\mathbf{C}(\mathbf{u}_I{}^{n-q})\mathbf{u}_I{}^{n-q} \tag{3.102}$$

$$\mathbf{E}p_{\mathrm{corr}_I} = -\zeta_1\mathbf{D}\widetilde{\mathbf{u}_I}^{n+1} \tag{3.103}$$

$$\mathbf{u}_I{}^{n+1} = \widetilde{\mathbf{u}_I}^{n+1} - \frac{1}{\zeta_1}\mathbf{B}^{-1}p_{\mathrm{corr}_I}. \tag{3.104}$$

$$p_I{}^{n+1} = \widetilde{p_I}^{n+1} + p_{\mathrm{corr}_I} \tag{3.105}$$

after which, the pressure forcing is determined and the solutions are superimposed. The forcing term is simply

$$f^{n+1} = \frac{Q^{n+1} - Q_I}{Q^*} \tag{3.106}$$

where the intermediate flow rate Q_I is

$$Q_I = \frac{1}{2l}\int_{\mathcal{D}^{\mathrm{EP}}} u_I\, d\mathbf{x}, \tag{3.107}$$

and the flow rate at step $n+1$ is the prescribed flow rate

$$Q^{n+1} = lV = \frac{4l}{3}. \tag{3.108}$$

The final step is the superposition of the solutions to obtain the velocity and the pressure at step $n+1$;

$$\mathbf{u}^{n+1} = f^{n+1}\mathbf{u}^* + \mathbf{u}_I, \tag{3.109}$$

$$p^{n+1} = f^{n+1}p^* + p_I. \tag{3.110}$$

The preprocessing stage of the solution needs to be done only once. The increase in solution time is very small in relation to the total time required to sufficiently advance the solutions to achieve a steady–periodic state. To solve 3.100, an Uzawa algorithm is used [46]

which decouples the pressure solve from the velocity solve and results in the two equations

$$\mathbf{S}p^* = \mathbf{D}_1\mathbf{H}^{-1}\mathbf{B}, \tag{3.111}$$

$$\mathbf{H}\mathbf{u}^* = \mathbf{D}^T p^* + \mathbf{B}\underline{1}, \tag{3.112}$$

where $\mathbf{S}$ is defined as

$$\mathbf{S} = \mathbf{D}_1\mathbf{H}^{-1}\mathbf{D}_1^T + \mathbf{D}_2\mathbf{H}^{-1}\mathbf{D}_2^T. \tag{3.113}$$

Equation 3.111 is solved with a nested conjugate gradient scheme and Equation 3.112 is solved for the velocity components with a conjugate gradient algorithm.

3.2.2 System Solution Strategy — Iterative and Direct Solvers

In this section, the solvers used to make the necessary matrix inversions at each step of the solution process are described. Matrices must be inverted for the solution of the preliminary Stokes solve (nested inversions for $\mathbf{S}$ in Equation 3.111 and of $\mathbf{H}$ in Equation 3.112), to obtain the approximate velocity solution in Equation 3.90, for the solution of the pressure correction term in Equation 3.91, and finally for the temperature solution update in Equation 3.96.

3.2.2.1 Iterative Solution — Conjugate Gradients

The iterative solution algorithm of choice for finite element solvers is the conjugate gradient method. The conjugate gradient algorithm is extremely efficient for solving well conditioned problems and requires very low storage. The conjugate gradient algorithm has been extensively reported [31, 68] and the underlying theory is not detailed here. The preconditioned conjugate gradient algorithm for the solution of $\mathbf{A}x = f$, for a symmetric, positive-definite matrix $\mathbf{A} \in \mathbb{R}^{n\times n}$, preconditioning matrix $\mathbf{M} \in \mathbb{R}^{n\times n}$, $x \in \mathbb{R}^n$, and $f \in \mathbb{R}^n$ is

$m = 0$, $r^0 = f - \mathbf{A}x^0$, $z^0 = \mathbf{M}^{-1}r^0$, $w^0 = z^0$,
while $\varepsilon(r^m) < tol$
$\quad m = m + 1$
$\quad \alpha^m = (z^m, z^m)/(w^m, \mathbf{A}w^m)$
$\quad x^{m+1} = x^m + \alpha^m w^m$
$\quad r^{m+1} = r^m = \alpha^m \mathbf{A}w^m$
$\quad z^{m+1} = \mathbf{M}^{-1}r^{m+1}$
$\quad \beta^m = (z^{m+1}, r^{m+1})/(z^m, r^m)$
$\quad w^{m+1} = r^{m+1}\beta^m w^m$
end

The stopping criterion is based on $\varepsilon(r^m)$, where

$$\varepsilon(r^m) = \left[\sum_{i=1}^{n} \frac{r_i^m}{\tilde{\mathbf{B}}_i} \right]^{\frac{1}{2}} . \tag{3.114}$$

It should be noted that, for the preconditioning to be efficient, the solution $z = \mathbf{M}^{-1}r$ must be easily obtained. The preconditioner used for all of the iterative solves was simply the matrix diagonal $\mathbf{M} = [A_{ii}], i = 1, \ldots, n$ which has only limited beneficial impact in practice.

3.2.2.2 Direct Solver — Sparse LU–Decomposition

A sparse matrix solution package written by Kundert [43] has been used to perform the direct matrix solves when the Navier–Stokes code is run in one of the the direct–solver modes. The package is Sparse Version 1.3 and is available at Netlib.[1] The Sparse package is written in C and manages all of the memory allocation internally making it very easy to integrate into other codes. It can handle arbitrary square, real and complex, linear systems and is also able to find determinants and estimate ill–conditioning errors. According to its documentation, it performs as fast or faster than other sparse matrix packages and, at least anecdotally, it seems to be very efficient.

The sparse solve consists of two stages. For the first stage, matrix factorization, the matrix elements are re–ordered and a LU factorization is performed [11]. The lower and upper triangular matrices are then stored. The second stage, forward and backward substitution, is performed on any number of right hand sides without having to re–factor the original matrix. For details of the algorithm, the reader is referred to [43].

As is well known, the factorization time is very large compared to each forward/backward solve. For the initial CPU cost of the LU factorization to be worthwhile, it must be prorated over enough time–steps to make the total solution time for the direct solve approach to be lower than for the iterative solver. The break-even point is easily exceeded by the total number of time–steps that are needed to obtain periodically varying, steady–periodic solutions.

3.3 Sample Code Performance

The Navier–Stokes code can be run in several modes, based on whether the iterative or direct solver is used for each matrix inversion. The lowest memory, most time consuming solution mode uses the iterative solver for all of the matrix inversions. Conversely, the

[1] The Netlib master index web address is `http://netlib.bell-labs.com/netlib/master/index.html` and the Sparse Version 1.3 package is located in the `sparse` directory http://netlib.bell-labs.com/netlib/sparse/index.html.

highest memory, fastest solution mode uses the direct solver for all of the matrix solutions. Various combinations of iterative/direct solves result in solution modes that fall in between the two extremes. The solution modes are described below.

Mode I Conjugate gradient solvers used for all matrix inversions: $\mathbf{H}$ in Equation 3.90, $\mathbf{E}$ in Equation 3.91, and $\mathbf{H}_\theta$ in Equation 3.96. This mode requires the least memory but highest CPU time.

Mode II Conjugate gradient solver used to invert $\mathbf{H}$ in Equation 3.90 and $\mathbf{H}_\theta$ in Equation 3.96. The direct solver is used to invert $\mathbf{E}$ in Equation 3.91.

Mode III Conjugate gradient solver used only to $\mathbf{H}_\theta$ in Equation 3.96. The direct solver is used to invert $\mathbf{E}$ in Equation 3.91 and $\mathbf{H}$ in Equation 3.90.

Mode IV Direct solver used for all of the required matrix inversions: $\mathbf{H}$ in Equation 3.90, $\mathbf{E}$ in Equation 3.91, and $\mathbf{H}_\theta$ in Equation 3.96. This mode has the highest memory requirement but the lowest CPU time.

It is important to note that the $\mathbf{H}$ and $\mathbf{H}_\theta$ matrices are dependent on the timestep size Δt_n. If the timestep size is changed during the time advancement, the $\mathbf{H}$ and $\mathbf{H}_\theta$ matrices must be updated and, if running in **Mode III** or **Mode IV**, one or both factorizations must be recomputed. The time penalty incurred by frequent timestep adjustments and re-factorizations would rapidly overwhelm the performance benefit realized by the direct solver. To avoid such a situation, a conservative timestep is selected as soon as the periodic-steady state is achieved and is held fixed for the remainder of the time advancement. Because the $\mathbf{E}$ matrix is not Δt_n dependent, timestep updates can be performed more frequently when the code is used in **Mode I** or **Mode II**.

To demonstrate the performance of the code, timings have been performed with the code running in each of the solution modes listed above. For the computational times that are reported, the factorization time has been neglected. It is reasonable to neglect this as the contribution to the total solution from the factorization for the $O(10,000)$ time steps that a solution is typically advanced is negligible. In all cases, the timestep size is constant throughout the run.

The sample problem consists of a two-body, eddy-promoter configuration with the grid shown in Figure 3-2. The number of nodes and elements are indicated in the figure resulting in matrices sized as $\mathbf{H} \in I\!R^{7156\times 7156}$, $\mathbf{E} \in I\!R^{1842\times 1842}$, and $\mathbf{H}_\theta \in I\!R^{7156\times 7156}$. Because the $\mathbf{E}$ operator is much smaller than $\mathbf{H}$ and $\mathbf{H}_\theta$, and its inversion requires the majority of the fully iterative solution time, it is the best candidate for solution by the direct solver. This result is evident from the solution times and memory requirements listed in Table 3.1.

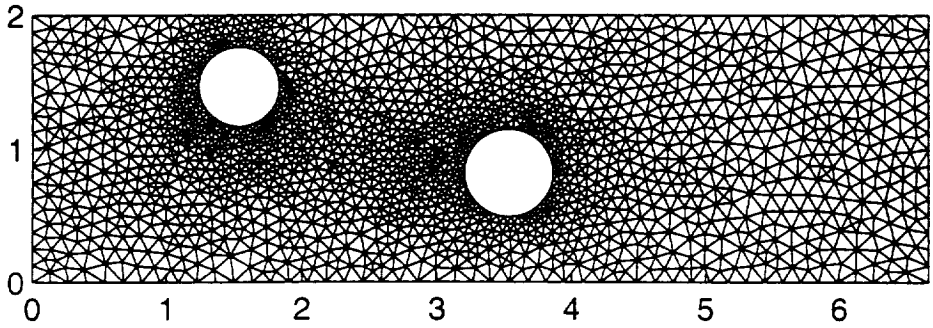

Figure 3-2: Mesh plot of the configuration used for code performance tests ($\mathcal{N}^{el} = 3471$, $\mathcal{N}^{v} = 7156$. $\mathcal{N}^{p} = 1842$).

Solution Mode	CPU seconds/timestep	Core memory (Mbytes)
Mode I	7.91	18.2
Mode II	2.51	26.5
Mode III	1.32	44.1
Mode IV	1.22	63.4

Table 3.1: CPU time and memory required for the four solution modes running on a Hewlett Packard C-160 workstation.

Chapter 4

Baseline Surrogate Approach

To begin the description of the baseline, non-parametric validated, surrogate framework it is first necessary to define a hierarchy of approximation models. Implicit in this discussion is the assumption that the governing equations (or experimental setup) accurately represent the problem under consideration. With this assumption, a hierarchy of three approximation models are defined:

Exact This is the exact, analytical solution to the governing equations. For the eddy-promoter problem, it is the solution to Equations 2.25—2.36. The exact solution can be obtained only for the very simplified cases (e.g. channel flow with no obstructions).

Truth The truth model is the 2^{nd}-order in time, $\mathbb{P}_2$—$\mathbb{P}_1$ finite element solution of the governing equations that is described in Chapter 3. While this is clearly not of the accuracy of the *exact* solution, it represents the best obtainable solution for the problem. The truth model serves as the reference for the validation and error analyses.

Surrogate The *surrogate* model is the very inexpensive (by design) approximation to the *exact* solution and typically consists of a simple input-output model (e.g. response surfaces, scattered data interpolation, etc.). The surrogate model is used in place of the truth model in design studies.

The non-parametric validated, baseline surrogate framework has been extensively reported [55, 57, 77, 78, 79] and is only repeated here to serve as a reference to the surrogate-Pareto optimization pursued in Chapter 5. In the baseline surrogate approach, a simple, inexpensive model (a surrogate) is substituted for an expensive simulation (or experiment as in Chapter 6) in the optimization process. The simulation serves *offline* first, to construct, and second, to validate the surrogates which are usually an inexpensive input-output functions. This is in contrast to *online* optimization approaches in which the simulation is called directly by the parent optimization process. In online approaches, the simulation serves as a subroutine call to the optimization routine.

Approximate, offline optimization approaches have been widely used but typically do not provide rigorous error estimates for surrogate–predicted designs. The distinguishing feature of the non–parametric, validated surrogate approach is the surrogate validation step of the framework that provides *a posteriori* error estimates on designs near the surrogate–predicted, optimal design(s). The surrogate approach is related to probably-approximately-correct approaches [74, 26] and information-based complexity theory [73]. It differs, however, from the former in that it is truly non-parametric (no assumption is made in regard to the distribution of optimal input points) and from the latter in that it requires no regularity estimates for the input-output function.

The surrogate approach is best suited to problems that meet at least some of the following classifications: **(1)** The underlying simulation or analysis is computationally expensive making the large number simulation queries required for the optimization intractable. **(2)** The integration of the analysis code with the optimization package is impractical because of difficult interfacing or the lack of sensitivity derivatives. **(3)** The problem is global in nature and the design space covers a wide range of potential designs in which there may be many, locally-optimal designs. **(4)** Flexibility is needed in terms of rapid turnaround, as in cases in which the design goals evolve with the design and more is learned.

In each section of this chapter, the surrogate framework is presented for a general problem with two outputs and two performance metrics that are functions of each output as well of the input vector. An important distinction to be made between the general problem presented here and those cases analyzed previously [55, 57, 77, 78, 79] is that here, surrogates for the simulation outputs are validated. The performance metrics which serve to quantify designer preferences are functions of the validated outputs as well as (possibly) of the inputs. This adds additional flexibility and generality to the surrogate framework in that the validated simulation outputs can be used in future design studies with different performance metrics and similar error bounds will obtain without the need for additional appeals to the simulation. In the earlier surrogate work, the performance metrics are validated directly. This restricts the design studies to that particular choice of performance metrics. A change in the form of the performance metrics therefore requires that the validation step be repeated, necessitating additional appeals to the simulation. The two–body, eddy–promoter problem serves as an example of the two output, two performance metric design problem presented in this chapter.

The baseline surrogate framework consists of four steps. The first step of the framework, surrogate construction, is discussed in Section 4.1. In the second step of the framework, presented in Section 4.2, the inexpensive surrogates are validated against the truth simulation at randomly selected points. In Section 4.3 the third step of the framework, surrogate based design, is presented. The fourth and final step is the *a posteriori* error analysis of the surrogate–predicted designs and this is presented in Section 4.4. The *a posteriori* error

analysis, which uses the validation results without requiring additional appeals to the simulation, gives error estimates for designs near the surrogate–predicted optimal designs as well as an estimate to the design optimality.

4.1 Surrogate Construction

The first step of the baseline surrogate framework is surrogate construction. To begin, given a vector of M_m modeled inputs, $\mathbf{p}_m \in \Omega_m \subset I\!R^{M_m}$ that lie in the model design (or input) space Ω_m, surrogates for two ($K = 2$) truth outputs of the simulation, $\phi_1^T(\mathbf{p}'_m) : \Omega_m \rightarrow I\!R$, and $\phi_2^T(\mathbf{p}'_m) : \Omega_m \rightarrow I\!R$, are constructed. Although the intent is that the surrogates, $\widetilde{\phi_1}(\mathbf{p}'_m) : \Omega_m \rightarrow I\!R$ and $\widetilde{\phi_2}(\mathbf{p}'_m) : \Omega_m \rightarrow I\!R$, approximate the simulation as closely as possible over Ω_m, $\widetilde{\phi_1}(\mathbf{p}'_m) \approx \phi_1^T(\mathbf{p}'_m)$, $\widetilde{\phi_2}(\mathbf{p}'_m) \approx \phi_2^T(\mathbf{p}'_m)$, the results that will be obtained in the later sections of this chapter are valid regardless of the quality of the surrogates. The surrogates can be constructed by any means, whether it be by appeals to the truth or to another simulation, by empirical relationships, by the use of limiting solutions, or some combination of all of these.

For the two-body, eddy-promoter problem, the two truth value outputs obtained from simulation are is the pressure forcing term required to achieve the target flow rate, $\psi_0^T(\mathbf{p}_m)$, and the inverse Nusselt number, $\theta_0^T(\mathbf{p}_m)$. The surrogate construction set

$$\mathcal{X}^{co} = \{(\mathbf{p}_m, \theta_0^T(\mathbf{p}_m), \psi_0^T(\mathbf{p}_m))_1, \ldots, (\mathbf{p}_m, \theta_0^T(\mathbf{p}_m), \psi_0^T(\mathbf{p}_m))_{N^{co}}\}. \tag{4.1}$$

is formed by appealing to the finite element simulation (Truth) at 91 points in the design space Ω_m (defined in Section 2.6.1) and by including an additional 165 limiting solutions for a total constuction sample size of $N^{co} = 256$ input-output pairs. The 91 simulation points have been chosen from an orthogonal array (Appendix D.2) that ensures a good space filling design. The additional 165 limiting solutions correspond to the upper and lower limits of p_{m2} ($p_{m2} = 0$ and $p_{m2} = 1$) and represent duplicate geometric realizations at different points of the design space Ω_m.

The approximation scheme used for the surrogates is a radial basis function fit through the construction set, $\mathcal{X}^{co}$, for each output. The particular radial basis function used here is described in Appendix D.1. The surrogates for the outputs are interpolating functions in that the output surface passes exactly through all of the points in the construction set $\mathcal{X}^{co}$. As demonstrated empirically in Section 2.5.4, the output functions are continuous over the entire model design space Ω_m and an interpolatory model is appropriate without the need to track and account for discontinuities. The plot in Figure 2-6 shows that the output function continuity is preserved across a topology change. Three-dimensional mesh plots of the surrogates are given in Figure 4-1. On the left in the figure are p_{m1}–p_{m2} slices of the surrogates for $p_{m3} = 0.50$ and on the right are p_{m1}–p_{m3} slices of the surrogates for

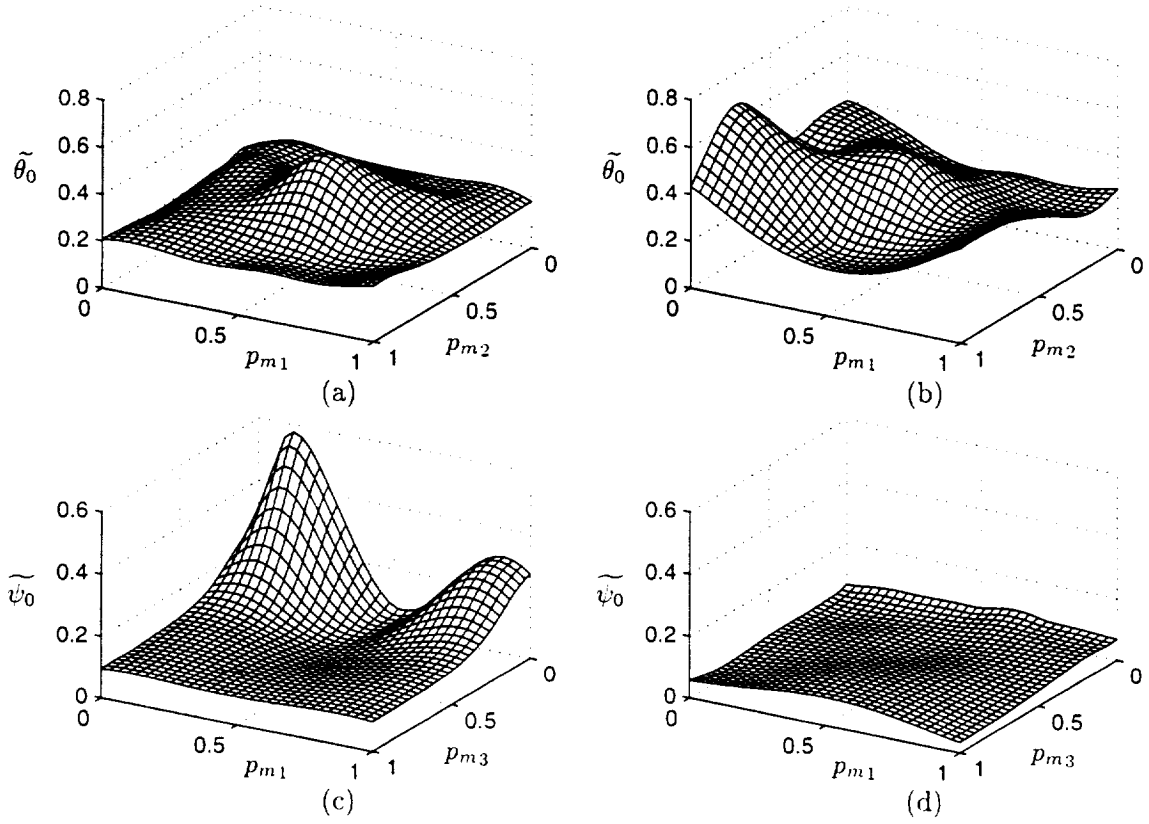

Figure 4-1: Mesh plots of the output surrogates: (a) $\widetilde{\theta}_0(\mathbf{p}_m)$ slice for $p_{m3} = 0.50$. (b) $\widetilde{\theta}_0(\mathbf{p}_m)$ slice for $p_{m2} = 0.50$. (c) $\widetilde{\psi}_0(\mathbf{p}_m)$ slice for $p_{m3} = 0.50$. (d) $\widetilde{\psi}_0(\mathbf{p}_m)$ slice for $p_{m2} = 0.50$.

$p_{m2} = 0.50$. The temperature output $\widetilde{\theta}_0(\mathbf{p}_m)$ is at the top and the pressure output $\widetilde{\psi}_0(\mathbf{p}_m)$ is at the bottom.

4.2 Surrogate Validation

The second step of the surrogate framework is surrogate validation. In this step, the surrogate models are validated against the truth at input points that are randomly chosen from the model design space Ω_m. To proceed with the description of the validation step, several functions must first be introduced.

The importance function $\rho(\mathbf{p}_m)$ serves as a probability density function for the selection of validation points from the model design space Ω_m:

$$\int_{\Omega_m} \rho(\mathbf{p}_m)\, d\mathbf{p}_m = 1. \tag{4.2}$$

The importance function leads to the notion of a ρ-measure of a subdomain of the design space Ω_m which is simply the weighted relative M_m-volume of the subdomain. For any

subdomain $\mathcal{D} \subset \Omega_m$, "the ρ–measure of $\mathcal{D}$," $\mu_\rho(\mathcal{D})$, is

$$\mu_\rho(\mathcal{D}) = \int_{\mathcal{D}} \rho(\mathbf{p}_m)\, d\mathbf{p}_m < 1. \tag{4.3}$$

The ρ–measure of of full model input domain Ω_m is one, $\mu_\rho(\Omega_m) = 1$.

Next, K scaling functions are introduced, one corresponding to each of the output surrogates that are to be validated. For the general two output problem examined here, the scaling functions $\hat{g}_{o_1}(\mathbf{p}'_m) : \Omega_m \to I\!R_-$ and $\hat{g}_{o_2}(\mathbf{p}'_m) : \Omega_m \to I\!R_+$ are the two strictly positive, error–scaling functions. The scaling functions serve primarily to make the errors between the truth value and the surrogate values for each of the outputs of the same magnitude. A secondary purpose for the scaling function is to reduce the impact of regions of the design space where large surrogate errors may exist.

With the importance function and error–scaling functions defined, the validation sample set $\mathcal{X}^{va}$ is formed as

$$\mathcal{X}^{va} = \{(\mathbf{P}_{m1}, \phi_1^T(\mathbf{P}_{m1}), \phi_2^T(\mathbf{P}_{m1})), \ldots, (\mathbf{P}_{mN}, \phi_1^T(\mathbf{P}_{mN}), \phi_2^T(\mathbf{P}_{mN}))\}, \quad \mathbf{P}_{mi} \sim \rho(\mathbf{p}_m). \tag{4.4}$$

where the input points $\mathbf{P}_{mi}$ are independent, identically distributed random points drawn according the probability density function $\rho(\mathbf{p}_m)$. The truth outputs in 4.4 are obtained by appeals to the simulation at each validation point $\mathbf{P}_{mi}$. The size of the validation sample set is

$$N = \left\lceil \frac{\ln \varepsilon_2}{\ln(1-\varepsilon_1)} \right\rceil \tag{4.5}$$

where $\lceil z \rceil$ is the smallest integer that is greater than z. Later, it will be shown that ε_1 represents the ρ–measure of the uncharacterized region (the region in Ω_m where the surrogate error magnitudes $|\phi_1^T(\mathbf{p}'_m) - \widetilde{\phi_1}(\mathbf{p}'_m)|$ and $|\phi_2^T(\mathbf{p}'_m) - \widetilde{\phi_2}(\mathbf{p}'_m)|$ are unknown) and ε_2 is the significance of the probabilistic error estimates that are developed.

With the validation sample set formed, the model prediction error U is computed as

$$U = \max_{\mathcal{X}^{va}} \left(\max \left(\frac{|\phi_1^T(\mathbf{P}_{mi}) - \widetilde{\phi_1}(\mathbf{P}_{mi})|}{\hat{g}_{o_1}(\mathbf{P}_{mi})}, \frac{|\phi_2^T(\mathbf{P}_{mi}) - \widetilde{\phi_2}(\mathbf{P}_{mi})|}{\hat{g}_{o_2}(\mathbf{P}_{mi})} \right) \right). \tag{4.6}$$

and the uncharacterized region Υ is defined as

$$\Upsilon = \left\{ \mathbf{p}_m \in \Omega_m \mid \max \left(\frac{|\phi_1^T(\mathbf{p}'_m) - \widetilde{\phi_1}(\mathbf{p}'_m)|}{\hat{g}_{o_1}(\mathbf{p}'_m)}, \frac{|\phi_2^T(\mathbf{p}'_m) - \widetilde{\phi_2}(\mathbf{p}'_m)|}{\hat{g}_{o_2}(\mathbf{p}'_m)} \right) > U \right\}. \tag{4.7}$$

The model prediction error is the maximum, absolute truth–surrogate difference over the set of randomly drawn, validation input points $\mathbf{P}_{mi}, i = 1, \ldots, N$. The uncharacterized region is that subset of the model design space Ω_m for which the scaled truth–surrogate error is greater than the model prediction error U. The validation provides no information

as to the location of the uncharacterized region nor does it provide any insight as to the magnitude of the errors in that region. This uncertainty manifests itself in the locality of the error estimates that are developed in Section 4.4.

The model prediction error provides a probabilistic estimate as to the maximum truth–surrogate error over a fraction of the model design space Ω_m. The precise validation statement reads:

$$Pr(\mu_\rho(\Upsilon) < \varepsilon_1) \geq 1 - \varepsilon_2. \tag{4.8}$$

What 4.8 says in words is that, with probability of at least $1 - \varepsilon_2$, the fraction of the model design space Ω_m for which the surrogate differs from the truth by more than U is less than ε_1. The relationship between N, ε_1, and ε_2 is entirely determined by the sampling theorem in Equation 4.5. The validity of 4.8 given 4.5 can be proved with order statistics. The proof is given in Appendix B.1.

The validation step is the final step in the surrogate design framework where truth calculations are needed. The results of the validation framework provide precise, probabilistic bounds on the prediction error of the surrogates for designs near surrogate–selected optimal designs. without having to appeal to the simulation. The estimates can be generated for any number of designs and can be obtained very rapidly as the only required function evaluations are of the surrogates. This gives near–instantaneous turnaround for the error estimates of each design and makes that design process interactive, which is extremely important in situations where the design goals evolve as more is learned.

The validation step has been performed for the global surrogates of the two outputs for the eddy–promoter problem. Because no prior importance had been assigned to any region of the model design space Ω_m, a uniform probability density function $\rho(\mathbf{p}_m) = 1$ has been chosen for the selection of the validation input points. A total of 24 simulation evaluations have been budgeted for the global validation which. from Equation 4.5, gives $\varepsilon_1 = 0.0561$ and $\varepsilon_2 = 0.2500$. The scaling functions have been set to constant values $\hat{g}_\theta(\mathbf{p}_m) = 2.00$ and $\hat{g}_\upsilon(\mathbf{p}_m) = 1.00$. Forming the validation sample, $\mathcal{X}^{va}$. and finding the maximum, unscaled surrogate error for each output gives

$$\max_{\mathcal{X}^{va}} |\theta_0^T(\mathbf{p}_m) - \widetilde{\theta}_0(\mathbf{p}_m)| = 0.0968, \tag{4.9}$$

$$\max_{\mathcal{X}^{va}} |\psi_0^T(\mathbf{p}_m) - \widetilde{\psi}_0(\mathbf{p}_m)| = 0.1910. \tag{4.10}$$

The model prediction error U is computed from Equation 4.6 and is $U = 0.9681$. From this, the following statement on the global quality of the surrogates can be made: With probability of at least 75% $(1 - \varepsilon_2)$,

$$|\theta_0^T(\mathbf{p}_m) - \widetilde{\theta}_0(\mathbf{p}_m)| \leq 0.0968\hat{g}_\theta(\mathbf{p}_m) = 0.1936, \tag{4.11}$$

$$|\psi_0^T(\mathbf{p}_m) - \widetilde{\psi_0}(\mathbf{p}_m)| \leq 0.0968\hat{g}_v(\mathbf{p}_m) = 0.0968, \tag{4.12}$$

over at least 94.39% $(1 - \varepsilon_1)$ of the model design space. The global bound for the two output surrogates hold for the same 94.39%-sized subset of the model design space Ω_m.

4.3 Surrogate Based Design

It is assumed that the design preferences are characterized by two performance metrics, each of which is a function of both surrogate outputs, $\widetilde{\phi_1}(\mathbf{p}'_m) : \Omega_m{}' \rightarrow I\!R$ and $\widetilde{\phi_2}(\mathbf{p}'_m) : \Omega_m{}' \rightarrow I\!R$, as well as of the full design vector $\mathbf{p}'$. For both metrics, lower values are assumed to correspond to better designs.

To form the surrogate metrics, the output surrogates, $\widetilde{\phi_1}(\mathbf{p}'_m) \approx \phi_1^T(\mathbf{p}'_m)$ and $\widetilde{\phi_2}(\mathbf{p}'_m) \approx \phi_2^T(\mathbf{p}'_m)$, are substituted into the performance metric functions. The resulting surrogate metrics $\tilde{\Phi}_1 = \Phi_1(\widetilde{\phi_1}(\mathbf{p}'_m), \widetilde{\phi_2}(\mathbf{p}'_m), \mathbf{p}') : \Omega' \rightarrow I\!R$ and $\tilde{\Phi}_2 = \Phi_2(\widetilde{\phi_1}(\mathbf{p}'_m), \widetilde{\phi_2}(\mathbf{p}'_m), \mathbf{p}') : \Omega' \rightarrow I\!R$ are then used for the design studies. Because the surrogate outputs are trivial to evaluate, any number of designs may be pursued and the trade-offs between improvements in one metric versus the other can be fully examined and understood. The *a posteriori* error bounds developed in the following sections will apply for any design chosen based on the surrogate performance metrics and will require no additional simulation evaluations. In addition, because the surrogate outputs have been validated (and not the full performance metric functions), different performance metrics (using the same inputs, outputs and design spaces) can be used as the basis for design studies and the error estimates will still be derivable. This gives additional flexibility to the design process.

The eddy-promoter problem that serves as the illustrative example here falls into the problem class just described. The output surrogates, constructed in Section 4.1 and validated in Section 4.2, are used to form the surrogate performance metrics. The output surrogates, $\widetilde{\theta_0}(\mathbf{p}_m)$ and $\widetilde{\psi_0}(\mathbf{p}_m)$, constructed in Section 4.1 are substituted into Equations 2.97 and 2.98. The resulting surrogate performance metrics are given by

$$\tilde{\Theta}(\mathbf{p}) = \Theta(\widetilde{\theta_0}(\mathbf{p}_m), p) = \log_{10}\left[\frac{1}{RePr} + \widetilde{\theta_0}(\mathbf{p}_m)\frac{1}{\eta_L}\right], \tag{4.13}$$

$$\tilde{\Psi}(\mathbf{p}) = \Psi(\widetilde{\psi_0}(\mathbf{p}_m), p) = \log_{10}\left[\widetilde{\psi_0}(\mathbf{p}_m) Re^3 \eta_L^3\right], \tag{4.14}$$

and are dependent on the full design vector $\mathbf{p} = (\mathbf{p}_m, \mathbf{p}_a) \in \Omega = [0,1]^{M=4}$. The range for the analytic input, $\eta_L \in [13.332, 106.656]$, is as stated in Section 2.6.1.

For the design study, two designs, $Q = 2$, are pursued. The first design problem $(q = 1)$ is to find the configuration that gives the best heat transfer. The second problem $(q = 2)$ imposes a constraint on the value for the pumping power Ψ. Both problems, $q \in \mathcal{Q} = \{1, 2\}$,

can be formulated as

$$\tilde{\mathbf{p}}^q = \arg \min_{\{\mathbf{p}\in\Omega \mid \tilde{\Psi}(\tilde{\psi}_0(\mathbf{p}_m),\mathbf{p})\leq\overline{\psi}^q\}} \tilde{\Theta}(\tilde{\theta}_0(\mathbf{p}_m),\mathbf{p}), \quad \forall q \in \mathcal{Q} \tag{4.15}$$

where $\tilde{\mathbf{p}}^q$ is the surrogate-predicted design point that minimizes the surrogate-based, wall temperature performance metric subject to the constraint that $\tilde{\Psi}^q = \Psi(\tilde{\psi}_0(\tilde{\mathbf{p}}^q_m), \tilde{\mathbf{p}}^q) \leq \overline{\psi}^q$. The temperature performance metric at the optimal point $\tilde{\mathbf{p}}^q$ is $\tilde{\Theta}^q = \Theta(\tilde{\theta}_0(\tilde{\mathbf{p}}^q_m), \tilde{\mathbf{p}}^q)$.

To perform the optimizations, a subspace searching, simplex algorithm (SUBPLEX) written by T. Rowan [61] and available on Netlib,[1] has been used. The algorithm is a generalization of the the Nelder–Mead [51] simplex algorithm in which high–dimensional problems are decomposed into low–dimensional subspaces that can be efficiently searched with the simplex algorithm. The SUBPLEX algorithm is well suited for the unconstrained optimization of noisy objective functions. The problem studied here (4.15) is a constrained optimization problem. The optimization results presented in this section have been obtained using the scalarization technique presented in Section 2.4.3. To find a global minimum for each design problem, 200 random restarts selected from a uniform distribution over Ω have been performed. The inexpensive nature of the surrogates makes such a "brute–force" approach tractable. The optimizer proved to be very robust in practice, and this was the primary reason for choosing it.

The two design problems have been carried out for the eddy–promoter heat exchanger example, and the results are summarized in Table 4.1. For the first design, the pumping power constraint $\overline{\psi}^q$ only needs to be set sufficiently high to ensure that it remains inactive. For the first design $\overline{\psi}^1 = 1 \times 10^3$ and for the second design $\overline{\psi}^2 = 9.4801$. The optimization process gives the optimal points $\tilde{\mathbf{p}}^1 = (0.1008, 0.2875, 1.0000, 1.0000)$, $\tilde{\mathbf{p}}^2 = (0.8549, 0.4729, 0.6449, 0.0000)$, and the corresponding surrogate–predicted, performance metric values $\tilde{\Theta}^1 = -2.2626$, $\tilde{\Psi}^1 = 12.5137$, and $\tilde{\Theta}^2 = -1.7106$, $\tilde{\Psi}^2 = 9.4801$. The inverse channel heights for each design are $\eta^1_L = 106.656$, and $\eta^2_L = 13.332$. The physical geometry for a single periodicity cell of each design point is given in Figure 4-2.

Design (q)	$\overline{\psi}^q$	$\tilde{\mathbf{p}}^q$	$\tilde{\Theta}^q$	$\tilde{\Psi}^q$
1	1×10^3	(0.1008, 0.2875, 1.0000, 1.0000)	−2.2626	12.5137
2	9.4801	(0.8549, 0.4729, 0.6449, 0.0000)	−1.7106	9.4801

Table 4.1: Baseline surrogate–based optimization results.

[1] The Netlib master index web address is `http://netlib.bell-labs.com/netlib/master/index.html` and the SUBPLEX software is located in the `opt` directory.

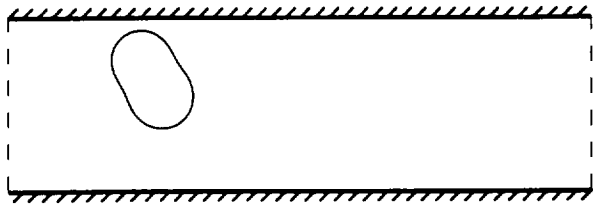

(a) Design 1.

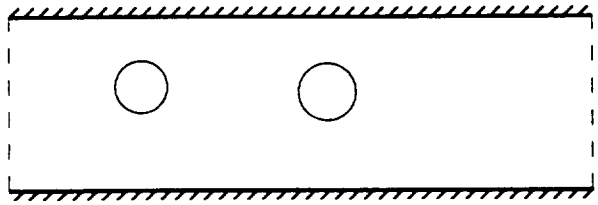

(b) Design 2.

Figure 4-2: Eddy-promoter configuration for each of the surrogate-predicted optimal designs.

4.4 *A Posteriori* Error Analysis

The *a posteriori* error analysis step of the surrogate framework takes as inputs the surrogates, the probability density and error-scaling functions, the model prediction error, and the surrogate-predicted design points. From these inputs, and without appealing to the simulation, probabilistic estimates of the difference between the surrogate and the truth at points in the design space near the surrogate-predicted designs are derived. Two formulations for the estimates are presented: proximal region, in which the estimates are valid for a region of non-zero measure, and proximal candidate, in which the estimates apply to a randomly selected design point near the surrogate-predicted optimal point. In addition, the *a posteriori* error analysis provides an assessment of the surrogate-predicted design optimality in terms of an estimate of how much effort is required to improve the design beyond a given amount. The proximal region and proximal candidate error analysis methods are presented in the next two sections, followed by the optimality analysis in the final subsection.

4.4.1 Surrogate Predictability — Proximal Region

To begin the Proximal Region error analysis, a model prediction region $\mathcal{P}^*_{\varepsilon_1} \in \Omega$ is defined as a subdomain in the full design space Ω of ρ-measure ε_1, and that contains the surrogate-predicted design point $\tilde{\mathbf{p}}^*$. Here, the ρ-measure of $\mathcal{P}^*_{\varepsilon_1}$ is computed only from the components in the model design space Ω_m. Recall that the design input vector $\mathbf{p}$ can

be decomposed into a modeled input vector $\mathbf{p}_m$ (the inputs over which the surrogates are constructed) and an analytic component $\mathbf{p}_a$ (the inputs for which the performance metric responses are known analytically). Likewise, the surrogate predicted optimizer can be decomposed into $\tilde{\mathbf{p}}^* = (\mathbf{p}_m^*, \mathbf{p}_a^*)$. The prediction neighborhood can then be defined as the tensor product $\mathcal{P}_{\varepsilon_1}^* = \mathcal{P}_{m\varepsilon_1}^* \times \mathbf{p}_a^*$ where $\mathcal{P}_{m\varepsilon_1}^*$ is the model prediction neighborhood with the ρ–measure defined in Equation 4.3, $\mu_\rho(\mathcal{P}_{m\varepsilon_1}^*) = \varepsilon_1$. The notion of how to precisely define the prediction region $\mathcal{P}_{\varepsilon_1}^*$ in practice is made more clear with the eddy–promoter example later in this section and in the following section. In general however, very limited assumptions are made as to the construction of $\mathcal{P}_{\varepsilon_1}^*$ and it is not required to be connected.

With the prediction neighborhood defined, probabilistic bounds on the outputs for designs near the surrogate predicted optimizer are first derived. The output bounds then serve to construct probabilistic bounds for the performance metrics for designs near the surrogate predicted designs.

The predictability statement for the outputs reads: With probability at least $1 - \varepsilon_1$, there will exist a region of non–zero measure $\Gamma'_m \subset \mathcal{P}_{m\varepsilon_1}^*$ in the neighborhood of $\mathbf{p}_m^*$ such that for all points $\mathbf{p}'_m \in \Gamma'_m$

$$l_{o_1} \leq \phi_1^T(\mathbf{p}'_m) \leq u_{o_1}, \tag{4.16}$$

$$l_{o_2} \leq \phi_2^T(\mathbf{p}'_m) \leq u_{o_2}, \tag{4.17}$$

where the truth–output bounds are

$$l_{\phi_1} = \min_{\{\mathbf{p}' \in \mathcal{P}_{m\varepsilon_1}^*\}} [\widetilde{\phi_1}(\mathbf{p}'_m) - U\hat{g}_{\phi_1}(\mathbf{p}'_m)], \tag{4.18}$$

$$u_{\phi_1} = \max_{\{\mathbf{p}' \in \mathcal{P}_{m\varepsilon_1}^*\}} [\widetilde{\phi_1}(\mathbf{p}'_m) + U\hat{g}_{\phi_1}(\mathbf{p}'_m)], \tag{4.19}$$

$$l_{\phi_2} = \min_{\{\mathbf{p}' \in \mathcal{P}_{m\varepsilon_1}^*\}} [\widetilde{\phi_2}(\mathbf{p}'_m) - U\hat{g}_{\phi_2}(\mathbf{p}'_m)], \tag{4.20}$$

$$u_{\phi_2} = \max_{\{\mathbf{p}' \in \mathcal{P}_{m\varepsilon_1}^*\}} [\widetilde{\phi_2}(\mathbf{p}'_m) + U\hat{g}_{\phi_2}(\mathbf{p}'_m)]. \tag{4.21}$$

The above result effectively bounds the truth values of the outputs near the surrogate predicted designs.

To extend the bounds to the performance metrics, a second step is pursued using the output bounds presented above. The predictability statement for the performance metrics reads: With probability at least $1-\varepsilon_2$, there will exist a region of non–zero measure $\Gamma' \subset \mathcal{P}_{\varepsilon_1}^*$ in the neighborhood of $\mathbf{p}^*$ such that for all points $\mathbf{p}' \in \Gamma'$

$$L_{\Phi_1} \leq \Phi_1(\phi_1^T(\mathbf{p}'_m), \phi_2^T(\mathbf{p}'_m), \mathbf{p}') \leq U_{\Phi_1}, \tag{4.22}$$

$$L_{\Phi_2} \leq \Phi_2(\phi_1^T(\mathbf{p}'_m), \phi_2^T(\mathbf{p}'_m), \mathbf{p}') \leq U_{\Phi_2}, \tag{4.23}$$

where the performance metric bounds are

$$L_{\Phi_1} = \min_{\{\mathbf{p}' \in \mathcal{P}^*_{\varepsilon_1}, z_1 \in \mathcal{Z}_1, z_2 \in \mathcal{Z}_2\}} \Phi_1(z_1, z_2, \mathbf{p}'), \tag{4.24}$$

$$U_{\Phi_1} = \max_{\{\mathbf{p}' \in \mathcal{P}^*_{\varepsilon_1}, z_1 \in \mathcal{Z}_1, z_2 \in \mathcal{Z}_2\}} \Phi_1(z_1, z_2, \mathbf{p}'), \tag{4.25}$$

$$L_{\Phi_2} = \min_{\{\mathbf{p}' \in \mathcal{P}^*_{\varepsilon_1}, z_1 \in \mathcal{Z}_1, z_2 \in \mathcal{Z}_2\}} \Phi_2(z_1, z_2, \mathbf{p}'), \tag{4.26}$$

$$U_{\Phi_2} = \max_{\{\mathbf{p}' \in \mathcal{P}^*_{\varepsilon_1}, z_1 \in \mathcal{Z}_1, z_2 \in \mathcal{Z}_2\}} \Phi_2(z_1, z_2, \mathbf{p}'), \tag{4.27}$$

and the output ranges, $\mathcal{Z}_1$ and $\mathcal{Z}_2$, are determined by Equations 4.18—4.21 and are

$$\mathcal{Z}_1 = \{z \mid l_{o_1} \leq z \leq u_{o_1}\}, \tag{4.28}$$

$$\mathcal{Z}_2 = \{z \mid l_{o_2} \leq z \leq u_{o_2}\}. \tag{4.29}$$

To define the prediction neighborhood $\mathcal{P}^*_{\varepsilon_1}$ precisely, a distance metric $\Delta(\mathbf{p}_{m1}, \mathbf{p}_{m2})$ that quantifies the distance between two points is introduced. The prediction neighborhood around the surrogate predicted optimal point $\tilde{\mathbf{p}}^q_m$ is then defined as that region $\mathcal{R}$, of size ε_1, that minimizes

$$r_\Delta = \max_{\mathbf{p}_m \in \mathcal{R}} \Delta(\mathbf{p}_m, \tilde{\mathbf{p}}^q_m). \tag{4.30}$$

For the eddy-promoter problem, the distance metric function has been defined based on the outputs and is

$$\Delta(\mathbf{p}_{m1}, \mathbf{p}_{m2}) = \max\left(\frac{\tilde{\theta}_0(\mathbf{p}_{m1}) - \tilde{\theta}_0(\mathbf{p}_{m2})}{h_\theta}, \frac{\widetilde{\psi_0}(\mathbf{p}_{m1}) - \widetilde{\psi_0}(\mathbf{p}_{m2})}{h_\psi}\right). \tag{4.31}$$

where h_θ and h_ψ are positive scalars. The definition for the distance function in 4.31 can be used to specify the neighborhood with minimum $\tilde{\theta}_0$ sensitivity (for h_ψ sufficiently large) or, likewise, the neighborhood with minimum $\widetilde{\psi_0}$ sensitivity (for h_θ sufficiently large). By setting the levels of the h_θ and h_ψ to match the relative variation of the surrogate over the region $\mathcal{R}$, a balance between the $\tilde{\theta}_0$ and $\widetilde{\psi_0}$ sensitivity can be obtained.

The output bounds in Equations 4.18—4.21 have been evaluated for each design. The output bounds have then been used to evaluate the bound quantities given in Equations 4.24—4.27. The resulting predictability statements for the truth values of the performance metrics are given below. For Design 1, the statement reads: With probability of at least 75%, there will exist points in $\Gamma^1 \subset \mathcal{P}^1_{\varepsilon_1}$ such that for $\mathbf{p}' \in \Gamma^1$

$$11.1809 \leq \Psi(\psi_0^T(\mathbf{p}'_m), \mathbf{p}') \leq 12.8194, \tag{4.32}$$

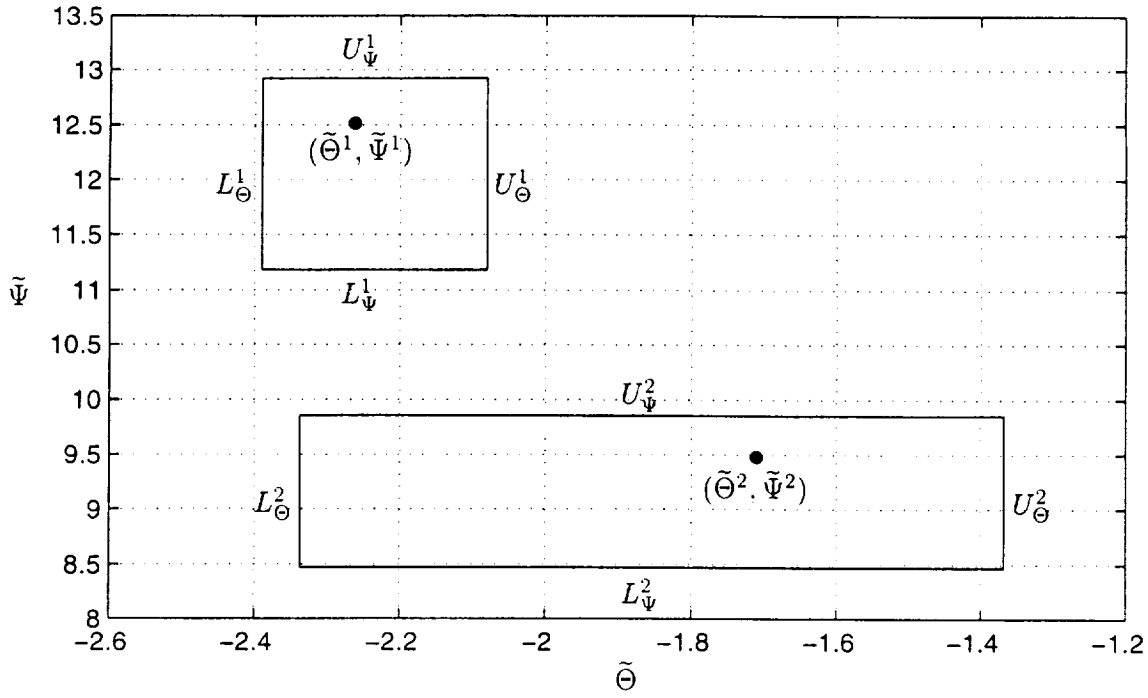

Figure 4-3: Output plane plot of the two design point performance pairs (•) and the associated predictability boxes.

$$-2.3899 \leq \Theta(\theta_0^T(\mathbf{p}'_m), \mathbf{p}') \leq -2.1152. \tag{4.33}$$

For Design 2, the statement reads: With probability of at least 75%, there will exist points in $\Gamma^2 \subset \mathcal{P}^2_{\varepsilon_1}$ such that for $\mathbf{p}' \in \Gamma^2$

$$8.4716 \leq \Psi(\psi_0^T(\mathbf{p}'_m), \mathbf{p}') \leq 9.8613, \tag{4.34}$$

$$-2.3372 \leq \Theta(\theta_0^T(\mathbf{p}'_m), \mathbf{p}') \leq -1.4601. \tag{4.35}$$

The predictability statements are valid for each design for the corresponding prediction neighborhood. For a given design q, the region $\Gamma^q \subset \mathcal{P}^q_{\varepsilon_1}$ for which the points satisfy the performance metric bounds is identical for each metric.

The results given above have been plotted in the output plane in Figure 4-3. In the figure, the surrogate performance metric values for each design are plotted as solid dots and the bounds on the truth performance metrics are plotted as boxes. It is evident from the predictability bounds for the two eddy-promoter designs given in 4.32—4.35 that the global output surrogates are quite poor. Even for the two very different designs that have been selected (based both on the associated geometries and the surrogate-predicted performance of each), the error bounds between the two design overlap. This implies that the surrogates are not accurate enough to distinguish between the two designs as regards temperature.

4.4.2 Surrogate Predictability — Proximal Candidate

The Proximal Candidate *a posteriori* error analysis requires that we define a prediction region $\mathcal{P}^*_\sigma \subset \Omega$ that is of ρ–measure σ, and that contains the surrogate-predicted optimal point $\tilde{\mathbf{p}}^*$, in a manner similar to that presented for the Proximal Region analysis of Section 4.4.1. A sample candidate design $\hat{\mathbf{P}}^*_m$ is selected randomly according to $\hat{\mathbf{P}}^*_m \sim \rho_{\mathcal{P}}(\mathbf{p}_m)$. The density function $\rho_{\mathcal{P}}(\mathbf{p}_m)$ is defined as

$$\rho_{\mathcal{P}}(\mathbf{p}_m) = \frac{1}{\sigma}\rho(\mathbf{p}_m)\Big|_{\mathcal{P}}, \quad \forall \mathbf{p}_m \in \mathcal{P}^*_{m\sigma} \tag{4.36}$$

where $\mathcal{P}^*_{m\sigma} \subset \Omega_m$ is the sub-manifold of $\mathcal{P}^*_\sigma$ that corresponds to the model design space and the full neighborhood is the tensor product $\mathcal{P}^*_\sigma = \{\mathcal{P}^*_{m\sigma} \times \mathbf{p}^*_a\}$. The full candidate design vector $\hat{\mathbf{P}}^*$ is given as $\hat{\mathbf{P}}^* = (\hat{\mathbf{P}}^*_m, \mathbf{p}^*_a)$ where $\mathbf{p}^*_a$ is the analytic inputs of the surrogate predicted optimizer $\tilde{\mathbf{p}}^* = (\tilde{\mathbf{p}}^*_m, \mathbf{p}^*_a)$. The candidate designs can easily be selected with acceptance–rejection techniques without having to formally construct the prediction neighborhood $\mathcal{P}^*_{m\sigma}$.

A second small parameter, ε_c, is introduced and is related to ρ–measure of $\mathcal{P}^*_{m\sigma}$, σ, by

$$\varepsilon_c = \frac{1}{\sigma(N+1)}(1-(1-\sigma)^{N+1}), \tag{4.37}$$

where $0 < \varepsilon_c, \sigma < 1$, and N is the validation sample size given in Equation 4.5. It will become evident below that ε_c is the significance of the probabilistic bound estimates that are derived.

Now, given the two inputs to the analysis ε_c and σ, and the model prediction error U, the following statement can be made: With probability of at least $1-\varepsilon_c$, the truth output values at $\hat{\mathbf{P}}^*_m$ are bounded by

$$l^c_{o_1} \le \phi^T_1(\hat{\mathbf{P}}^*_m) \le u^c_{o_1}, \tag{4.38}$$

$$l^c_{o_2} \le \phi^T_2(\hat{\mathbf{P}}^*_m) \le u^c_{o_2}, \tag{4.39}$$

where the bound values are

$$l^c_{\phi_1} = \widetilde{\phi_1}(\hat{\mathbf{P}}^*_m) - U\hat{g}_{o_1}(\hat{\mathbf{P}}^*_m), \tag{4.40}$$

$$u^c_{\phi_1} = \widetilde{\phi_1}(\hat{\mathbf{P}}^*_m) + U\hat{g}_{\phi_1}(\hat{\mathbf{P}}^*_m), \tag{4.41}$$

$$l^c_{o_2} = \widetilde{\phi_2}(\hat{\mathbf{P}}^*_m) - U\hat{g}_{o_2}(\hat{\mathbf{P}}^*_m), \tag{4.42}$$

$$u^c_{\phi_2} = \widetilde{\phi_2}(\hat{\mathbf{P}}^*_m) + U\hat{g}_{o_2}(\hat{\mathbf{P}}^*_m). \tag{4.43}$$

Equations 4.38—4.43 bound the truth value of the outputs for the candidate design point $\hat{\mathbf{P}}^*_m$.

To extend the analysis to the performance metrics, a procedure similar to that of Section 4.4.1 is pursued. Again, the following statement can be made: With probability of at least $1 - \varepsilon_c$, the truth performance metric values at $\widehat{\mathbf{P}}^*_m$ are bounded by

$$L^c_{\Phi_1} \leq \Phi_1(\phi_1^T(\widehat{\mathbf{P}}^*_m), \phi_2^T(\widehat{\mathbf{P}}^*_m), \widehat{\mathbf{P}}^*) \leq U^c_{\Phi_1}, \tag{4.44}$$

$$L^c_{\Phi_2} \leq \Phi_2(\phi_1^T(\widehat{\mathbf{P}}^*_m), \phi_2^T(\widehat{\mathbf{P}}^*_m), \widehat{\mathbf{P}}^*) \leq U^c_{\Phi_2}, \tag{4.45}$$

where the performance metric bounds are

$$L^c_{\Phi_1} = \min_{\{z_1 \in \mathcal{Z}^c_1, z_2 \in \mathcal{Z}^c_2\}} \Phi_1(z_1, z_2, \widehat{\mathbf{P}}^*), \tag{4.46}$$

$$U^c_{\Phi_1} = \max_{\{z_1 \in \mathcal{Z}^c_1, z_2 \in \mathcal{Z}^c_2\}} \Phi_1(z_1, z_2, \widehat{\mathbf{P}}^*), \tag{4.47}$$

$$L^c_{\Phi_2} = \min_{\{z_1 \in \mathcal{Z}^c_1, z_2 \in \mathcal{Z}^c_2\}} \Phi_2(z_1, z_2, \widehat{\mathbf{P}}^*), \tag{4.48}$$

$$U^c_{\Phi_2} = \max_{\{z_1 \in \mathcal{Z}^c_1, z_2 \in \mathcal{Z}^c_2\}} \Phi_2(z_1, z_2, \widehat{\mathbf{P}}^*), \tag{4.49}$$

and the ranges for the outputs, $\mathcal{Z}^c_1$ and $\mathcal{Z}^c_2$, at the candidate design point are obtained from Equations 4.40—4.43 and are

$$\mathcal{Z}^c_1 = \{z \mid l^c_{o_1} \leq z \leq u^c_{o_1}\}, \tag{4.50}$$

$$\mathcal{Z}^c_2 = \{z \mid l^c_{o_2} \leq z \leq u^c_{o_2}\}. \tag{4.51}$$

The proximal candidate error analysis produces estimates that apply to a specific design; the randomly chosen candidate design $\widehat{\mathbf{P}}^*$ near the surrogate–predicted optimal point $\tilde{\mathbf{p}}^*$. This is in contrast to the proximal region analysis presented in the previous section in which the error estimates applied to a region of finite measure in the neighborhood of $\tilde{\mathbf{p}}^*$. The proximal region analysis assures that the region will exist with $1 - \varepsilon_2$ confidence, but can not provide precise information as to where in $\mathcal{P}^*_{\varepsilon_1}$ the region exists. Although the proximal region analysis does provide a sense of stability, it may not be satisfying in some design scenarios. The error estimates for the candidate design developed in this section provide an alternative interpretation. In this scenario, the designer can be assured that the error bounds apply, with $1 - \varepsilon_c$ confidence, to the specific, randomly drawn candidate design.

For the eddy–promoter problem, the same two surrogate–predicted designs given in Table 4.1 are considered. The uncertainty parameters, σ and ε_c, in Equation 4.37 are set to $\sigma = 0.1578$, and $\varepsilon_c = 0.2500$ which agree with the $N = 24$ global validation points that have been computed in Section 4.2. A new distance metric that quantifies the distance between

two input points, $\mathbf{p}_{m1}$ and $\mathbf{p}_{m2}$, is introduced to define the prediction neighborhood

$$\Delta_c(\mathbf{p}_{m1}, \mathbf{p}_{m2}) = [(\mathbf{p}_{m1} - \mathbf{p}_{m2}) \cdot (\mathbf{p}_{m1} - \mathbf{p}_{m2})]^{\frac{1}{2}}, \tag{4.52}$$

where the $[() \cdot ()]$ term above is the vector dot product. The distance metric defined in Equation 4.52 is simply the Euclidean distance between the two input points in the model input space Ω_m. The metric in Equation 4.52 emphasizes designs that are "near" the surrogate-predicted optimal designs based on the eddy-promoter geometry (model inputs) whereas the distance metric given Equation 4.31 defines designs "near" the surrogate-predicted optimal design as similarly performing designs. The prediction neighborhood is then defined as that region $\mathcal{R}$, of size σ, that minimizes

$$r_{\Delta_c} = \max_{\mathbf{p}_m \in \mathcal{R}} \Delta_c(\mathbf{p}_m, \tilde{\mathbf{p}}_m^q). \tag{4.53}$$

With the prediction neighborhood defined as above, Monte-Carlo sampling is used to empirically measure the neighborhood and acceptance-rejection techniques are used to obtain a candidate for each design.

For Design 1, the candidate design input vector is drawn according to the density in Equation 4.36 is $\hat{\mathbf{P}}^1 = (0.2256, 0.4976, 0.8211, 1.0000)$ and the corresponding surrogate performance metric values are $\tilde{\Theta}_c^1 = \Theta(\tilde{\theta}_0(\hat{\mathbf{P}}_m^1), \hat{\mathbf{P}}^1) = -2.2192$ and $\tilde{\Psi}_c^1 = \Psi(\tilde{\psi}_0(\hat{\mathbf{P}}^1), \hat{\mathbf{P}}_m^1) = 12.6431$. The predictability statement for the candidate design point reads: With confidence of at least 75%, the truth performance metric bounds for the candidate design are bounded by

$$-2.3745 \leq \Theta(\theta_0^T(\hat{\mathbf{P}}_m^1), \hat{\mathbf{P}}^1) \leq -2.1050. \tag{4.54}$$

$$12.4085 \leq \Psi(\psi_0^T(\hat{\mathbf{P}}^1), \hat{\mathbf{P}}_m^1) \leq 12.7946. \tag{4.55}$$

For Design 2, the candidate design input vector is $\hat{\mathbf{P}}^2 = (0.7928, 0.3888, 0.6837, 0.0000)$ and the corresponding surrogate performance metric values are $\tilde{\Theta}_c^2 = \Theta(\tilde{\theta}_0(\hat{\mathbf{P}}_m^2), \hat{\mathbf{P}}^2) = -1.6766$ and $\tilde{\Psi}_c^2 = \Psi(\tilde{\psi}_0(\hat{\mathbf{P}}^2), \hat{\mathbf{P}}_m^2) = 9.4762$. The predictability statement for the candidate point for Design 2 reads: With confidence of at least 75%, the truth performance metric bounds for the candidate design are bounded by

$$-2.3372 \leq \Theta(\theta_0^T(\hat{\mathbf{P}}_m^2), \hat{\mathbf{P}}^2) \leq -1.4601. \tag{4.56}$$

$$8.4716 \leq \Psi(\psi_0^T(\hat{\mathbf{P}}^2), \hat{\mathbf{P}}_m^2) \leq 9.8613, \tag{4.57}$$

The two design points and candidate surrogate performance metric pairs, and the predictability boxes are plotted in the surrogate performance metric plane in Figure 4-4. The predictability boxes show graphically where the truth performance of the candidate design (shown as an open circle) will lie with the associated 75% confidence. Comparing the re-

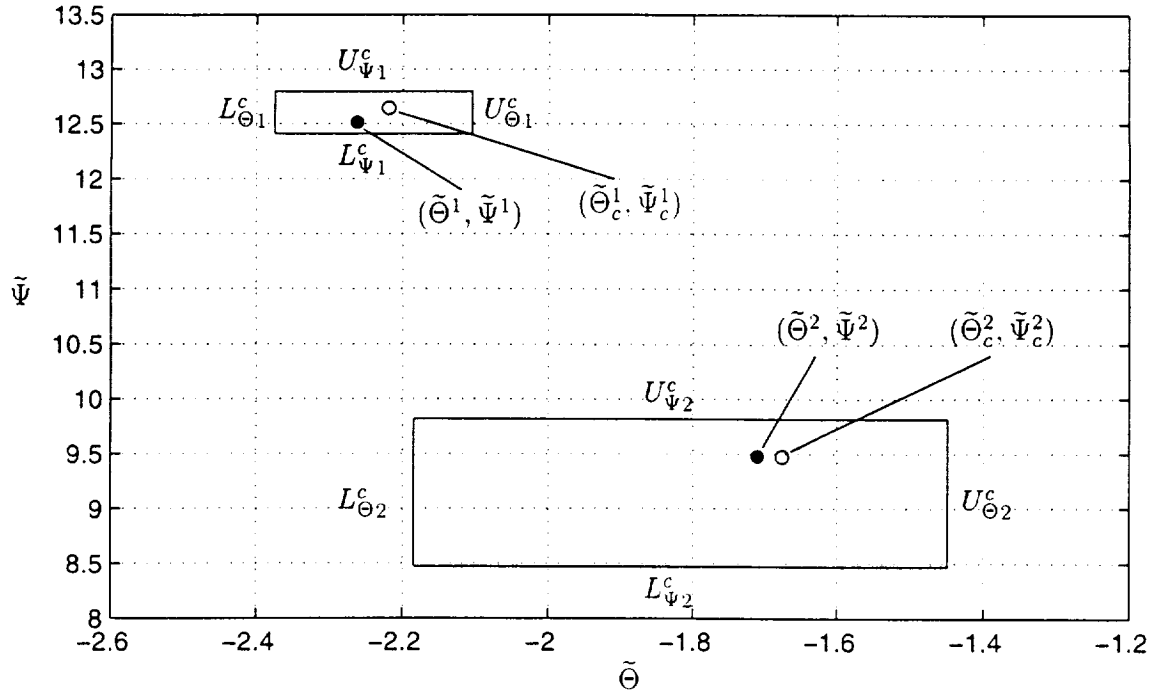

Figure 4-4: Output plane plot of the two design point peformance pairs (•), candidate design performance pairs (○), and the predictability boxes for the candidate designs.

sults in Figure 4-4 with the proximal region analysis results plotted in Figure 4-3 show that the predictability boxes for the candidate designs are sharper than for the proximal region. However, although both analyses indicate that the surrogates can discriminate between the designs based on the pumping power metric, neither can do so in terms of the temperature performance metric. This further reinforces the conclusion that the surrogates are not performing adequately to select designs based solely on the surrogate predictions. The geometry for each of the candidate designs is plotted in Figure 4-5 and these can be compared to the surrogate-predicted optimal designs shown in Figure 4-2.

4.4.3 Design Optimality

In earlier work [77, 78, 79], optimality estimates were obtained for surrogate-predicted optimizers in the neighborhood $\mathcal{P}^*_{\varepsilon_1}$ that relied on the assumption of quasi-convexity of the truth response in the region $\mathcal{P}^*_{\varepsilon_1}$. The resulting optimality bounds, however, are often times too large to be of use. Another approach to the optimality analysis is to estimate the effort required to improve upon the surrogate-predicted design. The procedure is to develop estimates as to the amount of improvement in each metric that could be realized by randomly drawing additional simulation points according to the probability density function used for the validation step. It is again assumed that lower values of the two performance metrics are preferred.

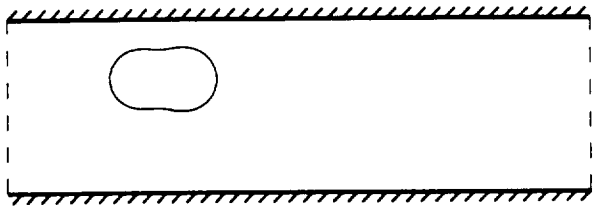

(a) Candidate design 1.

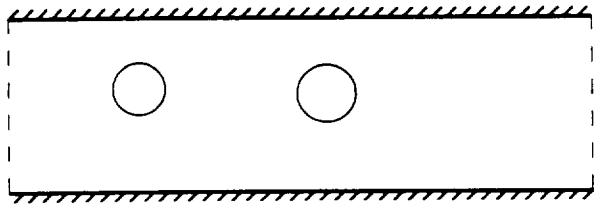

(b) Candidate design 2.

Figure 4-5: Eddy-promoter candidate design configurations for each of the surrogate-predicted optimal designs.

Given a surrogate predicted optimizer $\tilde{\mathbf{p}}^*$ with associated surrogate performance metric values $\tilde{\Phi}_1^* = \Phi_1(\widetilde{\phi_1}(\tilde{\mathbf{p}}_m^*), \widetilde{\phi_2}(\tilde{\mathbf{p}}_m^*), \tilde{\mathbf{p}}^*)$ and $\tilde{\Phi}_2^* = \Phi_2(\widetilde{\phi_1}(\tilde{\mathbf{p}}_m^*), \widetilde{\phi_2}(\tilde{\mathbf{p}}_m^*), \tilde{\mathbf{p}}^*)$, the extent that a surrogate-predicted, optimal design, $\tilde{\mathbf{p}}^*$, can be expected to be improved by randomly selecting design points, and evaluating the truth performance metric values for each, is bounded. For the analysis of this section, it is assumed that, because lower values of the performance metrics correspond to preferred designs, a lower value in at least one metric without an increase in the second, represents an improved design. This assumption has been shown, in Section 2.4.2, to be consistent with a wide class of multiobjective optimization formulations.

First, an unbounded set of points in the surrogate, performance-metric plane is defined as

$$\mathcal{A}^+ = \{\mathbf{s} \in I\!R^2 \,|s_1 < \Phi_1(\widetilde{\phi_1}(\tilde{\mathbf{p}}_m^*), \widetilde{\phi_2}(\tilde{\mathbf{p}}_m^*), \tilde{\mathbf{p}}^*),\ s_2 < \Phi_2(\widetilde{\phi_1}(\tilde{\mathbf{p}}_m^*), \widetilde{\phi_2}(\tilde{\mathbf{p}}_m^*), \tilde{\mathbf{p}}^*)\} \qquad (4.58)$$

which is the set of all performance metric pairs to the left, and below, the surrogate-predicted optimal point performance. As stated in the preceding paragraph, input points with performance metric pairs in $\mathcal{A}^+$ can arguably be called better than $\tilde{\mathbf{p}}^*$. A second set of points in the surrogate, performance-metric space is defined as

$$\begin{aligned}\mathcal{A}^{\text{opt}} = \{\mathbf{s} \in I\!R^2 \mid \exists \mathbf{p}' \in \Omega',\ z_1 \in \mathcal{Z}_1^{\text{opt}},\ z_2 \in \mathcal{Z}_2^{\text{opt}}\ \text{ s.t.} \\ \Phi_1(\widetilde{\phi_1}(\mathbf{p}'_m), \widetilde{\phi_2}(\mathbf{p}'_m), \mathbf{p}') \leq s_1, \Phi_2(\widetilde{\phi_1}(\mathbf{p}'_m), \widetilde{\phi_2}(\mathbf{p}'_m), \mathbf{p}') \leq s_2\}. \qquad (4.59)\end{aligned}$$

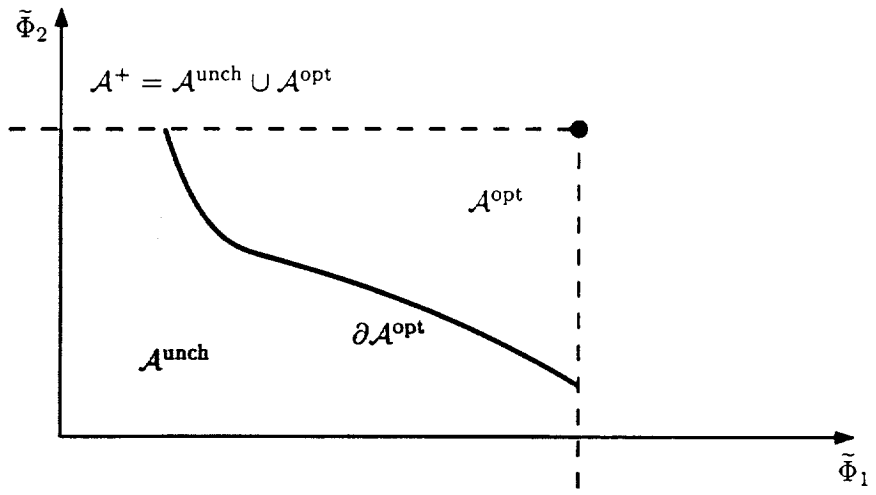

Figure 4-6: Surrogate performance metric plane plot showing the surrogate predicted optimizer performance (•), the expanded optimality set $\mathcal{A}^{\text{opt}}$ (light shade), the uncharacterized optimality set $\mathcal{A}^{\text{unch}}$ (dark shade), and boundary $\partial\mathcal{A}^{\text{opt}}$.

where the ranges $\mathcal{Z}_1^{\text{opt}}$ and $\mathcal{Z}_2^{\text{opt}}$ are

$$\mathcal{Z}_1^{\text{opt}} = \{z \mid \forall \mathbf{p}'_m \in \Omega'_m,\ [\widetilde{\phi_1}(\mathbf{p}'_m) - U\hat{g}_{\phi_1}(\mathbf{p}'_m)] \leq z \leq [\widetilde{\phi_1}(\mathbf{p}'_m) + U\hat{g}_{\phi_1}(\mathbf{p}'_m)]\}. \tag{4.60}$$

$$\mathcal{Z}_2^{\text{opt}} = \{z \mid \forall \mathbf{p}'_m \in \Omega'_m,\ [\widetilde{\phi_2}(\mathbf{p}'_m) - U\hat{g}_{\phi_2}(\mathbf{p}'_m)] \leq z \leq [\widetilde{\phi_2}(\mathbf{p}'_m) + U\hat{g}_{\phi_2}(\mathbf{p}'_m)]\}. \tag{4.61}$$

The third region in the surrogate performance metric plane is then simply defined as $\mathcal{A}^{\text{unch}} = \mathcal{A}^+ \setminus \mathcal{A}^{\text{opt}}$. The region $\mathcal{A}^{\text{unch}}$ is the set of possible performance metric values that improve upon the surrogate-predicted design performance and correspond to input points in the region of the design input space that is uncharacterized by the surrogate validation. A schematic of the region $\mathcal{A}^{\text{opt}}$ (shaded) and $\mathcal{A}^{\text{unch}}$ in the surrogate performance metric plane is given in Figure 4-6. In the figure, the surrogate performance metric response pair of the surrogate predicted optimizer plotted as a solid dot.

Next, a sequence of N^{opt}, independent, identically distributed, randomly selected inputs, $\hat{\mathbf{P}}_{m_1}, \ldots, \hat{\mathbf{P}}_{m_{N^{\text{opt}}}}$, is drawn according to the probability density function $\rho(\mathbf{p}_m)$; $\hat{\mathbf{P}}_{m_i} \sim \rho(\mathbf{p}_m), i = 1, \ldots, N^{\text{opt}}$. The optimality statement then follows that, the probability that at least one of the randomly selected design points will have truth performance values that lie in $\mathcal{A}^{\text{unch}}$ is less than $1 - \varepsilon_L$. The number of random input vectors drawn, N^{opt}, is computed as

$$N^{\text{opt}} \leq N\left(\frac{1}{\varepsilon_L} - 1\right), \tag{4.62}$$

where the parameter $\varepsilon_L \in]0, 1[$ is set independently. The optimality result states that, with a confidence of less than $1 - \varepsilon_L$, N^{opt} additional truth evaluations at randomly selected

points will produce a design with truth performance metric values better than $\mathcal{A}^{\text{opt}}$.

For the eddy-promoter design problem, the upper boundaries for $\mathcal{A}_1^+$ $\mathcal{A}_2^+$, have been plotted as dashed lines in Figure 4-7. The boundaries of $\mathcal{A}_1^{\text{opt}}$ and $\mathcal{A}_2^{\text{opt}}$ are plotted as thick solid lines and the uncharacterized optimality regions, $\mathcal{A}_1^{\text{unch}}$ and $\mathcal{A}_2^{\text{unch}}$, are shown shaded. Note that the regions $\mathcal{A}_1^{\text{unch}}$ and $\mathcal{A}_2^{\text{unch}}$ overlap in the lower left corner of the plot even though the lightly shaded $\mathcal{A}_2^{\text{unch}}$ supersedes $\mathcal{A}_1^{\text{unch}}$ in that region.

With the optimality regions evaluated, the optimality assessment follows directly. First, for Design 1, if ε_L is set to $\varepsilon_L = 0.25$, then according to 4.62, if an additional $N^{\text{opt}} = 72$ input points are drawn randomly, and the truth performance metrics for each evaluated, then the probability that at least one of the randomly chosen inputs, i, has truth metric output pair such that

$$\left(\Psi(\psi_0^T(\hat{\mathbf{P}}_{m_i}), \hat{\mathbf{P}}_i), \Theta(\theta_0^T(\hat{\mathbf{P}}_{m_i}), \hat{\mathbf{P}}_i)\right) \in \mathcal{A}_1^{\text{unch}}, \tag{4.63}$$

is less than $1-\varepsilon_L = 75\%$. Similarly, for Design 2, if an additional $N^{\text{opt}} = 72$ input points are drawn randomly, and the truth performance metrics for each evaluated, then the probability that at least one of the randomly chosen inputs, i, has truth metric output pair such that

$$\left(\Psi(\psi_0^T(\hat{\mathbf{P}}_{m_i}), \hat{\mathbf{P}}_i), \Theta(\theta_0^T(\hat{\mathbf{P}}_{m_i}), \hat{\mathbf{P}}_i)\right) \in \mathcal{A}_2^{\text{unch}}, \tag{4.64}$$

is less than $1 - \varepsilon_L = 75\%$.

The optimality analysis provides an additional evaluation as to the quality of the surrogates. For very accurate surrogates, which would in turn result in an extremely small model prediction error U, the boundary on the regions $\mathcal{A}_1^{\text{unch}}$ and $\mathcal{A}_2^{\text{unch}}$ would be very close to the surrogate-predicted optimal performance pairs. This would suggest that even with a great deal of computational effort, the performance of a given design can be improved only slightly (and only at best with a $1 - \varepsilon_L$ certainty) and is likely not worthwhile. However, the model prediction error for the eddy-promoter problem is fairly large and this is evident by the large improvement that can be realized (the large distance between $\mathcal{A}_1^{\text{unch}}$ and $\mathcal{A}_2^{\text{unch}}$ and the design point performance pairs) for the additional computational effort. The additional effort, would likely be worthwhile for the eddy-promoter problem suggesting that improvements in the surrogates are required.

4.5 Baseline Surrogate Summary

The primary drawback to the baseline surrogate approach is the difficult construction and validation of the surrogate in high dimensional input spaces. This can be easily illustrated by considering the uniform importance function $\rho(\mathbf{p})$ and a neighborhood of ρ-measure ε_1 in the input domain $\Omega = [0,1]^M$. The neighborhood will span at least $\varepsilon_1^{1/M}$ in one of

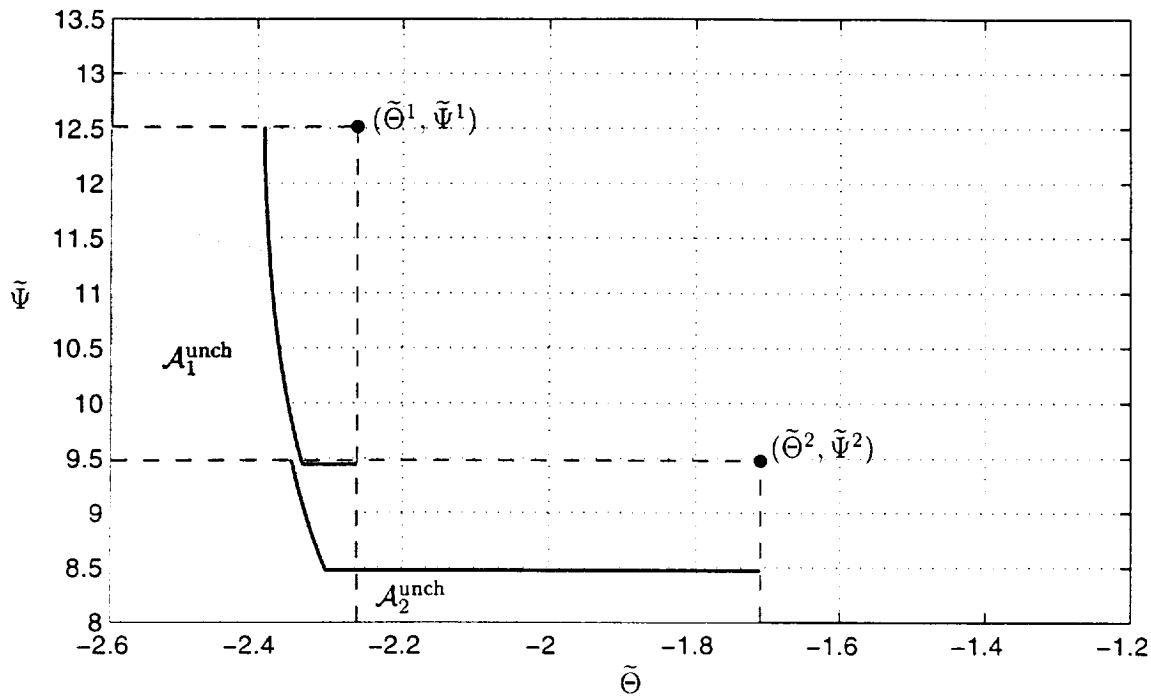

Figure 4-7: Uncharacterized optimality regions shown shaded for each of the surrogate-predicted designs (•).

the input directions which rapidly approaches one as $M \to \infty$. The loss of localization as $M \to \infty$ produces a corresponding loss in predictability through increased value of the neighborhood radius as given in Equation 4.30.

In certain instances, the surrogate approach can be effectively applied to problems with high dimensional input spaces. One such case occurs when the shape inputs are highly correlated. An example is the optimization of smooth body profiles in which highly oscillatory geometries are not likely optimizers [55, 56, 57]. For cases in which the inputs are highly correlated, the effective input dimension of the problem is reduced. The eddy-promoter problem is a second instance in which the surrogates can be effectively applied to a problem with a high input dimension. By pursuing a Pareto formulation for the two-criteria optimization problem, the effective dimension for the validation and predictability error analysis is reduced from the number of inputs to one fewer than the number of critera: here a single parameter. The surrogate-Pareto formulation has been applied previously [36]. In Chapter 5, the surrogate-Pareto formulation is applied to the eddy-promoter problem.

Chapter 5

Surrogate–Pareto Approach

In this chapter, the nonparametric-validated, surrogate-Pareto optimization framework is presented. The basic structure of this chapter follows the presentation employed to describe the baseline surrogate framework in Chapter 4. The identical Exact/Truth/Surrogate hierarchy of solution approximations will be assumed.

In Chapter 4, the weaknesses of the baseline surrogate framework in terms of design predictability was apparent for problems with more than "several" inputs. In fact, even for the eddy-promoter problem with only 3 modeled inputs, the surrogate construction is quite difficult due to the complexity of the input-output relationship. Although pursuing a surrogate-Pareto approach to the design optimization can not avoid the difficulties of surrogate construction, it does dramatically improve the predictability of designs for problems with many inputs and 2 or 3 performance metrics.

In the following sections, the steps of the surrogate-Pareto framework are presented. The format for each chapter is to present the theory for a general, two output, two performance metric problem and then to illustrate the techniques with the eddy-promoter problem which is a specialized case of the general problem. Throughout the chapter, it is assumed that lower values of the performance metrics are preferred although no such assumption is made for the outputs. In the first section, the surrogate construction stage is presented. Second, the validation stage of the framework is presented. Third, the surrogate-based design step is described. Fourth, the *a posteriori* error analysis is described.

5.1 Surrogate Construction

Surrogate construction takes two stages. In the first stage, global surrogates are constructed to approximate the truth input-output function over the model design space Ω_m. The surrogate models are $\widetilde{\psi_0}(\mathbf{p}_m) \approx \psi_0(\mathbf{p}_m)$ and $\widetilde{\theta_0}(\mathbf{p}_m) \approx \theta_0(\mathbf{p}_m)$ and are constructed exactly as they were for the baseline surrogate framework in Section 4.1. In the second stage of the surrogate construction, the global model surrogates are used to form the surrogate perfor-

mance metrics, which are then used to find the surrogate Pareto-optimal input manifold $\widetilde{\partial\mathcal{A}}$ and output manifold $\widetilde{\mathcal{L}^{\mathcal{A}}}$. The construction stages are presented in the next two sections.

5.1.1 Global Surrogates

The global surrogate construction step is identical to that presented in Section 4.1. Given M_m modeled inputs and the associated input (design) vector $\mathbf{p}_m \in \Omega_m \subset I\!R^{M_m}$ that lies in the model design space Ω_m, two truth outputs ($K = 2$), $\phi_1^T(\mathbf{p}'_m) : \Omega_m \rightarrow I\!R$ and $\phi_2^T(\mathbf{p}'_m) : \Omega_m \rightarrow I\!R$, are considered. Surrogates for the truth outputs are constructed, $\widetilde{\phi_1}(\mathbf{p}'_m) \approx \phi_1^T(\mathbf{p}'_m)$, $\widetilde{\phi_2}(\mathbf{p}'_m) \approx \phi_2^T(\mathbf{p}'_m)$, that approximate the truth input-output function as closely as possible. The surrogates can have any form, incorporate data from any source, and in general, no limiting assumptions are made concerning construction or quality. The validity of the results obtained later are not impacted by the surrogate approximation quality, however the utility of the results will be.

The global, eddy-promoter surrogate models, $\widetilde{\theta_0}(\mathbf{p}_m)$ and $\widetilde{\psi_0}(\mathbf{p}_m)$, constructed in this step of the surrogate-Pareto framework are identical to those constructed for the baseline surrogate framework (Chapter 4). The surrogates are a radial basis function fit to $N^{co} = 256$ construction input-output pairs. The radial basis function is described in Appendix D.1. Of the 256 construction points, 91 have been obtained by appealing to the truth simulation at model input points selected based on an orthogonal array (Appendix D.2). The remaining 165 construction points are duplicate points in the design space Ω_m that arise from the mapping from geometric inputs $\mathbf{Z}_{EP}$ to the normalized input vector $\mathbf{p}_m$ described in Section 2.5.3. The duplicate points correspond to input points for which $p_{m2} = 0, 1$. Slices of the surrogate surfaces are plotted in Figure 4-1.

5.1.2 Surrogate PO Manifolds

The goal of the design problem is find the design (or designs) that achieves lower values for the two performance metrics, $\Phi_1(\phi_1^T(\mathbf{p}'_m), \phi_2^T(\mathbf{p}'_m), \mathbf{p}')$ and $\Phi_2(\phi_1^T(\mathbf{p}'_m), \phi_2^T(\mathbf{p}'_m), \mathbf{p}')$. Because the truth values of the outputs are typically very expensive to evaluate, the global surrogates, $\widetilde{\phi_1}(\mathbf{p}'_m)$ and $\widetilde{\phi_2}(\mathbf{p}'_m)$, constructed in the previous section are used to form the surrogate performance metrics, $\tilde{\Phi}_1(\mathbf{p}) = \Phi_1(\widetilde{\phi_1}(\mathbf{p}'_m), \widetilde{\phi_2}(\mathbf{p}'_m), \mathbf{p}') : \Omega' \rightarrow I\!R$ and $\tilde{\Phi}_2(\mathbf{p}) = \Phi_2(\widetilde{\phi_1}(\mathbf{p}'_m), \widetilde{\phi_2}(\mathbf{p}'_m), \mathbf{p}') : \Omega' \rightarrow I\!R$. Because the output surrogates are (perforce) computationally inexpensive, the surrogate Pareto-optimal manifolds can be obtained to a sufficient resolution within a reasonable amount of time.

To determine the surrogate Pareto-optimal input manifold $\widetilde{\mathcal{L}^{\mathcal{A}}}$, the scalarization procedure described in Section 2.4.3 is used. With this approach, the multicriteria optimization based problem on the performance metrics $\tilde{\Phi}_1(\mathbf{p})$ and $\tilde{\Phi}_2(\mathbf{p})$ is reduced to a series of scalar problems parameterized by the scalarization parameter $w \in \mathcal{W} = [0, 1]$. A min-max formulation [22] for the scalarization has been used as it ensures that the full $\widetilde{\mathcal{L}^{\mathcal{A}}}$ is obtained.

The parameterized, scalar optimization problem has the form

$$\tilde{\xi}(w) = \arg \min_{\mathbf{p}' \in \Omega'} \max(w\tilde{\Phi}_1(\mathbf{p}), (1-w)\tilde{\Phi}_2(\mathbf{p})), \quad w \in \mathcal{W}_h, \tag{5.1}$$

and is solved for a sufficiently resolved, discrete set $\mathcal{W}_h = \{w_1, \ldots, w_{N^{PO}}\} \subset \mathcal{W}$. The curve $\tilde{\xi}(w)$, with duplicate points, and horizontal and vertical segments removed, is the surrogate Pareto-optimal input manifold $\widetilde{\mathcal{L}^{\mathcal{A}}}$. For each value of w, the solution to Equation 5.1 requires a global optimization. If the computational cost of $\tilde{\Phi}_1$ or $\tilde{\Phi}_2$ is even moderately high, the total computational effort required to obtain $\widetilde{\mathcal{L}^{\mathcal{A}}}$ would be prohibitive.

With the surrogate Pareto-optimal input manifold, $\widetilde{\mathcal{L}^{\mathcal{A}}}$, known, the surrogate Pareto-optimal output manifold $\widetilde{\partial\mathcal{A}}$ can be determined from the surrogate performance metric functions. The surrogate Pareto-optimal output manifold is

$$\widetilde{\partial\mathcal{A}} = (\tilde{\Phi}_1(\tilde{\xi}(\mathcal{W})), \tilde{\Phi}_2(\tilde{\xi}(\mathcal{W}))). \tag{5.2}$$

The result from the above process is similar to the curves shown in Figure 2-3 but, because the surrogates are only approximations of the truth outputs, there is no assurance that $\widetilde{\partial\mathcal{A}}$ and $\widetilde{\mathcal{L}^{\mathcal{A}}}$ will correspond to $\partial\mathcal{A}$ and $\mathcal{L}^{\mathcal{A}}$, respectively. The validation and error analysis steps of the surrogate Pareto framework presented in latter sections of this chapter address the impact that the surrogate errors have on the results.

The surrogate performance metrics for the eddy-promoter problem are obtained by substituting the surrogate output functions constructed in Section 5.1.1 in place of the exact output functions in Equations 2.98 and 2.97. The surrogate metrics,

$$\tilde{\Theta}(\mathbf{p}) = \Theta(\tilde{\theta}_0(\mathbf{p}_m), p) = \log_{10}\left[\frac{1}{RePr} + \tilde{\theta}_0(\mathbf{p}_m)\frac{1}{\eta_L}\right], \tag{5.3}$$

$$\tilde{\Psi}(\mathbf{p}) = \Psi(\widetilde{\psi_0}(\mathbf{p}_m), p) = \log_{10}\left[\widetilde{\psi_0}(\mathbf{p}_m)Re^3\eta_L^3\right], \tag{5.4}$$

are dependent on the full design vector $\mathbf{p} = (\mathbf{p}_m, \mathbf{p}_a) \in \Omega = [0,1]^{M=4}$. The range for the analytic input, $\eta_L \in [13.332, 106.656]$, is as stated in Section 2.6.1 and the value of η_L is prescribed by the design input $\mathbf{p}_a = p_4 \in [0,1]$ and is

$$\eta_L = \eta_{L\min} + p_4(\eta_{L\max} - \eta_{L\min}). \tag{5.5}$$

The next step of the process is to define the surrogate, performance-metric achievable set as

$$\tilde{\mathcal{A}} = \{s \in I\!R^2 \mid \exists \mathbf{p} \in \Omega \text{ s.t. } \tilde{\Theta}(\mathbf{p}) \leq s_1, \tilde{\Psi}(\mathbf{p}) \leq s_2\} \tag{5.6}$$

and find $\widetilde{\partial\mathcal{A}}$, the boundary of $\tilde{\mathcal{A}}$ not at infinity, with the min-max scalarization procedure in Equation 5.1. The surrogate performance metrics are used and the sequence of scalar

optimization problems that must be solved is

$$\tilde{\xi}(w) = \arg\min_{\mathbf{p}\in\Omega} \max(w\tilde{\Theta}(\mathbf{p}), (1-w)\tilde{\Psi}(\mathbf{p})), \quad w \in \mathcal{W}_h \tag{5.7}$$

where $\mathcal{W}_h \subset \mathcal{W} = [0,1]$. Because the surrogates are (by design) trivial to evaluate, solving for $\tilde{\xi}(\mathcal{W}_h)$ is a reasonable computational task. Once $\tilde{\xi}(\mathcal{W}_h)$ is obtained through the scalarization process, the surrogate PO output manifold is

$$\widetilde{\partial\mathcal{A}} = (\tilde{\Theta}(\tilde{\xi}(\mathcal{W}_h)), \tilde{\Psi}(\tilde{\xi}(\mathcal{W})h))). \tag{5.8}$$

Intervals of $[0,1]$ that are not PO are assumed removed and $\mathcal{W}$ is appropriately rescaled so that the full extent of $\mathcal{W} = [0,1]$ is PO.

To solve the optimization problem in Equation 5.7, a subspace searching, simplex optimization package, SUBPLEX, has been used [61]. The SUBPLEX method is based on the Nelder–Mead simplex algorithm [51], but reduces the searches to lower dimensional manifolds to more efficiently solve problems with high input dimensions. The primary reasons for the using the SUBPLEX package so solve the scalar optimization problems its demonstrated robustness, its availability at Netlib, and its ease of integration with the radial basis function surrogate routines. Because the SUBPLEX algorithm converges upon local optimizers, random restarts were used to ensure that a global optimal point was obtained for each value of w.

The surrogate PO manifolds have been obtained by solving Equation 5.7 over a sufficiently refined, discrete set $\mathcal{W}_h$. The surrogate PO output manifold is plotted as a solid line in Figure 5-1 and the corresponding PO input manifold is given in Figure 5-2 in four plots: in each plot, one component of the input vector $\mathbf{p}$ has been plotted versus the scalarization parameter w. An inner nested, bisection approach has been used to isolate points in $\mathcal{W}_h$ for which the PO input manifold is discontinuous. In total, Equation 5.7 has been solved for $N^{PO} = 932$ values of w to obtain sufficient data to reconstruct the PO manifolds accurately with linear interpolation between points in $\mathcal{W}_h$. In the presentation of the results, it is assumed that $\mathcal{W}_h \approx \mathcal{W}$ to sufficient accuracy to ignore the discrepancies. Even with the very inexpensive radial basis function surrogates, the solution to the scalarization problem at 200 w-points, with 300 random restarts for each value of w, requires approximately 3.6 CPU hours on a Hewlett-Packard C-160 workstation.

The surrogate PO output manifold, $\widetilde{\partial\mathcal{A}}$, for the eddy-promoter problem is plotted in Figure 5-1 as a solid line. The corresponding curve for a plane Poiseuille, heat exchanger (Appendix A) is labeled $\partial\mathcal{A}^{PP}$ and plotted in the figure as a dashed line. The only input available for the plane-channel heat exchanger is η_L^{PP} and the range required to achieve the same range of temperature performance metric as the eddy-promoter is $\eta_L^{PP} = [24.546, 507.849]$. The third line (plotted with a dash-dot) in the Figure is the PO

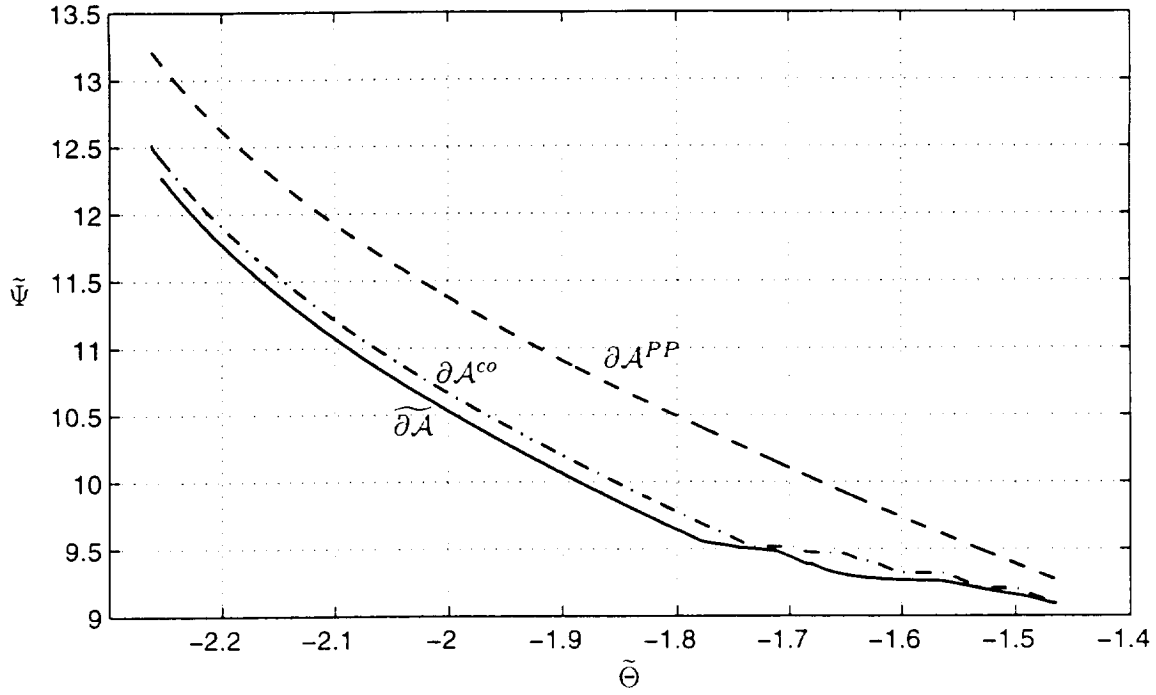

Figure 5-1: Surrogate-predicted, Pareto-optimal output manifolds for the eddy-promoter heat exchanger, $\widetilde{\partial\mathcal{A}}$, the plane Poiseuille heat exchanger, $\partial\mathcal{A}^{PP}$, and for the construction points, $\partial\mathcal{A}^{co}$.

output manifold for the $N^{co} = 256$ construction points, $\partial\mathcal{A}^{co}$. It is obtained by evaluating the performance metrics for each construction-point, truth-output value over the range $\eta_L \in [13.332, 106.656]$, forming the construction achievable set, and then finding the points that are PO.

The PO output manifolds plotted in Figure 5-1 suggest that a considerable performance improvement is realized for the eddy-promoter exchanger relative to the simple channel-flow exchanger. This is evident by considering the required pumping power, $\tilde{\Psi}$, for each exchanger for a given temperature performance value, $\tilde{\Theta}$. In all cases, to achieve a given heat transfer performance, the plane-channel exchanger requires a higher pumping power, and hence, is less efficient. The comparison between $\widetilde{\partial\mathcal{A}}$ and $\partial\mathcal{A}^{PP}$ shows that the surrogates at least predict better performance than obtained by simply selecting one of the construction point configurations. The uncertainty in the accuracy of the output surrogates, however, calls into question whether the eddy-promoter heat exchanger would actually perform better than the plane-channel exchanger, and the full set of construction point configurations, in practice. The surrogate validation and *a posteriori* error analysis steps will address this question.

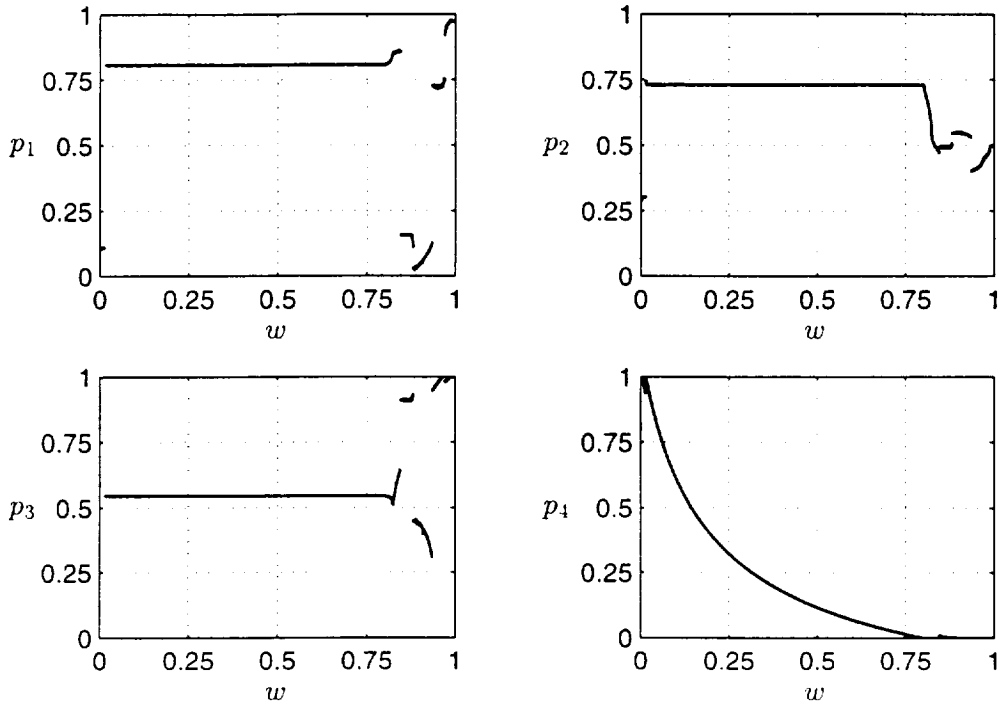

Figure 5-2: Surrogate-predicted. Pareto-optimal input manifold plotted for each input $\mathbf{p} \in \Omega$ versus the scalarization parameter w.

5.2 Surrogate Validation

The validation step of the surrogate-Pareto framework requires two steps. First, the surrogates are validated over the full input domain Ω as was done in the validation step of the baseline surrogate framework. The results of the global validation are used in the optimality analysis. Second, the surrogates are validated in the lower dimensional manifold of the design space "near" the PO input manifold. The results of the second validation step are used for predictability analyses of surrogate selected designs.

5.2.1 Global Validation

The global validation step for the surrogate Pareto framework is identical to the validation step of the baseline surrogate framework. The output surrogates $\widetilde{\phi_1}(\mathbf{p}'_m)$ and $\widetilde{\phi_2}(\mathbf{p}'_m)$ are validated over the model input domain Ω'_m. The details of the global validation step are given in Section 4.2 and are only briefly repeated here.

To begin, a sequence of N validation points, $\mathbf{P}_{m1}, \ldots, \mathbf{P}_{mN}$, is randomly drawn according to the probability density function $\rho(\mathbf{p}_m) : \Omega'_m \to I\!R$, $\mathbf{P}_{mi} \sim \rho(\mathbf{p}_m)$. The truth outputs

are evaluated at each validation input point and the validation sample set $\mathcal{X}^{va}$ is formed

$$\mathcal{X}^{va} = \{(\mathbf{P}_{m1}, \phi_1^T(\mathbf{P}_{m1}), \phi_2^T(\mathbf{P}_{m1})), \ldots (\mathbf{P}_{mN}, \phi_1^T(\mathbf{P}_{mN}), \phi_2^T(\mathbf{P}_{mN}))\} \tag{5.9}$$

The size of the validation sample set is exactly that given in Equation 4.5 and is

$$N = \left\lceil \frac{\ln \varepsilon_2}{\ln(1-\varepsilon_1)} \right\rceil \tag{5.10}$$

where $\lceil z \rceil$ is the smallest integer that is greater than z.

The global model prediction error U is computed by finding the maximum scaled difference between the surrogate and the truth over the full set of validation input points. The model prediction error is

$$U = \max_{\mathcal{X}^{va}} \left(\max \left(\frac{|\phi_1^T(\mathbf{P}_{mi}) - \widetilde{\phi_1}(\mathbf{P}_{mi})|}{\hat{g}_{o_1}(\mathbf{P}_{mi})}, \frac{|\phi_2^T(\mathbf{P}_{mi}) - \widetilde{\phi_2}(\mathbf{P}_{mi})|}{\hat{g}_{o_2}(\mathbf{P}_{mi})} \right) \right), \tag{5.11}$$

where $\hat{g}_{o_1}(\mathbf{p}'_m) : \Omega'_m \rightarrow \mathbb{R}_+$ and $\hat{g}_{o_2}(\mathbf{p}'_m) : \Omega'_m \rightarrow \mathbb{R}_+$ are the two strictly positive, scaling functions. Introducing the notion of the uncharacterized region Υ as defined in Equation 4.7, the following validation error statement can be made

$$Pr(\mu_\rho(\Upsilon) < \varepsilon_1) \geq 1 - \varepsilon_2. \tag{5.12}$$

The statement in 5.12 gives an assessment of the surrogate performance over the model input domain Ω'_m. It bounds, with a confidence of $1 - \varepsilon_2$, the maximum scaled difference between the surrogates and the truth over $1 - \varepsilon_1$ of the design space. The proof of the result given in Equation 5.12 given the validation sampling theorem of 5.10 is given in Appendix B.1.

The global validation step for the eddy-promoter problem follows exactly the validation step in Section 4.2. The validation sample size has been set to $N = 24$ and the validation input points have been selected according to a uniform probability density function $\rho(\mathbf{p}_m) = 1$. From the sampling theorem in Equation 5.10, $\varepsilon_1 = 0.0561$ and $\varepsilon_2 = 0.2500$. The scaling functions have been set to constant values $\hat{g}_\theta(\mathbf{p}_m) = 2.00$ and $\hat{g}_\psi(\mathbf{p}_m) = 1.00$. The validation sample set has been formed and the resulting model prediction error is $U = 0.0968$. This result is then used in Section 5.4.3 for the optimality analysis.

5.2.2 Surrogate PO Design Validation

The goal of the surrogate PO validation step is to provide information that will be used for predictability analyses of surrogate-predicted optimal designs. The strategy is similar to the global validation described in section 5.2.1, but instead of validating over the entire model design space Ω_m, the validation points are restricted to the vicinity of the surrogate PO

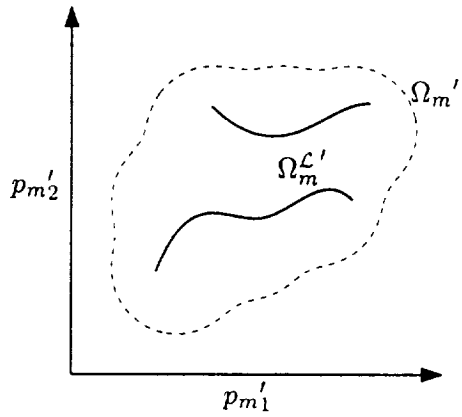

Figure 5-3: A schematic the Pareto-optimal input manifold (solid line), the PO design space $\Omega_m^{\mathcal{L}'}$ (shaded), and the model design space $\Omega_{m'}$ (dashed lines).

input manifold $\widetilde{\mathcal{L}^{\mathcal{A}}}$. As will be seen later, this restriction greatly improves the predictability of the *a posteriori* error analysis results. The improved predictability translates directly to error statements that are much more sharp, and hence, more meaningful and useful. As was demonstrated in section 2.4.2, the strategy outlined here achieves the improved predictability without losing design generality and flexibility.

For the general problem of validating the surrogate outputs, $\widetilde{\phi_1}(\mathbf{p}'_m) : \Omega'_m \rightarrow I\!R$ and $\widetilde{\phi_2}(\mathbf{p}'_m) : \Omega'_m \rightarrow I\!R$, in the vicinity of the PO input manifold $\widetilde{\mathcal{L}^{\mathcal{A}}}$, a PO design space $\Omega_m^{\mathcal{L}'} \subset \Omega'_m$ is introduced. The PO design space $\Omega_m^{\mathcal{L}'}$ is a finite-width (but narrow) "tube" in the model design space Ω'_m that contains the surrogate PO input manifold $\widetilde{\mathcal{L}^{\mathcal{A}}}$. A schematic of $\Omega_m^{\mathcal{L}'}$ is shown shaded in Figure 5-3 for a two-dimensional model design space Ω'_m. In the figure, the PO input manifold is plotted as a solid line and the boundaries of Ω'_m is shown as a dashed line.

An importance function, analogous to the importance function $\rho(\mathbf{p}_m)$ used in Section 5.2.1, is introduced $\rho_{\mathcal{L}}(\mathbf{p}'_m) : \Omega_m^{\mathcal{L}'} \rightarrow I\!R$. The PO importance function serves as a probability density function for the selection of validation points in $\Omega_m^{\mathcal{L}'}$. It is also used to introduce the notion of the ρ–measure of a set $\mathcal{R} \subset \Omega_m^{\mathcal{L}'}$

$$\mu_\rho(\mathcal{R}) = \int_{\mathcal{R}} \rho_{\mathcal{L}}(\mathbf{p}'_m)\, d\mathbf{p}'_m < 1, \tag{5.13}$$

which is the weighted volume of $\mathcal{R}$ relative to the PO design space $\Omega_m^{\mathcal{L}'}$; note $\mu_\rho(\Omega_m^{\mathcal{L}'}) = 1$.

Because of the complexity of the function that describes $\widetilde{\mathcal{L}^{\mathcal{A}}}$, it is often times not possible, or practical, to attempt to define a particular density function, $\rho_{\mathcal{L}}(\mathbf{p}'_m)$, explicitly. Instead, $\rho_{\mathcal{L}}(\mathbf{p}'_m)$ is defined implicitly through the procedure used to select random, validation input points $\mathbf{P} \sim \rho_{\mathcal{L}}(\mathbf{p}'_m)$. This approach is straightforward to describe and easy to implement in

practice. First, a random scalarization parameter is introduced

$$W' \sim f_{W'}(w') \tag{5.14}$$

distributed according to the probability density function $f_{W'}(w')$. The scalarization parameter specifies the coordinate of a point along the PO input and output manifolds. It can be, but is not restricted to, the scalarization parameter w used to obtain the PO manifolds in Section 5.1.2. Another coordinate such as the one of the performance metric values along the PO output manifold [36] may be used as well. Next, a uniformly distributed, unit vector V' and a radius $r_{\mathcal{V}'}$ are introduced. The density function is that function, $\rho_{\mathcal{L}}(\mathbf{p}'_m)$, that prescribes the distribution of the validation points

$$\mathbf{P}'_m \sim \rho_{\mathcal{L}}(\mathbf{p}'_m), \tag{5.15}$$

such that the random input points are given by

$$\mathbf{P}'_m = \widetilde{\xi}(W') + r_{\mathcal{V}'}V', \tag{5.16}$$

and the validation sample set is

$$\Omega_m^{\mathcal{L}'} = \{\mathbf{p}'_m \in \Omega_{m'} \mid \|\mathbf{p}'_m - \widetilde{\xi}(w')\| \leq r_{\mathcal{V}'},\ \forall w' \in \mathcal{W}'\}. \tag{5.17}$$

Although this implicit definition for $\rho_{\mathcal{L}}(\mathbf{p}_m)$ is difficult to express analytically, it is easy to sample in practice.

With the probability density function $\rho_{\mathcal{L}}(\mathbf{p}'_m)$ defined as above, N validation points are drawn randomly according to $\mathbf{P}'_i \sim \rho_{\mathcal{L}}(\mathbf{p}'_m), i = 1, \ldots N$. The validation sample $\mathcal{X}_{\mathcal{L}}^{va}$ set is formed

$$\mathcal{X}_{\mathcal{L}}^{va} = \{(\mathbf{P}_{m1}, \phi_1^T(\mathbf{P}_{m1}), \phi_2^T(\mathbf{P}_{m1})), \ldots (\mathbf{P}_{mN}, \phi_1^T(\mathbf{P}_{mN}), \phi_2^T(\mathbf{P}_{mN}))\},\ \ \mathbf{P}_{mi} \sim \rho(\mathbf{p}_m). \tag{5.18}$$

by appealing to the truth outputs at each of the $N_{\mathcal{L}}$ input validation points. The size of the sample set is given by the validation sampling theorem

$$N_{\mathcal{L}} = \left\lceil \frac{\ln \varepsilon_2}{\ln(1-\varepsilon_1)} \right\rceil \tag{5.19}$$

where $\lceil z \rceil$ is the smallest integer that is greater than z.

The model prediction error is then computed as

$$U_{\mathcal{L}} = \max_{\mathcal{X}^{va}} \left(\max \left(\frac{|\phi_1^T(\mathbf{P}_{mi}) - \widetilde{\phi_1}(\mathbf{P}_{mi})|}{\hat{g}_{o_1}(\mathbf{P}_{mi})}, \frac{|\phi_2^T(\mathbf{P}_{mi}) - \widetilde{\phi_2}(\mathbf{P}_{mi})|}{\hat{g}_{o_2}(\mathbf{P}_{mi})} \right) \right), \tag{5.20}$$

Where $\hat{g}_{\phi_1}(\mathbf{p}'_m) : \Omega_m^{\mathcal{L}'} \rightarrow I\!R_+$ and $\hat{g}_{\phi_2}(\mathbf{p}'_m) : \Omega_m^{\mathcal{L}'} \rightarrow I\!R_+$ are strictly positive scaling functions. The notion of the the uncharacterized region $\Upsilon_{\mathcal{L}}$ is defined as

$$\Upsilon_{\mathcal{L}} = \left\{ \mathbf{p}_m \in \Omega_m \mid \max \left(\frac{|\phi_1^T(\mathbf{p}'_m) - \widetilde{\phi_1}(\mathbf{p}'_m)|}{\hat{g}_{\phi_1}(\mathbf{p}'_m)}, \frac{|\phi_2^T(\mathbf{p}'_m) - \widetilde{\phi_2}(\mathbf{p}'_m)|}{\hat{g}_{\phi_2}(\mathbf{p}'_m)} \right) < U_{\mathcal{L}} \right\}. \qquad (5.21)$$

The model prediction error is the maximum, absolute difference between the truth and surrogate outputs over the set of randomly drawn, validation input points $\mathbf{P}_{mi}, i = 1, \ldots, N$. The uncharacterized region, $\Upsilon_{\mathcal{L}}$, is that subset of the PO model design space $\Omega_m^{\mathcal{L}'}$ for which the scaled surrogate error is greater than the model prediction error $U_{\mathcal{L}}$. The validation provides no information as to the location of the uncharacterized region nor does it provide any insight as to the magnitude of the errors in that region.

For the eddy-promoter problem, the scalarization parameter $w \in [0, 1]$ used to find the PO manifolds has been used (after being appropriately cleaned up to remove duplicate points and non-PO segments) to define the probability density function $\rho_{\mathcal{L}}(\mathbf{p}_m)$. The probability density for the randomly selected values of $W \sim f_W(w)$ is uniform, $f_W(w) = 1.0$. The radius r_W in Equation 5.16 has been set to $r_W = 0.01$. The validation sample size $N_{\mathcal{L}}$ has been set to $N_{\mathcal{L}} = 21$ and, according to the sampling theorem in Equation 5.19, $\varepsilon_1 = 0.0639$ and $\varepsilon_2 = 0.2500$. The scaling functions have been set to $\hat{g}_\theta = 1.0$ and $\hat{g}_\psi = 1.0$. The validation sample set has been formed through appeals to the simulation at each validation point and the model prediction error $U_{\mathcal{L}}$ has been computed and found to be $U_{\mathcal{L}} = 0.02506$.

It is immediately obvious that the model prediction error found in this section is significantly smaller than the global validation error computed in Section 5.2.1. The primary reason for the improvement is that the PO input manifold corresponds (through good fortune) to regions in the model design space Ω_m for which the surrogates do a very good job of approximating the truth. There is no reason to expect an improvement in general, and in fact, the opposite would more likely be true. The optimization process has the tendency to find the regions of the design space for which the surrogate approximations are the most poor. An example of this would be regions in which the surrogates have large undershoots that are not physically justified. The optimization process would seek these regions out and the surrogates would falsely indicate that they are PO. Therefore, the reduced error for the PO validation of this section is mostly attributable to good fortune and should not be expected in practice. The burden to construct accurate surrogates over the entire model design space Ω_m remains.

5.3 Surrogate Based Design

The goal of the design problem is to achieve lower values for the two performance metrics $\tilde{\Phi}_1 = \Phi_1(\widetilde{\phi_1}(\mathbf{p}'_m), \widetilde{\phi_2}(\mathbf{p}'_m), \mathbf{p}') : \Omega' \rightarrow I\!R$ and $\tilde{\Phi}_2 = \Phi_2(\widetilde{\phi_1}(\mathbf{p}'_m), \widetilde{\phi_2}(\mathbf{p}'_m), \mathbf{p}') : \Omega' \rightarrow I\!R$. In

most design problems of relevance however, the metrics represent competing goals and can not be simultaneously reduced to a single, optimal point. The purpose for pursuing the Pareto optimization approach has been to maintain the maximum amount of flexibility as to how to competing metrics will be prioritized during the design stage. The Pareto-optimal solutions were shown to satisfy a wide class of multicriteria optimization formulations in Section 2.4.2. Even with the design space reduced from Ω to $\widetilde{\mathcal{L}^{\mathcal{A}}}'$, the solution to most problems of interest are still available and any of the formulations given in Section 2.4.2 apply. Furthermore, the design problem, for the two performance metric case examined here, is trivial to analyze as the Pareto analysis reduces it to a single tradeoff curve.

For the general, two performance metric problem, a constrained optimization problem formulation is chosen. The optimal input points $\tilde{\mathbf{p}}^q$, $q \in \mathcal{Q} = (1, \ldots, Q)$, can be expressed as

$$\tilde{\mathbf{p}}^q = \arg \min_{\{\mathbf{p}' \in \Omega \mid \Phi_2(\widetilde{\phi_1}(\mathbf{p}'_m), \widetilde{\phi_2}(\mathbf{p}'_m), \mathbf{p}') \leq \overline{\Phi}_2^q\}} (\Phi_1(\widetilde{\phi_1}(\mathbf{p}'_m), \widetilde{\phi_2}(\mathbf{p}'_m), \mathbf{p}')). \quad \forall q \in \mathcal{Q}, \tag{5.22}$$

where $\overline{\Phi}_2^q$ is the upper bound for the constraint metric, $\Phi_2(\widetilde{\phi_1}(\mathbf{p}'_m), \widetilde{\phi_2}(\mathbf{p}'_m), \mathbf{p}')$. The optimizers, $\tilde{\mathbf{p}}^q$, are easily obtained from the PO output manifold and the impact of a changing constraint bound, $\overline{\Phi}_2^q$, is easily assessed.

For the eddy-promoter problem, the formulation that will be pursued will be to find the Q designs with the best pressure performance and that achieve a prescribed temperature performance, $\overline{\theta}^q$, $q \in \mathcal{Q} = (1, \ldots, Q)$. The constrained optimization problem can be expressed as

$$\tilde{\mathbf{p}}^q = \arg \min_{\{\mathbf{p} \in \Omega \mid \Theta(\widetilde{\theta_0}(\mathbf{p}_m), \mathbf{p}) \leq \overline{\theta}^q\}} \Psi(\widetilde{\psi_0}(\mathbf{p}_m), \mathbf{p}). \quad \forall q \in \mathcal{Q}. \tag{5.23}$$

where the different temperature performance bounds $\overline{\theta}^q$, $q \in \mathcal{Q}$ represent what, in practice might, be evolving design goals or a tradeoff analysis.

Three values ($Q = 3$) of the temperature performance bound in Equation 5.23 have been chosen. For the first, the design goal is the find minimum temperature performance design and, by inspection of the P0 output manifold in Figure 5-1, $\overline{\theta}^1 = -2.2626$. For the second design, the temperature performance constraint has been relaxed and is $\overline{\theta}^2 = -2.0239$. Finally, for the third design, $\overline{\theta}^3 = -1.7106$. The optimal design point has been found for each by finding the value of the scalarization parameter w that corresponds to each design and then appealing to the PO input manifolds. The surrogate-predicted, optimal input points are $\tilde{\mathbf{p}}^1 = (0.1008, 0.2875, 1.0000, 1.0000)$, $\tilde{\mathbf{p}}^2 = (0.8080, 0.7286, 0.5448, 0.1868)$, and $\tilde{\mathbf{p}}^3 = (0.8549, 0.4729, 0.6449, 0.0000)$ and the corresponding surrogate, performance metric pairs are $\tilde{\Pi}(\tilde{\mathbf{p}}^1) = (-2.2626, 12.5137)$, $\tilde{\Pi}(\tilde{\mathbf{p}}^2) = (-2.0239, 10.6495)$, and $\tilde{\Pi}(\tilde{\mathbf{p}}^3) = (-1.7106, 9.4801)$. The surrogate, performance metric pair at an input point $\mathbf{p}'$ is defined

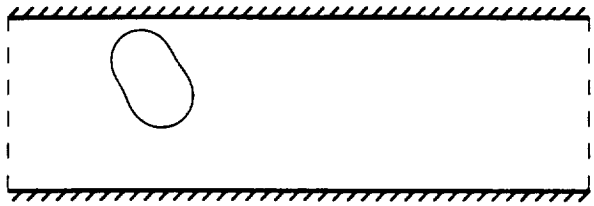

(a) Design 1; $\tilde{\mathbf{p}}^1 = (0.1008, 0.2875, 1.0000, 1.0000)$.

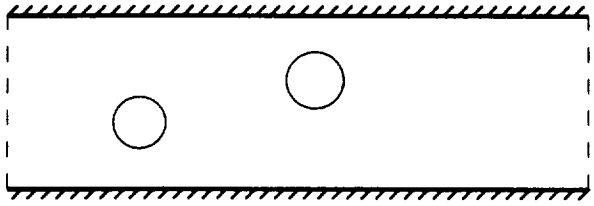

(b) Design 2; $\tilde{\mathbf{p}}^2 = (0.8080, 0.7286, 0.5448, 0.1868)$.

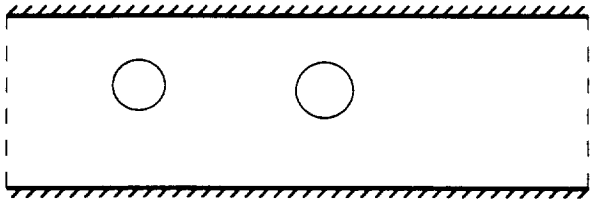

(c) Design 3; $\tilde{\mathbf{p}}^3 = (0.8549, 0.4729, 0.6449, 0.0000)$.

Figure 5-4: Eddy-promoter configurations of the surrogate-predicted, Pareto-optimal designs used in the design study.

as

$$\tilde{\Pi}(\mathbf{p}') = \left(\tilde{\Theta}(\mathbf{p}'), \tilde{\Psi}(\mathbf{p}')\right) = \left(\Theta(\tilde{\theta}_0(\mathbf{p}'_m), \mathbf{p}'), \Psi(\widetilde{\psi_0}(\mathbf{p}'_m), \mathbf{p}')\right). \tag{5.24}$$

The configuration for each of the surrogate-predicted optimal designs is plotted in Figure 5-4. From the results shown, it is evident that the topology-change capability does impact the results. Depending on the preferences given to each performance metric, the optimal geometry may consist of a single eddy-promoter inclusion as in Design 1, or two distinct bodies as is the case for Designs 2 and 3. However, the results presented here are not sufficient to assess whether the two-topology capability enables a significant improvement in the optimal results. One way to determine the extent of the two-topology impact is to pursue the Pareto analysis over the subset of the design space that corresponds to only single-body geometries. By overlaying the single-body, restricted PO output manifold on the PO output manifold plotted in Figure 5-1, the impact that the two-topology capability has could be quickly assessed.

5.4 *A Posteriori* Error Analysis

The *a posteriori* error analysis step of the surrogate–Pareto framework is identical to that of the baseline framework described in Section 4.4, but for the predictability analyses, the design space is restricted to narrow "tube" $\Omega^{\mathcal{L}}$ encompassing the surrogate PO input manifold $\widetilde{\mathcal{L}^{\mathcal{A}}}$. Two error estimate formulations for the predictability analysis are examined in this section: the proximal region analysis in which error bounds are valid for a finite sized region near the surrogate–predicted optimizers and the proximal candidate analysis in which the bounds are valid for a specific, randomly chosen design near the surrogate–predicted optimizer. The optimality analysis proceeds very similarly to that of the the baseline framework describe in Section 4.4.3 but is slightly modified to take into account the full Pareto family of optimal designs.

The three analyses, proximal region, proximal candidate, and optimality are examined in the following three sections. The format for each section is to present the theory for the general, two output, two performance metric problem and then to give the corresponding results for the two–body, eddy–promoter example.

5.4.1 Predictability — Proximal Region

To begin the predictability analysis, it is first assumed that a prediction region $\mathcal{P}^*_{\varepsilon_1} \subset \Omega^{\mathcal{L}'}$ has been defined that contains the surrogate–predicted optimizer $\tilde{\mathbf{p}}^*$. As was done for the baseline analysis, the surrogate–predicted optimal input design vector $\tilde{\mathbf{p}}^*$ has the form $\tilde{\mathbf{p}}^* = (\tilde{\mathbf{p}}^*_m, \tilde{\mathbf{p}}^*_a)$ where $\tilde{\mathbf{p}}^*_m$ is the vector of modeled inputs and $\tilde{\mathbf{p}}^*_a$ is the vector of inputs for which the performance metric response is known analytically. The prediction region can similarly be expressed as $\mathcal{P}^*_{\varepsilon_1} = \mathcal{P}^*_{m\varepsilon_1} \times \tilde{\mathbf{p}}^*_a$. The ρ–measure of the prediction region relative to the PO design space $\Omega^{\mathcal{L}'}_m$ is computed as

$$\mu_{\rho_{\mathcal{L}}}(\mathcal{P}^*_{m\varepsilon_1}) = \int_{\mathcal{P}^*_{m\varepsilon_1}} \rho_{\mathcal{L}}(\mathbf{p}_m) d\mathbf{p}_m = \varepsilon_1, \tag{5.25}$$

and, for the analysis to be valid, must be at least as large as ε_1. An example of how to precisely define and measure the prediction neighborhood is given for the eddy–promoter problem later in this section.

With the prediction neighborhood defined, probabilistic bounds on the truth output values for inputs points that are in a finite–sized, subset of $\mathcal{P}^*_{\varepsilon_1}$ are developed. The resulting predictability statement for the truth outputs follows: With probability of at least $1 - \varepsilon_2$, there will exist points $\mathbf{p}' \in \Gamma \subset \mathcal{P}^*_{\varepsilon_1}$ such that

$$l_{o_1} \leq \phi_1^T(\mathbf{p}'_m) \leq u_{o_1}, \tag{5.26}$$

$$l_{o_2} \leq \phi_2^T(\mathbf{p}'_m) \leq u_{o_2}, \tag{5.27}$$

where the truth-output bounds are based on the validation results and are

$$l_{\phi_1} = \min_{\{\mathbf{p}' \in \mathcal{P}^{-}_{m\varepsilon_1}\}} [\widetilde{\phi_1}(\mathbf{p}'_m) - U_{\mathcal{L}} \hat{g}_{\phi_1}(\mathbf{p}'_m)], \tag{5.28}$$

$$u_{\phi_1} = \max_{\{\mathbf{p}' \in \mathcal{P}^{-}_{m\varepsilon_1}\}} [\widetilde{\phi_1}(\mathbf{p}'_m) + U_{\mathcal{L}} \hat{g}_{\phi_1}(\mathbf{p}'_m)], \tag{5.29}$$

$$l_{\phi_2} = \min_{\{\mathbf{p}' \in \mathcal{P}^{-}_{m\varepsilon_1}\}} [\widetilde{\phi_2}(\mathbf{p}'_m) - U_{\mathcal{L}} \hat{g}_{\phi_2}(\mathbf{p}'_m)], \tag{5.30}$$

$$u_{\phi_2} = \max_{\{\mathbf{p}' \in \mathcal{P}^{-}_{m\varepsilon_1}\}} [\widetilde{\phi_2}(\mathbf{p}'_m) + U_{\mathcal{L}} \hat{g}_{\phi_2}(\mathbf{p}'_m)], \tag{5.31}$$

and $U_{\mathcal{L}}$ is the PO model prediction error computed from Equation 5.20. The bounds given in Equations 5.28—5.31 can be computed entirely from the surrogate values, require no additional truth calculations, and, therefore, are very inexpensive to evaluate.

Equations 5.26—5.31 effectively bound (within a confidence of $1 - \varepsilon_2$) the surrogate output error for points "near" the surrogate predicted optimizer in terms of the outputs. For the bounds to be useful to the designer however, they need to apply to the truth performance metrics, $\Phi_1(\phi_1^T(\mathbf{p}'_m), \phi_2^T(\mathbf{p}'_m), \mathbf{p}')$ and $\Phi_2(\phi_1^T(\mathbf{p}'_m), \phi_2^T(\mathbf{p}'_m), \mathbf{p}')$ The predictability statement on the performance metrics reads: With probability of at least $1 - \varepsilon_2$, there will exist a region of non-zero measure $\Gamma' \subset \mathcal{P}^{*}_{\varepsilon_1}$ in the neighborhood of $\mathbf{p}^*$ such that for all points $\mathbf{p}' \in \Gamma'$

$$L_{\Phi_1} \leq \Phi_1(\phi_1^T(\mathbf{p}'_m), \phi_2^T(\mathbf{p}'_m), \mathbf{p}') \leq U_{\Phi_1}, \tag{5.32}$$

$$L_{\Phi_2} \leq \Phi_2(\phi_1^T(\mathbf{p}'_m), \phi_2^T(\mathbf{p}'_m), \mathbf{p}') \leq U_{\Phi_2}, \tag{5.33}$$

where the performance metric bounds are

$$L_{\Phi_1} = \min_{\{\mathbf{p}' \in \mathcal{P}^{*}_{\varepsilon_1}, z_1 \in \mathcal{Z}_1, z_2 \in \mathcal{Z}_2\}} \Phi_1(z_1, z_2, \mathbf{p}'), \tag{5.34}$$

$$U_{\Phi_1} = \max_{\{\mathbf{p}' \in \mathcal{P}^{*}_{\varepsilon_1}, z_1 \in \mathcal{Z}_1, z_2 \in \mathcal{Z}_2\}} \Phi_1(z_1, z_2, \mathbf{p}'), \tag{5.35}$$

$$L_{\Phi_2} = \min_{\{\mathbf{p}' \in \mathcal{P}^{*}_{\varepsilon_1}, z_1 \in \mathcal{Z}_1, z_2 \in \mathcal{Z}_2\}} \Phi_2(z_1, z_2, \mathbf{p}'), \tag{5.36}$$

$$U_{\Phi_2} = \max_{\{\mathbf{p}' \in \mathcal{P}^{*}_{\varepsilon_1}, z_1 \in \mathcal{Z}_1, z_2 \in \mathcal{Z}_2\}} \Phi_2(z_1, z_2, \mathbf{p}'), \tag{5.37}$$

and the output ranges, $\mathcal{Z}_1$ and $\mathcal{Z}_2$, are determined by Equations 5.28—5.31 and are

$$\mathcal{Z}_1 = \{z \mid l_{\phi_1} \leq z \leq u_{\phi_1}\}, \tag{5.38}$$

$$\mathcal{Z}_2 = \{z \mid l_{\phi_2} \leq z \leq u_{\phi_2}\}. \tag{5.39}$$

As was the case for the output bounds, the truth performance metric bounds given in

Equations 5.34—5.37 require no additional truth calculations, and therefore, are inexpensive to evaluate.

To define the prediction neighborhood $\mathcal{P}^*_{\varepsilon_1}$ precisely, the distance metric $\Delta(\mathbf{p}_{m1}, \mathbf{p}_{m2})$ used in Section 4.4.1 and given in Equation 4.31 has been used. With this definition for the metric, the prediction neighborhood around the surrogate predicted optimal point $\tilde{\mathbf{p}}^q_m$ is then defined as that region $\mathcal{R}$, of size ε_1, that minimizes

$$r_\Delta = \max_{\mathbf{p}_m \in \mathcal{R}} \Delta(\mathbf{p}_m, \tilde{\mathbf{p}}^q_m). \tag{5.40}$$

For the eddy promoter problem, the distance metric function has been defined based on the outputs and is selected from the general form

$$\Delta(\mathbf{p}_{m1}, \mathbf{p}_{m2}) = \max\left(\frac{|\widetilde{\theta_0}(\mathbf{p}_{m1}) - \widetilde{\theta_0}(\mathbf{p}_{m2})|}{h_\theta}, \frac{|\widetilde{\psi_0}(\mathbf{p}_{m1}) - \widetilde{\psi_0}(\mathbf{p}_{m2})|}{h_\psi}\right). \tag{5.41}$$

where h_θ and h_ψ are positive scalars. The pressure output scalar h_ψ in Equation 5.41 has been set sufficiently high so that the the neighborhood with minimum $\tilde{\theta}_0$ sensitivity results. The distance metric in this case reduces to

$$\Delta(\mathbf{p}_{m1}, \mathbf{p}_{m2}) = |\widetilde{\theta_0}(\mathbf{p}_{m1}) - \widetilde{\theta_0}(\mathbf{p}_{m2})|. \tag{5.42}$$

The output bounds in Equations 5.28—5.31 have been evaluated for each of the three designs found in Section 5.3. The output bounds have then been used to evaluate the bound quantities given in Equations 5.34—5.37. The resulting predictability statements for the truth values of the performance metrics are given below. For Design 1, the statement reads: With probability of at least 75%, there will exist points in $\Gamma^1 \subset \mathcal{P}^1_{\varepsilon_1}$ such that for $\mathbf{p}' \in \Gamma^1$

$$12.1440 \leq \Psi(\psi_0^T(\mathbf{p}'_m), \mathbf{p}') \leq 12.5841 \tag{5.43}$$

$$-2.2816 \leq \Theta(\theta_0^T(\mathbf{p}'_m), \mathbf{p}') \leq -2.2359. \tag{5.44}$$

For Design 2, the statement reads: With probability of at least 75%, there will exist points in $\Gamma^2 \subset \mathcal{P}^2_{\varepsilon_1}$ such that for $\mathbf{p}' \in \Gamma^2$

$$10.5211 \leq \Psi(\psi_0^T(\mathbf{p}'_m), \mathbf{p}') \leq 10.7510, \tag{5.45}$$

$$-2.0631 \leq \Theta(\theta_0^T(\mathbf{p}'_m), \mathbf{p}') \leq -1.9880. \tag{5.46}$$

Finally, for Design 3, the statement reads: With probability of at least 75%, there will exist points in $\Gamma^3 \subset \mathcal{P}^3_{\varepsilon_1}$ such that for $\mathbf{p}' \in \Gamma^3$

$$9.1360 \leq \Psi(\psi_0^T(\mathbf{p}'_m), \mathbf{p}') \leq 9.6281, \tag{5.47}$$

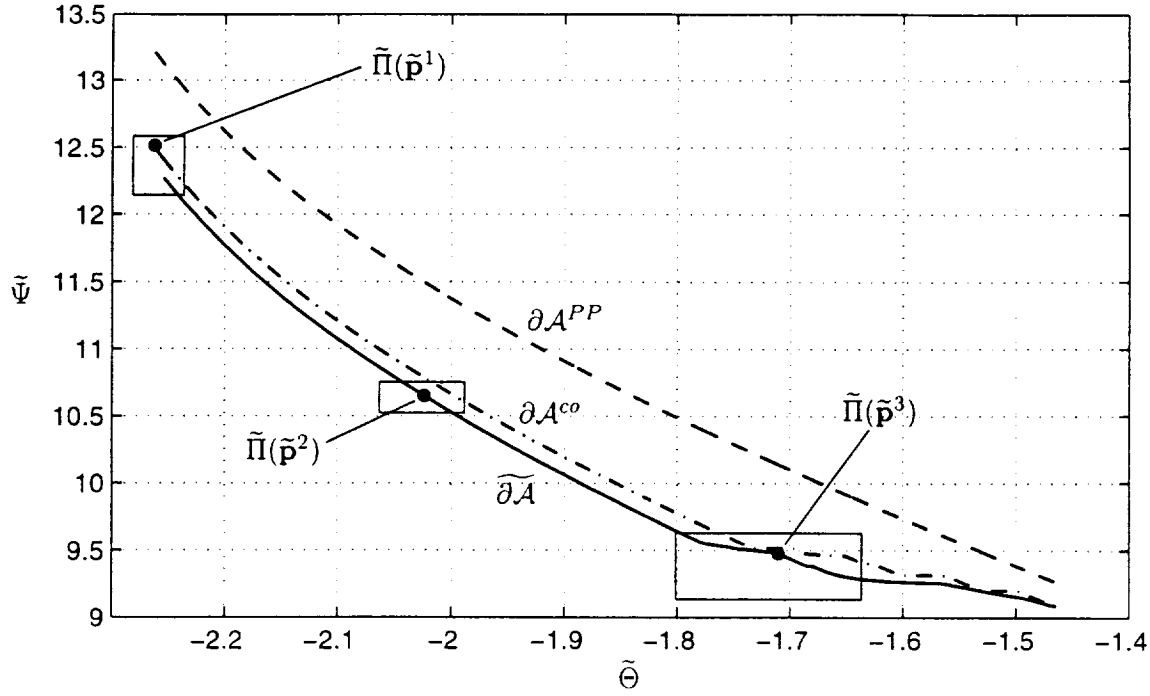

Figure 5-5: Output plane plot of the three design point, surrogate–performance pairs, $\tilde{\Pi}(\tilde{\mathbf{p}}^i)$, $i = 1, 2, 3$ (•), and the proximal region predictability boxes for each design.

$$-1.8010 \leq \Theta(\theta_0^T(\mathbf{p}'_m), \mathbf{p}') \leq -1.6361. \tag{5.48}$$

The predictability statements are valid for each design for the corresponding prediction neighborhood.

The results given above have been plotted in the output plane in Figure 5-5. In the figure, the surrogate performance metric values for each design are plotted as solid dots, the bounds on the truth performance metrics are plotted as boxes, and the surrogate PO output manifolds for the eddy–promoter and the plane–channel heat exchanger are shown as solid and dashed lines , respectively. This figure can be compared to the baseline surrogate framework results given in Figure 4-3 in which the boxes were significantly larger. The bounds in Figure 5-5 are quite sharp with a clear discrimination between each of three designs in terms of both the pressure and temperature performance metrics. Additionally, the surrogate predictability boxes indicate the the surrogates are accurate enough to clearly show (with 75% confidence) that the eddy–promoter heat exchanger performance is better than the plane channel performance for all three designs.

Several factors contribute to the improvement in the predictability boxes plotted in Figure 5-5 relative to the baseline framework results plotted in Figure 4-3. First, the model prediction error was significantly lower for the Pareto validation over $\Omega_m^{\mathcal{C}}$ than for the global validation over Ω_m. This is mostly good fortune, as PO input manifold happens to lie in regions of Ω_m for which the output surrogates are accurate. The second reason is

due to the increased predictability that can be contributed to reducing the dimension of the validation space from three (the three model inputs of the model design space Ω_m) to just a single input (the scalarization parameter w). A third and final contributor to the sharp predictability boxes is the input $\mathbf{p}_a = \eta_L$ for which the performance metric responses are known analytically. This effect was present in the baseline results as well, but was overwhelmed by the very poor model validation error computed in Section 4.2.

5.4.2 Surrogate Predictability — Proximal Candidate

The predictability can be evaluated in terms of a randomly selected design point near the surrogate-predicted optimizer in much the same manner as it is for proximal candidate analysis of the baseline surrogate framework. The only difference is that the prediction neighborhood for the Pareto framework analysis is a subset of one-dimensional PO design space $\Omega^{\mathcal{L}}$ instead of the full design space Ω. The remainder of the analysis is identical to that presented in Section 4.4.2.

Following the presentation of Section 4.4.2, a prediction region $\mathcal{P}_\sigma^* \subset \Omega^{\mathcal{L}'}$ of ρ-measure σ and that contains the surrogate-predicted optimal point $\tilde{\mathbf{p}}^*$ is defined in a manner similar to that presented for the Proximal Region analysis of Section 5.4.1. A sample candidate design $\widehat{\mathbf{P}}_m^*$ is selected randomly according to $\widehat{\mathbf{P}}_m^* \sim \rho_{\mathcal{P}_\mathcal{L}}(\mathbf{p}_m)$. The density function $\rho_{\mathcal{P}_\mathcal{L}}(\mathbf{p}_m)$ is defined as

$$\rho_{\mathcal{P}_\mathcal{L}}(\mathbf{p}_m) = \frac{1}{\sigma}\rho(\mathbf{p}_m)\Big|_{\mathcal{P}}, \quad \forall \mathbf{p}_m \in \mathcal{P}_{m\sigma}^*. \tag{5.49}$$

where $\mathcal{P}_{m\sigma}^* \subset \Omega_m^{\mathcal{L}'}$ is the sub-manifold of $\mathcal{P}_\sigma^*$ that corresponds to the model design space and the full neighborhood is the tensor product $\mathcal{P}_\sigma^* = \{\mathcal{P}_{m\sigma}^* \times \mathbf{p}_a^*\}$. The full candidate design vector $\widehat{\mathbf{P}}^*$ is given as $\widehat{\mathbf{P}}^* = (\widehat{\mathbf{P}}_m^*, \mathbf{p}_a^*)$ where $\mathbf{p}_a^*$ is the vector of analytic inputs of the surrogate predicted optimizer $\tilde{\mathbf{p}}^* = (\tilde{\mathbf{p}}_m^*, \mathbf{p}_a^*)$.

A second small parameter, ε_c, is introduced and is related to the ρ-measure of $\mathcal{P}_{m\sigma}^*$, σ, by

$$\varepsilon_c = \frac{1}{\sigma(N_\mathcal{L}+1)}(1-(1-\sigma)^{N_\mathcal{L}+1}), \tag{5.50}$$

where $0 < \varepsilon_c, \sigma < 1$, and $N_\mathcal{L}$ is the validation sample size given in Equation 5.19.

Now, given the two inputs to the analysis ε_c and σ, and the model prediction error $U_\mathcal{L}$, the following statement can be made: With probability of at least $1-\varepsilon_c$, the truth output values for the input vector $\widehat{\mathbf{P}}_m^*$ are bounded by

$$l_{o_1}^c \le \phi_1^T(\widehat{\mathbf{P}}_m^*) \le u_{o_1}^c, \tag{5.51}$$

$$l_{o_2}^c \le \phi_2^T(\widehat{\mathbf{P}}_m^*) \le u_{o_2}^c, \tag{5.52}$$

where the bound values are

$$l^c_{\phi_1} = \widetilde{\phi_1}(\widehat{\mathbf{P}}^*_m) - U_{\mathcal{L}}\hat{g}_{\phi_1}(\widehat{\mathbf{P}}^*_m), \tag{5.53}$$

$$u^c_{\phi_1} = \widetilde{\phi_1}(\widehat{\mathbf{P}}^*_m) + U_{\mathcal{L}}\hat{g}_{\phi_1}(\widehat{\mathbf{P}}^*_m), \tag{5.54}$$

$$l^c_{\phi_2} = \widetilde{\phi_2}(\widehat{\mathbf{P}}^*_m) - U_{\mathcal{L}}\hat{g}_{\phi_2}(\widehat{\mathbf{P}}^*_m), \tag{5.55}$$

$$u^c_{\phi_2} = \widetilde{\phi_2}(\widehat{\mathbf{P}}^*_m) + U_{\mathcal{L}}\hat{g}_{\phi_2}(\widehat{\mathbf{P}}^*_m). \tag{5.56}$$

Equations 5.51—5.56 bound the truth value of the outputs for the candidate design point $\widehat{\mathbf{P}}^*_m$.

The analysis can be extended to the performance metrics the same way as it has been in the previous sections. The following predictability statement results: With probability of at least $1 - \varepsilon_c$, the truth performance metric values at input point $\widehat{\mathbf{P}}^*_m$ are bounded by

$$L^c_{\Phi_1} \leq \Phi_1(\phi_1^T(\widehat{\mathbf{P}}^*_m), \phi_2^T(\widehat{\mathbf{P}}^*_m), \widehat{\mathbf{P}}^*) \leq U^c_{\Phi_1}. \tag{5.57}$$

$$L^c_{\Phi_2} \leq \Phi_2(\phi_1^T(\widehat{\mathbf{P}}^*_m), \phi_2^T(\widehat{\mathbf{P}}^*_m), \widehat{\mathbf{P}}^*) \leq U^c_{\Phi_2}. \tag{5.58}$$

where the performance metric bounds are

$$L^c_{\Phi_1} = \min_{\{z_1 \in \mathcal{Z}^c_1, z_2 \in \mathcal{Z}^c_2\}} \Phi_1(z_1, z_2, \widehat{\mathbf{P}}^*). \tag{5.59}$$

$$U^c_{\Phi_1} = \max_{\{z_1 \in \mathcal{Z}^c_1, z_2 \in \mathcal{Z}^c_2\}} \Phi_1(z_1, z_2, \widehat{\mathbf{P}}^*), \tag{5.60}$$

$$L^c_{\Phi_2} = \min_{\{z_1 \in \mathcal{Z}^c_1, z_2 \in \mathcal{Z}^c_2\}} \Phi_2(z_1, z_2, \widehat{\mathbf{P}}^*). \tag{5.61}$$

$$U^c_{\Phi_2} = \max_{\{z_1 \in \mathcal{Z}^c_1, z_2 \in \mathcal{Z}^c_2\}} \Phi_2(z_1, z_2, \widehat{\mathbf{P}}^*). \tag{5.62}$$

and the ranges for the outputs, $\mathcal{Z}^c_1$ and $\mathcal{Z}^c_2$, at the candidate design point are obtained from Equations 5.53—5.56 and are

$$\mathcal{Z}^c_1 = \{z \mid l^c_{\phi_1} \leq z \leq u^c_{\phi_1}\}, \tag{5.63}$$

$$\mathcal{Z}^c_2 = \{z \mid l^c_{\phi_2} \leq z \leq u^c_{\phi_2}\}. \tag{5.64}$$

The proximal candidate analysis has been carried out for each of the three eddy-promoter, heat exchanger design points selected in Section 5.3. Given the $N_{\mathcal{L}} = 21$ validation points used for the PO design validation, the values of $\varepsilon_c = 0.2500$ and $\sigma = 0.1795$ are obtained from Equation 5.50. The distance metric used to define the neighborhood $\mathcal{P}^*_\sigma$ is identical to the one used for the proximal region analysis Section 5.4.1 and is given in Equation 5.42. Monte-Carlo sampling has been used to obtain the three candidate designs.

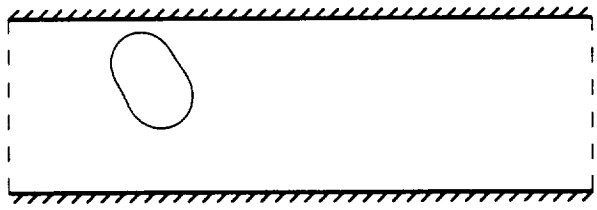

(a) Candidate Design 1: $\widehat{\mathbf{P}}^1 = (0.1004, 0.3018, 0.9950, 1.0000)$.

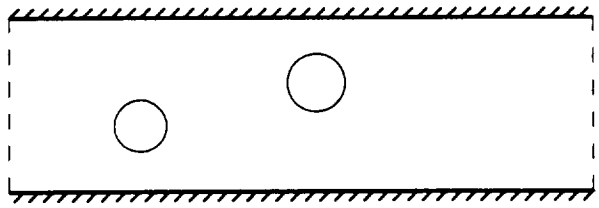

(b) Candidate Design 2: $\widehat{\mathbf{P}}^2 = (0.8062, 0.7290, 0.5434, 0.1868)$.

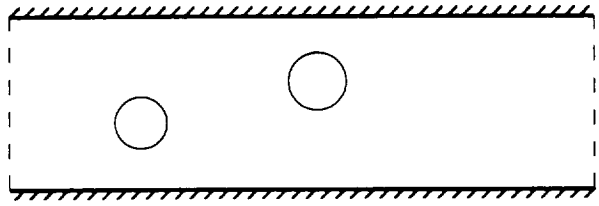

(c) Candidate Design 3: $\widehat{\mathbf{P}}^3 = (0.8083, 0.7211, 0.5527, 0.000)$.

Figure 5-6: Eddy-promoter candidate configurations for the three surrogate-predicted, Pareto-optimal designs used in the design study.

A single periodicity cell for each of the three candidate designs is given in Figure 5-6. The input values for each of the candidate designs are $\widehat{\mathbf{P}}^1 = (0.1004, 0.3018, 0.9950, 1.0000)$, $\widehat{\mathbf{P}}^2 = (0.8062, 0.7290, 0.5434, 0.1868)$, and $\widehat{\mathbf{P}}^3 = (0.8083, 0.7211, 0.5527, 0.000)$.

The candidate design geometries plotted in Figure 5-6 can be compared to the surrogate-predicted optimal design geometries plotted in Figure 5-4. The candidate and surrogate-predicted geometries for Design 1 are very similar, but do differ slightly. For Design 2, the candidate and surrogate-predicted geometries are nearly identical. There is a significant difference between the candidate and surrogate-predicted geometries for Design 3: in fact, the candidate geometry for Design 3 is almost identical to Design 2. The reason for the apparent preference toward geometries similar to the surrogate-predicted Design 2 is a consequence of using the scalarization parameter to randomize the design space in the $\rho_{\mathcal{L}}(\mathbf{p}'_m)$ definition. Because the model inputs $\mathbf{p}_m$ remain nearly constant over a large portion of the range of w (see Figure 5-3), the effective $\rho_{\mathcal{L}}(\mathbf{p}'_m)$ corresponding to this range is very large. The Design 2 input point falls into the single geometry range of w and Design 3 is near the. Because $\rho_{\mathcal{L}}(\mathbf{p}'_m)$ is very large over this range, there is a very high probability that randomly selecting points near Designs 2 and 3 will result in the candidate designs that we

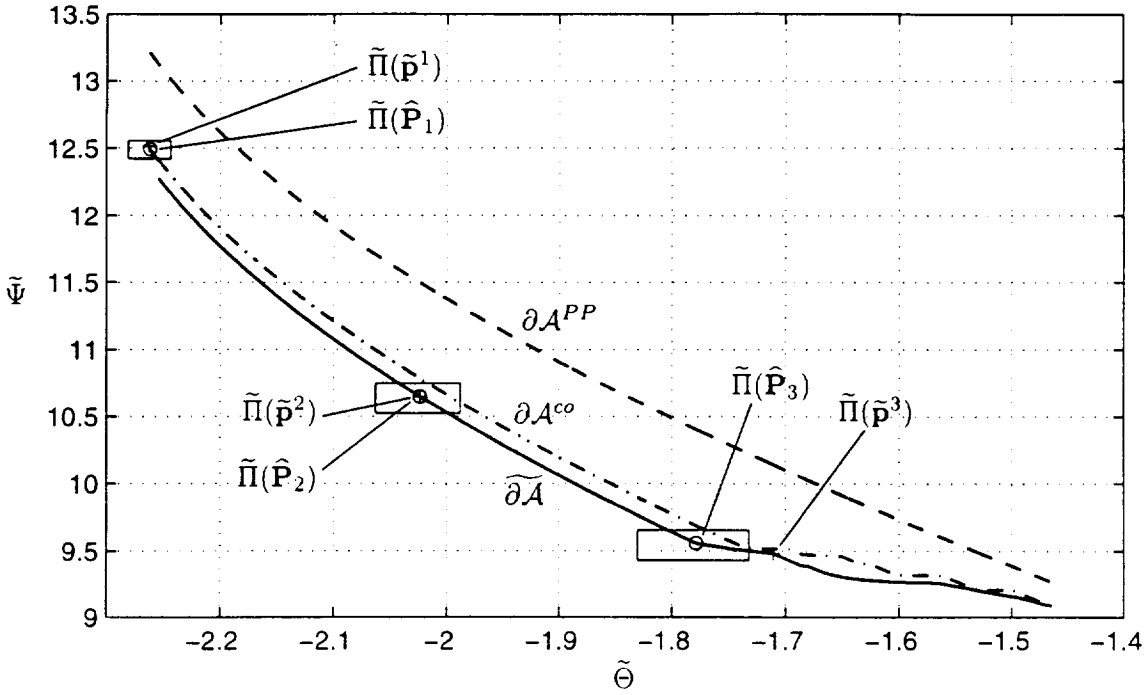

Figure 5-7: Output plane plot of the surrogate response for the three candidate design points (∘), the surrogate-predicted optimizers (+), and the proximal candidate predictability boxes for each design.

obtained. Design 1 is also very close to the Design 2 geometry in Figure 5-3 but the less likely outcome of selecting a candidate similar to Design 1 occurred.

The results of the analysis are given in terms of the predictability statements. For Design 1, the candidate predictability analysis reads: With probability of at least 75%, the truth performance bounds for the randomly drawn candidate design point $\hat{\mathbf{P}}^1$ are

$$-2.2805 \leq \Theta(\theta_0^T(\hat{\mathbf{P}}_m^1), \hat{\mathbf{P}}^1) \leq -2.2433. \tag{5.65}$$

$$12.4214 \leq \Psi(\psi_0^T(\hat{\mathbf{P}}^1), \hat{\mathbf{P}}_m^1) \leq 12.5549. \tag{5.66}$$

The surrogate-predicted performance metric values for $\hat{\mathbf{P}}^1$ are $\tilde{\Theta}_c^1 = \Theta(\widetilde{\theta_0}(\hat{\mathbf{P}}_m^2), \hat{\mathbf{P}}^2) = -2.2616$ and $\tilde{\Psi}_c^1 = \Psi(\widetilde{\psi_0}(\hat{\mathbf{P}}^2), \hat{\mathbf{P}}_m^2) = 12.4933$. The bounds are plotted as predictability boxes in Figure 5-7, along with the surrogate performance pair outputs at the optimal design point $\tilde{\Pi}(\tilde{\mathbf{p}}^1) = (\tilde{\Theta}^1, \tilde{\Psi}^1)$ (plus sign) and for the candidate design $\tilde{\Pi}(\hat{\mathbf{P}}_1) = (\tilde{\Theta}_c^1, \tilde{\Psi}_c^1)$ (open dot).

For Design 2, the candidate predictability analysis reads: With probability of at least 75%, the truth performance bounds for the randomly drawn candidate design point $\hat{\mathbf{P}}^2$ are

$$-2.0630 \leq \Theta(\theta_0^T(\hat{\mathbf{P}}_m^2), \hat{\mathbf{P}}^2) \leq -1.9881, \tag{5.67}$$

$$10.5215 \leq \Psi(\psi_0^T(\hat{\mathbf{P}}^2), \hat{\mathbf{P}}_m^2) \leq 10.7484. \tag{5.68}$$

The surrogate-predicted performance metric values for $\hat{\mathbf{P}}^2$ are $\tilde{\Theta}_c^2 = \Theta(\tilde{\theta_0}(\hat{\mathbf{P}}_m^2), \hat{\mathbf{P}}^2) = -2.0240$ and $\tilde{\Psi}_c^2 = \Psi(\widetilde{\psi_0}(\hat{\mathbf{P}}^2), \hat{\mathbf{P}}_m^2) = 10.6496$. These results are plotted in Figure 5-7 as well.

Finally, for Design 3, the candidate predictability analysis result reads: With probability of at least 75%, the truth performance bounds for the randomly drawn candidate design point $\hat{\mathbf{P}}^3$ are

$$-1.8307 \leq \Theta(\theta_0^T(\hat{\mathbf{P}}_m^3), \hat{\mathbf{P}}^3) \leq -1.7322, \tag{5.69}$$

$$9.4284 \leq \Psi(\psi_0^T(\hat{\mathbf{P}}^3), \hat{\mathbf{P}}_m^3) \leq 9.6568. \tag{5.70}$$

The surrogate-predicted performance metric values for $\hat{\mathbf{P}}^3$ are $\tilde{\Theta}_c^3 = \Theta(\tilde{\theta_0}(\hat{\mathbf{P}}_m^3), \hat{\mathbf{P}}^3) = -1.7786$ and $\tilde{\Psi}_c^3 = \Psi(\widetilde{\psi_0}(\hat{\mathbf{P}}^3), \hat{\mathbf{P}}_m^3) = 9.5574$. The results are plotted in Figure 5-7.

5.4.3 Design Optimality

The global validation results provide the information necessary to estimate the amount of effort required to improve a design beyond a computable amount determined by the the global model prediction error. Based on the global model prediction error, U, the maximum absolute output error over a $1 - \varepsilon_1$ fraction of the design space is known with a confidence level $1 - \varepsilon_2$. For the error at a point to be worse than the model prediction error, the point in question would have to lie in the uncharacterized region Υ. This notion is used in the development of the optimality estimates below.

To find the effort required to improve upon a design, an expanded achievable set $\mathcal{A}^\circ$ is first introduced

$$\mathcal{A}^\circ = \{s \in I\!R^2 \mid \exists \mathbf{p}' \in \Omega', z_1 \in \mathcal{Z}_{\Phi_1}, z_2 \in \mathcal{Z}_{\Phi_2} \text{ s.t. } \Phi_1(z_1, z_2, \mathbf{p}') \leq s_1, \Phi_2(z_1, z_2, \mathbf{p}') \leq s_2\}. \tag{5.71}$$

where

$$\mathcal{Z}_{\Phi_1} = \{z \in I\!R \mid l_{\phi_1}^\Omega \leq z \leq u_{\phi_1}^\Omega\} \tag{5.72}$$

$$\mathcal{Z}_{\Phi_2} = \{z \in I\!R \mid l_{\phi_2}^\Omega \leq z \leq u_{\phi_2}^\Omega\} \tag{5.73}$$

and

$$l_{\phi_1}^\Omega = \min_{\{\mathbf{p}' \in \Omega'\}} \widetilde{\phi_1}(\mathbf{p}'_m) - U\hat{g}_{\phi_1}(\mathbf{p}'). \tag{5.74}$$

$$u_{\phi_1}^\Omega = \max_{\{\mathbf{p}' \in \Omega'\}} \widetilde{\phi_1}(\mathbf{p}'_m) + U\hat{g}_{\phi_1}(\mathbf{p}'), \tag{5.75}$$

$$l_{\phi_2}^\Omega = \min_{\{\mathbf{p}' \in \Omega'\}} \widetilde{\phi_2}(\mathbf{p}'_m) - U\hat{g}_{\phi_2}(\mathbf{p}'), \tag{5.76}$$

$$u_{\phi_2}^\Omega = \max_{\{\mathbf{p}' \in \Omega'\}} \widetilde{\phi_2}(\mathbf{p}'_m) + U\hat{g}_{\phi_2}(\mathbf{p}'). \tag{5.77}$$

The boundary of $\mathcal{A}^\circ$ is denoted $\partial\mathcal{A}^\circ$ and is the expanded, Pareto-Optimal output manifold. The interest is in how much effort it would take to find a point $\mathbf{p}'$ that has performance metric response not in $\mathcal{A}^\circ$. For a point p' to exist such that

$$(\Phi_1(\widetilde{\phi_1}(\mathbf{p}'_m), \widetilde{\phi_2}(\mathbf{p}'_m), \mathbf{p}'), \Phi_2(\widetilde{\phi_1}(\mathbf{p}'_m), \widetilde{\phi_2}(\mathbf{p}'_m), \mathbf{p}')) \notin \mathcal{A}^\circ, \tag{5.78}$$

it would have to lie in the uncharacterized region Υ.

The remainder of the analysis is similar to the baseline surrogate optimality analysis that was presented in Section 4.4.3. A sequence of N^{opt}, independent, identically distributed, randomly selected inputs, $\widehat{\mathbf{P}}_{m_1}, \ldots, \widehat{\mathbf{P}}_{m_{N^{\text{opt}}}}$, is drawn according to the probability density function $\rho(\mathbf{p}_m)$: $\widehat{\mathbf{P}}_{m_i} \sim \rho(\mathbf{p}_m), i = 1, \ldots, N^{\text{opt}}$. The optimality statement then follows that, the probability that at least one of the randomly selected design points will have truth performance values that lie in $\mathcal{A}^{\text{unch}}$ is less than $1 - \varepsilon_L$. The number of random input vectors drawn, N^{opt}, is computed as

$$N^{\text{opt}} \leq N\left(\frac{1}{\varepsilon_L} - 1\right), \tag{5.79}$$

where the parameter $\varepsilon_L \in]0, 1[$ is set independently. The optimality result states that, with a confidence of less than $1 - \varepsilon_L$, N^{opt} additional truth evaluations at randomly selected points will produce a design better than the surrogate selected design. This is an estimate of how much work would have to be expended to improve the design beyond a given amount.

The optimality analysis has been performed for the eddy-promoter problem. The PO boundary of the expanded achievable set, $\mathcal{A}^\circ$, has been computed and is plotted as a dashed line in Figure 5-8 and the surrogate PO output manifold is plotted as a solid line. The parameter ε_L in Equation 5.79 is set to $\varepsilon_L = 0.333$ and, given the $N = 24$ validation points that have been sampled in Section 5-8, the value for for N^{opt} is $N^{\text{opt}} = 48$. The optimality statement follows: If an additional 48 input points are drawn randomly according to $\rho(\mathbf{p})$, $\widehat{\mathbf{P}}_{m_i} \sim \rho(\mathbf{p}_m), i = 1, \ldots, 48$, the probability that at least one will have truth output pair $\Pi^T(\widehat{\mathbf{P}}_{m_i}) = (\Psi(\psi_0^T(\widehat{\mathbf{P}}_{m_i}), \widehat{\mathbf{P}}_i), \Theta(\theta_0^T(\widehat{\mathbf{P}}_{m_i}), \widehat{\mathbf{P}}_i) \notin \mathcal{A}^\circ$ is less than 66.7%.

What the optimality statement gives is an estimate to how much additional work (48 additional truth evaluations in this case) would be required to have at least one point that achieves a performance better than $\mathcal{A}^\circ$ with confidence of $1 - \varepsilon_L$. For the eddy-promoter example, the distance between $\partial\mathcal{A}$ and $\partial\mathcal{A}^\circ$ is very large, suggesting that the potential improvement is likely worth the additional computational effort. Secondarily, the wide gap between $\partial\mathcal{A}$ and $\partial\mathcal{A}^\circ$ indicates that the output surrogates are not performing well enough to provide meaningful results in terms of global optimality. Although the predictability for the family of points selected by the Pareto optimization were acceptable according the predictability analyses in Sections 5.4.1 and 5.4.2, the surrogate predicted PO family of input points are not likely close (in performance) to the truth PO family.

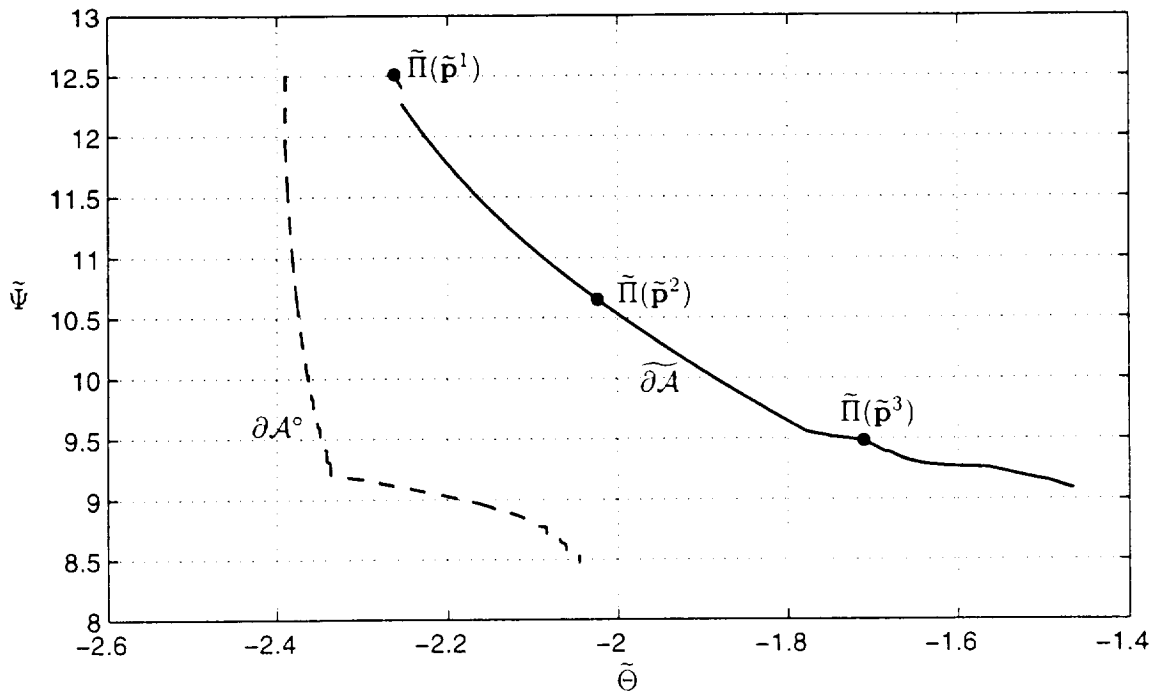

Figure 5-8: Output plane plot of optimality results for the surrogate Pareto framework.

For a final estimate of the surrogate performance, a hypothetical optimality analysis can be performed to determine the magnitude of the global model predication error U that would be necessary to achieve acceptable results. This has been performed for the eddy-promoter problem by assuming a model prediction error U_{hyp} that is lower than $U = 0.0968$ by a factor of 5. $U_{hyp} = U/5 = 0.0968 = 0.0193$. With the hypothetical model prediction error $U_{hyp} = 0.0193$, the associated expanded achievable set $\mathcal{A}^\circ_{hyp}$ has been defined as in Equation 5.71 and the expanded PO output manifold $\partial\mathcal{A}^\circ_{hyp}$ has been determined. The results from this analysis are plotted in Figure 5-9. In Figure 5-9, true expanded PO output manifold, $\partial\mathcal{A}^\circ$, is plotted as a dashed line, the hypothetical expanded PO output manifold, $\partial\mathcal{A}^\circ_{hyp}$, is plotted as a dashed-dotted line, and the surrogate PO output manifold $\widetilde{\partial\mathcal{A}}$ is plotted as a solid line. The very narrow gap between $\partial\mathcal{A}^\circ_{hyp}$ and $\widetilde{\partial\mathcal{A}}$ suggests that if the output surrogates were improved by a factor of 5, the surrogate designs may be close enough to the truth optimal designs to be acceptable.

The optimality analysis highlights how poorly the surrogates approximate the truth outputs for the eddy-promoter. The construction point density should be sufficient to approximate relatively smooth, well-behaved outputs; $N^{co} = 256$ translates roughly to 6 points in each of the 3 input directions for a full factorial design. However, the truth outputs are far from smooth for the eddy-promoter; in fact, for changes in the model input variables, the outputs undergo subcritical bifurcations in which the output is, possibly, discontinuous. The discontinuities in the input-output function are very difficult to precisely

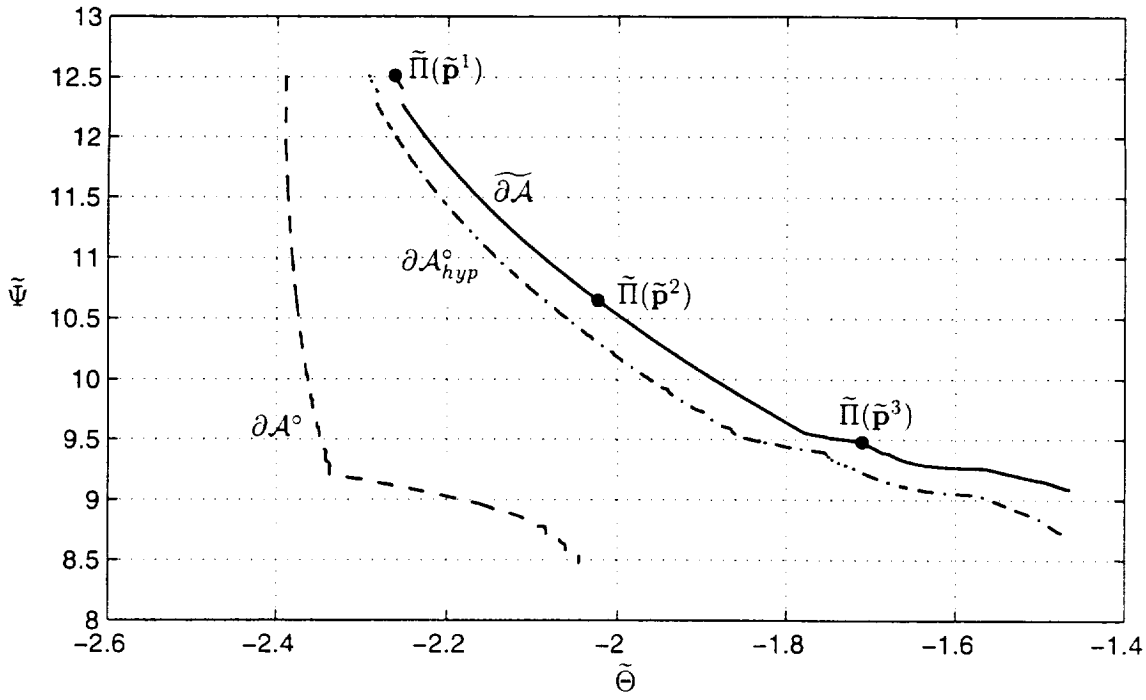

Figure 5-9: Output plane plot of hypothetical optimality results (dotted line) for a factor of five improvement in the model prediction error. the actual optimality bound (dashed line) and the surrogate Pareto output manifold (solid line).

isolate in three input dimensions and produce large surrogate dispersions from the truth output. No effort has been made in the global surrogate construction step to account for the possibility of discontinuous outputs and the radial basis interpolation method exacerbates the difficulties in these regions. A significant improvement in the surrogates (comparable to what was assumed for the hypothetical analysis above) would likely require that discontinuity locations be determined precisely, and accounted for separately. One approach is use linear interpolation across the discontinuities as has been done for the lift coefficient surrogate described in Section 6.4.1.

Chapter 6

Experimental Airfoil Optimization

In this chapter, the application of the baseline surrogate framework to the experimental optimization of a multielement airfoil is presented [54]. Although the application discussed in this chapter is experimental and, therefore, has a zero-mean, measurement error associated with the outputs, the errors are assumed to be small and the outputs are treated as noise-free. The surrogate framework has been extended to correctly handle noisy outputs [78], but these techniques are not used here.

The model has been developed, and the data generously provided, by Landman and Britcher at Old Dominion University (ODU) [44, 45]. The motivation for the development of the experimental model central to this chapter is the inherent difficulty in examining many design points experimentally. The model is a three-element airfoil model with internally embedded actuators (Figure 6-1). It has a nested chord of $c = 18$ in., a span of $b = 36$ in., and was designed for low-speed testing in several wind tunnels, including the NASA Langley Research Center 2- by 4-foot tunnel and the ODU 3- by 4-foot low-speed facilities. The main element chord is $c_{main} = 14.95$ in., and the flap and slat chords (expressed as a percentage of the nested chord) are 30 and 14.5 percent, respectively. The flap and slat are both deflected to 30° for all tests. The particular model used for the test reported here has been developed for low Reynolds number testing to prove the experimental testing concepts. However, the techniques that have been developed should be applicable to higher Reynolds number testing as well.

The flap actuators are computer controlled and position the flap horizontally and vertically (x and y, respectively). The model has been used in the ODU tunnel to compile baseline values for lift coefficient C_l versus flap gap and overhang at fixed angles of attack and slat riggings. A first-order optimizer that uses a variant of the method of steepest descent [24, 10] has been demonstrated in real time[45].

The capability of the computer controller to automatically take data at a prescribed set of (x, y) trailing edge flap coordinates makes the airfoil model setup ideal for application of the surrogate methods to an experimental problem. Additionally, the opportunity to

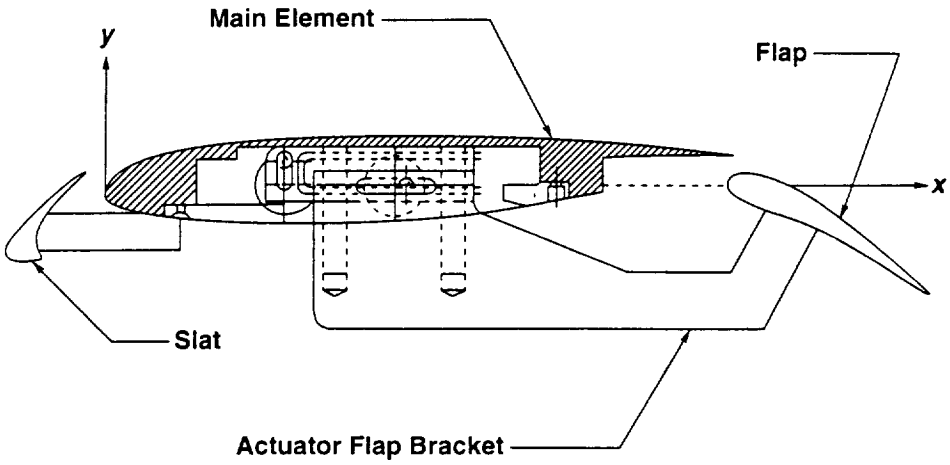

Figure 6-1: Three-element model with internal flap actuators.

compare the surrogate results to those obtained with in on-line optimizer is unique to this experimental test.

The baseline, nonparametric-validated surrogate framework presented in Chapter 4 is applied to the airfoil optimization problem. The problem examined here is a single output problem that is a function of only two inputs; the (x, y) coordinates of the trailing edge flap. The baseline surrogate framework provides a practical means to incorporate experimental data directly into the design optimization process. The off-line surrogate approach to the design optimization has several advantages to on-line optimization [48, 79]. First, by construction, surrogates are computationally inexpensive and are thus easily incorporated into optimization procedures. Additionally, the low computational requirements create a highly interactive and flexible design environment, which allows the designer to easily pursue and examine multiple design points. Second, the number of appeals to the experiment or simulation is known *a priori*, which ensures that the design can be accomplished without exhausting available resources. Third the surrogate approach offers a natural means to incorporate data from previous runs and/or other sources.

As regards disadvantages, the primary drawback is that in high dimensional design spaces, surrogate construction is difficult and design localization is poor. The poor design localization has been demonstrated for the baseline surrogate framework optimization of the eddy-promoter heat exchanger in Chapter 4. A second limiting factor in the application of the surrogate approach to experimental tests is the need to validate the surrogate at input points chosen randomly in the design space. This capability, present in the experiment central to this work, is not typical of most experimental tests. Finally, surrogate-based optimization introduces a new source of error. The surrogate validation strategy and error norms discussed in this paper seek to quantify the discrepancy between the surrogate and the experiment by providing estimates to the system predictability and optimality.

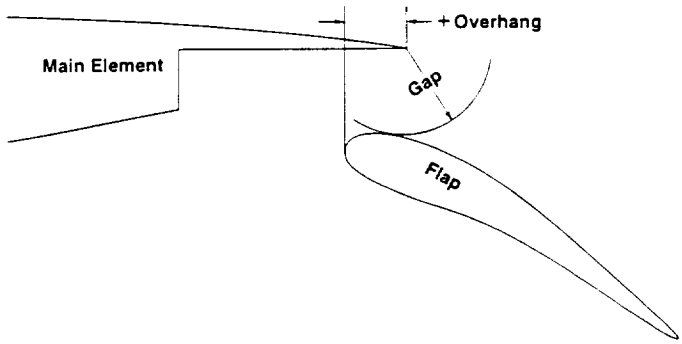

Figure 6-2: Definition of gap and overhang.

In this Chapter, the experimental model and testing methods used are briefly described first. Second, the optimization problem that is central to the work is presented. Third, the three steps steps of the baseline surrogate framework (i.e., construction/validation, surrogate-based optimization, and *a posteriori* error analysis) are presented, the inputs to the framework are summarized, and an overview of the more sophisticated surrogate algorithms is provided. Finally, sample results obtained from the surrogate framework for output maximization and multiple-target designs are presented, and a comparison between the surrogate approach and direct insertion results reported previously[45] is provided.

6.1 Experimental Testing Methods

An important practical problem encountered in wind-tunnel testing of multielement airfoils is the need to test a range of configurations to ensure that the optimum is selected. Unfortunately, this testing can be prohibitively time consuming if one considers all possible variables, such as flap position and deflection, slat position and deflection, overall angle of attack, and Reynolds number. For example, a range of flap locations and orientations relative to the main element is typically tested. In a cryogenic or pressurized facility, model geometry changes necessitate large delays in testing. These delays often result in investigators choosing a sparse test matrix and an optimum that is based on only a few points. The ability to move the flap under computer control provides a unique opportunity to explore the entire range of useful gap and overhang values (Figure 6-2). Two typical pressure distributions are shown in Figure 6-3, where the ordinate is the pressure coefficient C_p and the abscissa is distance from the leading edge expressed as a percent of the nested chord. The data for Figure 6-3(a) represents a point near the peak C_l for this configuration, and the plot in Figure 6-3(b) indicates full separation over the flap.

In this experiment (performed by Landman and Britcher), the flap actuators, tunnel flow setting, and data acquisition were controlled by a personal computer running Lab View [50]

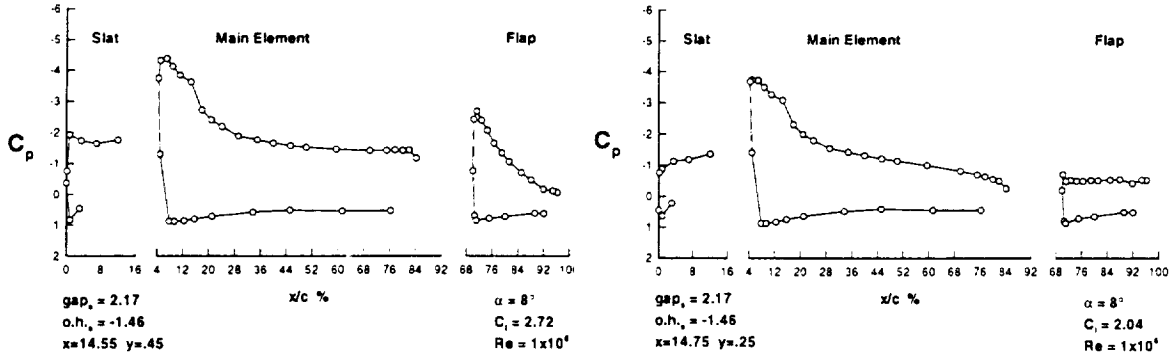

(a) Fully attached flow over all elements. (b) Detached flow over the flap.

Figure 6-3: Experimental pressure data.

software. A program was written to allow any number of flap positions (in x and y) to be sampled in any order. Wind tunnel power was controlled such that at the beginning of each test the tunnel was restarted to avoid hysteresis effects [45]. The experimental setup allowed the user to start the program, which at each location in turn automatically measured the free-stream properties, sampled and recorded pressures around the centerline of the model, and then calculated lift coefficients for the three-element airfoil. This process required approximately 2 min. for each data point.

Test matrices were developed to survey flap positions, which ranged from approximately 0.8 - 3.5 percent (gap) and -0.4 - 3.4 percent (overhang) relative to the nested chord c. Two angles of attack and two slat geometries were selected. An angle of attack α of 8° was chosen as representative of an approach value. An α of 14° represented the limit of good-quality two-dimensional flow for the ODU tunnel installation without tunnel wall boundary-layer control. Two slat settings were chosen: a slat gap of 3.03 percent with an overhang of 2.46 percent and, for a smaller gap setting, a slat gap of 2.17 percent with a slat overhang of -1.46 percent.

Positional accuracy was enhanced by requiring that the flap move to a reference point above and behind the desired evaluation points ($x_{ref} > x_{eval}$; $y_{ref} > y_{eval}$) and then back to the evaluation point. This eliminated any effect of backlash in the mechanical drive-train. Two simple tests provided an indication of the inherent collective error due to instrumentation and positioning. The first test involved two separate evaluation points; the first point was in a region in which the flow was known to be fully attached to all elements, and the second point was chosen in a region in which flow over the flap was fully separated. The positioning program was used to move the flap between a reference point and one of the evaluation points. The tunnel was restarted before every evaluation, and the test was repeated 30 times in each case. The standard deviation of C_l was found to be 0.004 for the separated case (0.16 percent) and 0.0118 for the attached case (.36 percent). For

the second test, the program automatically sampled 29 points over the entire test region for two different trials. The error in C_l between the two runs averaged 0.71 percent with a standard deviation of 0.75 percent. Although these tests are not exhaustive, they do provide a benchmark for the C_l error.

The turbulence intensity in the ODU tunnel was measured at less than 0.2 percent. Flow quality over the model was monitored through 12 spanwise taps: 6 on the flap, and 6 on the main element. The flow was considered to be two-dimensional if the magnitude of the spanwise nonuniformity was less than 5 percent of the total C_p variation over the entire model [49]. The data presented are uncorrected for boundary effects were taken at a Reynolds Re number of 1×10^6 based on the nested chord.

6.2 Optimization Problem

We begin by introducing a vector $\mathbf{p}$ of M design inputs that lie in the input (or "design") domain $\Omega \subset \mathbb{R}^M$, an input-output function $\mathcal{S}(\mathbf{p}) : \Omega \rightarrow \mathbb{R}$, and an objective function $\Psi(\mathcal{S}(\mathbf{p}), \mathbf{p}, \lambda)$ that characterizes our design goals, where λ is a vector (or possibly scalar) design parameter. For the work presented here, we set $\mathbf{p} = (x, y)$ (the x- and y-positions of the flap) as the $M = 2$ inputs and restrict ourselves to an input domain Ω of reasonable flap positions (described in more detail in the results section). The output of interest is the lift coefficient, $\mathcal{S}(\mathbf{p}) = C_l(x, y)$. The objective function is $\Psi(\mathcal{S}(\mathbf{p}), \mathbf{p}, \lambda) = |\mathcal{S}(\mathbf{p}) - \lambda|$ which has been referred to as the "discrimination" problem [62].

With the above terms defined, the minimizer $\mathbf{p}^* = (x^*, y^*)$ to the exact optimization problem is given by

$$\mathbf{p}^* = \arg\min_{\mathbf{p}\in\Omega} |\mathcal{S}(\mathbf{p}) - \lambda| \,. \tag{6.1}$$

In this formulation, the goal is to find that (or "an") input vector $\mathbf{p}^* = (x^*, y^*)$ that achieves as closely as possible the target lift coefficient value λ. If the target lift coefficient λ is set sufficiently small (large), the formulation describes the output minimization (maximization) problem, assuming that $\mathcal{S}(\mathbf{p})$ is bounded from below (above).

In the on-line approach, the experiment is invoked at every optimization step needed to solve Equation (6.1). In the off-line approach, a surrogate, $\widetilde{\mathcal{S}}(\mathbf{p}) \approx \mathcal{S}(\mathbf{p})$, for the experiment is inserted into the optimization problem. The minimizer, $\widetilde{\mathbf{p}}^* = (\widetilde{x}^*, \widetilde{y}^*)$, for the resulting, surrogate-based, discrimination problem is then given by

$$\widetilde{\mathbf{p}}^* = \arg\min_{\mathbf{p}\in\Omega} |\widetilde{\mathcal{S}}(\mathbf{p}) - \lambda| \,. \tag{6.2}$$

Here, the optimization proceeds exactly as it would for the on-line approach, but the lift coefficient surrogate $\widetilde{\mathcal{S}}(\mathbf{p})$ is invoked instead of the experiment. The surrogate problem that corresponds to Equation (6.1), but with a general objective function $\Psi(\mathcal{S}(\mathbf{p}), \mathbf{p}, \lambda)$, has been

reported by Yeşilyurt [77] and Yeşilyurt and Patera [79].

6.3 Surrogate Framework

The surrogate approach is broken into four steps. In the first stage, surrogate construction, experimental results and/or prior information are used to construct the approximation, $\widetilde{\mathcal{S}}(\mathbf{p}) \approx \mathcal{S}(\mathbf{p})$. In the second step, surrogate validation, additional queries to the experiment are used to validate the approximation. In the third step of the process, surrogate-based optimization, solutions to surrogate optimization problem of Equation (6.2) are obtained. In the fourth and final step, *a posteriori* error analysis, the results of the validation are used to analyze the consequences of the surrogate-for-simulation substitution. In the following subsections, the four steps of the *baseline* surrogate framework are presented and the designer inputs to the framework are summarized.

6.3.1 Surrogate Construction

A lift coefficient surrogate $\widetilde{\mathcal{S}}(\mathbf{p}) = \mathcal{A}(\mathcal{X}^{co}) \approx \mathcal{S}(\mathbf{p})$ is constructed using an approximation scheme, $\mathcal{A} : (\mathbb{R}^M, \mathbb{R})^{N^{co}} \rightarrow L^\infty(\Omega)$ and a construction sample set of input-output pairs

$$\mathcal{X}^{co} = \{(\mathbf{p}_i, R_{\mathbf{p}_i}), i = 1, \ldots, N^{co}\}, \tag{6.3}$$

where $R_{\mathbf{p}_i} = C_l(x_i, y_i)$ is a realization of the experimentally measured lift coefficient for the input flap position $\mathbf{p}_i = (x_i, y_i)$, and N^{co} is the number of input-output pairs in the construction sample. Although the general surrogate framework can handle noisy outputs [78], the noise contribution is neglected in the work presented here. Information from prior studies, outside sources, or asymptotic behavior can also be incorporated into the approximation process either through the definition of the approximation scheme or by including the input–output pairs in the construction sample. As already stated, the surrogate framework makes no assumptions in regard to the approximation technique and will accept, and assess, any approximation $\mathcal{A}(\mathcal{X}^{co})$. Also, no restriction is placed on either N^{co} or the distribution of the construction sample.

6.3.2 Surrogate Validation

To proceed with the description of the surrogate validation, and importance function $\rho(\mathbf{p})$ is first introduced. The importance function serves as a probability density function for the selection of the validation points:

$$\int_\Omega \rho(\mathbf{p}) d\mathbf{p} = 1. \tag{6.4}$$

The importance function also leads to the notion of a ρ–measure associated with $\rho(\mathbf{p})$: for any subdomain $\mathcal{D} \subset \Omega$,

$$\mu_\rho(\mathcal{D}) = \int_{\mathcal{D}} \rho(\mathbf{p})\mathbf{dp} < 1. \tag{6.5}$$

The ρ–measure of $\mathcal{D}$ is simply the weighted relative M-volume of $\mathcal{D}$.

With the importance function $\rho(\mathbf{p})$ defined, the validation sample set is formed

$$\mathcal{X}^{va} = \{(\mathbf{P}_i, R_{\mathbf{P}_i}), i = 1, \ldots, N^{va}\}\,,\ \mathbf{P}_i \sim \rho(\mathbf{p})\,, \tag{6.6}$$

where the input flap positions $\mathbf{P}_i$ for the validation sample set are drawn randomly according to the probability density function $\rho(\mathbf{p})$. In Equation (6.6), the $\sim$ is as "is drawn according to the probability density function." The validation sample size N^{va} is given by

$$N^{va} = \frac{\ln \varepsilon_2}{\ln(1-\varepsilon_1)}, \tag{6.7}$$

and ε_1 and ε_2 are the two uncertainty parameters described below. The model prediction error U is computed from the validation sample set $\mathcal{X}^{va}$ as

$$U = \max_{\mathbf{P}_i \in \mathcal{X}^{va}_{\mathbf{P}}} \frac{|R_{\mathbf{P}_i} - \tilde{S}(\mathbf{P}_i)|}{\hat{g}(\mathbf{P}_i)}\,, \tag{6.8}$$

where $\mathcal{X}^{va}_{\mathbf{P}}$ denotes the input points of the validation sample set and $\hat{g}(\mathbf{p})$ is a strictly positive, error-scaling function described in more detail below.

The result of the construction/validation process is a probabilistic statement that describes the global quality of the surrogate $\tilde{S}(\mathbf{p})$. The validation statement can be compactly written as

$$Pr\{\mu_\rho(\Upsilon) < \varepsilon_1\} \geq 1 - \varepsilon_2. \tag{6.9}$$

where $Pr\{event\}$ is the "probability of *event*" and $\Upsilon \subset \Omega$ is the uncharacterized region defined as

$$\Upsilon = \left\{\mathbf{p} \in \Omega |\, |S(\mathbf{p}) - \tilde{S}(\mathbf{p})| > U\hat{g}(\mathbf{p})\right\}\,. \tag{6.10}$$

The ρ-measure of the uncharacterized region is bounded by ε_1, and the significance level of the nonparametric statistical bound is ε_2. This result can be readily proved [77] with order statistics [15] and is included in Appendix B.1.

For the simple case of $\hat{g}(\mathbf{p}) = 1$, Equation (6.9) states that, with probability greater than or equal to $1-\varepsilon_2$, the surrogate error is bounded by U over a region of Ω of ρ-measure greater than $1-\varepsilon_1$. Although this statement is suggestive, it gives neither an indication as to the location of Υ nor the magnitude of the surrogate error in Υ.

6.3.3 Surrogate-Based Optimization

For the optimization problem, it is assume that the design is given Q target drag coefficient values λ^q, $q \in \mathcal{Q} = \{1, \ldots, Q\}$. The goal of the optimization is to find the surrogate-predicted flap positions that minimize the objective function,

$$\mathbf{p}^q = \tilde{\mathbf{p}}^*(\lambda^q) = \arg\min_{\mathbf{p}\in\Omega} |\tilde{\mathcal{S}}(\mathbf{p}) - \lambda^q|, \quad \forall q \in \mathcal{Q}. \tag{6.11}$$

The Q targets could represent different target lift coefficients during the flap deployment schedule, or reflect the goals at different flight conditions (e.g., take-off and landing).

6.3.4 *A posteriori* Error Analysis

To present the predictability results, the notion of a prediction neighborhood is first introduced. A distance metric $\Delta(\mathbf{a}, \mathbf{b})$ is defined for all $(\mathbf{a}, \mathbf{b}) \in \Omega \times \Omega$, which determines a "distance" between two input points $\mathbf{a}$ and $\mathbf{b}$. Then for any subdomain $\mathcal{D} \subset \Omega$ the radius of $\mathcal{D}$ about a point $\mathbf{p}$ is defined as $r_{\mathcal{D}}(\mathbf{p}) = \max_{\mathbf{p}'\in\mathcal{D}} \Delta(\mathbf{p}, \mathbf{p}')$. The prediction neighborhood located at point $\mathbf{p}$ with a ρ–measure of z, $\mathcal{P}(\mathbf{p}, z)$, is that (or a) region $\mathcal{D} \subset \Omega$ of ρ–measure z that minimizes $r_{\mathcal{D}}(\mathbf{p})$. It is assumed that $\mathbf{p}$ lies inside $\mathcal{P}(\mathbf{p}, z)$ and that $\mathcal{P}(\mathbf{p}, z_1) \subset \mathcal{P}(\mathbf{p}, z_2)$ for $z_1 < z_2$. It can then be stated that, with probability greater than $1 - \varepsilon_2$, for all $q \in \mathcal{Q}$, regions $\Gamma^q \subset \mathcal{P}(\mathbf{p}^q, \varepsilon_1)$ of nonzero measure exist such that for all $\mathbf{p}' \in \Gamma^q$,

$$|\mathcal{S}(\mathbf{p}') - \tilde{\mathcal{S}}(\mathbf{p}^q)| \leq e(\mathbf{p}^q). \tag{6.12}$$

It now remains to bound $e(\mathbf{p}^q)$ and make precise the extent of Γ^q.

Several bounds are possible on $e(\mathbf{p}^q)$, which is denoted the predictability gap. The predictability of each design can be bounded individually, to obtain

$$e(\mathbf{p}^q) \leq \mathcal{E}(\mathbf{p}^q, \varepsilon_1), \quad \forall q \in \mathcal{Q}, \tag{6.13}$$

where, for $\mathbf{p} \in \Omega$ and $0 < z < 1$,

$$\mathcal{E}(\mathbf{p}, z) = Ug(\mathbf{p}, z) + \delta(\mathbf{p}, z), \tag{6.14}$$

and

$$g(\mathbf{p}, z) = \max_{\mathbf{p}'\in\mathcal{P}(\mathbf{p},z)} \hat{g}(\mathbf{p}'), \tag{6.15}$$

$$\delta(\mathbf{p}, z) = \max_{\mathbf{p}'\in\mathcal{P}(\mathbf{p},z)} |\tilde{\mathcal{S}}(\mathbf{p}') - \tilde{\mathcal{S}}(\mathbf{p})|, \tag{6.16}$$

and U is the model prediction error from the validation step, Equation (6.8).

In addition to the joint estimates to the bound on $e(\mathbf{p}^q)$, the the average error over

the Q target designs can be bounded. In particular, if it is assumed that the $\mathcal{P}(\mathbf{p}^q, \varepsilon_1)$ are mutually disjoint, it can be shown that

$$\frac{1}{Q}\sum_{q=1}^{Q} e(\mathbf{p}^q) \leq \max_{\underline{\beta}\in\mathcal{C}_Q}\left[\frac{1}{Q}\sum_{q=1}^{Q}\mathcal{E}(\mathbf{p}^q, \beta_q\varepsilon_1)\right], \tag{6.17}$$

where $\underline{\beta} = \{\beta_1, \ldots, \beta_Q\}$, and

$$\mathcal{C}_L = \{\underline{\beta}' \in I\!R^L | 0 \leq \beta_l' \leq 1, l = 1, \ldots, L; \sum_{l=1}^{L}\beta_l' = 1\}, \tag{6.18}$$

is the set of convex L-tuples. The "nonparametric average" is relevant to multiple-target designs and represents the average, as opposed to the worst-case, estimate of the predictability. Also, it is important to note that this predictability bound is calculated entirely in terms of the inexpensive surrogate, $\tilde{\mathcal{S}}(\mathbf{p})$.

Finally, for a successful validation (i.e., $\mu_\rho(\Upsilon) < \varepsilon_1$), the expectation of the size of Γ^q can be bounded with respect to the validation sample joint probability density. The resulting bound is, $\forall q \in \mathcal{Q}$,

$$E\left(\frac{\mu_\rho(\Gamma^q)}{\varepsilon_1} \mid \mu_\rho(\Upsilon) < \varepsilon_1\right) \leq 1 + \frac{1}{\ln\varepsilon_2} + \frac{\varepsilon_2}{(1-\varepsilon_2)}. \tag{6.19}$$

The expression in Equation (6.19) bounds the average ρ-measure of the region Γ^q, with respect to ε_1, for many validations.

Several advantages to bounding the errors only to within a finite uncertainty exist [57]. First, a sense of stability is obtained in that the estimates apply not only to a single point, but to regions Γ^q of nonzero measure, assuring that many input points $\mathbf{p}^q$ exist that satisfy the error estimates. Second, for the multiple-target case the estimates become sharper because there is only a single uncharacterized volume of measure ε_1. Equation (6.17) is the upper bound for the distribution of the single ε_1-sized uncharacterized region among the Q designs. This analysis results in a bound on the average error which is less than the average of the individual predictability gap bounds $\mathcal{E}(\mathbf{p}^q, \varepsilon_1)$. Finally, because the predictability analysis is not premised on any particular set of points, the designer has flexibility in the choice of the metric $\Delta(\mathbf{a}, \mathbf{b})$ (discussed further in the next section).

6.3.5 Summary of Surrogate Inputs

To summarize the surrogate framework description, and to highlight the flexibility of the environment, we note that four inputs to the process are determined by the user. These are listed below:

i. An importance function $\rho(\mathbf{p}) : \Omega \to I\!R_+$.

ii. An error-scaling function $\hat{g}(\mathbf{p}) : \Omega \rightarrow \mathbb{R}_+$.

iii. Two uncertainty parameters, ε_1 and ε_2, that satisfy $0 < \varepsilon_1, \varepsilon_2 < 1$.

iv. A pseudometric $\Delta(\mathbf{a}, \mathbf{b})$.

Each input provides the designer with flexibility, and allows the designer's experience to impact and improve the final surrogate-predicted designs. Although poor choices for the inputs do not influence the validity of the surrogate results, they greatly reduce the sharpness of the results. A short description and explanation of each input follows.

The importance function $\rho(\mathbf{p})$ reflects the designers prejudices in regard to the regions of Ω that are more likely to contain optimizers. In this context, $\rho(\mathbf{p})$ is essentially a "prior" on $\tilde{\mathbf{p}}^*$. To serve this purpose, $\rho(\mathbf{p})$ is used as the probability density function in the random selection of validation points in Equation (6.6). A judicious choice of $\rho(\mathbf{p})$ (one that is large in the regions of the final designs and small elsewhere) can significantly increase the sharpness of the *a posteriori* error bounds. The increased sharpness is a consequence of much better physical localization (in terms of input variable extent) of the prediction neighborhood $\mathcal{P}(\tilde{\mathbf{p}}^*, \varepsilon_1)$, which in turn reduces the surrogate sensitivity contribution $\delta(\tilde{\mathbf{p}}^*, \varepsilon_1)$ to the error bound in Equation (6.14).

The error-scaling function $\hat{g}(\mathbf{p})$ can be used by the designer to reduce the impact of localized surrogate errors on the error bounds of the final design. Because the model prediction error U in Equation (6.8) is global, a large value of $\hat{g}(\mathbf{p})$ in regions for which the approximation is poor will result in a reduced value of the first term on the right-hand side of Equation (6.14), provided that the final design does not lie in a region where $\hat{g}(\mathbf{p})$ is large.

The uncertainty parameters ε_1 and ε_2 are related to the number of validation points through Equation (6.7). This formula allows the precise budgeting of resources and ensures that useful solutions can be obtained. In effect, Equations (6.7)-(6.10) describe what is known in a continuous sense about a function based on discrete sampling. Analysis of Equation (6.7) shows that, asymptotically for small ε_1 and ε_2, N^{va} increases linearly as ε_1 decreases and only logarithmically as ε_2 decreases. This relationship suggests that although we can easily (in terms of validation sample size) increase our confidence in the results (smaller ε_2), refining the localization of our results (through smaller ε_1) is much more difficult. The localization has a direct impact on the final error analysis through $\delta(\mathbf{p}, \varepsilon_1)$ in Equation (6.14). The relative difficulty in further refining the localization illustrates the need to intelligently select $\rho(\mathbf{p})$ and where appropriate, $\Delta(\mathbf{a}, \mathbf{b})$, both of which can have similar effects on the localization error.

The final input to the surrogate approach is the pseudometric $\Delta(\mathbf{a}, \mathbf{b})$. Because $\Delta(\mathbf{a}, \mathbf{b})$ can be chosen post-validation, various metrics can be examined, and the most appropriate selected. One possible trade-off is between design localization (in terms of input variable

extent) and predictability in terms of $\delta(\mathbf{p}, \varepsilon_1)$ in Equation (6.14). An example of the extreme of this trade-off is the sensitivity minimizing metric

$$\Delta(\mathbf{a}, \mathbf{b}) = |\tilde{\mathcal{S}}(\mathbf{a}) - \tilde{\mathcal{S}}(\mathbf{b})| \tag{6.20}$$

used for the single-point design study of the results section. This metric gives the lowest possible $\delta(\mathbf{p}, \varepsilon_1)$.

6.4 Results

To demonstrate the surrogate framework, it has been applied to the experimental design of multielement airfoils: specifically, the interest is in in the determination of the optimal location for the trailing edge flap, based on the lift coefficient C_l in low-speed, high-lift flight regimes. The $M = 2$ design inputs to the problem $\mathbf{p} = (x, y)$ are the x and y positions of the flap, measured from the leading edge of the main airfoil element and normalized by the main element chord $c_{main} = 14.95$ in. The output of interest is C_l. In addition, several other configuration and flow condition parameters are fixed for the study. These parameters are listed in Table 6.1 and are the Reynolds number Re, the airfoil angle of attack α, the flap and slat deflection angles δ_{flap} and δ_{slat}, respectively, and the gap and overhang of the slat (expressed as a percentage of the nested chord $c = 18.0$ in.).

In this section, the method used for the surrogate construction and the validation results are reported first. Second, the single-point design problem of output maximization is presented. Third, multiple-target design study is pursued that demonstrates the increased sharpness of the nonparametric average error results. Finally, the results of on-line optimization studies are given and are compared to the off-line, surrogate results.

6.4.1 Surrogate Construction/Validation

The construction sample set $\mathcal{X}^{co}$ consists of 119 input-output pairs that are uniformly spaced on a 17×7 grid. The (x, y) flap positions for the construction sample are plotted as

Re	1,000,000
α	14°
δ_{flap}	30°
δ_{slat}	−30°
gap_{slat}	2.17%
$overhang_{slat}$	−1.46%

Table 6.1: Fixed design study parameters.

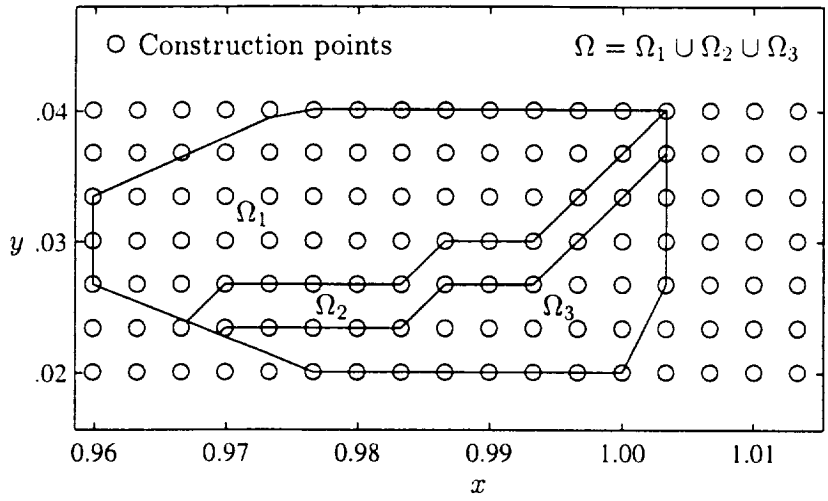

Figure 6-4: Surrogate construction points and the input ("design") domain.

circles in Figure 6-4. The input domain is divided into three subdomains, $\Omega = \Omega_1 \cup \Omega_2 \cup \Omega_3$, based on the flow conditions over the flap. In the first subdomain Ω_1, the flow over the flap is attached, with the exception of the extreme aft positions in which some trailing-edge separation may be present (and desirable). In this region, a radial basis function [18] (described in Appendix D.1) serves as the approximation method, which yields the surrogate $\tilde{\mathcal{S}}_1(\mathbf{p})$. In Ω_3, the flow over the flap is fully separated, and a second radial basis function fit serves as the surrogate $\tilde{\mathcal{S}}_3(\mathbf{p})$. In Ω_2, the resolution of the construction points is not sufficient to determine the precise location of the separation line. In this region, a simple linear triangulation between $\tilde{\mathcal{S}}_1(\mathbf{p})$ and $\tilde{\mathcal{S}}_3(\mathbf{p})$ is used as the surrogate, $\tilde{\mathcal{S}}_2(\mathbf{p})$. The error function, $\hat{g}(\mathbf{p})$, is set to unity in Ω_1 and Ω_3, and $\hat{g}(\mathbf{p}) = 50$ in Ω_2, reflecting our uncertainty in regard to the location of the separation line and, hence, the lack of confidence in the quality of the surrogate in this region of the input space. A three-dimensional surface plot of the surrogate is shown in Figure 6-5.

To validate the lift coefficient surrogate, a set of random input points in Ω is first selected and the experiment is conducted at each of these points to form the validation sample set $\mathcal{X}^{va}$. The input points are confined to the design space Ω described in the previous paragraph and shown in Figure 6-4. Because the construction data were obtained simultaneously with the validation data, there was no expectation in regard to those regions of the input space that would be of most interest; thus, a uniform probability density function $\rho(\mathbf{p})$ was used for the selection of the validation points. The number of points budgeted for the validation was $N^{va} = 45$ and, using the relationship in Equation (6.7), $\varepsilon_1 = 0.03$ and $\varepsilon_2 = 0.25$ were set. If the form of the surrogate had been known prior to taking the validation data, the design space could have been restricted to a more feasible region and a importance function $\rho(\mathbf{p})$ that would have concentrated validation points close

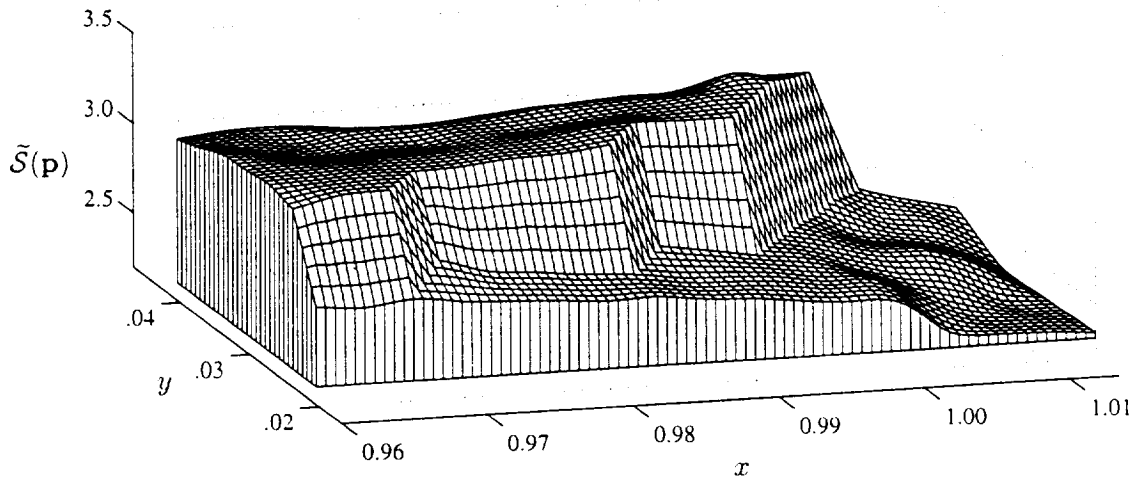

Figure 6-5: Three-dimensional mesh plot of the lift coefficient surrogate $\tilde{S}(\mathbf{p})$.

to potential designs could have been used. Both of these changes would have improved the predictability results for the designs. The scaled model prediction error computed according to Equation (6.8) is $U = .0482$. The maximum un-scaled error does in fact occur in Ω_2 as was presupposed and has a value of 0.4824. If $\hat{g}(\mathbf{p}) = 1$ had been used everywhere (instead of as described above), the model prediction error would have been approximately one order of magnitude larger, and would have overwhelmed the results.

The surrogate just described and the related validation results serve for all of the designs discussed in the remainder of this paper. One primary advantage to using the surrogate approach is the fact that no additional experimental data are required to bound the errors of future designs that are pursued with the surrogate. This characteristic, combined with the negligible computational time required for each surrogate evaluation, yields a highly flexible design environment that does not sacrifice predictability.

6.4.2 Single-Point Design, Surrogate Maximization

For the first study, single-point design is pursued that maximizes the surrogate output. The parameter λ is set sufficiently large in Equation (6.2) and the resulting function is minimized. To accomplish the optimization, an unconstrained quasi-Newton optimizer that is included in the optimization toolbox of Matlab [47] is used. The resulting surrogate-based optimizer is located at $\tilde{\mathbf{p}}^* = (x^*, y^*) = (.997, .036)$, and the surrogate-predicted lift coefficient value at this point is $\tilde{S}(\tilde{\mathbf{p}}^*) = 3.388$. The optimizer was started with an initial guess at $\mathbf{p}_0 = (.987, .033)$ and required 44 surrogate evaluations to arrive at $\tilde{\mathbf{p}}^*$. Because the surrogate is inexpensive to evaluate (and because there are only two inputs and the results can be easily visualized graphically), it can be verified that a surrogate-predicted, global maximum is indeed achieved. This verification is more difficult in a purely on-line

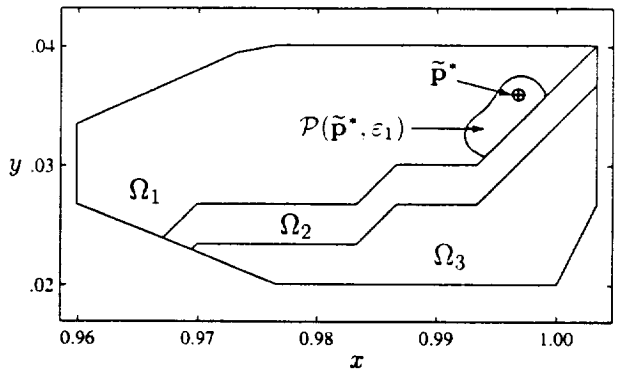

Figure 6-6: The surrogate-predicted optimizer, $\tilde{\mathbf{p}}^*$, and the associated prediction neighborhood, $\mathcal{P}(\tilde{\mathbf{p}}^*, \varepsilon_1)$.

optimization setting without restarting the optimizer at multiple initial points $\mathbf{p}_0$ until there is sufficient confidence that a global maximum has been obtained.

Finally, the sensitivity minimizing metric $\Delta(\mathbf{a}, \mathbf{b}) \equiv |\tilde{\mathcal{S}}(\mathbf{a}) - \tilde{\mathcal{S}}(\mathbf{b})|$ in Equation (6.20) is selected and the *a posteriori* error analysis for a single-point design is performed. The prediction neighborhood $\mathcal{P}(\tilde{\mathbf{p}}^*, \varepsilon_1)$ is constructed around $\tilde{\mathbf{p}}^*$ and the surrogate sensitivity parameter $\delta = .0328$ is found. The optimal point $\tilde{\mathbf{p}}^*$ and the associated prediction neighborhood $\mathcal{P}(\tilde{\mathbf{p}}^*, \varepsilon_1)$ are plotted in Figure 6-6. The resulting predictability statement reads as follows: with confidence level greater than .75, a region $\Gamma \subset \mathcal{P}(\tilde{\mathbf{p}}^*, \varepsilon_1)$ of nonzero measure exists such that for all $\mathbf{p}' \in \Gamma$

$$|\mathcal{S}(\mathbf{p}') - \tilde{\mathcal{S}}(\tilde{\mathbf{p}}^*)| \leq e(\tilde{\mathbf{p}}^*) \,, \tag{6.21}$$

where

$$e(\tilde{\mathbf{p}}^*) \leq Ug(\tilde{\mathbf{p}}^*, \varepsilon_1) + \delta = .0810 \,. \tag{6.22}$$

The predictability is relatively good with respect to the surrogate-predicted maximum lift coefficient, but quite poor with respect to the range of lift coefficients of interest (i.e., corresponding to flap positions in Ω_1).

6.4.3 Multiple-Target Designs

For the second design study, a multiple-target design is pursued. The motivation for such a study might be an interest in examining the lift coefficient at more than one point of the deployment of the flap. Specifically, the goal is to to obtain two target lift coefficients: $\lambda^1 = 3.31$ and $\lambda^2 = 3.25$. Isocontours of the surrogate indicate that a locus of points in Ω exists for each target that exactly satisfies the design goals. One input point for each design is arbitrarily selected: $\mathbf{p}^1 = (x^{[1]}, y^{[1]}) = (.987, .033)$ and $\mathbf{p}^2 = (x^{[2]}, y^{[2]}) = (.979, .033)$. Around each optimizer, a prediction neighborhood chosen from the family of ellipses that

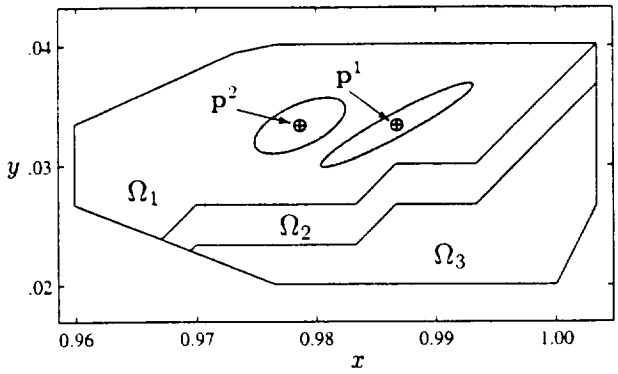

Figure 6-7: The surrogate–predicted optimizers and the associated prediction neighborhoods (shaded).

have area equal to ε_1 and centered at $\mathbf{p}^q$ is constructed. The neighborhoods are oriented such that they minimize surrogate sensitivity $\delta(\mathbf{p}^q, \varepsilon_1)$. The optimizers and associated prediction neighborhoods are plotted in Figure 6-7.

For each of the designs ($q = 1, 2$), it can be stated with confidence level greater than 0.75 that a region $\Gamma^q \subset \mathcal{P}(\mathbf{p}^q, \varepsilon_1)$ of nonzero measure exists such that for all $\mathbf{p}' \in \Gamma^q$

$$|\tilde{\mathcal{S}}(\mathbf{p}^q) - \mathcal{S}(\mathbf{p}')| < e(\mathbf{p}^q), \tag{6.23}$$

where

$$e(\mathbf{p}^1) = U + \delta(\mathbf{p}^1, \varepsilon_1) = .0482 + .0198 = .0680. \tag{6.24}$$

and

$$e(\mathbf{p}^2) = U + \delta(\mathbf{p}^2, \varepsilon_1) = .0482 + .0201 = .0683. \tag{6.25}$$

The above bounds jointly hold on each design. A slightly sharper bound on the average error of the two designs is obtained:

$$\frac{1}{2}[e(\mathbf{p}^1) + e(\mathbf{p}^2)] \leq U + .0149 = .0631. \tag{6.26}$$

The increased sharpness results from an analysis of the worst-case distribution of the uncharacterized region between the two prediction neighborhoods. Because of the low sensitivity of the surrogate in each of the prediction neighborhoods relative to model prediction error U, the improvement is slight.

6.4.4 Comparison with Direct Insertion

Cases at identical flow conditions have not been examined with both on-line (the method of steepest ascent) and off-line (the surrogate approach) optimization methods. However, rough comparisons of the resource requirements are of presented and are of guarded use.

The on-line results have been reported in an earlier paper by Landman and Britcher [45]. In that effort, they found the optimizer to be very robust (successful in 6 out of 6 attempts) and insensitive to the initial guess. For each case, they started the optimizer at in initial flap position with a low C_l value and obtained a final value within approximately 0.7 percent of the maximum C_l value in approximately 20 optimizer steps, requiring approximately 60 experimental data points (3 points per step). With the surrogate method, 119 points were required to construct the surrogate and an additional 45 were used for the validation, for a total of 164 experimental data points. For the maximization problem, the *a posteriori* error bound was 2.4 percent of the maximum surrogate value.

While the surrogate approach seems to compare unfavorably to the on-line method, several subtleties lie in its favor. First, for designs chosen with the validated surrogate in the future (e.g., the multiple-target design examined in this paper), similar error bounds still apply and do not require additional experimental data. In contrast, the on-line approach would require additional experimental results. Second, a total of 60 evaluations to obtain an optimal point with the on-line method can be deceptive: to be assured that the result is indeed optimal, additional information is required. The additional information for the study cited was in the form of contour plots of a matrix of data. If visualization is not possible, a number of optimizer restarts would be required to be assured of a global optimal. Third, in cases for which the objective function is less forgiving, restarts of the on-line optimizer would be unavoidable, which would further increase the required experimental data to a level surpassing that of the surrogate approach. Finally, the obvious difficulty in pursuing on-line optimization is related to the ultimate application: if the intent is to incorporate the data as a portion of a larger optimization study, no alternative is available other than to store the experimental data for later use and extract with some form of an approximation. If one is restricted to a purely experimental setting, then the ability to quickly, and automatically, find optimal operating points with the on-line optimizer is highly advantageous.

Chapter 7

Concluding Remarks

The work presented in this thesis represents several significant contributions. First, the level-set based geometry description provides a unified means to describe a family of shapes that encompasses multiple topologies. Second, several theoretical extensions to the nonparametric-validated surrogate framework have been derived and demonstrated. Third, the synergy that results from the marriage between the surrogate framework and a Pareto formulation of the multicriteria design problem have been documented.

The level-set based geometry definition presented in Section 2.5 represents a way to describe a family of shapes that encompasses multiple topologies and that is applicable to surrogate-based optimization approaches. The shape description is consistent regardless of the topology of the geometry (single or two bodies) and requires no additional logic for the different topologies. The critical characteristic of the method for its application to surrogate-based optimization is that, as shown empirically in Section 2.5.4, the input-output functions are continuous across the topology change. Continuity is required if interpolatory surrogate models are to be readily fitted through a collection of input-output points. The family of shapes defined by the level-set based geometry description includes cylindrical eddy-promoter configurations that have been examined previously, allowing improvements gained by a richer family of shapes to be identified. Additionally, the method uses a function superposition technique to define the geometries. It therefore can be extended in a straightforward manner by the superposition of additional functions to define richer families of geometries with more complex single body configurations, and configurations with more than two distinct bodies.

The surrogate framework has been extended in a number of ways. The formulation given in the thesis is applicable to a general, two performance metric, two output design problem. The performance metrics can be explicit functions of some or all of the inputs as well as of both outputs. The input variables that enter into the performance metrics only explicitly (i.e. the inputs that do not enter into the outputs) are handled independently from the modeled inputs (the inputs that enter through the outputs) so that as much analytic

information as possible is used. By validating the outputs instead of the performance metrics, flexibility is afforded the designer in that the validated outputs can be used any time in the future for other design problems using different performance metrics. If the performance metrics are validated, the designer is restricted to those functions for any future design studies.

A new formulation for the *a posteriori* error analysis, proximal candidates, has been derived. Previously, the proximal region error bounds similar to those given in Sections 4.4.1 and 5.4.1 were used. The proximal region error analysis bounds the truth values on points in a finite-sized subset of the prediction neighborhood. The proximal candidate error analysis bounds presented in Sections 4.4.2 and 5.4.2 apply to a randomly drawn input points selected from the prediction neighborhood according to the scaled validation sampling density. While the proximal region analysis provides a sense of stability to the results (not just one, but many designs near the surrogate predicted optimizer satisfy the bounds), the proximal candidate analysis gives a probabilistic bound on the truth performance for an actual design. If the designer determines the proximal candidate bounds to be satisfactory, the design process can be considered a success. In general, the proximal candidate bounds are likely to be sharper than those for the proximal region analysis.

Finally, by combining the surrogate optimization framework with a Pareto analysis for a two-criteria design problem, several benefits are realized. First, the Pareto analysis provides a great deal of information to the designer as to trade-offs and the results that is gives can be rapidly assessed. Little generality, in terms of applicability to other multicriteria formulations, is lost as was demonstrated in Section 2.4.2. Second, a full Pareto analysis is only possible under the best of circumstances. To be practical, the cost each evaluation of the performance metrics must be trivial. This qualification almost never applies for the truth (the simulation or the experiment) necessitating a surrogate approach. The combined surrogate-Pareto framework takes advantage of the inexpensive surrogates by using them to screen out uninteresting (non-Pareto-optimal) regions of the design space. The remaining space of surrogate-predicted, Pareto-optimal designs is used for any future design studies. Third, and finally, the Pareto analysis improves that predictability of the surrogate framework, error analysis. The scalarization procedure reduced the effective dimension of the design space from the number of inputs (M), to one less than the number of outputs. For the two-criteria eddy-promoter problem, the surrogates are validated for the predictability analysis over only a single dimension. This greatly increases the predictability of the results that suffers rapidly with increasing input dimension as demonstrated in Section 4.5.

The primary weakness of the surrogate framework is that the sharpness of the validation results suffers greatly as the input dimensionality increases. This weakness has been described in Section 4.5. For problems in which there are several performance metrics and in which there is a large number of inputs, it may be more practical to formulate the problem in

a Pareto sense. The Pareto formulation reduces the effective dimension of the problem and, provided there are only a few performance metrics, the predictability is greatly improved as was shown in Chapter 5. The baseline surrogate framework has been shown in prior work [77, 79] to be very efficient for problems with several inputs and a large number of outputs. The surrogate–Pareto approach provides a strategy for approaching problems with a large number of inputs and only a few outputs. Between the two surrogate frameworks, the only problems that are completely out of the question are those with a large number of inputs and a large number of outputs.

Appendix A

Plane Channel Heat Exchanger

In this appendix, the solution to the plane Poiseuille problem is presented. The channel problem can be solved exactly, and serves as a comparison to the eddy-promoter exchanger results presented in Chapter 5. The plane-channel can also be interpreted in a Pareto sense as a (admittedly trivial) trade-off problem with a single design variable $\eta_L = \frac{L'}{H'}$. The geometry for the plane channel is shown in Figure A-1. The lower wall of the channel is at $y = -1$ and the top wall at $y = 1$.

The nondimensional flow rate in the plane channel

$$Q = \int_{-1}^{1} u(x = 0, y, t)dy, \tag{A.1}$$

will be enforced to $Q = \frac{4}{3}$. With the flowrate fixed, the exact flow solution is

$$u^{PP}(x, y) = (1 - y^2), \tag{A.2}$$

$$v^{PP}(x, y) = 0. \tag{A.3}$$

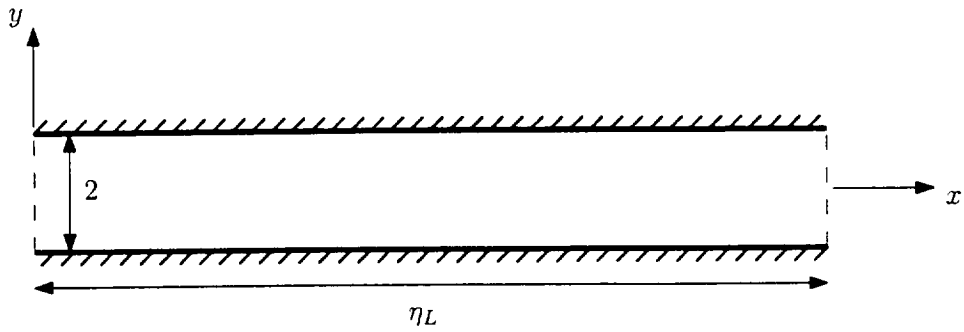

Figure A-1: Plane-Channel Heat Exchanger Geometry.

$$\theta^{PP}(x,y) = \frac{3}{4}\left(\frac{y^2}{2} - \frac{y^4}{12}\right) - \frac{y}{2}, \tag{A.4}$$

where the superscript 'PP' indicates the plane Poiseuille solution. The plane Poiseuille solution is steady and also invariant in the x-direction. The pressure forcing term on the right hand side of the x-momentum equation required to achieve the flowrate $Q = \frac{4}{3}$ is

$$f^{PP} = \frac{2}{Re}. \tag{A.5}$$

With the exact solutions given above, the plane Poiseuille outputs, analogous to $\theta_0(\mathbf{p}_m)$ and $\psi_0(\mathbf{p}_m)$ for the eddy-promoter, can be obtained analytically. The temperature output can be written as

$$\theta_0^{PP} = \overline{T_w - T_m}, \tag{A.6}$$

where T_w is the wall temperature and T_m is the mixed mean temperature

$$T_m = \frac{1}{Q}\int_{-1}^{1} u^{PP}(y)\theta^{PP}(y)dy. \tag{A.7}$$

The over-bar in A.6 means to average spatially over the periodicity cell length $l = 6.666$. The channel flow result for the temperature output is

$$\theta_0^{PP} = \overline{T_w} - \overline{T_m} = \frac{13}{16} - \frac{39}{560} = \frac{26}{35}. \tag{A.8}$$

The pressure output ψ_0^{PP} is identically given by Equation A.5

$$\psi_0^{PP} = \frac{2}{Re}. \tag{A.9}$$

The performance metrics can be formed by substituting the exact outputs in Equations A.8 and A.9 into the performance metric expressions in Equation 2.97 and 2.98. The resulting, exact performance metrics for the plane-channel heat exchanger are

$$\begin{aligned}\Theta^{PP}(\eta_L) &= \log_{10}\left[\frac{1}{RePr} + \theta_0^{PP}\frac{1}{\eta_L}\right] \\ &= \log_{10}\left[\frac{1}{RePr} + \frac{26}{35}\frac{1}{\eta_L}\right],\end{aligned} \tag{A.10}$$

$$\begin{aligned}\Psi^{PP}(\eta_L) &= \log_{10}\left[\psi_0^{PP} Re^3 \eta_L^3\right] \\ &= \log_{10}\left[2Re^2\eta_L^3\right].\end{aligned} \tag{A.11}$$

For the problems studied here, the Reynolds number has been fixed to $Re = 250$. The only remaining independent variable for the heat exchanger is the inverse height parameter

η_L. In this case, the Pareto-optimal output manifold $\partial\mathcal{A}^{PP}$ is identically the achievable set $\mathcal{A}^{PP}$. It is obtained by evaluating equations A.10 and A.11 for a range of $\eta_L \in \mathcal{Y} = [\eta_{L\,min}, \eta_{L\,max}]$. This has been done for $\eta_{L\,min} = 20.0$, $\eta_{L\,max} = 500.0$ and the results are plotted in Figure A-2. At the top of Figure A-2, the Pareto output curve with the pumping power metric $\Psi^{PP}(\eta_L)$ plotted versus the temperature performance metric Θ^{PP} is given. Directly below the Pareto curve is the inverse height parameter η_L plotted versus Θ^{PP}.

In Chapter5, the plane-channel heat exchanger is used as a reference case for evaluation of the eddy-promoter heat exchanger performace. Included on the Pareto-output plots presented for the eddy-promoter heat exhanger is the plane-channel Pareto curve. This curve has been obtained by by solving Equation A.10 for η_L over the range of temperature peformance metric values achieved by the eddy-promoter heat echanger. This η_L result is the inverse height value required by the plane-channel exchanger to achieve the given temperature performance which is then substituted into Equation A.11 to obtain the plane-channel exchanger pressure metric value that corresponds to the same temperature performance as the eddy-promoter heat exchanger.

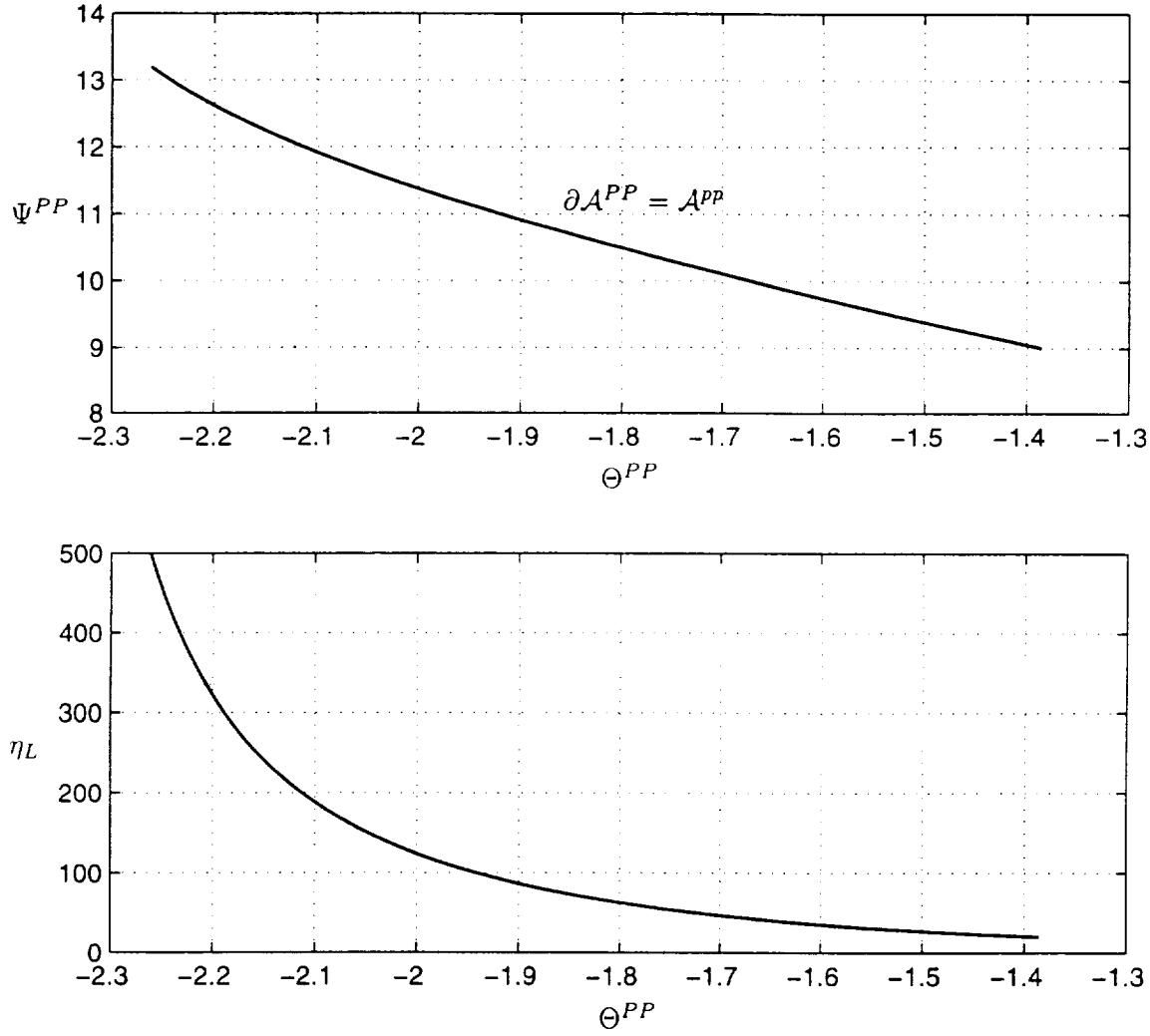

Figure A-2: Pareto–optimal output manifold (top) for the plane–channel exchanger and the channel inverse height versus the exchanger temperature peformance (bottom).

Appendix B

Surrogate Proofs

B.1 Baseline Surrogate Validation Proof

The relationship between the validation sample size theorem given in Equation 4.5 and the resulting validation statement given in Equation 4.8 can be proved using order statistics [15]. The proof of this result has been given previously in [36, 37, 77] and is included here for convenience. The proof is given for the most simple, single output function case, without error scaling functions is given in detail first. Finally, the generalization to the two output, scaled error analysis cases used throughout the thesis is given at the end of this appendix.

It is fist assumed that there is an input-output function $\mathcal{S}(\mathbf{p}) : \Omega \rightarrow I\!R$ and a corresponding surrogate $\tilde{\mathcal{S}}(\mathbf{p}) : \Omega \rightarrow I\!R$ to $\mathcal{S}(\mathbf{p})$. No assumptions are made as to the form, smoothness, or continuity of either $\mathcal{S}(\mathbf{p})$ or $\tilde{\mathcal{S}}(\mathbf{p})$ and, although in practice it is preferred that $\tilde{\mathcal{S}}(\mathbf{p})$ approximate $\mathcal{S}(\mathbf{p})$ as well as possible, the results are valid regardless of the quality of approximation. The model prediction error function $\mathcal{E}(\mathbf{p}) : \Omega \rightarrow I\!R$ is defined as

$$\mathcal{E}(\mathbf{p}) = |\mathcal{S}(\mathbf{p}) - \tilde{\mathcal{S}}(\mathbf{p})|. \tag{B.1}$$

A function $\mathcal{Z}(x) : [0, \infty) \rightarrow [0, 1]$ is introduced and is defined as

$$\mathcal{Z}(x) = \mu_\rho(\{\mathbf{p} \in \Omega \mid \mathcal{E}(\mathbf{p}) > x\}). \tag{B.2}$$

The function $\mathcal{Z}(x)$ gives the measure of the subset of the input domain Ω for which $\mathcal{E}(\mathbf{p})$ is strictly greater than $x \in [0, \infty)$. For situations in which there are regions of finite measure, $\Omega_c \subset \Omega$, for which $\mathcal{E}(\mathbf{p})$ is constant, $\{\mathcal{E}(\mathbf{p}) = x_c, \forall \mathbf{p} \in \Omega_c\}$, it is necessary to define the jump in $\mathcal{Z}(x)$ as

$$\lim_{y \searrow 0} (\mathcal{Z}(x_c - y) - \mathcal{Z}(x_c)) = \mu_\rho(\Omega_c). \tag{B.3}$$

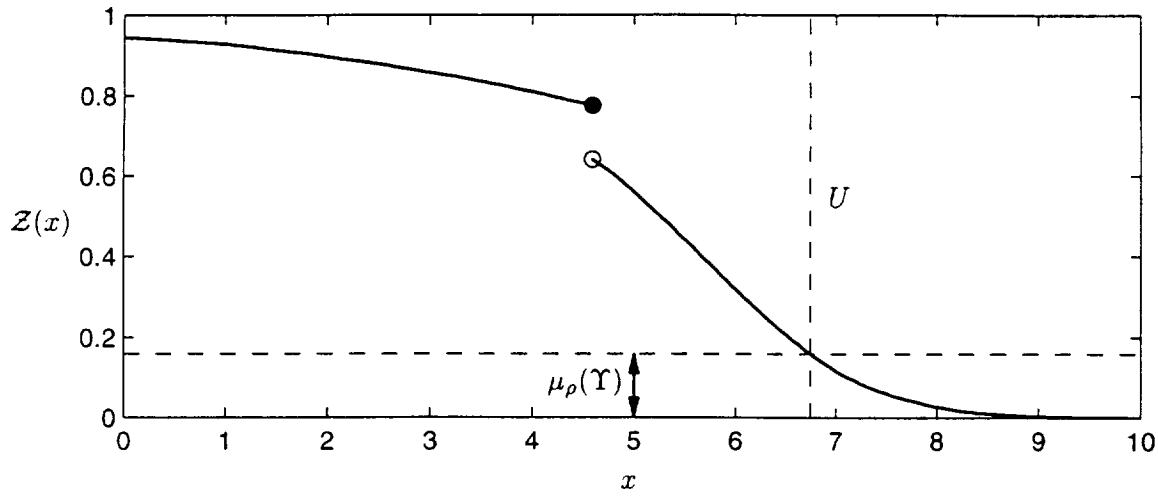

Figure B-1: Plot of the measure function $\mathcal{Z}(x)$ versus the surrogate error level x.

The model prediction error U is computed as

$$U = \max_{\{i=1,\ldots,N\}} |\mathcal{S}(\mathbf{P}_i) - \tilde{\mathcal{S}}(\mathbf{P}_i)| \tag{B.4}$$

where the input points $\mathbf{P}_1 \ldots, \mathbf{P}_N$ are drawn randomly according to the probability density function $\rho(\mathbf{p}) : \Omega \to \mathbb{R}$, $\mathbf{P}_i \sim \rho(\mathbf{p})$. The random, uncharacterized region is defined as

$$\Upsilon = \{\mathbf{p} \in \Omega \mid \mathcal{E}(\mathbf{p}) > U\}. \tag{B.5}$$

Next, a random variable $Z \in [0, 1]$ which is the measure of the random set Υ is introduced and defined as

$$Z = \mu_\rho(\Upsilon), \tag{B.6}$$

and the goal is to determine the cumulative distribution function for Z, $f_Z(z) = Pr\{Z \leq z\}$, from which the desired validation statement will follow directly.

If a variable x_z is introduced for $z \in [0, 1]$ and defined as

$$x_z = \min_{\{x \in [0,\infty) | \mathcal{Z}(x) \leq z\}} x, \tag{B.7}$$

it follows that

$$Pr\{\mathcal{Z}(U) \leq z\} = Pr\{U \geq x_z\}. \tag{B.8}$$

Introducing a set $\mathcal{D} \subset \Omega$ defined as

$$\mathcal{D} = \{\mathbf{p} \in \Omega \mid \mathcal{E}(\mathbf{p}) \geq x_z\}, \tag{B.9}$$

then the measure of the set $\mathcal{D}$, is given as

$$\mu_\rho(\mathcal{D}) = \inf_{\{x<x_z\}} \mathcal{Z}(x) \tag{B.10}$$

and can be bounded as

$$\mu_\rho(\mathcal{D}) \geq z. \tag{B.11}$$

From the definition for the model prediction error, the following statement can be made

$$\begin{aligned} Pr\{U \geq x_z\} &= Pr\{\exists j \in (1,\ldots,N) \mid \mathbf{P}_j \in \mathcal{D}\} \\ &= 1 - Pr\{\mathbf{P}_j \in \Omega \setminus \mathcal{D}, \forall j \in (1,\ldots,N)\}. \end{aligned} \tag{B.12}$$

By making use of the relationship that the validation points $\mathbf{P}_i$ are i.i.d., the probability that they will all lie outside of $\mathcal{D}$ can be evaluated as

$$\begin{aligned} Pr\{\mathbf{P}_j \in \Omega \setminus \mathcal{D}, \forall j \in (1,\ldots,N)\} &= (Pr\{\mathbf{P}_1 \in \Omega \setminus \mathcal{D}\})^N \\ &= (\mu_\rho(\Omega \setminus \mathcal{D}))^N \\ &= (1 - \mu_\rho(\mathcal{D}))^N. \end{aligned} \tag{B.13}$$

From B.10, it is known that $(1 - \mu_\rho(\mathcal{D})) \leq (1 - z)$, which gives

$$Pr\{\mathbf{P}_j \in \Omega \setminus \mathcal{D}, \forall j \in (1,\ldots,N)\} \leq (1 - z)^N, \tag{B.14}$$

and the cumulative distribution function $F_z(z)$ can then be bounded by $\hat{F}_z(z)$ as

$$F_z(z) \geq \hat{F}_z(z), \tag{B.15}$$

where

$$\hat{F}_z(z) = 1 - (1 - z)^N. \tag{B.16}$$

For cases in which $\mathcal{Z}(x)$ is continuous, $F_z(z) = \hat{F}_z(z)$. Note that, even with the strict inequality, $Pr\{Z < z\}$ satisfies

$$Pr\{Z < z\} \geq Pr\{\hat{F}_z(z)\} \tag{B.17}$$

although $Pr\{Z < z\} \geq Pr\{F_z(z)\}$ can be false for $\mathcal{Z}(x)$ discontinous.

Recognizing that ε_1 can be substitued for z in Equation B.16 and that $\varepsilon_2 = 1 - \hat{F}_z(z)$, and the solving for the sample size N, the validation sampling theorem follows

$$N = \left\lceil \frac{\ln \varepsilon_2}{\ln(1 - \varepsilon_1)} \right\rceil, \tag{B.18}$$

where $\lceil z \rceil$ is the smallest integer that is greater than z.

The extension to the two-output analysis cases examined in the body of this thesis is straighforward. By redefining the error function $\mathcal{E}(\mathbf{p})$ to be identical to the function validated in Equation 4.6

$$\mathcal{E}(\mathbf{p}) = \max\left(\frac{|\phi_1^T(\mathbf{P}_{mi}) - \widetilde{\phi_1}(\mathbf{P}_{mi})|}{\hat{g}_{\phi_1}(\mathbf{P}_{mi})}, \frac{|\phi_2^T(\mathbf{P}_{mi}) - \widetilde{\phi_2}(\mathbf{P}_{mi})|}{\hat{g}_{\phi_2}(\mathbf{P}_{mi})}\right), \tag{B.19}$$

the remainder of the analysis follows exactly as has been outlined above.

B.2 Predictability Analysis: Proximal Region

The proof of the predictability results given in Section 4.4 is based on the validation result in Equation 4.8. For a point $\mathbf{p}'_m$ to exist such that at least one of the outputs bounds

$$l_{o_1} \leq \phi_1^T(\mathbf{p}'_m) \leq u_{o_1}, \tag{B.20}$$

$$l_{o_2} \leq \phi_2^T(\mathbf{p}'_m) \leq u_{o_2}, \tag{B.21}$$

are not valid, the point would have to be in Υ. This follows from the result that if $\mathbf{p}'_m \in \Omega'_m \backslash \Upsilon$, then 4.8 holds, and the bounds given in Equations 4.16—4.19 hold as well.

The prediction region $\mathcal{P}^*_{\varepsilon_1}$ is selected by the designer. The worst case scenario in terms of the error bounds is for the prediction to fully contain the uncharacterized region Υ. If this is the case, then the region $\Gamma' \in \mathcal{P}^*_{\varepsilon_1}$ will exist given the strict inequality on the size of Υ in Equation 4.8. This result highlights the necessity of having a prediction region $\mathcal{P}^*_{\varepsilon_1}$ that is of at least ρ–measure ε_1.

The proof of the performance metric bounds in Equations 4.22—4.27 is similar. Because the output have been shown to be correctly bounded by 4.16—4.21 for $\mathbf{p}'_m \in \Gamma'_m$, then for points $\mathbf{p}' \in \Gamma'$, the metric bounds will hold as well.

B.3 Predictability Analysis: Proximal Candidates

The proof of the proximal candidate predictability result begins by considering the the error function $\mathcal{E}(\mathbf{p}) : \Omega \rightarrow I\!R$ defined as

$$\mathcal{E}(\mathbf{p}) = |\mathcal{S}(\mathbf{p}) - \tilde{\mathcal{S}}(\mathbf{p})|. \tag{B.22}$$

The validation sample set is formed by selecting N points, $\mathbf{P}_1, \ldots \mathbf{P}_N$, randomly according to probability density function $\rho(\mathbf{p})$. The validation sample set $\mathcal{X}^{va}$ is

$$\mathcal{X}^{va} = \{(\mathbf{P}_1, \mathcal{S}(\mathbf{P}_1)), \ldots, (\mathbf{P}_N, \mathcal{S}(\mathbf{P}_N)),\}, \quad \mathbf{P}_i \sim \rho(\mathbf{p}). \tag{B.23}$$

and the model prediction error is computed as

$$U = \max_{i \in \{1,\ldots,N\}} \mathcal{E}(\mathbf{P}_i) = \max_{i \in \{1,\ldots,N\}} |\mathcal{S}(\mathbf{P}_i) - \tilde{\mathcal{S}}(\mathbf{P}_i)|. \tag{B.24}$$

Next, the random variable $\overline{z}$ is introduced and is

$$\overline{z} = \int_{\Xi} \rho(\mathbf{p})\, d\mathbf{p} \tag{B.25}$$

where

$$\Xi = \{\mathbf{p} \in \Omega \mid \mathcal{E}(\mathbf{p}) \leq U\}. \tag{B.26}$$

The cumulative distribution function for $\overline{z}$, $F_{\overline{z}}(\overline{z})$, is

$$F_{\overline{z}}(\overline{z}) = \overline{z}^N. \tag{B.27}$$

which can be easily shown by order statistics [15]. The complement to $\overline{z}$, $z = 1 - \overline{z}$ is introduced and it follows that it has cumulative distribution function

$$F_z(z) = 1 - F_{\overline{z}}(z) = 1 - (1 - z)^N. \tag{B.28}$$

The random variable z is the ρ–measure of the uncharacterized region Υ. Next, consider a prediction region $\mathcal{P}_\sigma$, of ρ–measure σ. The expected fraction of designs $\mathcal{P}_\sigma$ for which $\mathcal{E}(\mathbf{p}) < U$ can be bounded by

$$a > \int_0^\sigma \left(\frac{\sigma - z}{\sigma}\right) f_z(z)\, dz \tag{B.29}$$

where $f_z(z)$ is the probability density function for z and is

$$f_z(z) = \frac{dF_z(z)}{dz} = N(1 - z)^{N-1}. \tag{B.30}$$

The integration in Equation B.29 gives the conditional expectation for the uncharacterized region completely inside of the prediction neighborhood. Substituting B.30 into B.29 gives

$$a > \int_0^\sigma \left(1 - \frac{z}{\sigma}\right) N(1 - z)^{N-1}\, dz \tag{B.31}$$

$$= 1 - \frac{1}{\sigma(N+1)} \left(1 - (1 - \sigma)^{N+1}\right). \tag{B.32}$$

Finally, recognizing that $a = 1 - \varepsilon_c$, the expression in Equation 4.37 and given in Section 4.4.2 is obtained

$$\varepsilon_c = \frac{1}{\sigma(N+1)}(1 - (1 - \sigma)^{N+1}). \tag{B.33}$$

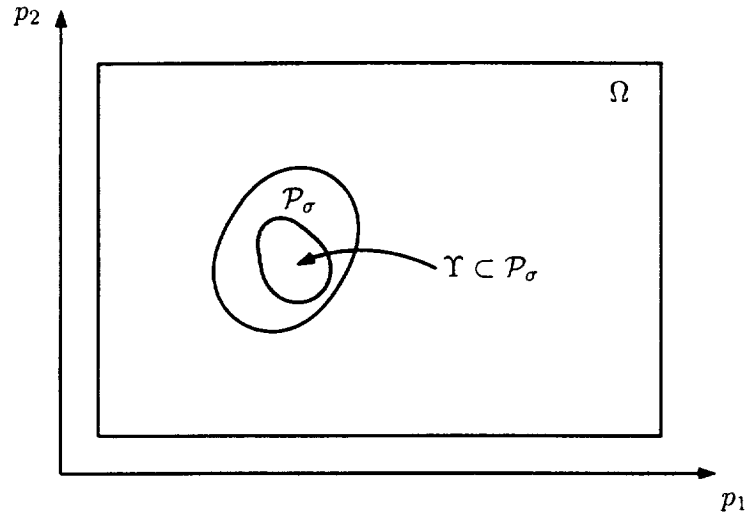

Figure B-2: Schematic of the input domain Ω, prediction region $\mathcal{P}_\sigma$, and uncharacterized region Υ which is contained completely inside of $\mathcal{P}_\sigma$.

B.4 Optimality Analysis

For a sequence of identically distributed, randomly selected inputs $\hat{\mathbf{P}}_1, \ldots, \hat{\mathbf{P}}_j$, is drawn according to the probability density function $\rho(\mathbf{p}_m)$. The random variable

$$L = \min j \text{ such that } \Phi_1(\hat{\mathbf{P}}_j) \leq \Phi_{1\min}, \text{ and } \Phi_2(\hat{\mathbf{P}}_j) \leq \Phi_{2\min}, \tag{B.34}$$

is introduced. It can then be shown that [36], for the validation sample size N, that

$$Pr\{L > l\} \geq \frac{N}{N+l}. \tag{B.35}$$

It follows that, for $\varepsilon_L \in]0,1[$, that if m is set such that

$$m \leq N\left(\frac{1}{\varepsilon_L} - 1\right), \tag{B.36}$$

that the probability of drawing a sequence of random input vectors $\hat{\mathbf{P}}_1, \ldots, \hat{\mathbf{P}}_m$ according to $\rho(\mathbf{p}_m)$ and finding a point such that both

$$\Phi_1(\phi_1(\hat{\mathbf{P}}_{m_j}), \phi_2(\hat{\mathbf{P}}_{m_j}), \hat{\mathbf{P}}_j) \leq \Phi_{1\min}, \tag{B.37}$$

$$\Phi_2(\phi_1(\hat{\mathbf{P}}_{m_j}), \phi_2(\hat{\mathbf{P}}_{m_j}), \hat{\mathbf{P}}_j) \leq \Phi_{2\min}, \tag{B.38}$$

is less than $1 - \varepsilon_L$. The lower bounds on the performance metrics are given by

$$\Phi_{1\min} = \min_{\{\mathbf{p}' \in \Omega', z_1 \in \mathcal{Z}_1^{\text{opt}}, z_2 \in \mathcal{Z}_2^{\text{opt}}\}} \Phi(z_1, z_2, \mathbf{p}'), \tag{B.39}$$

$$\Phi_{2\min} = \min_{\{\mathbf{p}' \in \Omega', z_1 \in \mathcal{Z}_1^{\text{opt}}, z_2 \in \mathcal{Z}_2^{\text{opt}}\}} \Phi(z_1, z_2, \mathbf{p}'), \tag{B.40}$$

where $\mathcal{Z}_1$ and $\mathcal{Z}_2$ are

$$\mathcal{Z}_1^{\text{opt}} = \{z \mid \forall \mathbf{p}'_m \in \Omega'_m,\ [\widetilde{\phi_1}(\mathbf{p}'_m) - U\hat{g}_{\phi_1}(\mathbf{p}'_m)] \le z \le [\widetilde{\phi_1}(\mathbf{p}'_m) + U\hat{g}_{\phi_1}(\mathbf{p}'_m)]\}, \tag{B.41}$$

$$\mathcal{Z}_2^{\text{opt}} = \{z \mid \forall \mathbf{p}'_m \in \Omega'_m,\ [\widetilde{\phi_2}(\mathbf{p}'_m) - U\hat{g}_{\phi_2}(\mathbf{p}'_m)] \le z \le [\widetilde{\phi_2}(\mathbf{p}'_m) + U\hat{g}_{\phi_2}(\mathbf{p}'_m)]\}. \tag{B.42}$$

For a point $\mathbf{p}'$ to have truth peformance metrics such that the lower bounds $\Phi_{1\min}$ and $\Phi_{2\min}$ in Equations B.37 and B.38 do not hold, the point must lie in Υ. If $\mathbf{p}' \in \Upsilon$, then the output bounds

$$[\widetilde{\phi_1}(\mathbf{p}'_m) - U\hat{g}_{\phi_1}(\mathbf{p}'_m)] \le \phi_1(\mathbf{p}'_m) \le [\widetilde{\phi_1}(\mathbf{p}'_m) + U\hat{g}_{\phi_1}(\mathbf{p}'_m)] \tag{B.43}$$

$$[\widetilde{\phi_2}(\mathbf{p}'_m) - U\hat{g}_{\phi_2}(\mathbf{p}'_m)] \le \phi_2(\mathbf{p}'_m) \le [\widetilde{\phi_2}(\mathbf{p}'_m) + U\hat{g}_{\phi_2}(\mathbf{p}'_m)] \tag{B.44}$$

embedded in Equations B.41 and B.42 will not hold, and the performance metrics evaluated at $\mathbf{p}'$ *can* satisfy Equations B.37 and B.38. Note that if the point $\mathbf{p}'$ is in Υ, there is no guarantee that the performance metrics will satisfy B.37 and B.38, only that the possibility exists, and the confidence level $1 - \varepsilon_L$ represents an upper bound.

A random variable $z = \mu_\rho(\Upsilon)$ is defined as the ρ–measure of the uncharacterized region Υ. It follows that

$$Pr\{L > l\} = \int_0^1 Pr\{L > l \mid z\} dF_Z. \tag{B.45}$$

It is assumed that the point $\mathbf{p}' \in \mathcal{R} \subset \Upsilon$ and that the measure of the subset $\mathcal{R}$ is given as $h(z) = \mu_\rho(\mathcal{R}) \le z$. The probability that of the l randomly drawn points that none of them lie in $\mathcal{R}$ is given by

$$\Pr\{\hat{\mathbf{P}}_j \notin \mathcal{R}(z),\ j = 1, \ldots, l\} = (1 - h(z))^l, \tag{B.46}$$

which is then substituted into Equation B.45 to obtain

$$\begin{aligned} Pr\{L > l\} &= \int_0^1 Pr\{L > l \mid z\} dF_Z && \text{(B.47)} \\ &= \int_0^1 (1 - h(z))^l dF_Z && \text{(B.48)} \\ &\ge \int_0^1 (1 - z)^l dF_Z && \text{(B.49)} \\ &\ge \int_0^1 (1 - z)^l d\widehat{F}_Z. && \text{(B.50)} \end{aligned}$$

The step in B.49 follows from the relationship that $h(z) \leq z$, and B.50 uses the results given in Equations B.15 and B.16. Finally, substituting Equation B.16 into Equation B.50 and evaluating the integral gives

$$Pr\{L > l\} \geq \int_0^1 (1-z)^l N(1-z)^{N-1}, \tag{B.51}$$

$$= \frac{N}{N+l}. \tag{B.52}$$

At this point, all that is left is to recognize that $Pr\{L > l\} = \varepsilon_L$ and to substitute into Equation B.52 to get the expression in Equation B.36.

Appendix C

Numerical Methods

C.1 Gaussian Quadrature

The general formula for the Gaussian quadrature used to evaluate the elemental matrices is detailed below. To approximate the integral of a function $g(\mathbf{x}) : \widehat{\Omega}^{k_e} \rightarrow I\!R$ over a triangular element, $\widehat{\Omega}^{k_e}$, the following quadrature rule is used

$$\int_{\widehat{\Omega}^{k_e}} g(\mathbf{x})\, d\mathbf{x} \approx A^{\widehat{\Omega}^{k_e}} \sum_{i=1}^{\mathcal{N}^q} \varpi_i g(\mathbf{x}(\boldsymbol{\xi}_i)). \tag{C.1}$$

where $A^{\widehat{\Omega}^{k_e}}$ is the area of the element, ϖ is the quadrature weight at that point, and $\mathbf{x}(\boldsymbol{\xi}_i)$ is the quadrature point position in terms of the barycentric coordinates $\boldsymbol{\xi}$. A Gaussian quadrature integration scheme that can exactly integrate a 5^{th}-order polynomial requires $\mathcal{N}^q = 7$ quadrature points. The weights ϖ_i and weight-points $\boldsymbol{\xi}_i = (\xi_{1i}, \xi_{2i}, \xi_{3i})$, $i = 1, \ldots, \mathcal{N}^q$ are listed in Table C.1 [39].

i	ϖ_i	ξ_{1i}	ξ_{2i}	ξ_{3i}
1	0.225	1/3	1/3	1/3
2	0.1323941527	a	b	b
3	0.1323941527	b	a	b
4	0.1323941527	b	b	a
5	0.1259391805	c	d	d
6	0.1259391805	d	c	d
7	0.1259391805	d	d	c

Table C.1: Fifth-order, Gaussian quadrature points, $\mathcal{N}^q = 7$: $a = 0.0597158717$, $b = 0.4701420641$, $c = 0.7974269853$, $d = 0.1012865073$.

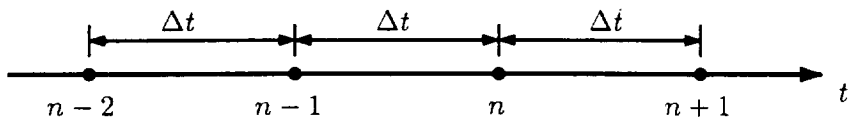

Figure C-1: Uniform-in-time difference mesh

C.2 Variable Time–Step, 3rd–Order Adams–Bashforth

C.2.1 Fixed Time–Step Schemes

The Adams-Bashforth difference schemes are a family of explicit, multipoint integration methods [11, 27]. In general, a k^{th}-order Adams-Bashforth scheme requires k function evaluations at time-steps $n, n-1, \ldots, n-k+1$. The general problem

$$u'(t) = f(u(t), t) \tag{C.2}$$

will be central to the discussion of this section.

The uniform, finite difference grid upon which the derivation is based is given in Figure C-1. To derive the 3rd-order Adams-Bashforth scheme for fixed time-step, Δt, the general form of the resulting scheme is assumed to be

$$u_{n+1} = u_n + \Delta t(\beta_0 f_n + \beta_1 f_{n-1} + \beta_1 f_n). \tag{C.3}$$

where the $u_m = u(m\Delta t)$, $f_m = f(u(m\Delta t), m\Delta t)$, and β_i, $i = 0, \ldots, 2$ are the unknown coefficients that must be determined to yield a 3rd-order scheme. Next, each term is expanded about time-step n with a Taylor series, noting that from Equation C.2 $u = f'$, and $u' = f''$. The Taylor series are substituted into Equation C.3, and the expressions for the coefficients are solved that eliminate 2nd-order and lower error terms. The result is the familiar 3rd-order, fixed Δt, Adams-Bashforth scheme [27].

$$u_{n+1} = u_n + \frac{\Delta t}{12}(23 f_n - 16 f_{n-1} + 5 f_n). \tag{C.4}$$

Because, the 3rd-order Adams-Bashforth scheme is fully explicit and has a very good combination of accuracy and stability properties, it is an attractive choice to advance the nonlinear convective part of the Navier-Stokes equations. The intersection of the region of stability with the Imaginary axis is 0.723. For the pure convection equation $u_t = uu_x$, the

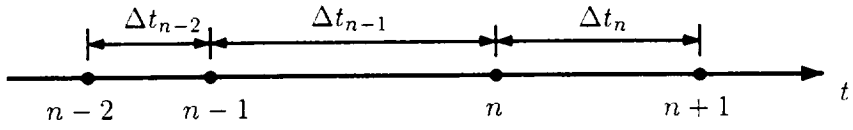

Figure C-2: Variable time step size difference mesh

stability limit is thus given as

$$\Delta t < 0.723 \frac{h}{\max(u)}. \tag{C.5}$$

The stability limit is known as the Courant condition.

C.2.2 Variable Time-Step Schemes

For problems in which the convective velocity varies significantly over time, a fixed time-step scheme is impractical. A solver constrained by a fixed step would require that the user be able to anticipate maximum convective velocity *a priori* so that the time-step could be set at the beginning of the run according to C.5. Not only is it difficult to anticipate the maximum convective velocity, for problems in which it varies significantly, such a restriction greatly increases the required number of steps and hence, the required computational time to obtain a solution. For these reasons, a variable time-step size version of C.4 is derived. In the following section, an Adams-Bashforth scheme consistent with the 2^{nd}-order time advancement is derived.

To proceed, the non-uniform finite difference grid shown in Figure C-2 is considered. Using the method of undetermined coefficients, the terms in Equation C.3 are first expanded about time-step n with a Taylor series:

$$u_{n+1} = u_n + a u'_n + \frac{a^2}{2} u''_n + \frac{a^3}{6} u'''_n + O(a^4) \tag{C.6}$$

$$u_{n-1} = u_n - b u'_n + \frac{b^2}{2} u''_n - \frac{b^3}{6} u'''_n + O(b^4) \tag{C.7}$$

$$f_n = u'_n \tag{C.8}$$

$$f_{n-1} = u'_n - b u''_n + \frac{b^2}{2} u'''_n - \frac{b^3}{6} u''''_n + O(b^4) \tag{C.9}$$

$$f_{n-2} = u'_n - c u''_n + \frac{c^2}{2} u'''_n - \frac{c^3}{6} u''''_n + O(c^4) \tag{C.10}$$

where, in the interest of brevity, $a = \Delta t_n$, $b = \Delta t_{n-1}$, and $c = \Delta t_{n-1} + \Delta t_{n-2}$. If Equations C.6—C.10 are substituted into C.3, and like terms are collected, the following set of

equations that must be satisfied to obtain a 3rd-order accurate scheme are obtained;

$$\begin{bmatrix} 1 & 1 & 1 \\ 0 & -b & -c \\ 0 & \frac{b^2}{2} & \frac{c^2}{2} \end{bmatrix} \begin{bmatrix} \beta_0 \\ \beta_1 \\ \beta_2 \end{bmatrix} = \begin{bmatrix} a \\ \frac{a^2}{2} \\ \frac{a^3}{6} \end{bmatrix}. \tag{C.11}$$

The matrix Equation C.11 is solved for β_0, β_1, and β_2. Substituting for a, b, and c, and simplifying gives the variable time-step size, 3rd-order Adams-Bashforth scheme [28]

$$u_{n+1} = u_n + \sum_{i=0}^{2} \beta_i f_{n-i} \tag{C.12}$$

where,

$$\beta_0 = \frac{\Delta t_n}{12}\left[\frac{12\Delta t_{n-1}(\Delta t_{n-1}+\Delta t_{n-2}) + 6\Delta t_n(2\Delta t_{n-1}+\Delta t_{n-2}) + 4\Delta t_n^2}{\Delta t_{n-1}(\Delta t_{n-1}+\Delta t_{n-2})}\right]. \tag{C.13}$$

$$\beta_1 = \frac{\Delta t_n}{12}\left[\frac{6\Delta t_n(\Delta t_{n-1}+\Delta t_{n-2}) + 4\Delta t_n^2}{\Delta t_{n-1}\Delta t_{n-2}}\right]. \tag{C.14}$$

$$\beta_2 = \frac{\Delta t_n}{12}\left[\frac{6\Delta t_n\Delta t_{n-1} + 4\Delta t_n^2}{\Delta t_{n-2}(\Delta t_{n-1}+\Delta t_{n-2})}\right]. \tag{C.15}$$

As expected, when $\Delta t_{n-2} = \Delta t_{n-1} = \Delta t_n = \Delta t$, the scheme in Equation C.4 is recovered.

The derivation of the 3rd-order Adams-Bashforth scheme consistent with the 2nd-order, backward difference, time advancement of the velocity is similar to the derivation just described. In this case, the resulting scheme must satisfy the difference form

$$\alpha_1 u_{n+1} + \alpha_2 u_n - \alpha_1 u_{n-1} = \beta_0 f_n + \beta_1 f_{n-1} + \beta_2 f_{n-2}. \tag{C.16}$$

where

$$\alpha_1 = \frac{2\Delta t_n + \Delta t_{n-1}}{\Delta t_n(\Delta t_n + \Delta t_{n-1})}, \quad \alpha_2 = -\frac{\Delta t_n + \Delta t_{n-1}}{\Delta t_n \Delta t_{n-1}}, \quad \alpha_3 = \frac{\Delta t_n}{\Delta t_{n-1}(\Delta t_n + \Delta t_{n-1})}. \tag{C.17}$$

Again, the Taylor series substitution into Equation C.16 is made and solved for β_i, $i = 0, \ldots, 2$ that eliminate all errors that are 2nd-order and lower. The resulting coefficients are

$$\beta_0 = \frac{\Delta t_n}{12}\left[\frac{12\Delta t_{n-1}(\Delta t_{n-1}+\Delta t_{n-2}) + 6\Delta t_n(2\Delta t_{n-1}+\Delta t_{n-2}) + 4\Delta t_n^2}{\Delta t_{n-1}(\Delta t_{n-1}+\Delta t_{n-2})}\right], \tag{C.18}$$

$$\beta_1 = \frac{\Delta t_n}{12}\left[\frac{6\Delta t_n(\Delta t_{n-1}+\Delta t_{n-2}) + 4\Delta t_n^2}{\Delta t_{n-1}\Delta t_{n-2}}\right], \tag{C.19}$$

$$\beta_2 = \frac{\Delta t_n}{12}\left[\frac{6\Delta t_n \Delta t_{n-1} + 4\Delta t_n^2}{\Delta t_{n-2}(\Delta t_{n-1} + \Delta t_{n-2})}\right]. \tag{C.20}$$

For the fixed time-step case in which $\Delta t_{n-2} = \Delta t_{n-1} = \Delta t_n = \Delta t$, the coefficients reduce to

$$\beta_0 = \frac{\Delta t_n}{12}, \qquad \beta_1 = \frac{\Delta t_n}{12}, \qquad \beta_2 = \frac{\Delta t_n}{12}. \tag{C.21}$$

Appendix D

Surrogate Models

D.1 Radial Basis Function

We use a radial basis function model as a surrogate. Radial basis functions are a well known class of fuctions used in a number of applications [18]. We begin the description of the surrogate used by assuming that we want to construct a surrogate model valid in the design space $\Omega \in I\!R^M$ for the general function $f(\mathbf{p}) : \Omega \rightarrow I\!R$. $\tilde{f}(\mathbf{p}) \approx f(\mathbf{p})$. The radial basis function surrogate has the general form

$$\tilde{f}(\mathbf{p}) = \sum_{i=1}^{N^{co}} a_i \varphi_i(r_i(\mathbf{p})) + P_m(\mathbf{p}) \tag{D.1}$$

where $\varphi_i(r_i(\mathbf{p}))$ is the radial basis function and $P_m(\mathbf{p})$ is the polynomial of degree $m-1$. For a d-dimension input space, we use the notation $\mathbf{p} = \{p_1, \ldots, p_d\}$ and $\mathbf{p}_i^{co} = \{p_{i,1}^{co}, \ldots, p_{i,d}^{co}\}$. Given this notation, the radius $r_i(\mathbf{p})$ is simply the Euclidean distance from construction point i

$$r_i(\mathbf{p}) = \left[\sum_{j=1}^{d} (p_{i,j}^{co} - p_j)^2 \right]^{\frac{1}{2}}, \quad i = 1, \ldots, N^{co}. \tag{D.2}$$

For the surrogate used in the work reported here, we have used the radial basis function $\varphi(r) = r^{2(m-1)} \log r$ and have set $m = 2$. The coefficients a_i of the general form (D.1) are determined from

$$\sum_{i=1}^{N^{co}} a_i \varphi_i(r_i(\mathbf{p}_k^{co})) + \sum_{j=1}^{d} b_j q_j(\mathbf{p}_k^{co}) = f(\mathbf{p}_k^{co}), \quad k = 1, \ldots, N^{co}, \tag{D.3}$$

$$\sum_{i=1}^{N^{co}} a_i q_j(\mathbf{p}_i^{co}) = 0, \quad j = 1, \ldots, d+1. \tag{D.4}$$

The polynomial contribution for $m = 2$ is $\mathbf{q}(\mathbf{p}_i^{co}) = \{1, p_{i,1}^{co}, \ldots, p_{i,d}^{co}\}^T$.

Appeals to the simulation provide $f(\mathbf{p}_j^{co})$. The solution for the unknown coefficients $\mathbf{a} = \{a_1, \ldots, a_{N^{co}}\}^T$ and $\mathbf{b} = \{b_1, \ldots, b_{d+1}\}^T$ is the solution to the following matrix equation

$$\begin{bmatrix} \mathbf{A}_{RBF} & \mathbf{E}_{RBF} \\ \mathbf{E}_{RBF}^T & \mathbf{0} \end{bmatrix} \begin{bmatrix} \mathbf{a} \\ \mathbf{b} \end{bmatrix} = \begin{bmatrix} \mathbf{f} \\ \mathbf{0} \end{bmatrix}, \tag{D.5}$$

where $\mathbf{f} = \{f(\mathbf{p}_1^{co}), \ldots, (\mathbf{p}_{N^{co}}^{co})\}^T$ is the solution vector at the construction points. There is a very real possibility that the matrix equation (D.5) could be ill-conditioned [18], but for all of the models generated here for a modest number of construction points (on the order of a couple of hundred), we have not experienced any difficulties with the required inversion.

D.2 Orthogonal Arrays

A critical consideration in approximate optimization approaches is how to best select construction points from the input domain Ω in order to extract as much information as possible without having to sample at an inordinate number of points. The method used to select points for the output surrogates constructed in Sections 4.1 and 5.1.1 is based on the work of Bose [8, 9]. The methods have formulated and coded into C-routines by Owen [58], and are part of a very useful package for generating experimental designs.

The array that has been generated for the eddy-promoter surrogate construction point selection has $k = 3$ columns, strength $t = 2$, and $q = 11$ levels [58]. An orthogonal array of strength t is a matrix with n rows and k columns such that for any $n \times t$ sub-matrix, the q^t possible rows occur the same number of times. The strength $k = 2$ array with $q = 11$ levels has $N^{orth} = q^k = 121$ rows (input points). The rows were permuted and the construction points were selected from the $N^{orth} = 121$, randomly permuted, orthogonal array points.

Bibliography

[1] G. Anagnostou, E. M. Ronquist, and A. T. Patera. A computational procedure for part design. *Computer Methods in Applied Mechanics and Engineering*, 97:33–48, 1992.

[2] H. Ashley and M. Landahl. *Aerodynamics of Wings and Bodies*. Dover Publications Inc., New York, 1985. Originally published by Addison-Wesley Publishing Company, Reading, MA, 1965.

[3] J. M. Barthelemy and R. Haftka. Approximation concepts for optimum structural design — a review. *Structural Optimization*, 5:129–144, 1993.

[4] M. P. Bendsoe. *Optimization of Structural Topology, Shape, and Material*. Springer-Verlag, Berlin, 1995.

[5] M. P. Bendsoe and N. Kikuchi. Generating optimal topologies in structural design using a homogenization method. *Computer Methods in Applied Mechanics and Engineering*, 71:197–224, 1988.

[6] M. P. Bendsoe and C. A. Mota Soares, editors. *Topology Design of Structures*. Kluwer Academic Publishers, Dordrecht, 1993. Proceedings of the NATO Advanced Research Workshop on Topology Design of Structures at Sesibra, Portugal, June 20–26, 1992.

[7] T. Bohlin. *Interactive System Identification: Prospects and Pitfalls*. Springer-Verlag, Berlin, 1991.

[8] R. C. Bose. *Sankhya*, 3:323–338, 1938.

[9] R. C. Bose and K. A. Bush. Orthogonal arrays of strength two and three. *Annals of Mathematical Statistics*, 23:508–524, 1952.

[10] G. E. P. Box and N. Draper. *Empirical Model Building and Response Surfaces*. John Wiley & Sons, 1987.

[11] R. L. Burden and J. D. Faires. *Numerical Analysis*. PWS-Kent, Boston, 1989.

[12] J. Cea. Numerical methods of shape optimal design. In E. J. Haug and J. Cea, editors, *Optimization of Distributed Parameter Structures*, volume II, pages 1049–1087. Sijthoff & Noordhoff, Rockville, MD, 1981.

[13] D. L. Chopp. Computing minimal surfaces via level set curvature flow. *Journal of Computational Physics*, 106:77–91, 1993.

[14] I. Das and J. Dennis. Normal-boundary intersection: A new method for generating pareto optimal points in multicriteria optimization problems. *CAAM Technical Report*, TR 96–19, 1996. To appear in the SIAM Journal of Optimization.

[15] H. A. David. *Order Statistics*. John Wiley and Sons, New York, 1981.

[16] A. R. Díaz and M. P. Bendsoe. Shape optimization of structures for multiple loading conditions using a homogenization method. *Structural Optimization*, 4:17–22, 1992.

[17] P. G. Drazin and W. H. Reid. *Hydrodynamic Stability*. Cambridge University Press, Cambridge, 1981.

[18] N. Dyn, D. Levin, and S. Rippa. Numerical procedures for surface fitting of scattered data by radial functions. *SIAM Journal of Scientific Computing*, 7(2):100–100, 1986.

[19] E. R. G. Eckert, T. F. Irvine, Jr., R. J. Goldstein, and J. P. Hartnett. *Heat Transfer Reviews, 1976–1986*. John Wiley and Sons, New York, 1990.

[20] F. Y. Edgeworth. *Mathematical Physics*. P. Keagan, London, 1881.

[21] W. C. Engelund, D. O. Stanley, R. A. Lepsch, M. M. McMillin, and R. Unal. Aerodynamic configuration design using response surface methodology analysis. Technical report, AIAA Paper 93–3967, 1993.

[22] H. A. Eschenauer. Multicriteria optimization techniques for highly accurate focusing systems. In W. Stadler, editor, *Multicriteria Optimization and Engineering and in the Science*, pages 309–354. Plenum Press, New York, 1988.

[23] P. F. Fisher and A. T. Patera. Parallel simulation of viscous incompressible flows. *Annual Review of Fluid Mechanics*, 26:483–527, 1994.

[24] R. L. Fox. *Optimization Methods for Engineering Design*. Addison Wesley, 1971.

[25] A. P. Fraas. *Heat Exchanger Design*. John Wiley and Sons, New York, second edition, 1989.

[26] S. I. Gallant. A connectionist learning algorithm with provable generalization and scaling bounds. *Neural Networks*, 3:191–201, 1990.

[27] C. W. Gear. *Numerical Initial Value Problems in Ordinary Differential Equations.* Prentice Hall, Inc., Englewood Cliffs, New Jersey, 1971.

[28] C. Ghaddar. *Parallel Analytico-Computational Methods for Multicomponent Media: Application to Thermal Composites and Porous-Media Flows.* PhD thesis, Massachusetts Institute of Technology, 1995.

[29] C. Ghaddar, Y. Mady, and A. T. Patera. Analysis of a part design procedure. *Numerische Mathematik*, 71:465–510, 1995.

[30] N. K. Ghaddar, G. E. Karniadakis, and A. T. Patera. A conservative isoparametric spectral element method for forced convection: application to fully developed flow in periodic geometries. *Numerical Heat Transfer*, 9:277–300. 1986.

[31] G. H. Golub and C. F. Van Loan. *Matrix Computations.* Johns Hopkins University Press. Baltimore, Maryland, 1983.

[32] A. A. Guinta, V. Balabonov, M. Kaufman, S. Burgee, B. Grossman, R. T. Haftka, W. H. Mason, and L. T. Watson. Variable-complexity response surface design of an HSCT configuration. In N. M. Alexandrov and M. Y. Hussaini, editors, *Multidisciplinary Design Optimization: State of the Art*, pages 348–367, 1995.

[33] M. D. Gunzburger. *Finite Element Methods for Viscous Incompressible Flows: A Guide to Theory, Practice, and Algorithms.* Academic Press, 1989.

[34] R. T. Haftka and M. P. Kamat. *Elements of Structural Optimization.* Nijhoff Publishers, Netherlands, 1985.

[35] J. Jahn and W. Krabs. Applications of multicriteria optimization in approximation theory. In W. Stadler, editor, *Multicriteria Optimization and Engineering and in the Science*, pages 49–75. Plenum Press, New York, 1988.

[36] M. E. Kambourides. Nonparametric-validated computer-simulation surrogates: A pareto formulation. Master's thesis, Massachusetts Institute of Technology, 1997.

[37] M. E. Kambourides, S. Yeşilyurt, and A. T. Patera. Nonparametric–validated computer–simulation surrogates: A pareto formulation. *International Journal of Numerical Methods in Engineering*, to appear.

[38] K. Karamcheti. *Principles of Ideal-Fluid Aerodynamics.* Robert E. Krieger Publishing Company, Malabar, Florida, 1966. Reprinted by John Wiley & Sons, Inc., 1980.

[39] H. Kardestuncer, editor. *Finite Element Handbook.* McGraw Hill, New York, 1987.

[40] G. E. Karniadakis, B. B. Mikic, and A. T. Patera. Minimum-dissipation transport enhancement by flow destabilization: Reynolds' analogy revisited. *Journal of Fluid Mechanics*, 192:365-391, 1988.

[41] H. Kozlu, B. B. Mikic, and A. T. Patera. Minimum-dissipation heat removal by scale-matched flow destabilization. *International Journal of Heat and Mass Transfer*, 31(10):2023-2032, 1988.

[42] A. M. Kuethe and C.-Y. Chow. *Foundations of Aerodynamics: Bases of Aerodynamic Design*. John Wiley & Sons, Inc., New York, fourth edition, 1986.

[43] K. S. Kundert. Sparse matrix techniques. In A. Ruehli, editor, *Circuit Analysis, Simulation and Design*. North-Holland, 1986.

[44] D. Landman and C. P. Britcher. Advanced experimental methods for multi-element airfoils. Technical report, AIAA Paper 95-1784, 1995.

[45] D. Landman and C. P. Britcher. Experimental optimization methods for multi-element airfoils. Technical report, AIAA Paper 96-2264, 1996.

[46] Y. Maday, D. Meiron, A. T. Patera, and E. M. Ronquist. Analysis of iterative methods for the steady and unsteady stokes problem: Application to spectral element discretizations. *SIAM Journal of Scientific Computing*, 14:310-337, 1993.

[47] The MathWorks Inc., Natick, Ma. MATLAB *Reference Guide*, 1992.

[48] M. D. McKay, R. J. Beckman, and W. J. Conover. A comparison of three methods for selecting values of input variables in the analysis of output from a computer code. *Technometrics*, 21:239-245, 1979.

[49] A. Nakayama, H.-P. Kreplin, and H. L. Morgan. Experimental investigation of flowfield about a multielement airfoil. *AIAA Journal*, 28(1):14-21, 1990.

[50] National Instruments Corporation. *LabView for Windows User Manual*, 1993.

[51] J. A. Nelder and R. Mead. A simplex method for function minimization. *Computer Journal*, 7:308-313, 1965.

[52] Y.-L. O, A. Toet, D. Foster, H. J. A. M. Heijmans, and P. Meer, editors. *Shape in Picture: Mathematical Description of Shape in Grey-Level Images*. Springer-Verlag, Berlin, 1992.

[53] S. Osher and J. A. Sethian. Fronts propagating with curvature-dependent speed: Algorithms based on Hamilton-Jacobi formulations. *Journal of Computational Physics*, 79:12-49, 1987.

[54] J. C. Otto, D. Landman, and A. T. Patera. A surrogate approach to the experimental optimization of multielement airfoils. Technical report, AIAA Paper 96–4138CP, 1996.

[55] J. C. Otto, M. Paraschivoiu, S. Yeşilyurt, and A. T. Patera. Bayesian-validated computer-simulation surrogates for optimization and design. In N. M. Alexandrov and M. Y. Hussaini, editors, *Multidisciplinary Design Optimization: State of the Art*, pages 368–392, 1995.

[56] J. C. Otto, M. Paraschivoiu, S. Yeşilyurt, and A. T. Patera. Computer–simulation surrogates for optimization: Application to trapezoidal ducts and axisymmetric bodies. Technical report, Proceedings of the Forum on CFD for Design and Optimization, ASME International Mechanical Engineering Conference and Exposition, 1995.

[57] J. C. Otto, M. Paraschivoiu, S. Yeşilyurt, and A. T. Patera. Bayesian-validated computer-simulation surrogates for optimization and design: Error estimates and applications. *IMACS Journal of Mathematics and Computers in Simulation*, 1997. to appear.

[58] A. B. Owen. Orthogonal arrays for computer experiments, integration and visualization. *Statistica Sinica*, 2(2):439–452, 1992.

[59] V. Pareto. *Manual of Political Economy*. The McMillan Press Ltd., London–Basingslohe, 1971. Translation of the French edition by A. S. Schwier.

[60] W. C. Reynolds and M. C. Potter. Finite–amplitude instability of parallel shear flows. *Journal of Fluid Mechanics*, 27:465–492, 1967.

[61] T. Rowan. *Functional Stability, Analysis of Numerical Algorithms*. PhD thesis, University of Texas, Austin, TX, 1990.

[62] G. A. F. Seber and C. J. Wild. *Nonlinear Regression*. John Wiley and Sons, New York, 1989.

[63] A. A. Seireg and J. Rodriguez. *Optimizing the Shape of Mechanical Elements and Structures*. Marcel Dekker, Inc., New York, 1997.

[64] J. A. Sethian. *Level Set Methods: Evolving Interfaces in Geometry, Fluid Mechanics, Computer Vision, and Materials Science*. Cambridge University Press, Cambridge, 1996.

[65] J. Sokolowski and J.-P. Zolesio. *Introduction to Shape Optimization: Shape Sensitivity Analysis*. Springer–Verlag, Berlin, 1992.

[66] W. Stadler, editor. *Multicriteria Optimization and Engineering and in the Science*. Plenum Press, New York, 1988.

[67] D. O. Stanley, W. C. Engelund, R. A. Lepsch, M. M. McMillin, K. E. Wurster, R. W. Powell, A. A. Guinta, and R. Unal. Rocket-powered single-stage vehicle configuration selection and design. Technical report, AIAA Paper 93-1053, 1993.

[68] G. Strang. *Introduction to Applied Mathematics.* Wellesley-Cambridge Press, Wellesley, Massachusetts, 1986.

[69] G. Strang and G. J. Fix. *An Analysis of the Finite Element Method.* Prentice-Hall, Englewood Cliffs, New Jersey, 1973.

[70] C. Taylor and P. Hood. A numerical solution of the navier-stokes equations using the finite element method. *Computers and Fluids*, 1:73-100, 1973.

[71] P. T. Thatch, H. Konno, and D. Yokota. Dual approach to minimization on the set of pareto-optimal solutions. *Journal of Mathematics and Analytical Applications*, 98:562-580, 1984.

[72] J. Thomsen. Topology optimization of structures composed of one or two materials. *Structural Optimization*, 5:108-115, 1992.

[73] J. F. Traub, G. W. Wasilkowski, and H. Woźniakowski. *Information-Based Complexity.* Academic Press, San Diego, 1988.

[74] L. G. Valiant. A theory for the learnable. *CACM*, 27:1134-1142, 1989.

[75] G. N. Vanderplaats. *Numerical Optimization Techniques for Engineering Design: With Applications.* McGraw Hill, New York, 1984.

[76] G. Walker. *Industrial Heat Exchangers: A Basic Guide.* Hemisphere Publishing Co., New York, second edition, 1990.

[77] S. Yeşilyurt. *Construction and Validation of Computer-Simulation Surrogates For Engineering Design and Optimization.* PhD thesis, Massachusetts Institite of Technology, Cambridge, MA, 1995.

[78] S. Yeşilyurt, C. Ghaddar, M. Cruz, and A. T. Patera. Bayesian-validated surrogates for noisy computer simulations; application to random media. *SIAM Journal of Scientific Computing*, to appear.

[79] S. Yeşilyurt and A. T. Patera. Surrogates for numerical simulations: optimization of eddy-promoter heat exchangers. *Comp. Methods Appl. Mech. Engr.*, 121:231-257, 1995.

[80] J.-P. Zolesio. The material derivative (or speed) method for shape optimization. In E. J. Haug and J. Cea, editors, *Optimization of Distributed Parameter Structures*, volume II, pages 1089–1151. Sijthoff & Noordhoff, Rockville, MD, 1981.